Photopyroelectric study of thermal properties and phase transitions in selected solids

Thesis submitted to
COCHIN UNIVERSITY OF SCIENCE AND TECHNOLOGY
in partial fulfilment of the requirements for the award of the degree of
DOCTOR OF PHILOSOPHY

By

Preethy Menon C

Department of Instrumentation
Cochin University of Science and Technology
Cochin – 682 022

September 2001

CERTIFICATE

Certified that the work presented in this thesis is based on the bona fide work done by Ms. Preethy Menon C under my guidance in the Department of Instrumentation, Cochin University of Science and Technology, and has not been included in any other thesis submitted previously for the award of any degree.

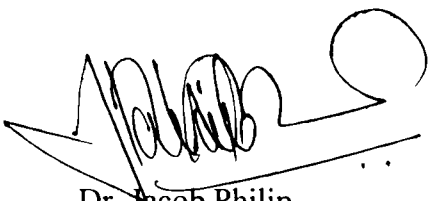

Cochin-682022

2nd September, 2001

Dr. Jacob Philip

Supervising Guide

DECLARATION

Certified that the work presented in this thesis is based on the original work done by me under the guidance of Dr. Jacob Philip, Professor, Department of Instrumentation, Cochin University of Science and Technology, and has not been included in any other thesis submitted previously for the award of any degree.

Preethy Menon

Cochin-682022

Preethy Menon C

2nd September, 2001

Contents

PREFACE

In recent years there has been an increasing interest in optically excited thermal processes, known as photothermal effects, which use lasers as optical heat sources. The photothermal effect in a material is a consequence of the deposition of heat in the sample following absorption of a light beam and subsequent thermal deexcitaions, or other nonthermal deexcitation processes, which result in the indirect heating of the sample. If the excitation is modulated, the corresponding temperature variations developed in the sample gives rise to a variety of different effects and most directly, to periodic temperature variations of the sample, which constitute the basis for a distinct experimental technique, known as photopyroelectric (PPE) effect.

The PPE technique involves measurement of the temperature variations in the sample due to absorption of radiation, by placing a pyroelectric detector in thermal contact with the sample. The PPE technique is the only technique based on the direct detection of photothermal heating, and therefore has a number of advantages over other detection schemes involving secondary mechanisms (like photoacoustic technique). A PPE experiment is rather simple to design and the materials that can be investigated range from weakly absorbing solids like thin films or liquids, to strongly absorbing solids and liquids or highly diffusing materials.

Even though much progress has been made on both theoretical and experimental fronts, enough efforts have not been made to exploit the advantages of the photopyroelectric technique in the measurement of thermal parameters, like thermal diffusivity (α), thermal effusivity (e), thermal conductivity (K) and heat capacity (c_p) of solid samples. The technique is particularly useful to study thermal

properties of samples undergoing transitions such as ferroelectric phase transitions, metal-insulator transitions etc. In this thesis we present the results of our systematic investigation of the variations in the thermal parameters across phase transitions in selected systems employing photopyroelectric technique.

Para-ferroelectric phase transitions are always associated with atomic rearrangements or structural changes. The change of structure during a phase transition can occur in two distinct ways. Firstly, there are transitions where the atoms of a solid reconstruct a new lattice as in the case of an amorphous solid changing to a crystalline state. Secondly, there are transitions where a regular lattice is distorted slightly without disrupting the linkage of the network. This can occur as a result of small displacements in the lattice position of single atoms or groups, or the ordering of molecules among various equivalent positions. Most of the ferroelectric phase transitions belong to the second group.

Since all the phase transitions involve configurational changes, one can identify a physical quantity that is characteristic of the new ordered configuration. Such a concept of order parameter was introduced by Landau. In a ferroelectrc transition the order parameter is the spontaneous polarization and he expanded the Gibbs free energy in powers of the order parameter in the vicinity of a transition where the value of order parameter is very small. Accordingly, a transition is said to be of the same order as the derivative of the Gibb's function, which shows a discontinuous change at the transition. If there is a discontinuity in quantities such as volume and entropy, which are first order derivatives of Gibb's function, the transition is said to be of first order. If specific heat, compressibility, thermal expansion etc. are quantities undergoing discontinuity, which are second order

derivatives of Gibb's free energy function, the transition is said to be second order. Our aim has been to study the variations of heat capacity and thermal conductivity of selected ferroelectrics and analyze the nature of phase transitions associated with it.

Mixed valence perovskites, with the general formula $R_{1-x}A_xMnO_3$ with (R = La, Nd or Pr and A = Ba, Ca, Sr or Pb) have been the materials of intense experimental and theoretical studies over the past few years. These materials show colossal magneto resistance (CMR) in samples with $0.2 < x < 0.5$. In such a doping region, resistivity exhibits a peak at temperature $T = T_p$, the metal-insulator transition temperature. The system exhibits metallic characteristics with $d\rho / dT > 0$ below T_p (where ρ is the resistivity of the sample) and insulating characteristics with $d\rho / dT < 0$ above T_p. Despite intensive investigations of the CMR phenomena and associated electrical properties, not much work has been done on the variation of thermal parameters of these samples.

In this thesis, we have taken up work on photopyroelectric investigation of thermal parameters of ferroelectric crystals such as Glycine phosphite ($NH_3CH_2COOH_3PO_3$), Triglycine sulfate and Thiourea, and mixed valence perovskite samples such as Lead doped Lanthanum Manganate ($La_{1-x}Pb_xMnO_3$), Calcium doped Lanthanum Manganate ($La_{1-x}Ca_xMnO_3$) and Nickel doped Lanthanum Stroncium Cobaltate ($La_{0.5}Sr_{0.5}Ni_{1-x}Co_xO_3$).

The thesis is organized into eight chapters as outlined in the following paragraphs. To place the work in a better perspective, a detailed review of the photopyroelectric technique and its theory are presented in the first section of the introductory chapter. In the following section, Landau theory of ferroelectric phase

derivatives of Gibb's free energy function, the transition is said to be second order. Our aim has been to study the variations of heat capacity and thermal conductivity of selected ferroelectrics and analyze the nature of phase transitions associated with it.

Mixed valence perovskites, with the general formula $R_{1-x}A_xMnO_3$ with (R = La, Nd or Pr and A = Ba, Ca, Sr or Pb) have been the materials of intense experimental and theoretical studies over the past few years. These materials show colossal magneto resistance (CMR) in samples with $0.2 < x < 0.5$. In such a doping region, resistivity exhibits a peak at temperature $T = T_p$, the metal-insulator transition temperature. The system exhibits metallic characteristics with $d\rho / dT > 0$ below T_p (where ρ is the resistivity of the sample) and insulating characteristics with $d\rho / dT < 0$ above T_p. Despite intensive investigations of the CMR phenomena and associated electrical properties, not much work has been done on the variation of thermal parameters of these samples.

In this thesis, we have taken up work on photopyroelectric investigation of thermal parameters of ferroelectric crystals such as Glycine phosphite ($NH_3CH_2COOH_3PO_3$), Triglycine sulfate and Thiourea, and mixed valence perovskite samples such as Lead doped Lanthanum Manganate ($La_{1-x}Pb_xMnO_3$), Calcium doped Lanthanum Manganate ($La_{1-x}Ca_xMnO_3$) and Nickel doped Lanthanum Stroncium Cobaltate ($La_{0.5}Sr_{0.5}Ni_{1-x}Co_xO_3$).

The thesis is organized into eight chapters as outlined in the following paragraphs. To place the work in a better perspective, a detailed review of the photopyroelectric technique and its theory are presented in the first section of the introductory chapter. In the following section, Landau theory of ferroelectric phase

transitions and a detailed review on the thermal conductivity and heat capacity measurements in these types of samples is given. In the last section of chapter 1, an elaborate introduction to materials exhibiting metal-insulator transition and various models employed to explain the phenomena are given.

In the second chapter we present an improved photopyroelectric technique, which we have developed, for the simultaneous determination of thermal parameters using a pyroelectric transducer kept in contact with a thermally thick backing medium. The principle of the technique, calibration of the experimental set up and measurement technique are described in detail in this chapter. In order to see how well the technique enables one to measure the above thermal parameters during phase transitions, we have carried out investigations on Triglycine sulfate (TGS), which undergoes a para-ferroelctric phase transition at 49.4 ^{0} C. The PPE technique enables one to measure the anisotropy in thermal conductivity in crystalline samples. The results of these measurements on TGS are presented and discussed in the last section of chapter 2.

Chapter 3 highlights the studies carried out on ferroelectric glycine phosphite (GPI) single crystals. The crystal has a monoclinic structure and is reported to have a para-ferroelectric phase transition at 224 K. Details of crystal growth, identification of crystal morphology, sample preparation and measurement of all the four thermal parameters (thermal diffusivity, thermal effusivity, heat capacity and thermal conductivity) of GPI are outlined in this chapter. The measurements have been carried down to a temperature of 100 K. The variations of thermal conductivity along the three principal axes are interpreted in terms of phonon contribution. The

anisotropy in thermal conduction are explained in terms of the ordering of protons in the strong hydrogen bonds present in this sample.

A detailed photopyroelectric investigation of the thermal conductivity anisotropy along the three principal directions in single crystals of thiourea and its variation with temperature are presented in Chapter 4 of the thesis. Thiourea is known to exist in five different phases between room temperature and 77 K. At room temperature thiourea crystallizes in to a centrosymmetric orthorhombic structure. At T_1 = 202 K, there is a transition to an incommensurate phase and at T_2 = 169 K it transforms to an orthorhombic structure which is ferroelectric. Details of crystal growth, identification of the morphology of the grown crystal and preparation of the specimen for the measurements are described in detail. The variations of thermal parameters along the three principal directions are measured and the results are discussed in this chapter.

Chapter 5 is a treatise on the thermal characterization of mixed valence perovskite samples – $La_{0.7}Ca_{0.3}MnO_3$ and $La_{0.8}Ca_{0.2}MnO_3$ - using PPE technique. The system is known to exhibit metal- insulator transition in the temperature range 220 -240 K. Electrical resistivity and thermoelectric power undergo anomalous variations in this temperature range. It is seen that the thermal conductivity undergoes anomalous variations in the same temperature range. Details of sample preparation, experimental method and results obtained are described in this chapter. The anomaly observed in thermal conductivity and heat capacities for these two samples are explained in terms of the Anderson Localization applicable to such systems.

A systematic study of the thermal properties of three samples of Lead doped Lanthanum Manganese ($LaMnO_3$), namely $La_{0.5}Pb_{0.5}MnO_3$, $La_{0.5}Pb_{0.5}Mn_{0.85}Cr_{0.15}O_3$ and $La_{0.85}Pb_{0.15}MnO_3$ + 2.5 wt. % of Ag, are carried out using the photopyroelectric technique. This constitutes Chapter 6 of the thesis. Details of sample preparation and the results of the measurement are given. A discussion of the results is given towards the end of the chapter.

Chapter 7 reports our investigations on thermal properties of $La_{0.5}Sr_{0.5}Co_{1-x}Ni_xO_3$ across M-I transition employing photopyroelectric technique. More recently $La_{0.5}Sr_{0.5}CoO_3$ (LSCO) perovskite is reported to be a suitable material for many applications, and investigations of its thermal parameters are interesting from this point of view. It is seen that the system is metallic throughout the temperature range and no temperature dependent M-I transition is observed. The results are explained in terms of existing models and presented in this chapter.

Chapter 8 is the concluding chapter of the thesis. This chapter discusses the general aspects of the results obtained on the above five samples. It also reviews the scope for future studies on thermal properties of samples, which undergo ferroelectric or M-I transition. Scope for doing further work using photopyroelectric effect is also outlined in this chapter.

The following papers have been published/ accepted for publication / presented in various journals / symposia

1. Simultaneous determination of thermal conductivity and specific heat near solid state phase transitions employing photopyroelectric technique

   Measurement Science and Technology, **11** No. 12 (2000) 1744.

2. Thermal properties of Glycine phosphite across ferroelectric phase transition: A photopyroelectric study

   Materials Research Bulletin (in press) 2001.

3. Thermal properties o thiourea single crystals during an commensurate-incommensurate phase transition (communicated).

4. Thermal properties of LCMO system employing photopyroelectric technique (communicated).

5. Thermal conductivity and heat capacity of La-Pb-Mn-O system during metal-insulator transition (communicated).

6. Thermal properties of $La_{0.5}Sr_{0.5}Co_{1-x}$ Ni_xO_3 system using photopyroelectric technique (communicated).

7. Simultaneous determination of thermal conductivity and specific heat near solid state phase transitions employing photopyroelectric technique,

   Proc. DAE Solid State Physics Symposium, Vol.**42** (1999) p 243.

8. Thermal conductivity and heat capacity across para-ferroelectric phase transition in GPI crystals

   Proc.DAE Solid State Physics Symposium, Bilaspur, Dec 27–31, 2000.

9. Thermal properties of La-Pb-Mn-O system across metal-insulator transition: A photopyroelectric study

   Proc. National Seminar on Current Trends in Materials Science, M. G. University, Kottayam, March 23-24, 2001.

10. Thermal properties of thiourea studied using photopyroelectric technique

    DAE Solid State Physics Symposium, Bombay, Dec 27-31, 2001 (communicated).

In addition to these, another 5 papers that are not included in this thesis have also been published during the course of this work

11. **Carrier type reversal** in Pb-Ge-Se glasses – Photopyroelectric measurement of thermal conductivity and specific heat

    Applied Physics Letters **78** (2001) 745.

12. Photpyroelectric determination of thermal parameters of Pb-Ge-Se glasses exhibiting a carrier type reversal.

    Analytical Sciences (accepted) 2000.

13. Photpyroelectric determination of thermal parameters of Pb-Ge-Se glasses exhibiting a carrier type reversal.

    Proc. XI International Conference on Photoacoustic and Photothermal Phenomena, Kyoto, Japan, June 25-28, 2000.

14. Carrier type reversal in Pb-In-Se glasses reflected in thermal transport measurements

    Proc. DAE solid state physics symposium, Bilaspur, Dec 27–31, 2000.

15. Carrier type reversal in chalcogenide glasses: Some thermal facts and figures

Proc. National Seminar on Current Trends in Materials Science, M. G. University, Kottayam, March 23-24, 2001.

16. Themal properties across thresholds in Ge-As-Se glasses

DAE Solid State Physics Symposium, Bombay, Dec 27-31, 2001 (communicated).

Acknowledgements

First and foremost, I wish to express my profound sense of gratitude to my research guide, Dr. Jacob Philip, Professor, Department of Instrumentation for his gentle and inspiring guidance. I am deeply indebted to him or his invaluable suggestions, forbearance, constant encouragement and support. Working with him has been a very informative and wonderful experience.

I would like to extend my deep sense of gratitude to the Head of the Dept. of Instrumentation, Dr. Stephen Rodriquez and former Head, Dr. K. N. Madhusoodanan for allowing me to use the facilities of the department. Thanks are due to the present and past Heads of Department of Physics, for granting me the permission to use library facilities for my research work. I also extend my deep sense of gratitude to Dr. P. R. S. Pillai, of Department of Electronics, for the timely help extended by providing the detectors for my measurements.

I am highly obliged by the help and cooperation of all the staff of our departmental office and workshop. Thanks are due to. Mr. Murali, Mr. Gopi Menon, Mr. Sukumaran, Mr. Jose, Mr. Jose Jacob, Mr. Casmir and Mr. Joshy are gratefully acknowledged for their help. The technical and library staffs of Physics department also need a special mention for their timely help at various stages of my research.

I express deep sense of gratitude to Dr. B. K. Chaudhari, Indian Association for Cultivation of Science, Calcutta, Dr. P. A. Joy, National Chemical Laboratory, Pune and Dr. K. L. Sebastian, Regional Research Laboratory, Trivandrum for providing the samples for measurements.

With a sense of gratitude, I remember all the faculty members, especially Dr. K. N. Neelakandan and Dr. P. Rameshan, of Department of Physics, Calicut University, whose inspiration and guidance enabled me to embark upon research.

I express my heartfelt thanks to all my lab mates - Alex Sir, Alex, Vasanth, Raghu, Vimala and Manjusha, for all the timely help extended when needed. I owe a special sense of gratitude to my seniors - Dr. Gregorios Mathew, Dr. Sheenu Thomas, Dr. Johney Issac, Dr. A. A. Sudhakaran, Dr. M. S. Kala, Dr. R. Sreekumar, and Dr. Nelson Rodriques. I fondly recall all the little, nameless, unremembered acts of kindness and love of my dear friends – Aldrin, Alex and Vimala. Thanks are due to Shaji, Shibu, Deepthy, Bindu, Manoj, Reshmi, Mukhitha (CUSAT), Srimag, Balika and Hari (IISc, Bangalore), Aritra Banerjee (IACS, Calcutta), and Surendran (RRL, TVM) for all their help and concern. I do not have words to express my

feelings for my best friends- Swapna and Shiny, for all the affection and care they bestowed upon me all through my life.

I would like to thank Mr. M. V. Peter for his unreserved help at various stages. I thank Mrs. Radhika for her wholehearted help during final stages of the thesis work.

I thank Cochin University of Science and Technology and CSIR for the financial support offered during the course of research.

My family deserves the ultimate accolades for their selfless support, encouragement and patience. The largest debt of gratitude I owe is to my loving Achan, Amma, Baluchettan, Ravi, Sindhu, Ammoma, Ambika and all my cousins. My two little cousins – Patchy and Ammu deserves a special mention for all the happiness they gave me by their little acts of love. Much of what I am, cannot have been but for my understanding parents and brothers. My achan was the pillar of strength behind all my achievements in life. Words can't express my love to Induchechy, Roopa, Rohith, Vijayettan, Omama chechy, Veenakutty and Vidyakutty for their care and support during my days away from the house.

I owe my husband Rajesh and our family a lot for their unstinting support and encouragement. As a true friend and partner, he has inspired and motivated me during my research life. He has provided me with the vital support without which this endeavor would not have had its successful culmination.

Finally I convey my sincere thanks to my entire well - wishers and friends who have directly or indirectly helped me.

Preethy Menon C

CHAPTER 1

Introduction

This chapter embodies a general introduction to the experimental technique used in the work presented in this thesis and the materials under investigation. Part A of this chapter outlines the principles of photopyroelectric technique, theory of the signal generation from solids and applications of the technique to different solids. Part B of this chapter describes the features and theory of ferroelectric phase transitions with a special reference to the variation of thermal parameters during a ferroelectric phase transition. Part C gives an overall review on the metal-insulator transition in solids, with focus being mainly on the mixed valence perovskite systems. The various theoretical models, to explain the metal-insulator transition and the magnetic and transport properties of mixed valence perovskites are reviewed.

Part A: The Photopyroelectric effect and its applications

1.1 Introduction

In recent years there has been a surge of interest in investigations of materials - solids and liquids, using photothermal diagnostic techniques, which use lasers as precisely controlled optical heat sources. The development of lasers as convenient and powerful sources of localized energy has contributed greatly to the success of

photothermal techniques over the conventional methods. The photothermal effects are generated by the deposition of energetic beams via direct heating provided by thermal deexcitations or by other non-thermal deexcitation processes like photoelectric, photochemical, luminescence and energy transfer processes, which result in indirect heating of the sample. If the excitation is modulated, the corresponding time and space dependent temperature variations developed in the sample gives rise to a variety of effects and most directly to temperature increase of the sample, which constitutes the basis of a distinct experimental technique, known as photopyroelectric (PPE) effect.

The pyroelectric effect consists in the induction of spontaneous, rapid polarization in a non-centrosymmetric, piezoelectric crystal as a result of temperature changes in the crystal. The measurements of the pyroelectric effect first appeared shortly before World War I [1-3]. The use of pyroelectric detectors for the detection of infrared radiation was suggested early by Yeou [4] and Chynoweth [5]; however the practical pyroelectric detectors have been developed only over the last two decades [6, 7]. Historically, the search for pyroelectric materials has been focused on their infrared radiation detectivity [8, 9] and their efficient high frequency responsivity [7, 10]. It is surprising that the sensitivity and the unique intrinsic capability of thermal sensors based on the pyroelectric effect to respond very rapidly to thermal excitations have not been exploited with photothermal phenomena until recently.

The impetus for an exploitation of the capabilities of the pyroelectric detection technique has come from the need for a spectroscopic technique that would provide reliable information about samples, which are difficult to examine by

conventional optical transmission or reflectance spectroscopy in the UV-Visible and near IR regions of the electromagnetic spectrum. The combined use of the quick response to radiation and temperature measurement capabilities of a pyroelectric detector led to the development of a new spectroscopic technique for solids, designated as photopyroelectric spectroscopy in 1984 [11-13].

The PPE technique consists of the measurement of the temperature increase of a sample due to the absorption of radiation, by placing a pyroelectric transducer in thermal contact with the sample. Both in PPE experiments and pyroelectric radiometry, one needs essentially a radiation source and a sensor composed of a pyroelectric element and an absorber. The PPE technique is the only photothermal technique based on the direct detection of photothermal heating (the temperature change) and therefore it has a number of advantages over other detection schemes involving secondary mechanisms [14, 15]. In all other techniques, each conversion step in the signal-generation chain degrades the overall signal-to-noise ratio, sensitivity and bandwidth performance and complicates the theoretical interpretation of the results. A PPE experiment is rather simple to design and the specimen needs no preparation, the material that can be investigated range from weakly absorbing solids like thin films [11, 16-18] or liquids [19], semiconductors [20], surfaces and absorbates [14, 17, 21, 22] to strongly absorbing solids [13] and liquids [23, 24] or diffusing materials [12]. The obtained spectra are comparable to those obtained using pure optical methods if the nonradiative quantum efficiency reaches unity or wavelength independent. By comparing two such spectra, intermolecular energy transfer processes and non-radiative quantum efficiencies can be studied [14, 16, 25, 26]. Due to the fact that the PPE signal depends on the optical properties and also on

the thermal properties of the sample, non-spectroscopic problems such as thermal microscopy [27, 28], depth profiling [16, 29], investigation of multilayered structures [30, 31], thermal diffusivity measurements [32-39] and measurement of temperature dependence of specific heat [40] can be investigated very effectively. Several approaches are possible in which the excitation and detection is harmonic, pulsed and modulated in a wide bandwidth [41], each having specific advantages and drawbacks.

1.2 Theory of photopyroelectric effect in solids

The first successful attempt to derive a general expression for the photopyroelectric signal voltage developed in the pyroelectric detector, in intimate contact with a sample was made by Andreas Mandelis and Martin Zver in 1985 [42]. They put forward a one-dimensional photopyroelectric model of a solid sample in contact with a pyroelectric thin film, supported on a backing material. The emphasis is placed on the conditions and / or restrictions imposed on the values of the system parameters so that the technique can produce signals linear with the optical absorption coefficient of the material under investigation. The limits of validity of photopyrolectric spectroscopy as a spectroscopic technique are also identified herewith.

A one-dimensional geometry of a photopyroelectric system, as suggested by Mandelis and Zver is shown in Fig. 1.1(a). They considered a solid sample of thickness L_s, irradiated by a monochromatic light of wavelength λ, whose intensity is modulated at an angular frequency ω_o by a chopper. The sample has optical absorption coefficient $\beta_s(\lambda)$ and is in intimate contact with a pyroelectric detector of

thickness L_p. The optical absorption coefficient and pyroelectric coefficient of the detector are $\beta_p(\lambda)$ and p respectively. The detector is supported on a backing material of thickness L_b, large compared to L_s or L_p. The incident light is assumed to illuminate the sample surface uniformly. Light absorption by the sample surface and non-radiative energy conversion to heat causes the temperature increase of the pyroelectric thin film. This temperature increase results in a potential difference between the upper and lower surfaces of the pyroelectric detector. This voltage $V[\omega_o, \beta_s(\lambda)]$ causes an electrical signal, which is measured in the external circuit through the connections to the pyroelectric detector as in Fig. 1.1(b).

The charge accumulated in the pyroelectric, due to a change ΔT in temperature is given by

$$Q = p\,\Delta T \tag{1.1}$$

For a pyroelectric film of thickness L_p, the average charge induced due to the pyroelectric effect is

$$\langle Q \rangle = p\,\Delta T = \left(\frac{p}{L_p}\right) \int_{\text{Thickness } L_p} T(x) e^{i\omega_o t}\, dx$$

$$= \left(\frac{p}{L_p}\right) Re\left[\left(\int_{L_p} T(x)\, dx\right) e^{i\omega_o t}\right] \tag{1.2}$$

The average pyroelectric voltage is then given by

$$V = \frac{\langle Q \rangle}{C} \tag{1.3}$$

where C is the capacitance per unit area of the thin film.

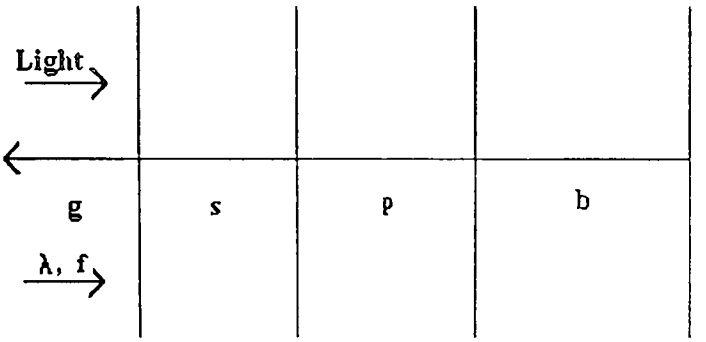

Fig. 1.1(a): One-dimensional geometry of the photopyroelectric set up. *g*, *s*, *p* and *b* stand for the gas medium in front of the sample, sample, pyroelectric detector and backing respectively

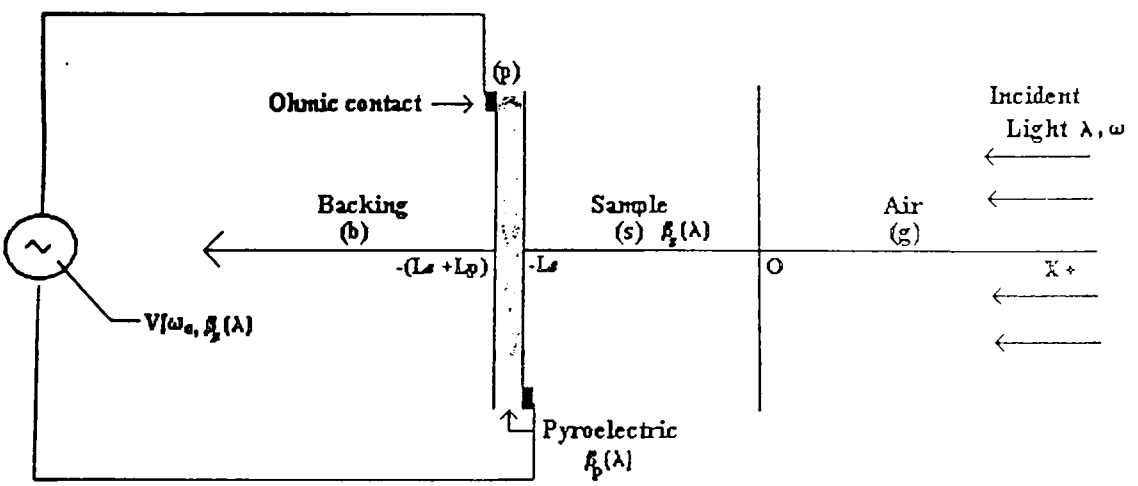

Fig. 1.1(b): Electrical equivalent circuit of the photopyroelectric set up

For two parallel charged plates of thickness L_p and dielectric constant K, Eq. (1.3) becomes

$$V(\omega_o) = \left[\frac{p L_p \theta_p(\omega_o)}{K \varepsilon_o}\right] exp(i\omega_o t) \tag{1.4}$$

where $\theta_p(\omega_o) = \frac{1}{L_p}\int T_p(\omega_o, x)\,dx$ (1.5)

Here, ε_0 is the permittivity constant of vacuum (8.854 x 10^{-12} C/Vm), $T_p(\omega_0, x)$ is the temperature field in the pyroelectric detector as a result of heat conduction processes through the solid. For the geometry shown in Fig. 1.1(b), $T_p(\omega_0, x)$ can be found from the solution of one-dimensional thermal transport equations. Assuming that there is negligible optical reflection and radiative heat transfer coefficients on the sample surface and pyroelectric-sample interface [9], the appropriate heat diffusion equations have the form

$$\left(\frac{\partial^2 T_g(\omega_0,x)}{\partial x^2}\right) - \left(\frac{i\omega_0}{\alpha_g}\right) T_g(\omega_0,x) = 0; \qquad x \geq 0 \tag{1.6a}$$

$$\left(\frac{\partial^2 T_s(\omega_0,x)}{\partial x^2}\right) - \left(\frac{i\omega_0}{\alpha_s}\right) T_s(\omega_0,x) = -\left(\frac{I_0 \beta_s \eta_s}{2k_s}\right) exp(\beta_s x);$$

$$-L_s \leq x \leq 0 \tag{1.6b}$$

$$\left(\frac{\partial^2 T_p(\omega_o,x)}{\partial x^2}\right) - \left(\frac{i\omega_0}{\alpha_p}\right) T_p(\omega_0,x) = -\left(\frac{I_0 \beta_s \eta_p exp(-\beta_s L_s)}{2k_s}\right) exp(\beta_p(x+L_s))$$

$$-(L_p + L_s) \leq x \leq -L_s \tag{1.6c}$$

$$\left(\frac{\partial^2 T_b(\omega_o,x)}{\partial x^2}\right) - \left(\frac{i\omega_0}{\alpha_b}\right) T_b(\omega_0,x) = 0; \qquad x \leq -(L_p + L_s) \tag{1.6d}$$

The subscript j refer to the respective media $j = s, p, b$ or g as in Fig. 1.1(a). The various terms in the above equations are defined as follows

I_0 = Intensity of light source

k_j = Thermal conductivity of the respective media j (= s, p,g or b)

α_j = Thermal diffusivity of j

η_s, η_p = Non radiative conversion efficiencies for the absorbing solid and pyroelectric.

The boundary conditions of temperature and heat flux continuity at all interfaces are given by

$$T_i(\omega_0, boundary) = T_j(\omega_0, boundary) \tag{1.7a}$$

$$k_i \frac{\partial}{\partial x} T_i(\omega_0, boundary) = k_j \frac{\partial}{\partial x} T_j(\omega_0, boundary) \tag{1.7b}$$

So the complex solutions to equations (1.6) are

$$T_g(\omega_0, x) = C_1 exp(-\sigma_g x) \tag{1.8a}$$

$$T_s(\omega_0, x) = \left(\frac{I_0 \beta_s \eta_s}{2k_s(\sigma_s^2 - \beta_s^2)}\right) exp(\beta_s x) + C_2 exp(\sigma_s x) + C_3 exp(-\sigma_s x) \tag{1.8b}$$

$$T_p(\omega_0, x) = \left[\frac{I_0 \beta_p \eta_p exp(-\beta_s L_s)}{2k_p(\sigma_p^2 - \beta_p^2)}\right] exp\left[\beta_p (x + L_s)\right] + C_4 exp(\sigma_p x) + C_5 exp(-\sigma_p x) \tag{1.8c}$$

$$T_b(\omega_0, x) = C_6 exp(\sigma_b x) \tag{1.8d}$$

where $\sigma_j \equiv (1+i) a_j$ and $a_j = \left(\frac{\omega_0}{2\alpha_j}\right)^{1/2}$ (1.9)

and a_j is the thermal diffusion coefficient of the respective media.

The quantity of interest is the function for the temperature variations in the pyroelectric $T_p(\omega_0, x)$. The coefficients in Eq. (1.8c) can be determined using the

boundary conditions (1.7a) and (1.7b). So after a considerable amount of algebraic manipulation, the general expression for $\theta_p(\omega_0)$ is obtained as

$$\theta_p(\omega_0)=\left(\frac{I_0}{2\sigma_p\omega_0}\right)\left\{\left(\frac{\beta_s\eta_s}{k_s(\beta_s^2-\sigma_s^2)}\right)\left(\{[exp(\sigma_p L_p)-1](b_{bp}+1)-[1-exp(-\sigma_p L_p)](b_{bp}-1)\}\right.\right.$$

$$x\{2(b_{sg}\gamma_s+1)-[(\gamma_s+1)(b_{sg}+1)exp(\sigma_s L_s)+(\gamma_s-1)(b_{sg}-1)exp(-\beta_s L_s)]$$

$$\left.exp(-\beta_s L_s)\}\right)+\left(\frac{\beta_p\eta_p exp(-\beta_s L_s)}{k_p(\beta_p^2-\sigma_p^2)}\right)\{[(\{[exp(\sigma_p L_p)-1](b_{bp}+1)-$$

$$[1-exp(-\sigma_p L_p)](b_{bp}-1)\}(b_{ps}\gamma_p+1)+\{[exp(\sigma_p L_p)-1](b_{ps}+1)+$$

$$[1-exp(-\sigma_p L_p)](b_{ps}-1)\}(b_{bp}-\gamma_p)exp(-\beta_p L_p))-\gamma_p^{-1}\{(b_{bp}+1)(b_{ps}+1)$$

$$exp(\sigma_p L_p)+(b_{bp}-1)(b_{ps}-1)exp(-\sigma_p L_p)\}[1-exp(-\beta_p L_p)]](b_{sg}+1)$$

$$exp(\sigma_s L_s)+[(\{[exp(\sigma_p L_p)-1](b_{bp}+1)-[1-exp(-\sigma_p L_p)](b_{bp}-1)\}$$

$$(b_{ps}\gamma_p-1)+\{[exp(\sigma_p L_p)-1](b_{ps}-1)+[1-exp(-\sigma_p L_p)](b_{ps}+1)\}$$

$$(b_{bp}-\gamma_p)exp(-\beta_p L_p))-\gamma_p^{-1}\{(b_{bp}+1)(b_{ps}-1)exp(\sigma_p L_p)$$

$$+(b_{bp}-1)(b_{ps}+1)exp(-\sigma_p L_p)\}[1-exp(-\beta_p L_p)]x(b_{sg}-1)exp(-\sigma_s L_s)\}\}$$

$$\div((b_{sg}+1)[(b_{bp}+1)(b_{ps}+1)exp(\sigma_p L_p)+(b_{bp}-1)(b_{ps}-1)exp(-\sigma_p L_p)]$$

$$exp(\sigma_s L_S)+(b_{sg}-1)[(b_{bp}+1)(b_{ps}-1)exp(\sigma_p L_p)+(b_{bp}-1)(b_{ps}+1)$$

$$exp(-\sigma_p L_p)]exp(-\sigma_s L_s)) \qquad (1.10)$$

Further, substitution of Eq. (1.10) into Eq. (1.4) gives the expression for the complex pyroelectric voltage as a function of modulation frequency of light and optical, thermal and geometric parameters of the sample/pyroelectric system.

Special cases

Equation (1.10) demonstrates explicitly that the thickness averaged photopyroelectric signal is a function of both the optical and thermal parameters of the sample under investigation. The complicated dependence of the signal on the sample parameters makes it difficult to give a physical interpretation to the general case. Therefore several special cases are considered according to the optical opacity and transparency of the sample. The classification scheme used here is adopted from Rosencwaig and Gersho [43]. All cases considered here have been classified according to the relative magnitudes of three characteristic lengths in the solid and the pyroelectric namely

i. Thickness L_s or L_p

ii. Optical absorption depth μ_β or μ_{β_p} defined as

$$\mu_{\beta_j} \equiv \beta_j^{-1} \tag{1.11}$$

iii. Thermal diffusion length μ_s or μ_p defined as

$$\mu_j = a_j^{-1} = \left(\frac{2\alpha_j}{\omega_0}\right)^{1/2} \tag{1.12}$$

For the special cases of the photopyroelectric signal discussed below, the time dependent factor $exp\ (i\omega_0 t)$ in Eq. (1.4) has been omitted, as it does not affect the amplitude or the phase lag of the complex envelope of the signal.

A. Optically opaque and thermally thick pyroelectric

This case occurs experimentally at high chopping frequencies ω_0 or for thick detectors.

For this limit $\mu_{\beta_p} << L_p$, $\mu_p < L_p$ and $\mu_{\beta_p} < \mu_p$. So in Eq. (1.10), we set

$exp(-\beta_p L_p) \cong 0$, $exp(-\sigma_p L_p) \cong 0$ and $|\gamma_p| > 1$

Then

$$V(\omega_0,\beta_s) = \left(\frac{pI_0}{2k\varepsilon_0}\right)\left(\frac{\beta_s\eta_s}{k_s(\beta_s^2-\sigma_s^2)\sigma_p}\right)\{2(b_{sg}\gamma_s+1)-[(\gamma_s+1)(b_{sg}+1)exp(\sigma_s L_s)$$
$$+(\gamma_s-1)(b_{sg}-1)exp(-\sigma_s L_s)]\,exp(-\beta_s L_s)\} + \left(\frac{\eta_p exp(-\beta_s L_s)}{k_p\beta_p\sigma_p}\right)$$
$$\{(b_{sg}+1)(b_{ps}\gamma_p+1)exp(\sigma_s L_s)+(b_{sg}-1)(b_{ps}\gamma_p-1)exp(-\sigma_s L_s)\}]$$
$$\div[(b_{sg}+1)(b_{ps}+1)exp(\sigma_s L_s)+(b_{sg}-1)(b_{ps}-1)exp(-\sigma_s L_s)] \quad (1.13)$$

A. 1: Optically opaque sample ($\mu_{\beta_s} << L_s$)

In Eq. (1.13), we set $exp(-\beta_s L_s) \cong 0$

Case A.1(a):Thermally thin sample ($\mu_s >> L_s$, $\mu_s >> \mu_{\beta_s}$)

In Eq. (1.13), set $exp(\pm\sigma_s L_s) \approx 1$ and $|\gamma_s| >> 1$

$$\text{So } V(\omega_0) = A\left(\frac{\eta_s\alpha_p}{k_p(1+b_{sp})\omega_0}\right)exp(-i\pi/2) \quad (1.14)$$

$$\text{where } A = \frac{pI_0}{2k\varepsilon_0} \quad (1.15)$$

Eq. (1.14) shows that the photopyroelectric signal voltage is independent of β_s. This behaviour is termed as photopyroelectric saturation. The signal depends on the thermal properties of both the gas and the pyroelectric and it varies with the chopping frequency as ω_0^{-1} and its phase lags by 90^0 to that of the reference signal.

Case A.1 (b): Thermally thick sample ($\mu_s << L_s$, $\mu_s > \mu_{\beta_s}$)

In Eq. (1.13) we set $exp(-\sigma_s L_s) \cong 0$ and $|\gamma_s| > 1$

Assuming that $|\gamma_s| > b_{gs}$, Eq. (1.13) reduces to

$$V(\omega_0) = A\left(\frac{\eta_s \alpha_p}{k_p(1+b_{sg})\omega_0}\right) exp\left[-\left(\frac{\omega_0}{2\alpha_s}\right)^{1/2} L_s\right] exp\left[-i\left(\frac{\pi}{2} + \left(\frac{\omega_0}{2\alpha_s}\right)^{1/2}\right)\right] \quad (1$$

In this limit the photopyroelectric signal, initially saturated with res the thermal properties of the contact gas, have now been replaced with those solid. Eq. (1.16) indicates that in this limit the photopyroelectric signal can be in principle to determine its thermal diffusivity α_s if the thickness L_s is knov vice versa.

Case A.1(c): Thermally thick sample ($\mu_s << L_s$, $\mu_s < \mu_{\beta_s}$)

In Eq. (1.13), set $exp(-\sigma_s L_s) \cong 0$ and $|\gamma_s| < 1$

Here two possibilities can occur

(i) $|\gamma_s| < b_{sg} < 1$, then

$$V(\omega_0, \beta_s) = A\beta_s\left(\frac{\eta_s b_{sg} \alpha_s \sqrt{\alpha_p}}{k_p(1+b_{sp})\omega_0^{3/2}}\right) exp\left[-\left(\frac{\omega_0}{2\alpha_s}\right)^{1/2} L_s\right] exp\left\{-i\left[\left(\frac{\omega_0}{2\alpha_s}\right)^{1/2} L_s - \pi/4\right]\right\}$$

(1.17)

This is called thermal transmission spectroscopy. As long as $\mu_s < \mu_{\beta_s}$, the exponential tail of the heat wave generated within μ_s in the sample is communicated to the pyroelectric transducer, thus producing a signal linear in β_s and of small magnitude. Therefore, the technique can be used in this limit as a spectroscopy, yielding signal information similar to the absorption spectra.

The other possibility considered is

(ii) $b_{sg} < |\gamma_s| < 1$

So Eq. (1.13) becomes

$$V(\omega_0,\beta_s) = A\beta^2\left(\frac{\eta_s\alpha_p\alpha_s}{k_p(1+b_{sp})\omega_0^2}\right)exp\left[-\left(\frac{\omega_0}{2\alpha_s}\right)^{1/2}L_s\right]exp\left[-i\left(\frac{\omega_0}{2\alpha_s}\right)^{1/2}L_s\right] \quad (1.18)$$

Eq. (1.18) predicts a spectral nonlinearity. i.e., $V(\omega_0,\beta_s) \propto \beta_s^2$. This dependence will distort the spectral information from the sample. Therefore it is regarded as undesirable.

A. 2: Optically transparent sample ($\mu_{\beta_s} > L_s$)

In this limit, $exp(-\beta_s L_s) \cong 1 - \beta_s L_s$

Case A. 2(a): Thermally thin sample ($\mu_s >> L_s$, $\mu_s > \mu_{\beta_s}$)

In Eq. (1.13), we set $exp(\pm\sigma_s L_s) \cong 1$ and $|\gamma_s| > 1$

So Eq. (1.13) becomes

$$V(\omega_0,\beta_s) = A\left(\frac{\eta_p + (\eta_s - \eta_p)\beta_s L_s}{k_p(1+b_{gp})\omega_0}\right)exp\left(-i\pi/2\right) \quad (1.19)$$

The photopyroelectric voltage is proportional to $\beta_s L_s$, provided that $\eta_s \neq \eta_p$. In the experimentally common case, where $\eta_s \sim \eta_p \sim 1$ and $b_{gp} < 1$, the signal carries neither optical nor thermal information about the samples and it is entirely generated by the light absorption in the pyroelectric.

Case A. 2(b): Thermally thin sample ($\mu_s > L_s$, $\mu_s < \mu_{\beta_s}$)

In Eq. (1.13), set $exp(\pm\sigma_s L_s) \cong 1 \pm \sigma_s L_s$ and $|\gamma_s| < 1$

Further, if we assume that

(i) $|\gamma_s| >> |\sigma_s L_s|$ i.e., $\mu_s^2 > \mu_{\beta_s} L_s$

So Eq. (1.13) reduces to

$$V(\omega_0,\beta_s) = A\alpha_p\left(\frac{\eta_p + (\eta_s - \eta_p)\beta_s L_s}{k_p\omega_0}\right)exp\left(-i\pi/2\right) \qquad (1.20)$$

This case is similar to **A. 2(a)**, in that for $\eta_s \sim \eta_p \sim 1$, no optical or thermal information about the sample is obtained.

Now, if we assume that

(ii) $|\gamma_s| << |\sigma_s L_s|$, then

$$V(\omega_0,\beta_s) = A\alpha_p\left[\frac{(\eta_p + \eta_s\beta_s L_s)(1 - \beta_s L_s)}{k_p\omega_0}\right]exp\left(-i\pi/2\right) \qquad (1.21)$$

Here, if $\eta_s \sim \eta_p \sim 1$, the photopyroelectric output will be proportional to $[1 - (\beta_s L_s)^2]$ with a ω_0^{-1} frequency dependence. This limit is nonlinear in β_s and the spectral information from the system will be similar to distorted transmission spectra.

Case A. 2 (c): Thermally thick sample ($\mu_s < L_s$, $\mu_s < \mu_{\beta_s}$)

The approximations in Eq. (1.13) are $exp(-\sigma_s L_s) \cong 0$ and $|\gamma_s| << 1$. The photopyroelectric output is

$$V(\omega_0,\beta_s) = A(1 - \beta_s L_s)\left(\frac{\eta_p}{k_p(1 + b_{sp})\omega_0}\right)exp\left(-i\pi/2\right) \qquad (1.22)$$

In this limit, the technique is equivalent to optical transmission spectroscopy. This is of great experimental interest, because the photopyroelectric signal is proportional to $[1 - \beta_s L_s]$. Therefore the technique can yield information similar to the transmission spectrum.

Cases **A. 1 (c, i) and A. 2 (c)** are the only spectroscopically important cases which give direct information about the optical absorption coefficient of the sample material as a result of thermal and optical transmission respectively.

B. Optically opaque and thermally thin pyroelectric

This case is likely to occur at low chopping frequencies ω_0 and / or very thin pyroelectric films. Under this condition, $\mu_{\beta_s} >> L_p$ and $\mu_p >> \mu_{\beta_s}$

On setting $exp(-\beta_p L_p) \cong 0$, $exp(\pm\sigma_p L_p) \cong 1 \pm \sigma_p L_p$; $|\gamma_p| >> 1$ in Eq. (1.13), we get the expression as

$$V(\omega_0,\beta_s) = A\left[\left(\frac{\beta_s \eta_s L_p}{k_s(\beta_s^2 - \sigma_s^2)}\right)\{2(b_{sg}\gamma_s + 1) - [(\gamma_s + 1)(b_{sg} + 1)exp(\sigma_s L_s) + (\gamma_s - 1)(b_{sg} - 1)exp(-\sigma_s L_s)]exp(-\beta_s L_s)\} + \left(\frac{\eta_p exp(-\beta_s L_s)}{k_p \beta_p \sigma_p}\right)\{(b_{sg} + 1)[(b_{ps}\gamma_p + 1)\sigma_p L_p - \gamma_p^{-1}\{(b_{hs} + 1) + (b_{ps} + b_{hp})\sigma_p L_p\}]exp(\sigma_s L_s) (b_{sg} - 1)[(b_{ps}\gamma_p - 1)\sigma_p L_p - \gamma_p^{-1}\{(b_{hs} - 1) + (b_{ps} - b_{hp})\sigma_p L_p\}exp(-\sigma_s L_s)\}] \div \{(b_{sg} + 1)[(b_{hs} + 1) + (b_{ps} + b_{hp})\sigma_p L_p]exp(\sigma_s L_s) + (b_{sg} - 1)[(b_{hs} - 1) + (b_{ps} - b_{hp})\sigma_p L_p]exp(-\sigma_s L_s) \quad (1.23)$$

There are six spectral limits of Eq. (1.23) involving relationships between μ_s, μ_{β_s} and L_s, identical to cases **A.1** and **A.2**. For each limit, in the case of a thermally thin pyroelectric transducer, the simplified expression for $V(\omega_0, \beta_s)$, which results from Eq. (1.23) is similar to the respective expression in the case of the thermally thick detector previously discussed, with the substitutions – $1/\sigma_p$ replaced by L_p and $k_p\sigma_p$ with $k_b\sigma_b$. According to these substitutions, the cases of spectroscopic interest in the limit of a thermally thin pyroelectric are

Case B.1 (c, i): Thermal transmission mode

$$V(\omega_0,\beta_s) = -A\left(\frac{\eta_s \beta_s L_p b_{sg} exp(-\sigma_s L_s)}{\sigma_s (k_b \sigma_b + k_s \sigma_s)}\right) \tag{1.24}$$

Case B. 2 (c): Optical transmission mode

$$V(\omega_0,\beta_s) = A\left(\frac{\eta_p L_p (1 - \beta_s L_s)}{k_b \sigma_b + k_s \sigma_s}\right) \tag{1.25}$$

The frequency dependence of the photopyroelectric voltage in all cases **(B)** is consistently with a factor $\omega_0^{-1/2}$ lower than all cases in **(A)**

The results obtained shows some trends familiar from other thermal wave spectroscopies, such as photoacoustic and photothermal deflection spectroscopy, as well as some unique features. The calculations show that the photopyroelectric voltage is governed by the interplay between the optical absorption in the sample and in the pyroelectric transducer itself. This suggests that it is experimentally advantageous to work with optically opaque transducers whose flat (i.e., photopyroelectrically saturated) spectral response does not interfere with the spectral measurements on the sample. Opaqueness can be achieved through coating the photopyroelectric surface with metallic thin layers (e.g. nickel) [44] or black absorbing materials [9].

The present theoretical considerations help to establish photopyroelectric spectroscopy as a valid spectroscopic technique, with high promise in the realm of flexible *in-situ* non-destructive probing of samples and in applications at very high frequencies as piezoelectric or pyroelectric thin films (such as PVF_2) [45]. These features set this technique ahead of photoacoustics and photothermal spectroscopies.

Mandelis, in his theory assumed total absorption of radiation by the pyroelectric sensor. Chirtoc and Mihâilescu [46] in 1989 put forward another theory to understand the role played by the finite reflectance at the sample-pyroelectric interface and the mechanisms responsible for the peak inversions observed in the reflection-mode PPE spectroscopy [24, 47], since these questions have found no satisfactory answers in the framework of the former theory. It has been shown that the assumption of an arbitrary value for the reflectance completely changes the physical nature of the PPE effect, featuring simultaneous optical absorption and transmission characteristics. Hence it creates very diverse experimental opportunities for optical and thermal investigations of solid, liquid or even gaseous substances. So the full potential of the PPE technique for the investigations of optical and thermal properties of materials remains to be demonstrated by future experiments.

1.3 Experimental set up

There are three main types of photopyroelectric analysis depending on the signal generation and detection mode.

1. Frequency domain scheme (FD) – Harmonic modulation of the incident light at a single frequency and simple pyroelectric calorimetric detection [42]
2. Frequency multiplexed excitation – spectral analysis of input and output signal channel [48].
3. Time domain measurements – pulsed optical excitation of the sample and pyroelectric detection [49-53].

Of the three, frequency domain PPE instrumentation is the simplest of the three modes. The experimental set up of this technique does not present any particular problems. The cost of the instruments is relatively low. Fig. 1.2 shows a general set up of the frequency domain PPE experimental set up. As it is shown, either a broadband source or a CW laser can be used [54].

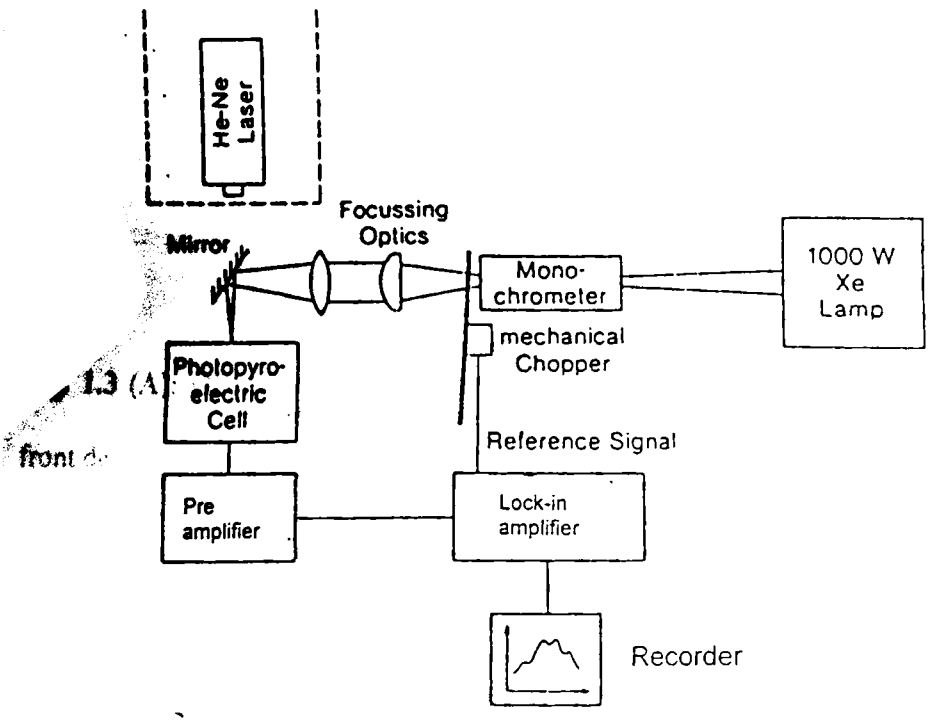

Fig.1 2:Block diagram for the Frequency domain PPE experimental apparatus

Frequency domain photopyroelectric measurements can be divided into two main groups.

i) The back detection technique (BDT)

ii) The front detection technique (FDT)

This thesis deals only with the back detection technique. However, for completeness, we first describe the front detection technique.

Marinelli *et al.*, [55] were the first to use the PPE technique in the front detection mode. The configuration of the technique is given in Fig. 1.3.

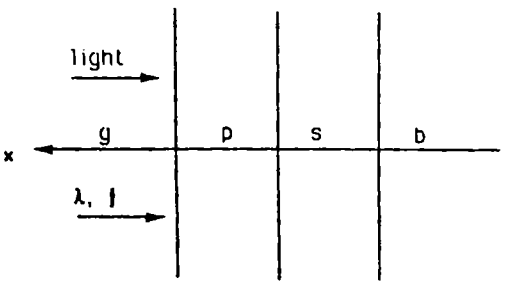

back detec

Fig. 1.3 (A): One-dimensional geometry for the photopyroelectric technique in the front detection configuration

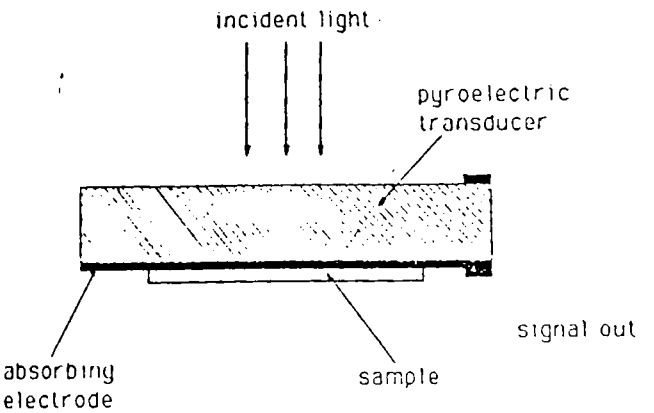

Fig. 1.3(B): Experimental configuration of the sample and detector for photopyroelectric front detection

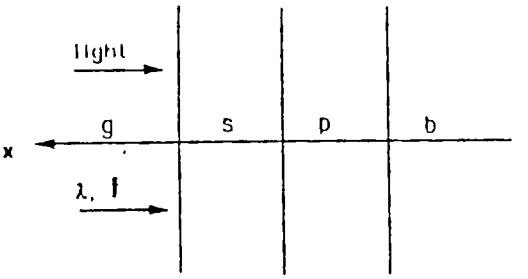

Fig. 1.4(A): One-dimensional geometry for the photopyroelectric technique in the back detection configuration

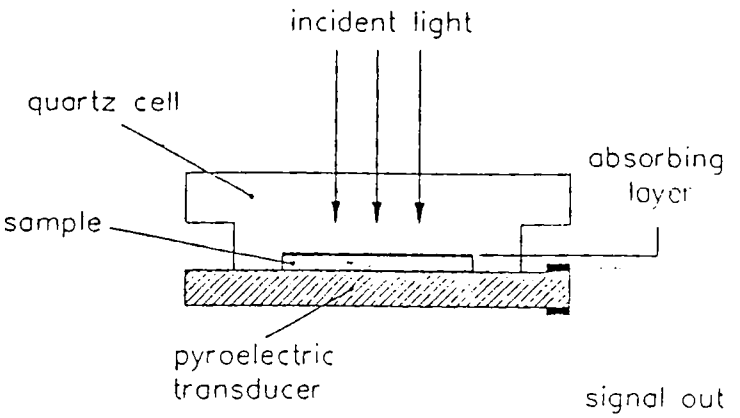

Fig. 1.4(B): Experimental configuration of the sample and pyroelectric transducer for photopyroelectric back detection

As it is seen in Fig. 1.3, one side of the detector is in contact with the sample, while the opposite side is illuminated. In this case, light strikes directly on the

detector and not on the sample. In back detection technique, one side of the sample is in contact with the detector, while the opposite side is illuminated. The configuration for the technique is shown in Fig. 1.4. The advantage of the FDT is that it can be used in a wide frequency range and it can attain a large signal at a high frequency limit, which allows a high depth resolution in the sample.

1.3.1 Frequency response characterization

Christofides *et al.* [56] used two different thickness of polyvinylidene difluoride (PVDF), 28 μm and 52 μm as pyroelectric detectors in order to obtain thermally thick pyroelectric conditions. The thickness of the detector and the modulation frequency must be such that the condition

$$f >> f_c \equiv \frac{\alpha_p}{\pi L_p^2} \tag{1.26}$$

is satisfied according to the definition of the thermally thick limit. α_p and L_p are the thermal diffusivity and the thickness of the detector respectively [42]. In Eq. (1.26), f_c, the critical frequency equals 22 Hz and 5 Hz for the PVDF film of thickness 28 μm and 52 μm respectively. The thermal time response of the PVDF film depends upon its thickness, since a longer time is needed for a thicker detector to reach thermal equilibrium within the pyroelectric after excitation [44]; yet for a range of low frequencies (0.5 to 600 Hz) this dependence is significant. The frequency response characterization experiments is necessary to work in a frequency range greater than 25 Hz or so in order to satisfy the conditions of the theoretical models.

So we can say the PPE spectroscopy is technically less complex and less expensive than any other photothermal methods. The necessary condition for the experiment depends only on the thermal thickness of the detector, which is very easy

to satisfy. However, one disadvantage of PPE spectroscopy is its susceptibility to acoustic noise [57]. This problem can be partially alleviated by isolating the mechanical chopping system from the optical table that supports the rest of the instrumentation.

1.4 Applications of the technique

The pyroelectric (PE) property offers the possibility to use PE materials for a number of applications. In fact PE sensors present five main advantages that make them suitable for many applications.

1. Sensitive in a very large spectral bandwidth
2. Sensitive in a wide temperature range without the need of cooling
3. Low power requirements
4. Fast response
5. Generally low cost materials

In this subsection, we briefly describe the state of the art of the pyroelectric sensors in the field of measurement science. In the beginning, the pyroelectric effect has employed mainly in the detection of infrared radiation and in laser power measurements. The pyroelectric phenomenon has led to many applications in recent years. In fact, since the beginning of the 20^{th} century pyroelectricity has been exploited in different areas, especially for the detection of radiation. In an excellent review, Putley has described the use of pyroelectricity for the detection of radiation [7].

With these added advantages of PE detectors make the photopyroelectric technique an ideal one for the thermal and optical characterization of samples

ranging from metals to insulators. Now we will discuss some of the important applications of the photopyroelectric technique.

1.4.1. PPE spectroscopy in semiconductors

In 1984, Coufal and Mandelis [11, 12] used for the first time, thin polyvinylidene difluoride (PVDF) films for photothermal wave spectroscopic detection. Shortly thereafter, Coufal showed that photopyroelectric spectroscopy can be a very sensitive qualitative tool for thin film spectroscopic applications [16]. Mandelis *et al.* [58] used the PPE spectroscopy for electronic defect center characterization of crystalline *n*-CdS. These authors performed several experiments in open circuit as well as in conjunction with photocurrent spectroscopy in the presence of a.c. or d.c. transverse electric field. This study [59] showed the potential of the technique to give information concerning the non-radiative de-excitation mechanisms at defect centers. Tanaka [60] and Tanaka *et al.* [61] showed that frequency domain PPE spectroscopy is also very promising for qualitative analysis.

PPE spectroscopy was also used for the characterization of thin semiconducting films. Mandelis *et al.* [61] have performed spectroscopic measurements of an α-Si:H thin film on quartz. These authors further compared their experimental PPE spectra with similar spectra obtained by conventional widely used photothermal deflection spectroscopy (PDS). It was shown that PPE spectroscopy has the ability for easy and consistent experimental acquisition of non-radiative quantum efficiency spectra, a property not shown by PDS. It is the necessity for a coupling fluid that is partly the cause of the lack of spectroscopic applications of PDS at cryogenic temperatures. Another disadvantage is the pump-

probe beam alignment requirement for PDS detection. This frequently led to the need for three-dimensional models to interpret the data quantitatively. The consideration of these advantages led to the development of PPE spectroscopy.

1.4.2. PPE spectroscopy in paramagnetic and ferromagnetic materials

In 1982, Melcher and Arbach [62] reported the use of pyroelectric sensors to detect the temperature gradients associated with magnetic resonance absorption in thin films and layers of paramagnetic and ferromagnetic materials. Photopyroelectric technique to study the magnetic phase transitions in ferroelectrics and itinerant electron antiferromagnetic materials were first done by Dâdarlat *et al.*, [63] in 1990. In their paper these authors have reported the application of PPE technique for the study of magnetic phase transitions in $Ni_{100-x}Cu_x$ alloys with x = 28 to 33%. The samples were found to exhibit magnetic phase transitions (ferromagnetic-paramagnetic). According to Dâdarlat *et al.*, [63] due to the features of the PPE method, the high signal to noise ratios that were obtained allowed higher sensitivities for monitoring phase transitions in itinerant electron antiferromagnets than classical magnetic and electronic measurements.

In another work, Dâdarlat *et al.*, [64] demonstrated the ability of the PPE method to detect the phase transitions in solids. He made measurements on TGS, which exhibited a ferroelectric-paraelectric phase transition at 49 °C and $NiCu_{30}$ had a ferromagnetic–paramagnetic phase transition at 50 °C. It has shown that the PPE voltage amplitude clearly reflects the phase transition. He made the inference that the thermally thin and thick conditions largely influence the results.

1.4.3. PPE spectroscopy in liquid crystals

Marinelli [55] used the photothermal front detection configuration (Fig. 1.4) to perform measurements on liquid crystal samples in the range 0.2 Hz to 200 kHz. The sample was 9CB liquid crystal and the author studied the PPE signal as a function of modulation frequency. It has been proved that with the PPE technique, it is possible, at a given frequency, to obtain the temperature dependence on the thermal parameters of the sample, which is particularly interesting in the case of phase transition studies.

Marinelli *et al.* [65] have also performed several experiments comparing the photoacoustic and photopyroelectric technique for the characterization of liquid crystal second order phase transitions. In their measurements they evaluated simultaneously thermal conductivity, specific heat and thermal diffusivity of 9CB liquid crystal that undergoes a second order phase transition at 47.9 ^{0}C from Smectic-A (SA) to Nematic (N) phase [66]. The variation of PPE signal amplitude and phase as a function of temperature for the liquid crystal sample has been plotted. It is seen that in the plot, the obtained dip for the PPE phase at the phase transition temperature, because of the "critical slowing down" of thermal fluctuations [65, 67] is about 160^{0}, while in PA it was only 4^{0}. This proves the superior sensitivity of the PPE technique over PA. Apart from the sensitivity factor, the PPE technique presents a better signal-to-noise (SNR) ratio, which makes this an ideal one for studies in liquid crystals.

1.4.4. PPE gas sensors

Photothermal and photoacoustic techniques have been used successfully in optical and thermo physical characterization of solids [68-72]. Recent developments in monitoring and measuring the properties of gases using photothermal techniques have attracted much attention for environmental quality control and manufacturing safety reasons [73-77]. Christofides and Mandelis [78] used the photopyroelectric gas sensor, a new type of solid-state devices for the detection of minute concentrations of hydrogen gas under environmental flow-through conditions. Sensitivity to exposures in a hydrogen partial pressure has been demonstrated down to concentrations as small as 40 ppm, in a flowing $H_2 + N_2$ mixture.

A newly developed [79] thermal wave resonant cavity (TWRC) sensor using a pyroelectric thin film transducer (polyvinylidene fluoride), proved to offer a powerful method for measuring thermal diffusivities of gases with very high precision and gas species resolution [76, 77, 80].

This section on photopyroelectric effect would not be complete if we do not emphasize the fact that high sensitivity of the PPE detector in temperature change is a great challenge for measurement scientists. Juhl and Bimberg [81] have recently proved that with calorimetric absorption and transmission spectroscopy one can achieve spectroscopic sensitivities of $\beta l = 10^{-8}$. So we can say that from an experimental and instrumental point of view, the progress of the experimental technique has been consistent and encouraging. However, the full potentiality of the PPE technique for optical and thermal material characterization remains to be demonstrated by future experiments.

Part B: Ferroelectric phase transitions

1.5 Introduction

The cross-disciplinary subject of phase transition is of great interest in the study of condensed matter. This is a very interesting phenomenon found to occur in a variety of ways in many physical systems. Literature abounds in theoretical and experimental studies of phase transitions in solids and newer kinds of phase transitions in newer systems are constantly reported [82, 83]. In the following paragraphs, a brief outline of the basic facts regarding phase transitions in solids are presented.

A homogenous assembly of atoms or molecules called a phase is characterized by thermodynamic properties like volume, pressure, temperature and free energy. The stability of the isolated phase is determined by whether its energy more generally, its free energy - is a minimum for the specified thermodynamic conditions. If the phase is present in a local minimum of free energy instead of a unique minimum and is separated by still lower minima (under the same thermodynamic conditions) by energy barriers, the system is said to be in a metastable state. If the barriers do not exist, the states of the system become unstable and the system move into a stable or equilibrium state characterized by the lowest value for free energy. As the temperature, pressure or any other variable like electric or magnetic field acting on the system is varied, the free energy of the system changes smoothly and continuously. Whenever such variations are associated with

changes in the structural details of the phase (atomic or electronic configuration) a phase transition is said to occur.

During a phase transition, even as the free energy of the system remains continuous, thermodynamic quantities like entropy, volume, specific heat etc. undergo discontinuous changes. Ehrenfest [84] classified phase transitions depending on the relation between the thermodynamic quantity undergoing discontinuity and the Gibb's free energy function. According to this scheme, a Gibb's function shows a discontinuous change at the transition. Thus if there is discontinuity in quantities such as volume and entropy, which are first order derivatives of the Gibb's free energy, the transition is said to be of first order, whereas if specific heat, compressibility, thermal expansion etc. are the quantities undergoing discontinuity, which are second order derivatives of Gibb's free energy function, the transition is said to be of second order and so on. However, several of the known transformations do not strictly belong to any one kind [85, 86] as described above. For example the phase transition in $BaTiO_3$, which has second order character, also shows a small latent heat effect. The ferroelectric transition in KH_2PO_4 should theoretically be of first order, but conforms more closely to the second order. There is superposition of second order behaviour in many first order transitions and vice versa. It is possible that many of the transitions are really of mixed order.

Phase transitions are always associated with configurational changes within the system. Magnetic phase transitions are driven by the alignment of unpaired spins in a specified direction and one usually does not observe any changes in the atomic configuration. On the other hand, several other types of phase transitions like para-

ferroelectric transitions are generally associated with atomic rearrangement or structural changes. The change of structure at a phase transition in a solid can occur in two distinct ways. Firstly, there are transitions where the atoms of a solid reconstruct a new lattice as in the case of amorphous solid to crystalline state. Secondly, there are transitions where a regular lattice is distorted slightly without in any way disrupting the linkage of the networks. This can occur as a result of small displacements in the lattice position of single atoms or molecular groups or the ordering of atoms or molecules among various equivalent positions. Most of the ferroelectric phase transitions belong to the second group. The displacive type transitions are often driven by the freezing out of a vibrational mode called soft mode. In the case of ferroelectric transition, the soft mode is an optical phonon belonging to the centre of the Brillouin zone while in the case of an antiferroelectric transition, is a zone boundary phonon. Soft acoustic phonons are associated with ferroelastic transitions.

Since all the phase transitions involve configurational changes, one can identify a physical quantity that is characteristic of a new ordered configuration. Such a concept of an order parameter was introduced by L. Landau [87] in his thermodynamic theory of phase transitions. The order parameter has a non-zero value in the ordered phase below the transition temperature T_c and is zero above T_c. Thus in a ferroelectric transition, the order parameter is the spontaneous polarization while in a ferroelastic transition, it is the spontaneous strain. Landau assumed that Gibb's free energy can be expanded in powers of the order parameter is which is assumed to be very small. The results of Landau theory support Ehrenfest's classification and reveal many basic features of phase transitions.

1.6 Landau theory of second order ferroelectric phase transitions

It was pointed out earlier that during a second order transition, the entropy and volume of the system remain continuous, while the heat capacity and thermal expansivity undergo discontinuous changes. Landau [87] proposed an account for this behaviour. He suggested that the transition from a high temperature to a low temperature corresponds to the onset of an ordering process. In the ordered, less symmetrical (low temperature) phase of the material, there exists an order parameter, which decreases continuously with temperature and becomes zero at the transition temperature. The disordered high temperature phase will have high symmetry.

The free energy can be written in terms of the order parameter ξ, (for the ferroelectric phase transition, the order parameter is the spontaneous polarization). For small values of ξ (near the transition temperature) the free energy $\phi(P, T, \xi)$ can be written as

$$\phi(P,T,\xi) = \phi_0(P,T) + a\xi + b\xi^2 + c\xi^3 + d\xi^4 + \ldots\ldots\ldots\ldots \qquad (1.27)$$

where $\phi_0(P, T)$, a, b, c and d are constants. Now, if the value of $\phi(P, T, \xi)$ to remain unaltered by the change of sign of ξ, coefficients of odd powers of ξ should be zero. Therefore,

$$\phi(P,T,\xi) = \phi_0(P,T) + b\xi^2 + d\xi^4 + \ldots\ldots\ldots\ldots \qquad (1.28)$$

The equilibrium value of the long-range order parameter is obtained by the following conditions

$$\left(\frac{\partial \phi}{\partial \xi}\right)_{P,T} = \xi\left(b + 2d\xi^2\right) = 0 \tag{1.29}$$

$$\left(\frac{\partial^2 \phi}{\partial \xi^2}\right)_{P,T} = b + 6d\xi^2 \geq 0 \tag{1.30}$$

From Eq. (1.29) we obtain the solutions as $\xi = 0$ and $\xi^2 = -b/2d$. Since $\xi = 0$ corresponds to the disordered state, it follows from Eq. (1.30) that $b > 0$ on one side of the transition temperature. Similarly on using the value $\xi^2 = -b/2d$ in Eq. (1.30), we get $b < 0$ for the ordered phase. So b should change sign through a second order transition. Since b is negative for the ordered phase in the vicinity of a transition, d should be positive (since $-b/2d = \xi^2 > 0$).

Assuming b to vary linearly with temperature near the transition point

$$b(P,T) = B(T - T_c) \tag{1.31}$$

where T_c is the 'critical' or transition temperature. ξ^2, then becomes

$$\xi^2 = \frac{-b}{2d} = -\frac{B}{2d}(T - T_c) \tag{1.32}$$

Neglecting higher order terms, entropy is given by,

$$S = -\left(\frac{\partial \phi}{\partial T}\right)_{P,\xi} = S_0 - \xi^2\left(\frac{\partial b}{\partial T}\right)_{P,\xi} \tag{1.35}$$

In the symmetrical phase (above the transition temperature), $\xi = 0$ and $S = S_0$. Below the transition temperature, using Eq. (1.32) we get

$$S = S_0 + \frac{b(P,T)}{2d}\left(\frac{\partial b}{\partial T}\right) = S_0 + \frac{B^2}{2d}(T - T_c) \tag{1.34}$$

This guarantees the continuous nature of the entropy during a second order transition.

Since $C_p = T\left(\partial S/\partial T\right)_{p,\xi}$, we have two phases at the transition

$$C_p = \left(\frac{\partial S_0}{\partial T}\right)_p = C_{p_0} \text{ and } C_p = C_{p_0} + \frac{B^2 T_c}{2d} \tag{1.35}$$

on either side of the transformation. So the change in heat capacity during a second order transition will have a finite value given by

$$\Delta C_p = B^2 T_c / 2d \tag{1.36}$$

So we see that Landau theory provides the basis for Ehrenfest's second order transition. Extension of Landau treatment has been attempted by various workers in conjunction with fluctuation theory [88].

1.7 Variation of thermal conductivity and heat capacity during ferroelectric phase transitions

Phase transitions in solids are often accompanied by interesting changes in their properties. Several techniques are employed to investigate phase transitions, depending on the nature of the solid and properties of interest. Such studies are not only of academic value in understanding the structural and mechanistic aspects of phase transitions, but can also be of technological importance. The literature abounds in studies of phase transitions in solids using a wide range of techniques, including diffraction, thermal, optical, electrical, magnetic, dielectric, spectroscopic and other measurements [86, 89-93].

It would be difficult here to describe all the techniques and material properties that have been employed to study phase transitions. We shall therefore

limit our discussion to the thermal properties namely thermal conductivity and heat capacity of solid materials.

Thermal measurements have been widely used to identify and characterize transitions. Heat capacity measurements provide enthalpy changes and indicate the thermodynamic order of transitions. Differential scanning calorimetry (DSC) is a popular technique for obtaining heat capacity data and ΔH of transitions. Another technique that is widely used for the phase transition studies is the photothermal technique.

Photoacoustic technique has been gained wide interest as a powerful tool for the study of phase transitions in solids. The wealth of information contained in the PA signal can be used to investigate the variation in the optical and thermal properties of materials during phase changes. Florian *et al.*, [94] were the first to publish results of measurements of PA effect in the temperature region of first order phase transitions in solids. In their paper, results of measurements of the PA signal at the liquid-solid transition of gallium and of water and the structural phase transition in K_2SnCl_6 were reported.

Pichon *et al.*, [95] examined the specific heat anomaly of thermally thick dielectric samples in the neighbourhood of a magnetic phase transition using PA technique. R.G theory has been used to obtain relative values of the specific heat. Results obtained with $CrCl_3$ and MnF_2 are given therein. In case of MnF_2 the observed anomaly is comparable to that observed using conventional calorimetric techniques.

By exploring the dependence of photoacoustic signal in the thermal properties of the sample, Siquerra *et al.*, [96] demonstrated the usefulness of PA

effect for investigating phase transitions in solids. Their studies have been on aluminium doped VO_2. A theoretical model for the PA effect during a first order phase transition has been described by Korpiun and Tilgner [97]. Bibi and Jenkins [98] have reported observations of a first order phase transition in $CoSiF_6$. $6H_2O$ using photoacoustic technique. The PA technique has been applied for the study of series of phase transitions in tetra methylammonium tetrachloride cobaltate (TMTC-CO) by Fernandez *et al.* [99]. But in practice gas coupled PAS at high frequencies is virtually impossible due to very poor signal-to-noise ratios and microphone frequency response limitations.

Extebarria *et al.* [100, 101] have shown theoretically, using the Jackson and Amer's theory [102] and experimentally that the piezoelectric photoacoustic signal is a function of sample specific heat only, and independent of thermal conductivity, in the optically and thermally thick limits. This observation is indicative of further restrictions on the opacity of the sample, in addition of high modulation frequency requirements similar to the gas coupled PAS.

The PPE technique has been employed by different authors for the study of phase transitions in solids [11, 12, 42, 103].

Part C: Metal-Insulator transition in solids

1.8: Introduction

An early success of quantum mechanics was attributed to the explanation by Wilson [104, 105] for the sharp distinction between metals and non-metals. In crystalline materials, the energies of the electron states lie in bands, a non-metal is a material in which all bands are full or empty, while in a metal, one or more bands are party full. Any metal-insulator transition in a crystalline material is identified as a transition at zero temperature from a situation in which bands overlap to situations when they do not overlap.

Interest in a metal-insulator transition arose long way back in 1937. de Boer and Verwey pointed out [106] that nickel oxide, a transparent non-metal, according to the Wilson model, should be metallic because of the eight electrons of the Ni^{2+} ions would only partly fill one of the *d*-bands. Peierls said this must be due to the correlation and gave a satisfactory explanation of how this could occur. At the time, it wasn't known that nickel oxide was antiferromagnetic, as Slater pointed out in 1951 [107]. Slater suggested that an antiferromagnetic lattice can split the *d*-bands, allowing all bands to be full or empty, making them insulators.

Mott [108-110] described a metal-insulator transition by imagining a crystalline array of hydrogen-like atoms with a lattice constant '*a*' that could be varied. The example of nickel oxide suggested that for large values of '*a*', the material would be insulating, while the example of monovalent metal like sodium showed that for small values it would metallic. To satisfactorily explain the values

of 'a' at which a metal-insulator transition can occur, Mott [108] made an assumption that this would occur when the screened potential around each positive charge

$$V(r) = -\frac{e^2}{r} e^{-qr} \tag{1.37}$$

with the screening potential calculated by the Thomas-Fermi method, was just strong enough to trap an electron. The transition would be discontinuous with varying n and q and there would be a discontinuous transition from the state with all electrons trapped to that where all are free. It was found that this would occur when

$$n^{1/3} a_H = 0.2 \tag{1.38}$$

where n is the number of electrons per unit volume and a_H is the hydrogen radius. The Eq. (1.38) was applied with success to the metal-insulator transition in doped semiconductors and the disorder resulting from the random positions of the centers being neglected. The disorder was believed to be the cause of the absence of a discontinuous change in conductivity. However the success of Eq. (1.38) was fortuitous if the many valley nature of the conduction bands of silicon and germanium is taken into account, and also the central cell corrections, totally different results are obtained [111-113].

The next important step in the development of the theory was the introduction by Hubbard [114, 115] of a model in which the interaction between electrons is included only when they are on the same atom, long-range Coulomb forces being neglected. For large values of 'a', this model leads to an antiferromagnetic insulator which splits the band, so that an electron's energy lie in a full band and an empty one [107]. However, Hubbard's work was criticized by

Herring [116] for lack of clear recognition that low-density form is antiferromagnetic. But work on '*resonating valence bond*' materials by Anderson [117] has shown that an antiferromagnetic lattice is not essential in the insulating state.

When two bands exist, they are named as lower and upper Hubbard bands. The metal-insulator transition then appears as a band crossing transition, from an antiferromagnetic metal to an antiferromagnetic insulator. There is another antiferromagnetic metal to normal metal transition and is one which is highly correlated and this leads to the great enhancement of the electronic specific heat and Pauli susceptibility, as first pointed out by Brinkman and Rice [118] and observed in vanadium oxides. The Hubbard model, which does not include long range forces, does not predict a discontinuous change in n, the number of carriers when long range forces are included, as first shown by Brinkman and Rice [119]. For a crystalline system, a discontinuity will always occur when a full and an empty band cross, as a result of the long-range electron-hole interaction and whether the bands are of Hubbard type or those generated by the crystal structure. Mott [120] has discussed the conditions under which disorder can remove the discontinuity. Actually, in many doped semiconductors, the transition is of Anderson type and not directly a consequence of short-range (intra atomic) interaction, both disorder and long-range interaction contributing to an equation similar to Eq. (1.37).

For disordered systems, a quite different form of metal-insulator transition occurs - the Anderson transition. In these systems, a range of energies exists in which the electron states are localized, and if at zero Kelvin, the Fermi level lies in this range then the material will not conduct even though the density of states is not

zero. The Anderson transition can be discussed in terms of non-interacting electrons though in real systems, electron-electron interaction plays an important part.

Many systems are known to exhibit metal-insulator transitions. Mixed valence perovskites are an important class of materials. In this subsection we give an outline of properties of mixed valence perovskites and various theoretical models to better understand the phenomena of metal-insulator transition found in these materials.

1.9 Mixed valence perovskites: An overview

Mixed valence manganites with the perovskite structure has been studied for almost 60 years. The system offers a degree of chemical flexibility that permits the relation between the oxide's structure, electronic and magnetic properties to be examined in a systematic way. Research on the manganites have revealed new phenomena such as colossal [121] and dense granular magnetoresistance [122] and has led to the formulation of important physical concepts such as double exchange [123, 124] and the Jahn-Teller polaron [125, 126]. Early research was motivated by a need to develop insulating ferromagnets with a large magnetization for high frequency applications. More recent work has been driven by a desire to understand and exploit the large negative magnetoresistance effects that appear above and below the Curie temperature. The manganites also have potential as solid electrolytes, catalysts, sensors and novel electronic materials.

Mixed valence oxides are represented by $R_{1-x}A_xMnO_3$ (where R = La, Nd, Pr and A = Ca, Sr, Ba, Pb) have been the materials of intense experimental interest. Besides manganese, many perovskite structure oxides form with Al, Ga or other

3*d* elements such as Chromium, Iron, Cobalt or Nickel. The rare earth orthoferrites $RFeO_3$ is one example of a series of perovskite structure oxides. An exhaustive compilation of data on perovskite-structure compounds by Goodenough and Longho [127] was published in a 1970 *Landholdt-Börnstein* volume. The mixed valence oxides can be considered as solid solutions between end members such as $RMnO_3$ and $AMnO_3$, with formal valence state states $R^{3+}Mn^{3+}O_3^{2-}$ and $A^{2+}Mn^{4+}O_3^{2-}$ leading to mixed valence compounds such as $\left(R^{3+}_{1-x}A^{2+}_{x}\right)\left(Mn^{3+}_{1-x}Mn^{4+}_{x}\right)O_3$. The nominal electronic configurations of Mn^{3+} are Mn^{4+} are $3d^4$ and $3d^3$ respectively. Chemically, the system is characterized by the wide range of cations, which can occupy the A-site in the perovskite structure, which may be set at the body centre or the cube corner. The structure of mixed valence oxides can be considered as a cubic close packed array formed of O_3^{2-} anions and large A cations with small B cations in the octahedral interstitial sites as shown in Fig. 1.5. The ideal cubic structures is distorted by cation size mismatch and the Jahn-Teller effect, where by a distortion of the oxygen octahedron surrounding the B site cation splits the energy levels of a 3*d* ion such as Mn^{3+}, thus lowering the energy. The distorted structures are frequently orthorhombic.

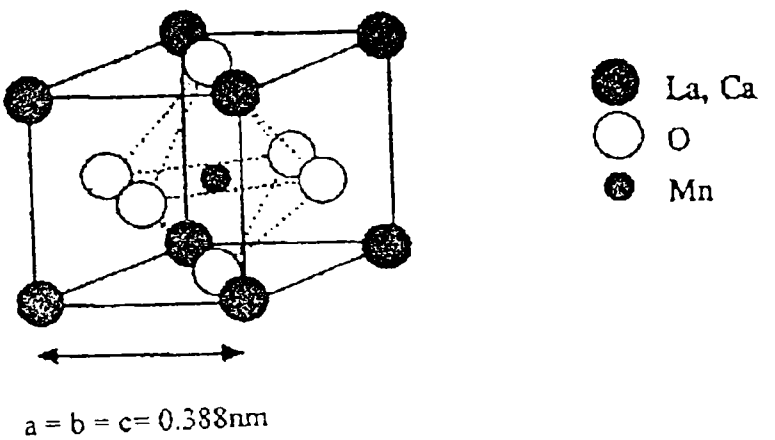

Fig. 1.5: Ideal cubic perovskite structure ABO_3 for the mixed valence perovskites

The broad feature of mixed valence perovskites were described by polycrystalline ceramic samples by Jonker and van Santen [128], van Santen and Jonker [129] and Jonker [130] in the late 1940s. They discussed the preparation, crystal structure and magnetic properties of the $(La_{1-x}Ca_x)MnO_3$ series [128] and gave an account for the electrical conductivity [129]. Similar results were found for the $(La_{1-x}Sr_x)MnO_3$ and $(La_{1-x}Ba_x)MnO_3$ series, but the range of solid solutions was limited to $x < 0.7$ or $x < 0.5$ respectively. Magnetoresistance and other transport properties were first described in 1954 by Volger [131] who showed that the magnetoresistance of $La_{0.8}Sr_{0.2}MnO_3$ is negative with a peak near the Curie temperature.

The crystallographic and magnetic structure for the $(La_{1-x}Ca_x)MnO_3$ compounds were determined in 1955 by Wolkan and Koehler [132] in a remarkably complete neutron and X-ray diffraction study as a function of Mn^{4+} content. In particular, the neutron data revealed a very rich magnetic phase diagram where, for different doping levels, there are three main regions. For small amounts of Mn^{4+}, the compounds have essentially antoferromagnetic properties. For $x \cong 0.3$, they become ferromagnetic, but for $x > 0.5$ they revert to antiferromagnetism upto the end member $CaMnO_3$. From magnetization and susceptibility results, Jonker [130] concluded that the exchange is weakly positive (ferromagnetic) between the two $3d^4$, Mn^{3+} ions, negative (antiferromagnetic) between two $3d^3$ Mn^{4+} and positive between a $3d^4$ Mn^{3+} and $3d^3$ Mn^{4+} ion, these measurements provided a first clear evidence for a ferromagnetic exchange interaction in an oxide. Resistivity measurements also revealed a strong correlation between electron transport and magnetic properties. The resistivity is lowest for the $x \sim 0.3$ compounds corresponding to best

ferromagnetism, where as high resistivity is associated with the antiferromagnetic compositions.

An extensive study of flux grown single crystals of $(La_{1-x}Pb_x)\ MnO_3$ with $0.2 < x > 0.4$ was carried out by Searle and Wang [133, 134], Morrish *et al.* [135] and Leung *et. al.* [136] in 1969 and 1970. They found metallic conductivity below the Curie point T_c and a large negative magnetoresistance effect of about 20% at 1 T in the vicinity of T_c, similar to that in polycrystalline $(La_{1-x}Sr_x)\ MnO_3$.

Interest in the mixed valence manganites revived in the 1990s, following the preparation of high quality thin films with large magnetoresistance by von Helmholt *et. al.* [137] and Chahara *et. al.* [138]. Optimised films show remarkable magnetoresistance effects near T_c that were epitomised by Jin *et al.* as the 'colossal magnetoresistance' (CMR) [121]. The Curie point coincides with the metal - insulator transition and there are associated anomalies in various physical properties. It is seen that the $x \cong 3$ corresponds to the best ferromagnetism, where high resistivities are associated with the antiferromagnetic compositions.

Despite intensive investigations of the CMR phenomenon, the nature of the metal-insulator (M-I) transition remains an open question. The manganese oxides are usually modeled by the double-exchange Hamiltonian that describes the exchange of electrons between neighbouring Mn^{3+} and Mn^{4+} ions with strong on-site Hund's coupling. So the inquisitiveness as to the origin of the mechanism of the effect, a great deal of effort is being devoted. Zener [123] paved the way by offering first satisfactory explanation for this phenomenon. In the next subsection, we will give an outline of the double-exchange model put forward by Zener to explain the M-I transition.

1.10 Double exchange model

Zener in 1951, offered an explanation for the behaviour of mixed valence manganites with doping, in terms of his theory of indirect magnetic exchange between 3*d* atoms. Starting from the insulating antiferromagnetic $RMnO_3$ end member whose electrons are localized in the atomic orbitals, he gave an explanation how the system should gradually become more ferromagnetic upon hole doping (introduction Mn^{4+}). He suggested that there will be an exchange of electron between Mn^{3+} and Mn^{4+} ion via oxygen and introduced the concept of simultaneous transfer of an electron from the Mn^{3+} to the oxygen and from the oxygen to the neighbouring Mn^{4+} as in Fig. 1.6. Such a transfer is called double exchange.

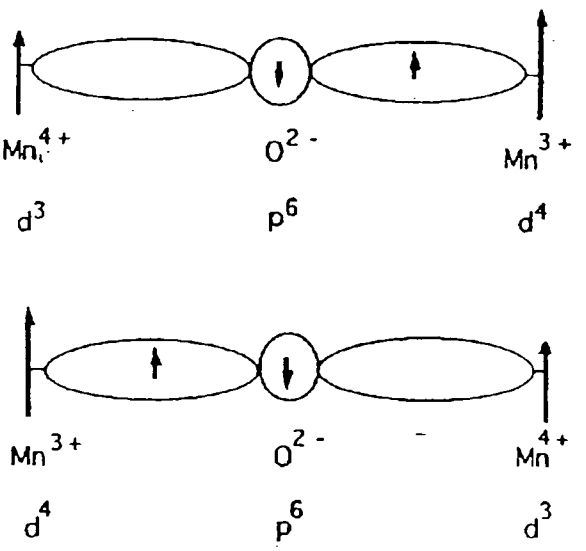

Fig. 1.6: Schematic diagram of the double-exchange mechanism. The two states Mn^{3+}-Mn^{4+} and Mn^{4+}-Mn^{3+} are degenerate if the manganese spins are parallel

In the case of magnetic ions, the configurations Mn^{3+} - O^{2-} - Mn^{4+} and Mn^{4+}-O^{2-}- Mn^{3+} are degenerate if the spins of the 2*d* shells are parallel and the lowest energy of the system at low temperature corresponds to parallel alignment of the

spins of the two adjacent cations. Double exchange is always found to be ferromagnetic unlike super exchange interaction that involves virtual electron transfer and is frequently antiferromagnetic.

He considered that the interatomic Hund rule exchange was strong and that carriers do not change their spin orientation upon hopping from one ion to the next, so that they can only hop if the spins of the two ions are parallel. On minimizing the total free energy of the system, Zener found that ferromagnetic interactions are favoured when the magnetic atoms are fairly well separated and conduction electrons are present. If the manganese spins are not parallel or if the Mn-O-Mn bond is bent, the electron transfer becomes more difficult and the mobility decreases. It follows that there is a direct connection between conductivity and ferromagnetism and a qualitative relation with Curie temperature has been proposed.

$$\sigma = \left(\frac{xe^2}{ah}\right)\left(T_c/T\right) \tag{1.39}$$

where x is the doping and a is the Mn-Mn distance, which agreed with the available experimental results of Jonker and van Santen in the limited region $0.2 < x < 0.4$.

Anderson and Hasegawa [139] generalized the double exchange mechanism by considering interaction between a pair of magnetic ion with general spin direction. They calculated the transfer integral t, to be

$$t = t_0 \cos\left(\theta/2\right) \tag{1.40}$$

where t_o is the normal transfer integral which depends on the spatial wave functions and the term $\cos(\theta/2)$ is due to the spin wave function and θ is the angle between two spin direction. This is quite unlike super exchange when the coupling is proportional to $\cos\theta$. They also considered the problem of high temperature

paramagnetic state of the manganites where the exchange energy is much larger than the transfer integral and predicted that χ should be Curie like, which contradicted the experimental results showing Curie-Weiss behaviour. The point was corrected by deGennes [140] who pointed out that the prediction is erroneous when the carrier bandwidth is large with respect to kT. Double exchange therefore leads to normal Curie - Weiss behaviour of the susceptibility $\frac{1}{\chi} = \frac{C}{T - T_P}$ with $\theta_P > 0$.

It is seen that even though double exchange plays an important role for metallic conductivity and ferromagnetism in these materials, it alone can't explain all the aforementioned phenomena. It has been pointed out by various workers [141 -143] that other effects such as localization, electron-electron correlation, electron magnon scattering, electron-phonon interaction etc., strongly modify the temperature dependence of many physical properties. It will be an uphill task to give details of all effects mentioned above. So we will give an outline of the localization phenomena and describe the Anderson transition in detail, in the next subsection.

1.11 Theoretical models

Localization-delocalization phenomenon in the physics of amorphous solids concerns the motion, not of atoms, but of electrons. Liquid-glass transition that involves atomic motion can be visualized in a classical picture of molecular movements, whereas the metal-insulator transition is an electronic phenomenon and is intrinsically quantum mechanical in character. Moreover, important features of this phenomenon represent conceptual departures from the traditional quantum mechanical treatment of electrons in crystalline solids. In order to introduce some of the main ideas and to place the issue of disorder induced localization in the context

of other basic electronic phenomena, we present three popular models of atomic scale metal-insulator transitions as given in Table (1.1)

Table 1.1: Major classification of metal-insulator transitions

Transition	*Electron Wave functions*		Characteristic Energies	Change at the M→I Transition	Criterion for Localization
	Metal side of Transition	Insulator side of Transition			
Bloch	Extended	Extended	Bandwidth B	Partly filled→ all bands filled or empty	–
Mott	Extended	Localized	Electron-electron (e^2/r_{ij}) correlation energy U	Correlation-induced localization	$U > B$
Anderson	Extended	Localized	Width W of the distribution of random site energies	Disorder-induced localization	$W > B$

1.11.1 Bloch theory of Metal – Insulator transitions

The first class of transition considered in Table (1.1) is one that is encompassed within the Bloch or band theory framework for electronic states in crystalline solids. Band theory is a one-electron independent particle theory that assumes that there exists a set of stationary states available to any one electron and that all of the electrons are distributed among these states according to Fermi-Dirac statistics. The states ψ_{nk} are given by the solutions of a Schrödinger equation $H\psi_{nk} = E_{nk}\psi_{nk}$ in which the Hamiltonian operator H is given by the sum of electronic kinetic energy term $\frac{p^2}{2m} = \left(-\frac{\hbar^2}{2m}\right)\left(\frac{d^2}{dx^2}\right)$ and a crystal potential term $V(x)$, to account for the interaction of one electron with all other particles in the crystal. Since V (and therefore H) is periodic in space with the translational periodicity of the crystal structure, $V(x + a) = V(x)$, where a is the lattice constant.

In the Bloch (or more properly the Bloch-Peierls-Wilson) theory of electrons in crystals, a solid is an insulator if each band is either completely filled or completely empty and it is a metal if atleast one band is partly filled. At zero temperature, (which is often assumed for the purpose of making a perfectly sharp metal - insulator distinction), all states lying lower in energy than the Fermi energy E_F are occupied by electrons, while all states lying higher than E_F are empty. For a metal, the band structure and the number of electrons are such that E_F lies within a band, which is only partly filled. For an insulator E_F lies between the bands and there is an energy gap separating the highest lying valence band and the lowest lying empty conduction band. This is very clearly illustrated in Fig (1.7)

The type of metal - insulator (M-I) transition envisioned in the first row of Table (1.1), is illustrated by the schematic band structure shown in Fig. 1.7. A crystalline material, composed of atoms with even number of electrons, sufficient to populate an integral number of bands, close to the Fermi level either just overlap in energy or just miss overlapping. A small change in pressure or temperature may cause the crystal's band structure to cross over to the other situation. Such a band - overlap M-I transition occurs in Ytterbium, in which a variation in pressure produces a cross over between band structures of types 'a' and 'b'.

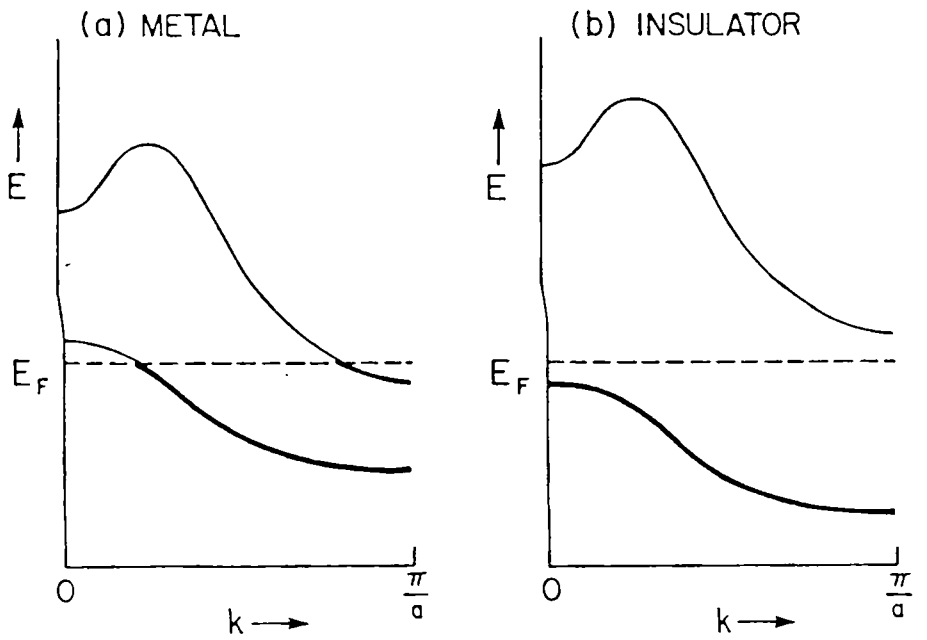

Fig. 1.7: Metal-insulator transition within the Bloch theory for electrons in crystals

As indicated in Table (1.1), on the both the metallic and insulating side of the above type of transition, the electronic wave function in the vicinity of E_F correspond to 'extended' states. Such wave functions have appreciable amplitude throughout the solid. For a crystal, the Bloch functions have the form as in Fig 1.8. The solid line in the figure represents the real and imaginary part of ψ, while the

dashed line indicates the plane-wave envelope corresponding to the wave vector eigen value $\tilde{k}$. For amorphous solids, $\tilde{k}$ is not a good quantum number, since the validity of Bloch-function depends upon the presence of crystalline long-range order. Long-range order is totally absent in amorphous solids and this is an obvious way in which band theory breaks down for amorphous solids.

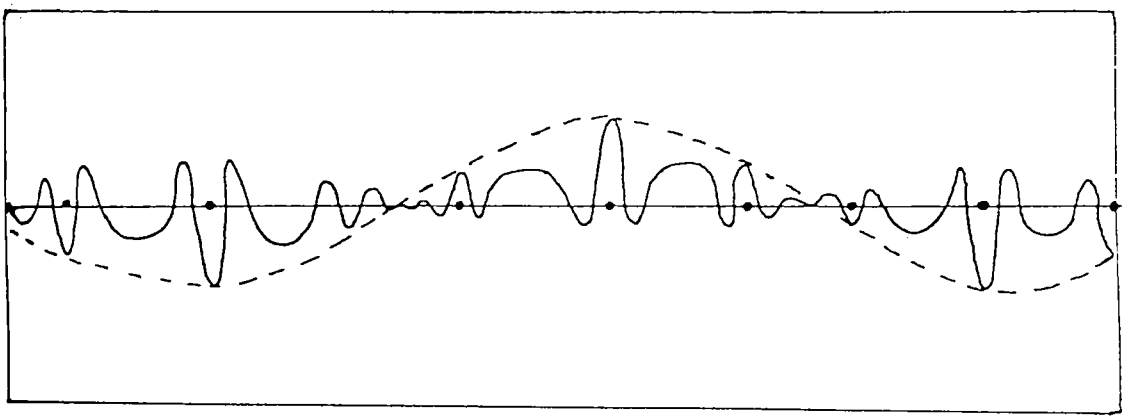

Fig. 1.8: A Bloch type extended wave function as in a crystal

Before proceeding to the discussion of disorder-induced localization and the Anderson transition, it is useful to introduce the concepts involved in another type of M-I transition, contributed to condensed matter physics by Sir Nevill Mott. The Mott transition [144, 145] is philosophically and physically related to Anderson transition. Philosophically both transitions are dramatic demonstrations of situations in which the conventional theory (Bloch functions, band structures etc) used for electrons breaks down. Band theory, often successful in explaining the electrical and optical properties of crystalline solids fails completely in these situations.

1.11.2 The Mott transition

The Mott transition illuminates a regime in which the one electron or independent particle theory of solids fails, within a crystalline material. In quantum mechanical calculations for electronic states in a crystal, standard procedure is to assume that the atomic nuclei are fixed in position on the sites of a crystalline lattice. But suppose we set 'a' at a very large value, then in the independent particle theory, as the translational periodicity is retained, the one electron solutions are still Bloch functions, the highest band is only half filled and the material is still predicted to be a metal. But this is not true as we are dealing with a set of isolated atoms and the true solutions must be just the atomic solutions. The above argument shows that the band theory fails in the atomic limit $a \rightarrow \infty$ for a system with a half- filled highest band.

The physical reason for this failure is disclosed with the aid of Fig. 1.9. There are two electronic configurations that in the independent electron picture, have the same potential energy. In configuration 'b' of Fig. 1.9, two of the outer most or valence electrons have been shifted from their positions in 'a' to translationally equivalent positions in another unit cell. Because of the translational periodicity of the crystal potential $V(r)$ which approximates the average interaction of each electron with all of the other 10^{24} charged particles in the solid, configurations 'a' and 'b' have the same potential energy in the independent particle picture. This is manifestly unreasonable as configuration 'b' has a substantially higher energy than 'a' because of the repulsive Coulomb interaction among the valence electrons. This energy cost associated with the electronic crowding in 'b', is

a '*many body effect*' that is left out of the independent particle picture of one electron theory.

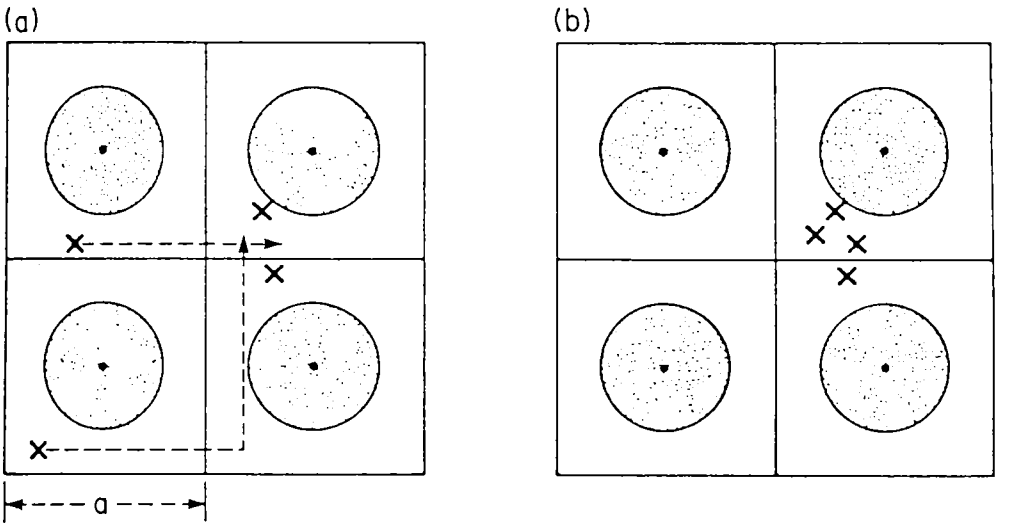

Fig. 1.9: Two electronic configurations within a four-unit cell region of a crystal

One electron theory is therefore unable to discriminate against configuration as (b), since it does not perceive their extra energy *vis-à-vis* configurations such as in (a). In a real solid, however, the electrons definitely do tend to correlate their movements in order to avoid such energetically unfavourable mutual proximity as in Fig (1.9a). The amount by which band theory overestimates the ground state energy of the system because of this neglect of electron correlations is called the correlation energy. The point embodied by the Mott transition concept is that the correlation energy can under certain conditions cause a solid to have an insulating ground state when the neglect of correlation band picture would erroneously predict it to be a metal. Such a solid is called a Mott Insulator. An example is NiS_2 and the condition required for its occurrence is described in Fig. 1.10.

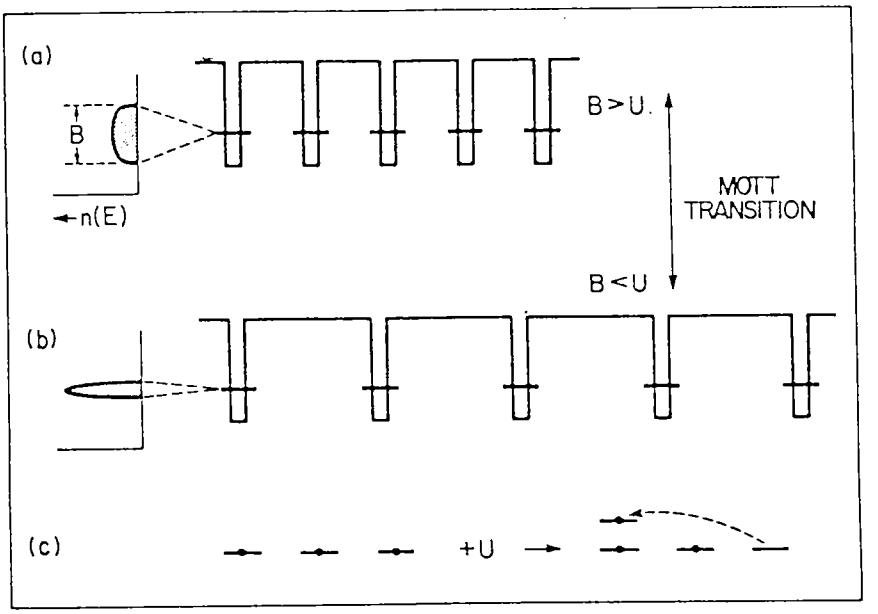

Fig. 1.10: Schematic picture for the Mott transition

In this figure, the atoms are represented by potential wells and single valence electron of each atom occupies, in the isolated atom limit, a bound state energy level that is indicated on each atomic well by a horizontal line. In the crystal, the level gives rise to an energy band of band width *B*. Relative to the energy level of free atom, the crystal band extends in energy from roughly *–B/2 to + B/2*. This lowering in energy relative to the free atom is responsible for metallic cohesion. It arises from a lowering of kinetic energy that is achieved by the delocalization of the electrons into extended states in the crystal. Delocalization smooths the wave function oscillations and thus reduces the ∇^2 kinetic energy contribution to the total energy. This energy lowering is relatively ineffective when there is little overlap between orbitals on neighbouring atoms. *B* thus decreases with increasing lattice constant '*a*', as suggested by Fig. 1.10 and the bandwidth vanishes in the $a \rightarrow \infty$ limit.

In figures 1.10(a) and 1.10(b), single horizontal line at each well denotes the energy level of the valence electron of the isolated atom. This energy level is doubly degenerate and this view neglects the e^2/r_{12} interaction. In the case when two electrons occupy the same site, repulsive interaction dominates and raises the energy and this occupation number dependent feature introduced by e^2/r_{12}. It is represented by an equivalent two-level diagram shown in Fig. 1.10(c). Two levels are associated with each site. The lower level, which corresponds to the level used in (a) and (b) is available to the first electron to occupy the atom. The upper level exists only when the lower level is filled and is lifted by the amount U and is available to the second electron to occupy the site. Hence the delocalized wave functions and the failure of electrons to maximally avoid each other, introduces an average potential energy cost per electron of $U/4$. Since the average kinetic energy incentive for band formation is $B/4$, it follows that the correlation cost exceeds the delocalization gain if $U > B$ This is the condition for the occurrence of a Mott insulator. i.e., $U > B$ represents the criterion for correlation induced localization

If this inequality criterion is satisfied, then electrons are localized. Unlike the Bloch type of metal-insulator transition (in which extended states apply to both sides), the Mott transition is a delocalization–localization transition for electron states. It occurs as implied in a↔b, when a change in interatomic separation causes a cross over in the relative importance of the two characteristic energies of the valence electron system the bandwidth B and the electron-electron correlation energy U. The Mott transition is an exemplary embodiment of a recurrent theme in condensed matter physics. Electron localization in the low density limit signals the triumph of potential energy over kinetic energy in that regime. The kinetic energy

cost of localization becomes negligible in comparison to the coulomb interaction and the electrons from a lattice to maximally avoid each other inorder to minimize the totally dominant potential energy.

1.11.3 Disorder induced localization-Anderson transition

The type of metal insulator transition that is most relevant to amorphous solids is the Anderson transition. Here the insulating side of the transition corresponds not to extended states in filled bands as in a Bloch type transition in crystals, but instead to electron states which are localized. The meaning of localized states is indicated in Fig. 1.11. The wave function is concentrated near a centre composed of just few atoms and has negligible amplitude elsewhere in the solid. Away from the small regions that contain essentially all of its integrated possibility $\int|\psi|^2 dr$, the amplitude spatially decays away with distance. This behaviour is schematically shown by the dashed line wave functions envelope in Fig. 1.11, and falls off as $e^{-\alpha R}$ at large distances R from the localization centre. The quantity α is an important parameter for a given localized state known as inverse localization length.

In crystalline solids, localized states are often introduced by chemical impurities. An illustration of Anderson transition is shown in Fig. 1.12. As in the case of the Mott and Wigner transitions, electron localization in the Anderson transition reflects the passage to a regime in which the potential energy pins over the kinetic energy, while the a↔b delocalization-localization transition in Mott case of Fig. 1.10 occurs via the kinetic energy considerations with decreasing band width at low densities. In the Anderson case of Fig. 1.12 it occurs via the superposition of disorder-induced potential energy of sufficient depth.

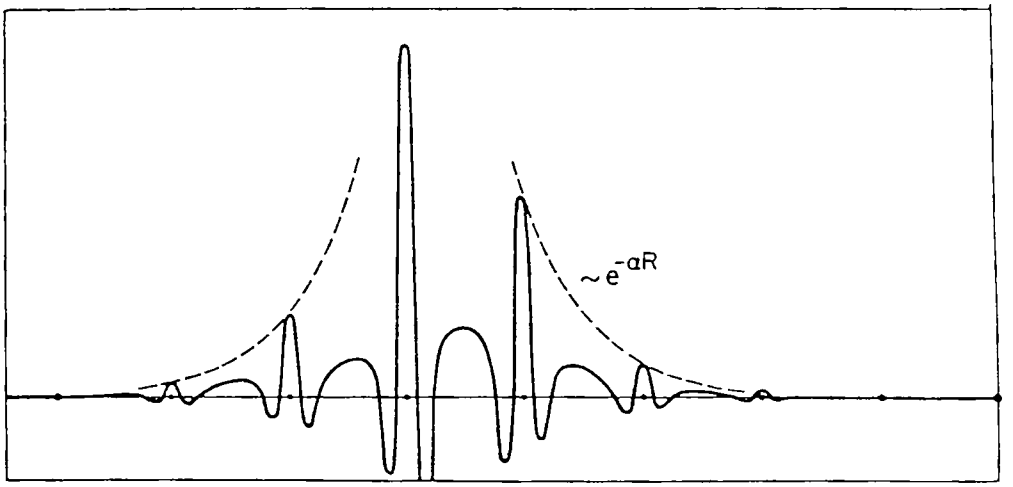

Fig. 1.11: Schematic representation of a localized wave function as in amorphous solids

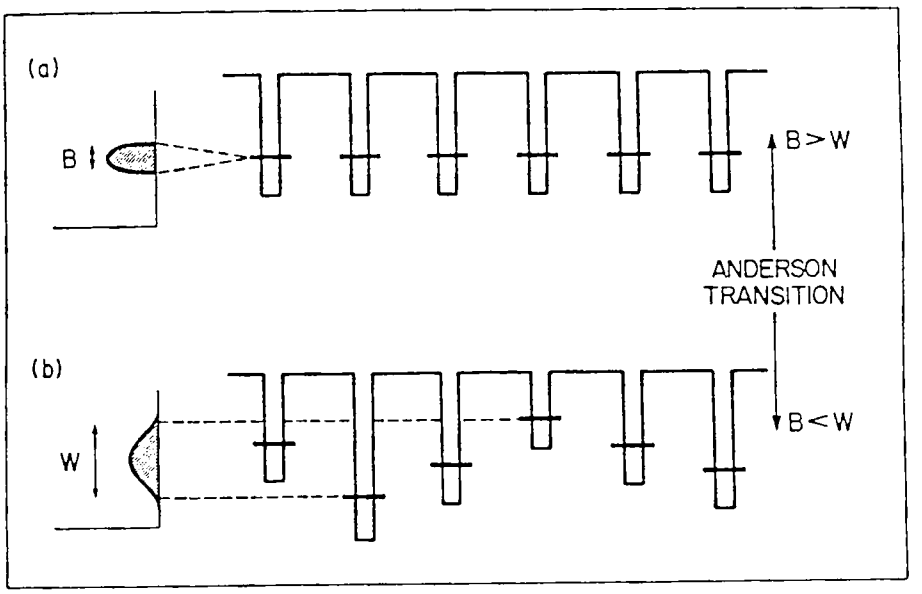

Fig. 1.12: One electron tight binding picture for the Anderson transition

Here the potential wells representing the atomic sites are no longer all the same. Instead, the well depths vary from sites in a random way. Such a disordered potential is present in an amorphous solid. Instead of single well depth as in a crystalline case, there is a distribution of well depths. W denotes the width of this distribution, which specifies the energy range of the disorder-induced spatial fluctuations of the potential energy seen by an electron at the atomic site.

The competition between kinetic energy and potential energy influences on the electron states now resides on the ratio W/B; W the magnitude of the random potential and B, the crystal bandwidth in the absence of disorder are the two relevant characteristic energies. Anderson showed that when the dimensionless parameter W/B is sufficiently large, all of the states in the valence band are localized. i.e., $W > B$ denotes the disorder-induced localization

Andersen's model is a quantum mechanical calculation that invokes a tight binding independent electron picture, which corresponds to Fig (1.12b). Unlike the Mott insulator, in which the extended states predicted by an independent electron picture are overturned when electron-electron correlation is introduced, Anderson localization appears as a consequence of disorder in a purely independent electron picture.

The notion of disorder-induced localization was subsequently extended by Mott and others [146, 147]. When the disorder is great enough for W/B to satisfy the Anderson's criterion, all of the states in the band become localized. Mott pointed out that even for smaller degrees of disorder, states in the tails of the band are localized as in Fig. 1.13 and the energies for which states are localized (the shaded regions) correspond to the tails of top of the valence band and bottom of the conduction band.

Within each band, the states are extended. As shown in Fig. 1.13(b), the demarcation energies separating regions of localized and extended states are referred to as mobility edges. The Anderson transition then refers to a localization→delocalization transition in which a change in composition, pressure, applied electric field etc. pushes the Fermi level through such a mobility edge. The energy separation between the mobility edges of Fig. 1.13(b) is called the mobility gap [148]. It plays a role, with respect to the electrical properties of amorphous semiconductors that is similar to the role played by the energy gap in a crystalline semiconductor.

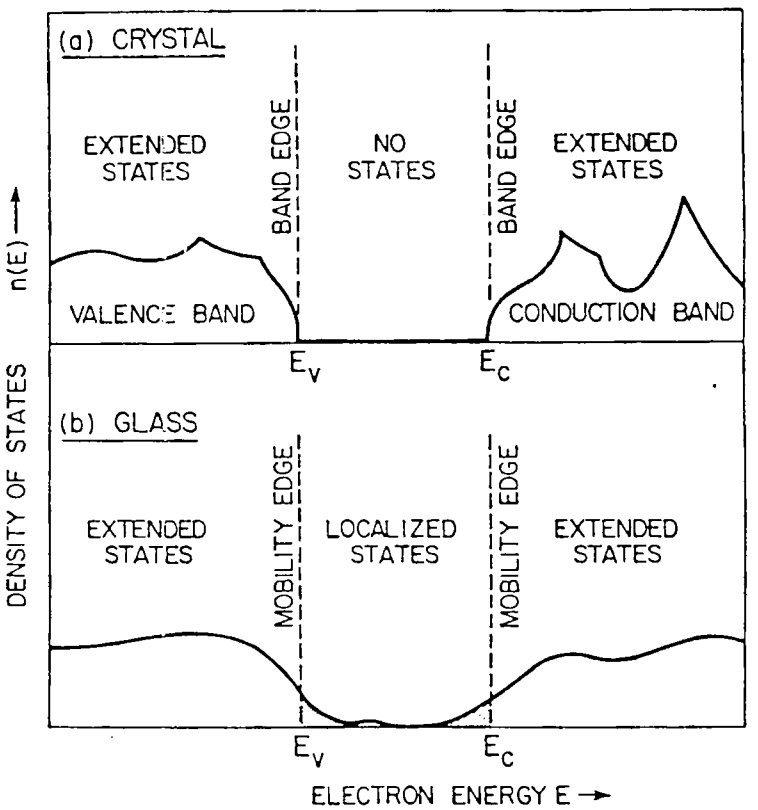

Fig. 1.13: Schematic density of states diagram for a crystalline and amorphous materials

Even these models couldn't successfully explain the M-I transition phenomena found in mixed valence perovskites. Based on the strong electron-phonon coupling in these materials, Mills [149] *et al.*, proposed that the M-I transition involves a cross over from a high-T polaron dominated magnetically disordered regime to a low-T metallic magnetically ordered regime. Now, some authors have concluded that M-I transition in CMR materials is the Anderson transition - a quantum phase transition, driven by magnetic order, because quantum localization effect plays an important role in the system around and above the magnetic transition.

1.12 Review of experiments

In the first study of mixed valence perovskites, van Santen and Jonker [129] and Jonker [150] have reported resistivity measurements on ceramic samples of $(La_{1-x}A_x)$ MnO_3 (A= Ba, Ca or Sr), as a function of temperature and composition. Their main result was the striking correlation between the magnitude of the resistivity and the magnetic state of the compounds. Outside the ferromagnetic concentration range, resistivities are high and thermally activated, but a resistance anomaly appears around T_c for the ferromagnetic compositions, where there is a transition to metallic like conductivity.

When Volger [131] discovered the large negative magneto resistance effect near T_c in 1954, he showed it to be isotropic-independent of the relative orientation of the current and the field and frequency dependent. He also made the first measurements of Hall effect, thermopower and specific heat. The single crystal magnetoresistance measurements reported 15 years later for the $(La_{1-x}Pb_x)$ MnO_3

system [134], showed the effect to be quite substantial, with a 20% decrease in resistivity at 310K in an applied field if 1T. Twenty more years elapsed before the effect was rediscovered, at a time of interest in using magnetoresistance in sensors operating at room temperature. The largest magnetoresistance for the manganites usually appears near T_c that can be above room temperature for some compositions. Examples are La-Na or La-K with $x \approx 0.15$ [151-153]; La-Ba, La-Pb or La-Sr with $x \approx 0.3$. The resistivity peak temperature T_m, almost coincides with T_c for crystals with $x \approx 0.3$. The saturation magnetoresistance in the vicinity of T_c is bounded by a drop in resistivity below T_c, which depends in turn on T_c itself [154, 155].

Volger [131] in his first measurements of the Hall effect in $(La_{1-x}Sr_x)MnO_3$, obtained a very low value for mobility in the paramagnetic state. The Hall coefficient is negative and the deduced electron concentration contradicts thermopower measurements. In the ferromagnetic state, Volger reported that the extraordinary Hall effect is small and negative and the upper limit obtained for mobility is only 10^{-5} m^2 V^{-1} s^{-1}. Thirty years later, Tanaka *et al.* [156] reported Hall effect measurements on polycrystalline $(La_{0.8}Ca_{0.2})$ MnO_3. Because of the smallness of the signals, only an upper limit on the mobility edge could be estimated as 7×10^{-6} $m^2V^{-1}s^{-1}$ at 300K. A similar mobility was measured in a crystal of $(Nd_{0.5}Pb_{0.5})$ MnO_3 near T_c [157] and a carrier concentration of 5×10^{26} m^{-3} below 100K was deduced. Liu *et al.*, [158] reported successful Hall effect measurements on single crystals of $La_{0.65}(PbCa)_{0.35}MnO_3$ at 5K where the resistivities were in the micro ohm- meter range. The inferred electron density is typically metallic with $n_H \approx 10^{29}$ m^{-3}. The result is consistent with the density of states deduced from low temperature

heat capacity measurements that lead to a metallic density of states for a range of polycrystalline samples [158].

Measurement of the electric field induced by a temperature gradient across a sample provides complementary information to the resistivity. These have been many measurements of the thermopower (S) of samples with $x \approx 0.3$, which exhibit a metal-insulator transition [131, 159, 167]. There is strong magnetic field dependence of S in the vicinity of T_c, which demonstrates that carriers are magnetic in character. When a large positive anomaly is observed around T_c, the thermopower is reduced by the field [159, 165, 168]. At higher temperatures, when the thermopower has become negative, the effect of the field is to reduce its absolute value [162]. Well above T_c, the magnetic field has little effect on S, and it is thought that transport is due to hopping and dielectric polarons [164].

The pressure dependence of S has been measured by Zhou and co workers [164,169], who found that the large positive bump across T_c is reduced in magnitude as the Curie temperature is increased by pressure. Thermopower measurements were carried out across the entire composition range for $(La_{1-x}Sr_x)\ MnO_3$ [131], $(La_{1-x}Ca_x)\ MnO_3$ [170] and $(Pr_{1-x}Ca_x)\ MnO_3$ [171] series. The Seebeck coefficient of $Nd_{0.5}(Sr, Pb)_{0.5}MnO_3$ is negative for $T > 100K$ [165]. Likewise those of $(La_{1-x}Ca_x)\ MnO_3$ and $(La_{1-x}Sr_x)\ MnO_3$ become negative for $x > 0.25$ [172-174]. Cation deficient $(LaMn)_{1-\delta}O_3$ shows a positive thermopower at all temperatures, indicating that the holes are produced by cation deficiency [166, 175].

1.13 Variation of thermal conductivity and heat capacity during an M-I transition.

1.13.1 Heat capacity

The heat capacity of several ferromagnetic manganite compositions with $x \approx 0.3$ have been measured at low temperature [176-178]. There are also low temperature data on $(La_{1-x}Sr_x)\ MnO_3$ [176] for $0 \leq x \leq 0.3$ and nonstoichiometric $LaMnO_3$ [179] as well as data as $(La_{1-x}Ca_x)\ MnO_3$ for $T > 50K$ [180] and $(La_{0.8}Ca_{0.2})\ MnO_3$ for $T >$ 100 K [181]. In compounds of magnetic rare earths, the low temperature specific heat is dominated by single ion excitations of the rare earth.

By fitting low temperature data on $x \approx 0.3$ compositions of a non magnetic rare earth to just an electronic and a lattice term, of the form,

$$C = \gamma T + \beta T^3 \ , \qquad (1.41)$$

Coey and co-workers [182] deduced γ = 5-8 mJ $mol^{-1}K^{-2}$ which corresponds to a density of carriers at Fermilevel $N(E_F) = {}^{3\gamma}/_{\pi k_B^2}$ of about 4 x 10^{-3} m^{-3} eV^{-1}. This is a relatively high value for a metal, but the value of γ is uncorrelated with the residual resistivity ρ_0 that varies by several orders of magnitude in these compounds.

The low temperature heat capacity of the stoichiometric $LaMnO_3$ and end member has been fitted with T^{-2}, T^3 and T^2 terms, with the latter being ascribed to two-dimensional ferromagnetic magnons. A comparison of the two cation deficient $(LaMn)_{1-\delta}O_3$ samples, one ferromagnetic and other antiferromagnetic, shows an unexpectedly large heat capacity at low temperatures in both cases. γ is > 20 mJ

$mol^{-1} K^{-2}$ for both cases, which has been ascribed to a high density of localized states below the mobility edge [179].

Heat capacity anomalies have been observed in the vicinity of the Curie temperatures for $(La_{1-x}Ca_x)MnO_3$ system, where a typical lambda anomaly is observed or $x \approx 0.33$ [180,181]. The associated entropy of $0.4R$ ln2 per mole is attributed to the spin disorder entropy contribution due to charge localization above T_c [180]. Heat capacity anomalies appear at the two-phase transition in samples with $x \geq 0.5$, one of which is associated with charge order and also at the $O \rightarrow O'$ structural transition [181,182].

1.13.2 Thermal conductivity

It has been reported that like the electrical conductivity, the thermal conductivity K exhibits an anomaly in the vicinity of T_c that can be modified by applied field [183]. It increases by 30% in 6T at 265K. An unusual positive temperature coefficient $dK/dT > 0$ above T_c is associated with scattering from large dynamic lattice distortions accompanying charge transport near T_c in the insulating phase. Thermal diffusivity has been measured in $(La_{0.67}Ca_{0.33})\ MnO_3$ [184], where there is a broad dip near T_c related to K and the magnetic part of the specific heat.

Chen *et al.*, [185] measured the magnetothermal conductivity behaviour of polycrystalline $(La_{0.8}Ca_{0.2})MnO_3$. The temperature dependence of the thermal conductivity displays a striking dip, while the resistivity and the thermopower have a peak near 240 K. The temperature and field dependences of the thermal conductivity are attributed to the scattering of phonons by spin fluctuations.

References

1. F.Hayashi, *Doctoral dissertation*, (Göttingen University, Göttingen, Germany, 1912).
2. W. C. Roentgen, Ann. Phys. **45** (1914) 737.
3. W. Ackerman, Ann. Phys. **46** (1916) 197.
4. T. Yeou, C. R. Acad. Sci. **207** (1938) 1042.
5. A. G. Chynoweth, J. Appl. Phys. **27** (1956) 78.
6. H. P. Beerman, Am. Ceram. Soc. Bull. **46** (1967) 737. a
7. E. H. Putley, *Semiconductors and Semimetals*, edited by R. K. Willardson and A. C. Beer, Vol.5 (Academic, New York, 1970) 259.
8. B. R. Holeman, Infrared Phys. **12** (1972) 125.
9. W. R Belvin and J. Geist, Appl. Opt. **13** (1973) 1171.
10. S. T. Liu, Ferroelectrics **10** (1976) 83.
11. H. Coufal, Appl. Phys. Lett. **44** (1984) 59.
12. A. Mandelis, Chem. Phys. Lett. **108** (1984) 388.
13. D. Dadarlat, M. Chirtoc, R. M. Cândea and I. Bratu, Infrared Phys. **24** (1984) 469.
14. H. Coufal, Fresenius Z. Anal. Chem. **324** (1986) 456.
15. H. Coufal, *IEEE Trans Ultrason. Ferroelec. Freq. Ccontrol. UFFC* **33** (1986) 507.
16. H. Coufal, Appl. Phys. Lett. **45** (1984) 516.
17. H. Coufal, R. Grygier, D. Horne and J. Fromm, J. Vac. Sci. Technol. A **5** (1985) 2875.

18. H. Coufal, J. Stöhr and K. Baberschke, *Photoacoustic and Photothermal Phenomena*, edited by P. Hess and J. Pelzl (Springer, Heidelberg, 1988) 25.

19. T. Hinoue, S. Kawada, M. Murata and Y. Yokoyama, Chem. Lett. Jpn. 2061 (1988).

20. *Photoacoustic and Thermal wave phenomena in Semiconductors*, edited by A. Mandelis (Elsevier, New York, 1987).

21. R. K. Grygier, W. Knoll and H. Coufal, Can. J. Phys. **64** (1986) 1067.

22. T. J. Chuang, H. Coufal and F. Trager, J. Vac. Sci. Technol. A **1** (1983) 236.

23. M. Chirtoc, D. Dadarlat, I. Chirtoc and D. Bicanic, *Photoacoustic and Photothermal Phenomena*, edited by P. Hess and J. Pelzl, (Springer, Heidelberg, 1988) 55.

24. M. Chirtoc, D. Dadarlat, I. Chirtoc and D. Bicanic, Spectrosc. Lett. **21** (1988) 413.

25. H. Coufal, H. F. Winters and F. Sequeda, *Photoacoustic and Photothermal Phenomena*, edited by P. Hess and J. Pelzl, (Springer, Heidelberg, 1988) 201.

26. W. Knoll and H. Coufal, *Photoacoustic and Photothermal Phenomena*, edited by P. Hess and J. Pelzl, (Springer, Heidelberg, 1988) 209.

27. T. Baumann, Appl. Phys. Lett. **43** (1983) 71.

28. I. F. Faria, J. C. Ghizoni and L. C. M. Miranda, Appl. Phys. Lett. **47** (1985) 1154.

29. M. Liezers and R. M. Miller, *Photoacoustic and Photothermal Phenomena*, edited by P. Hess and J. Pelzl (Springer, Heidelberg, 1988) 437.

30. M. Byfuss, R. Tilgner and J. Baumann, *Photoacoustic and Photothermal Phenomena*, edited by P. Hess and J. Pelzl (Springer, Heidelberg, 1988) 392.

31. M. V. Iravani and H. K. Wickramasinghe, J. Appl. Phys. **58** (1985) 122.

32. T. J. Negran, Ferroelectrics **34** (1981) 285.

33. H. Coufal and P. Hefferle, Appl. Phys. A **38** (1985) 213.

34. C. C. Ghizoni and L. C. Miranda, Phys. Rev. B **32** (1985) 8392.

35. P. K. John, L. C. Miranda and A. C. Rastogi, Phys. Rev. B **34** (1986) 4342.

36. H. Coufal and P. Hefferle, Can. J. Phys. **64** (1986) 1200.

37. M. Liezers and R. M. Miller, *Photoacoustic and Photothermal Phenomena*, edited by P. Hess and J. Pelzl, (Springer, Heidelberg, 1988) 344.

38. S. B. Lang, Ferroelectrics **11** (1976) 315.

39. C. Jeack, R. Melcher and S. Jha, J. Appl. Phys. **53** (1982) 3947.

40. Mandelis, F. Care, K. K. Chan and L. C. M. Miranda, Appl. Phys. A 38 (1985) 117.

41. J. F. Power and A. Mandelis, Rev. Sci. Instrum. **58** (1987) 2024.

42. A. Mandelis and M. M. Zver, J. Appl. Phys. **57** (1985) 4421.

43. A. Roscencwaig and A. Gersho, J. Appl. Phys. **47** (1976) 64.

44. Kynar™ Piezo Film Technical Manual, (Pennwatt Corp. Pennsylvania. 1983) 17.

45. L. Bui, H. J. Shaw and L. T. Zitelli, Electron Lett. **12** (1976) 393.

46. M. Chirtoc and G. Mihâilescu, Phys. Rev B **40** (1989) 9606.

47. M. Chirtoc and I. Chirtoc, Infrared Phys. **29** (1989) 847.

48. S. B. Peralta, S. C. Ellis, C. Christofides, A. Mandelis, H. Sang and B. Faranbakhsh, Res. Nondestr. Eval. **3** (1991) 69.

49. J. F. Power and A. Mandelis, Rev. Sci. Instrum. **58** (1987) 2018.

50. J. F. Power and A. Mandelis, Rev. Sci. Instrum. **58** (1987) 2024.

51. J. F. Power and A. Mandelis, Rev. Sci. Instrum. **58** (1987) 2033.

52. J. F. Power, Appl. Spectrosc. **45** (1991) 1240.

53. J. F. Power, Appl. Spectrosc. **45** (1991) 1252.

54. H. Coufal and A. Mandelis, Ferroelectrics **118** (1991) 379.

55. M. Marinelli, F. Mercuri. U. Zammit and R. Pizzoferrato, Appl. Phys. Lett. **00** (1990) 000.

56. C. Christofides, K. Gandhi and A. Mandelis, Meas. Sci. Technol. **1** (1990) 1363.

57. A. Rosencwaig, *Photoacoustics and Photoacoustic spectroscopy, Chemical Analysis*, Vol. 57 (Wiley-Interscience, New York, 1980).

58. A. Mandelis, W. Lo and R. W. Lo and R. Wagner, Appl. Phys. A **44** (1987) 123.

59. H. Tanaka, *Photoacoustic and thermal wave phenomenon in semi conductors*, edited by A. Mandelis (North Holland, New York, 1987) ch.16

60. K. Tanaka, Y. Ichimura and K. Sindoh, J. Appl. Phys. **63** (1988) 1815.

61. A. Mandelis, R. E. Wagner, K. Gandhi, R. Baltman and P. Dao, Phys. Rev. B **39** (1989) 5254.

62. R. L. Melcher and Arbach, Appl. Phys. Lett. **40** (1982) 911.

63. D. Dâdarlat, M. Chirtoc, C. Neamtu and D. Bicanic, J. Phys. Chem. Solids **00** (1990) 000.

64. D. Dâdarlat, M. Chirtoc and D. Bicanic, *6th International Topical Meetings on Photoacoustics and Photothermal Phenomena* II, edited by Murphy *et al.* Vol. **62** (1991) 300.

65. M. Marinelli, U. Zammit, F. Mercuri, R. Pizzoferrato, J. Appl. Phys. **72** (1991) 1096.

66. F. Murthas, M. G. Mecozzi, M. Marinelli, V. Zammit, R. Pizzoferrato, F. Scudieri, S. Martellucci and M. Marinelli, *6th International Topical Meetings on Photoacoustics and Photothermal Phenomena* II, edited by Murphy *et al.* Vol. **62** (1992) 208.

67. V. Zammit, M. Marinelli, R. Pizzoferrato, F. Scudieri and S. Martellucci, *Photoacoustics and Photothermal Phenomena* II, Vol. **62** (1993).

68. A. Mandelis, J. Vanniasinkam and S. Budhudu, Phys. Rev. B **48** (1993) 6808.

69 A. K. Ghosh and B. K. Chaudhari, J. Appl. Phys. **80** (1996) 5292.

70. J. Philip, Rev. Sci. Instrium. **67** (1996) 3621.

71. J. Shen, K. Fjeldsted, J. Vanniasinkam and A. Mandelis, Opt. Mater. **4** (1995) 823.

72. M. Munidassa, F. Funak and A. Mandelis, J. Appl. Phys **83** (1998) 3495.

73. A. Bozoki, J. Sneider, G. Szabo, A. Miklos, M. Serenyi, G. Nagy and M Feher, Appl. Phys. B: Lasers Opt. **63** (1996) 399.

74. M. Feher, Y. Jiang, J. P. Maier and A. Miklos, Appl. Opt. **33** (1994) 1655.

75. J. Shen, A. Mandelis and H. Tsai, Rev. Sci. Instrum. **69** (1998) 197.

76. J. Shen, and A. Mandelis, Rev. Sci. Instrum. **66** (1995) 4999.

77. J. Shen, A. Mandelis and B. Aloysius, Int. J. Thermophys. **17** (1996) 12

78 . Christofides and A. Mandelis, J. Appl. Phys. **68** (1990) R1.

79 . Shen, A. Mandelis and T. Ashe, Int. J. Thermophys. **19** (1998) 510.

80 C. H. Wang and A. Mandelis, Rev. Sci. Instrum. **70** (1999) 2372.

81 Juhl and Bimberg, J. Appl. Phys. **64** (1988) 303.

82 C. N. R. Rao and K. J. Rao, *Phase transitions in solids*, (Mc Graw Hill, New York, 1978).

83 H. E. Stanley, *Introduction to phase transitions and critical phenomena*, (Clarendon press, Oxford, 1971).

84 P. Ehrenfest, Proc. Amsterdam Acad. **36** (1943) 153.

85 K. J. Rao and C. N. R. Rao, J. Materials Sci. **1** (1966) 238.

86 C. N. R. Rao and K. J. Rao, *Progress in Solid State Chemistry*, edited by H. Reiss, Vol. **4** (Pergamon Press, Oxford, 1967)

87 L. D. Landau and E. M. Lifshitz, *Statistical Physics*, (Pergamon Press, Oxford, 1959).

88 A. Richard, Am. J. Phys. **40** (1972) 3.

89 C. N. R. Rao and M. Natarajan, *Crystal Structure Transformation in Binary Halides*, NSRDS-NBS Monograph **41** (National Bureau of Standards, Washington DC, 1972)

90 C. N. R. Rao and G. V. Subha Rao, *Transition Metal Oxides - Crystal Chemistry, Phase transitions and related aspects*, NSRDS-NBS Monograph **49** (National Bureau of Standards, Washington DC, 1974)

91 C. N. R. Rao and K. P. R. Pisharody, *Transition Metal Sulfides. Progress in solid state chemistry*, Vol. **10** (Pergamon Press, Oxford, 1975).

J. B. Goodenough and J. M. Longo, *Crystallographic and Magnetic properties of perovskite and perovskite related compounds*, Landolt-Bornstein New series, Group III, Vol. **40** (Springer –Verlag, Berlin, 1970).

Structural Phase transitions I, edited by K. A. Muller and H. Thomas (Springer-Verlag, NewYork, 1981).

R. Florian, J. Pelzl, M. Rosenberg, H. Vargas and R. Wemhardt, Phys. Stat. Solidi (a) **48** (1978) K35.

C. Pichon, M. Lelibaux, D. Fournier and A.C. Boccara, Appl. Phys. Lett. **35** (1979) 435.

M. A. Siqueria, C. C. Ghizoni, J. I. Vargas, E. A. Menezes, H. Vargas and L C. M. Miranda, J. Appl. Phys. **51** (1980) 1403.

P. Korpiun and R. Tilgner, J. Appl. Phys. **51** (1980) 6115.

I. Bibi and T. E. Jenkins, J. Phys. C **16** (1987) L57.

J. Fernandez, J. Extebarria, M. G. Telco and S. A. Lopez Echarri, J. Phys. D. Appl. Phys. **16** (1983) 269.

J. Exlebarria, S. Uriarte, J. Fernandez, M. J. Tello and A. Lopez Echarri Phys. D **16** (1983) 269.

J. Extebarria, J. Fernandez, M. A. Arriandiaga, M. J. Tello, Phys. C **18** (1985) L13.

W. Jackson and N. M. Amer, J. Appl. Phys. **51** (1980) 3343.

A. Mandelis, F. Care and K. K. Chan, Appl. Phys. A **38** (1985) 117

A. H. Wilson, Proc. R. Soc. Lond. A **133** (1931) 458.

A. H. Wilson, Proc. R. Soc. Lond. A **134** (1931) 277.

J. H. de Boer and E. J. W. Verwey, Proc. Phys. Soc. A **49** (1937) 59.

107. J. C. Slater, Phys. Rev. **82** (1951) 538.

108. N. F. Mott, Proc. Phys. Soc. A **62** (1949) 416.

109. N. F. Mott, Can. J. Phys. **34** (1956) 1356.

110. N. F. Mott, Phil. Mag. **6** (1961) 287.

111. J. B. Kreiger and M. Nightingale, Phys. Rev. **134** (1971) 1266.

112. M. Martino Phys. Rev. D **8** (1973) 603.

113. M. P. Green, C. Aldridge, K. K. Bajaj, Phys. Rev. B **15** (1977) 2217.

114. J. Hubbard, Proc. R. Soc. Lond. A **227** (1964) 237.

115. J. Hubbard, Proc.R.Soc.Lond A **281** (1964) 401.

116. C. Herring, *Magnetism* edited by G. T. Rado and H. Suhl, Vol. IV, (Academic press, New York, 1966).

117. P. W. Anderson, Mater. Res. Bull. **8** (1973) 153.

118. P. W. Anderson, Solid State Electron. **28** (1985) 204.

119. W. F. Brinkman and T. M. Rice, Phys. Rev. B **2** (1970) 4302.

120. N. F. Mott, Phil. Mag. B **7** (1978) 377.

121. S. Jin, T. H. Tiefel, M. Mc Cormack, R. A. Fastnacht, R. Ramesh, L. H. Chen, Science **264** (1994) 413.

122. H. Y. Hwang, S. W. Cheong, N. P. Ong and B. Batlogg, Phys. Rev. Lett. **77** (1996) 2041.

123. C. Zener, Phys. Rev. **81** (1951) 440.

124. C. Zener, Phys. Rev. **82** (1951) 403.

125. E. Pollert, S. Krupicka, E. Kuzwicova, J. Phys. Chem. Solids **43** (1982) 1137.

126. G. Zhao, K. Conder, H. Keller and K. A. Muller, Nature **381** (1996) 676.

J. B. Goodenough and J. Longho, *Landholdt-Bo7nstein*, Vol. **4a** (Springer, Berlin 1970).

G. Jonker and J. H. van Santen, Physica **16** (1950) 337.

J. H. van Santen, C. H. Jonker, Physica **16** (1950) 599.

G. H. Jonker, Physica **22** (1956) 707.

J. Volger, Physica **20** (1954) 49.

E. O. Wollan and W. C. Kehler, Phys. Rev. **100** (1955) 545.

C. W. Searle and S. T. Wang, Can. J. Phys. **47** (1969) 2703.

C. W. Searle and S. T. Wang, Can. J. Phys. **48** (1970) 2023.

A. H. Morrish, B. J. Evans, J. A. Eaton and L. K. Leung, Can. J. Phys. **47** (1969) 2691.

L. K. Leung, A. H. Morrish and C. W. Searle, Can. J. Phys. **47** (1969) 2697.

R. Von Helmholt, J. Wecker, B. Holzapfel, L. Schultz and K. Samwer, Phys. Rev. Lett. **71** (1993) 2331.

K. Chahara, T. Ohno, M. Kasai and Y. Kozono, Appl. Phys. Lett. **63** (1993) 1991.

P. W. Anderson and H. Hasegawa, Phys. Rev. **100** (1955) 675.

P. G. de Gennes, Phys. Rev. **118** (1960) 141.

A.J Mills *et al.*, Phys. Rev. Lett **77** (1996) 175.

C. M. Varma, Phys. Rev. B **54** (1996) 7328.

E. Muller-Hartmann and E. Daggoto, Phys. Rev. B **54** (1996) R6819.

N. F. Mott, *Metal-Insulator Transitions* (Taylor and Francis, London, 1974).

N. F. Mott, Proc. Phys. Soc. Lond. A **62** (1949) 416.

N. F. Mott, Phil. Mag. **17** (1968) 1259.

147. M. H. Cohen, H. Fritzsche and S. R. Ovshinsky, Phys. Rev. Lett. **22** (1969) 1065.

148. D. J. Thouless, Phys. Rep. **13** (1974) 93.

149. A.J Mills *et al.*, Phys. Rev. Lett **77** (1996) 175.

150. G. H. Jonker, Physica **20** (1954) 1118.

151. M. Sahana, R. N. Singh, C. Shivakumar, N. Y. Vasanthacharya *et al.*, Appl. Phys. Lett. **70** (1997) 2909.

152. M. Imura, T. Takahashi, H. Takamura, T. Tanaka, S. Sugimoto, M. Homma, M. Okada, Mater. Trans. Jpn. Inst. Materials **37** (1996) 1219.

153. M. Imura, H. Takamura, T. Tanaka, M. Homma and M. Okada, J. Ceram. Soc. Jpn. **104** (1996) 151.

154. M. F. Hundley, J. J. Neumeier, R. H. heffner, Q. X. Jia, X. D. Wu and J. D. Thompson, J. Appl. Phys. **79** (1996) 4535.

155. K. Khazeni, Y. X. Jia, V. H. Crespi, M. Cohen and A. Zoffil, Phys. Rev. Lett. **76** (1996) 1295.

156. J. Tanaka, M. Umehara, S. Tamura, M. Tsukioba, S. Ehara J. Phys. Soc. Jpn. **512** (1982) 1236.

157. R. M. Kusters, J. Singleton, D. A. Keen, R. Mc Greevy and W. Hayes, Physica B **155** (1989) 362.

158. J. Z. Liu, I. C. Chang, S. Irons, P. Klavins, R. N. Shetton K. Song and S. R. Wasserman, Appl. Phys. Lett. **66** (1995) 3218.

159. M. Jaime, M. B. Salamom, K. Pettit, M. Rubinstein, R. E. Treece, J. S. Horwitz and D. B. Christey, Appl. Phys. Lett. **68** (1996) 1576.

160. J. Tanaka, M. Umehara, S. Tamura, M. Tsukioka, S. Ehara, J. Phys. Soc. Jpn. **512** (1982) 1236.

161. J. Hejtmanek, Z. Jirak, D. Sedmidubsky, A. Maugnan, C. Simon, V. Caignaret, C. Martin and B. Raveal, Phys. Rev. B **54** (1996) 11974.

162. Asamitsu, Y. Moritomo and Y. Tokura, Phys. Rev. B **53** (1996) 122952.

163. J. Leebe, E. Koraus, L. Haupt, P. Mandal and K. Bamer, Appl. Phys. Lett. **68** (1996) 2343.

164. J. S. Zhou, W. Archibald and J. B. Goodenough, Nature **381** (1996) 770.

165. V. H. Crespi, L. Lu, Y. Y. Jia, K. Khazeni, A. Zeltil and M. L. Cohen, Phys. Rev. B **53** (1996) 14303.

166. R. Mahendran, S. Tiwary, A. Raychaudhari, R. Mahesh and C. N. R. Rao, Phys. Rev. B **54** (1996) R9604.

167. B. Fisher, I. Patlagan and G. M. Reisner, Phys. Rev. B **54** (1996) 9359.

168. J. M. D. Coey, M. Viret, L. Ranno and K. Ounodjela, Phys. Rev. Lett. 75 (1995) 3910.

169. W. Archibald, J. S. Zhou and J. B. Goodenough, Phys. Rev. B **53** (1996) 14445.

170. R. Mahendran, R. Mahesh, N. Rangavittal, S. Tewari, A. Raychaudhari, T. Ramakrishnan and C. Rao, Phys. Rev. B **53** (1996) 3348.

171. Z. Jirak, S. Krupicka, Z. Simsa, M. Dlouha and S. Vratistlav, J. Plagn. Magn. Mater. **53** (1985) 153.

172. H. V. Hwang, S. W. Cheong, P. G. Radaeli, M. Marezio and B. Batlog, Phys. Rev. Lett. **75** (1995) 914.

173. M. F. Hundley and J. J. Neumier, Phys. Rev. B **11** (1997) 511.

174. R. Mahendran, S. Tiwari and A. Raychaudhari, Solid State Commun. **98** (1996) 701.

175. B. F. Woodfield, M. L. Wilson and I. M. Byers, Phys. Rev. Lett. **78** (1997) 3201.

176. J. M. D. Coey, M. Viret, L. Ranno and K. Ovanadjela, Phys. Rev. Lett. **75** (1995) 3910.

177. J. J. Hamitton, E. L. Keating, H. L. Ju, A. K. Raychaudhuari, N. V. Smolyaninova and E. L. Greene, Phys. Rev. B **54** (1996) 14926.

178. L. Ranno, M. Viret and J. M. D. Coey (unpublished).

179. A. P. Ramirez, P. Schiffer, S. W. Cheong, W. Bao, T. T. M. Palstra, P. L. Gammel, D. J. Bishop and B. Zegarski, Phys. Rev. Lett. **76** (1996) 3188.

180. J. Tanaka and T. Mitsuhashi, J. Phys. Soc. Japan **53** (1984) 24.

181. M. Viret, L. Ranno and J. M. D. Coey, Phys. Rev. B **55** (1997) 8067.

182. G. J. Sunder, R. Hiskers, S. Di Carolis, M. R. Beasly and T. H. Geballe, Phys. Rev. B **53** (1996) 14434.

183. D. W. Visser, A. P. Ramirez and M. A. Subramanian, Phys. Rev. Lett. **78** (1992) 3947

184. J. Liebe, E. Kraus, L. Haupt, P. Mandal and K. Barner, Appl. Phys. Lett. **68** (1996) 2343.

185. B. Chen, A. G. Rojo, C. Uher, H. L. Liu and R. L. Greene, Phys. Rev. B **55** (1997) 15471.

CHAPTER 2

Experimental techniques

2.1 Introduction

Complete characterization of thermal properties of a material requires the determination of thermal transport properties such as thermal conductivity as well as specific heat capacity. Conventional techniques used to measure thermal conductivity include the well-known steady state and transient methods [1-3]. Comparatively large size samples, typically greater than 5 mm^3 are needed for these measurements, in order to obtain a reasonable signal-to-noise ratio, leading to considerable temperature gradients being set up in the sample. These drawbacks make these techniques unsuitable for studying critical thermal conductivity behaviour near phase transitions. But, techniques for high-resolution measurement of the specific heat capacity, on the other hand, are well established [4, 5].

Photothermal techniques have been applied to the measurement of thermal parameters of liquids and solids. Configurations with a gas-microphone [6] and piezoelectric transducer [7] have been used depending on the experimental conditions. It has also been shown, under particular operating conditions that photoacoustic (PA) technique allows for simultaneous determination of specific heat (c_p), thermal conductivity (K) and thermal diffusivity (α) [8]. Due to small temperature perturbations introduced in the sample by this technique, it has been possible to use PA technique to study the dynamic as well as the static critical

phenomena associated with thermal parameters near a liquid crystal phase transition [9]. For low temperature studies, some restrictions are imposed on the use of the gas-microphone photoacoustic methods and considerable complication arises in the cell design due to the presence of coupling fluid. These restrictions and complications are not present in configurations involving a pyroelectric detector, which therefore seems more appropriate for such studies.

Photopyroelectric technique has been used for the measurement of the thermal diffusivity (α) and heat capacity (c_p) of solids at room temperature using a photopyroelectric (PPE) detector [10, 11]. Use of this technique for the simultaneous determination of thermal diffusivity, thermal effusivity, thermal conductivity and heat capacity as a function of temperature would be highly informative since it would allow studies of critical behaviour of thermal parameters when the material undergoes a transition. Marinelli *et al.* [12] were quite successful in developing a technique for determining the thermal diffusivity, thermal conductivity and specific heat capacity simultaneously at low temperatures with the pyroelectric detector kept in vacuum. At temperatures above room temperature, the boundary conditions involved in the theory of this method are not easy to satisfy, so that application of the method can lead to errors in measurement.

In this chapter, we give details of a photopyroelectric technique for the simultaneous determination of thermal conductivity and specific heat capacity near solid-state phase transitions using a pyroelectric detector kept in contact with a thermally thick backing medium. The PPE technique has some distinct advantages such as its extreme simplicity, good sensitivity and ability to perform nondestructive probing over other photothermal methods. PPE spectroscopy is technically less

complex and less expensive than photoacoustic spectroscopy. In this measurement, the sample is heated by a modulated light source on one side and the temperature oscillations on the opposite side of the sample are detected by a pyroelectric detector, supported on a copper backing. We try to measure all these thermal parameters above room temperature with the pyroelectric detector kept in contact with a thermally thick backing medium. Since the PPE signal depends on the properties of the detector, which are also temperature dependent, an accurate temperature calibration of the system need to be carried out. The advantage of a thermally thick backing is that there will be sufficient heat exchange between the heated pyroelectric detector and the backing, so that the signal fluctuations are reduced to a minimum. This method can in principle, be adapted to all temperature ranges for all samples and is not limited by thermal properties of the sample.

A brief outline of the principle of the method and the theory involved, experimental details, details of detector calibration and results on few selected samples are given in the following sections. Results on triglycine sulfate (TGS), a sample that undergoes a para-ferroelectric phase transition above room temperature are presented. A discussion of the applications and advantages of the technique is given at the end.

2.2. Simultaneous determination of thermal conductivity and heat capacity by PPE technique

2.2.1 Principle of the technique

The photopyroelectric effect is based on the use of a pyroelectric transducer to detect the temperature rise due to periodic heating of a sample by induced light. A one-dimensional geometry of the type shown in Fig. 2.1(a) is assumed where *g*, *s*, *d* and *b* refer to the gas medium in front of the sample, the sample, the pyroelectric detector and the backing medium of the pyroelectric detector respectively.

The temperature variations in the detector give rise to an electrical current, which is proportional to the rate of change of the average heat content, given by [13]

$$i_d = P A \left(\frac{\partial \theta(t)}{\partial t} \right) \tag{2.1}$$

where P is the pyroelectric coefficient of the detector, A is the detector area and

$$\theta(t) = \left(\frac{1}{L_d} \right) \int_0^{L_d} \theta(x,t)\, dx \tag{2.2}$$

is the spatially averaged temperature variation over the detector thickness, L_d.

Now, bearing in mind the fact that the observed signal output is affected by the impedance of the detector and subsequent detection electronics, we consider an equivalent circuit shown in Fig. 2.1(b). Here the pyroelectric detector is described as an ideal current source with a parallel leakage resistance R_d and a capacitance C_d supported on a backing having an equivalent parallel load resistance R_b and capacitance C_b, while the detection electronics is represented by an input capacitance C_e and a parallel load resistance R_e. Since the backing material is assumed to be of

copper, the resistance and capacitance values of the detection electronics get altered depending on the resistance and capacitance values of the backing.

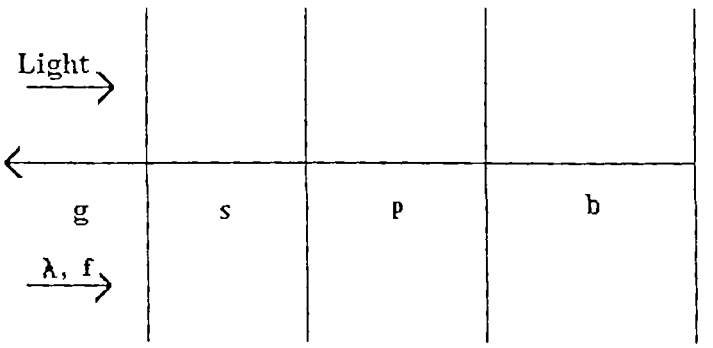

Fig. 2.1(a): One-dimensional geometry of the PPE set up

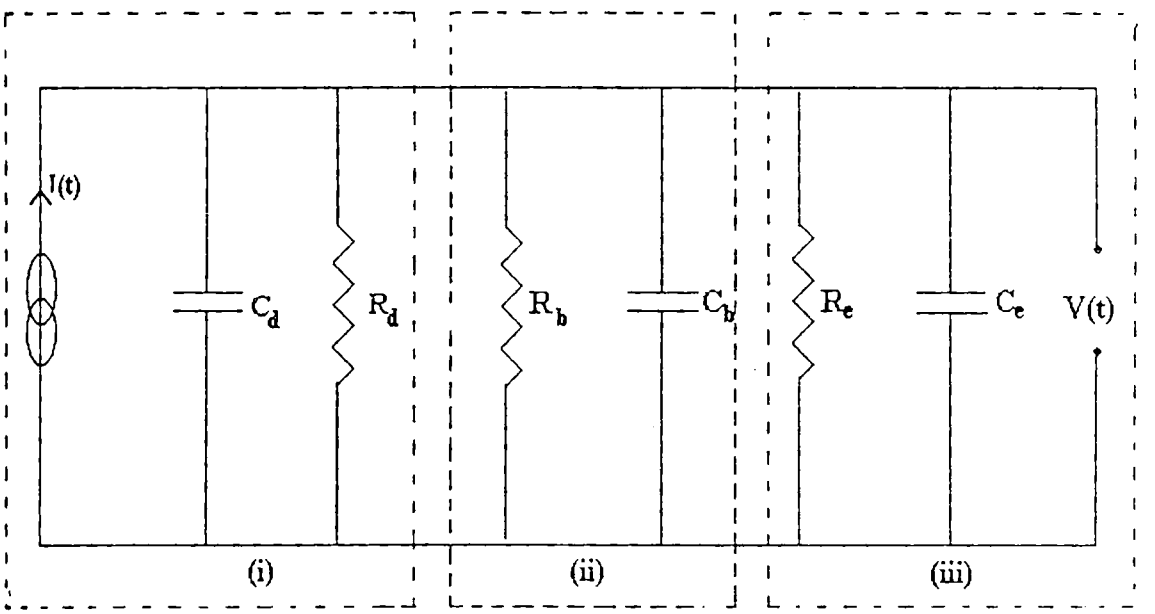

Fig. 2.1(b): Equivalent circuit for the (i) photopyrolectric transducer (ii) the copper backing and (iii) the detection electronics

For an optically opaque sample and pyroelectric detector, the complex amplitude of the output signal in frequency domain is given by [13]

$$V(f)=\left(\frac{j2\pi f PRA\theta(f)}{(1+jf/f_c)}\right)exp(j2\pi ft) \tag{2.3}$$

where $f_c=\frac{1}{2\pi RC}$, with $\frac{1}{R}=\left(\frac{1}{R_d}+\frac{1}{R_b}+\frac{1}{R_e}\right)$ and $C=(C_d+C_e+C_b)$ and f is the modulation frequency.

The function $\theta(f)$ is given by [12]

$$\theta(f)=\frac{I_0\beta_s\eta_s(b_{sg}\gamma_s+1)\left\{\left[exp\left((1+j)\sqrt{f/f_{cd}}\right)-1\right](b_{bd}+1)-\left[1-exp\left(-(1+j)\sqrt{f/f_{cd}}\right)\right](b_{bd}-1)\right\}}{(1+j)\left(\sqrt{f/f_{cd}}\right)K_s\left(\beta_s^2-\frac{2jf}{L_s^2 f_{cs}}\right)X} \tag{2.4}$$

where

$$X=(b_{sg}+1)\left\{(b_{bd}+1)(b_{ds}+1)e^{(1+j)\sqrt{f/f_{cd}}}+(b_{bd}-1)(b_{ds}-1)e^{-(1+j)\sqrt{f/f_{cd}}}\right\}e^{(1+j)\sqrt{f/f_{cs}}}+$$
$$(b_{sg}-1)\left\{(b_{bd}+1)(b_{ds}-1)e^{(1+j)\sqrt{f/f_{cd}}}+(b_{bd}-1)(b_{ds}+1)e^{-(1+j)\sqrt{f/f_{cd}}}\right\}e^{-(1+j)\sqrt{f/f_{cs}}} \tag{2.5}$$

The subscripts refer to the respective media indicated in Fig. 2.1(a). In general, we define the various parameters in Eq. (2.4) as

$\mu_i=\sqrt{\frac{\alpha_i}{\pi f}}$ = the thermal diffusion length of the respective media with

($i = s, d, b$ or g);

$$\gamma_s = \left(\frac{\beta_s L_s}{(1+j)}\right)\sqrt{f_{cs}/f}$$

$f_{ci} = \frac{\alpha_i}{\pi L_i^2}$ = critical frequency at which the respective medium goes from a thermally thin to a thermally thick regime,

L_i = thickness of the respective medium

$b_{ij} = \frac{e_i}{e_j}$ = ratio of thermal effusivities of the media i and j

$\beta_i = \frac{1}{\mu_{\beta i}}$ = optical absorption coefficient, μ_{β_i} being the optical absorption length of the respective medium.

η_s = fraction of absorbed radiation converted to heat (nonradiative quantum efficiency of the sample) and is assumed to be 1.

For a thermally thick sample, with $\mu_s < L_s$, and thermally thick pyroelectric, with $\mu_d < L_d$, the expressions for the PPE amplitude and phase give expressions for the values of the thermal diffusivity and effusivity, which allow a simultaneous determination of thermal conductivity and heat capacity if the sample density ρ_s is known.

The expressions for the temperature dependent PPE amplitude and phase under the above conditions are given by

$$V(f,T)=\left(\frac{I_0\eta_s A R_d}{L_d\sqrt{\left[1+\left(f/f_c\right)^2\right]}}\right)\left(\frac{P(T)}{\rho_d(T)c_{pd}(T)}\right)\frac{exp\left(-\left\{\sqrt{\frac{\pi f}{\alpha_s}}\right\}L_s\right)}{\left(\frac{e_s(T)}{e_d(T)}+1\right)} \quad (2.6a)$$

$$\phi(f,T)=-tan^{-1}\left(\frac{f}{f_c}\right)-\left(\sqrt{\pi f/\alpha_s(T)}\right)L_s \quad (2.6b)$$

where T is the temperature and c_{pd} and ρ_d are the heat capacity (at constant pressure) and density of the PPE detector respectively.

From these two expressions, it is clear that the sample thermal diffusivity α_s can be calculated from the phase of the PPE signal, which when substituted in the expression for PPE amplitude gives the thermal effusivity of the sample. From these the thermal conductivity and heat capacity of the sample can be calculated from the following relations

$$K_s(T)=e_s(T)\sqrt{\alpha_s(T)} \quad (2.7a)$$

$$c_{ps}(T)=\frac{e_s(T)}{\rho_s(T)\sqrt{\alpha_s(T)}} \quad (2.7b)$$

Since all the parameters in equations (2.6a) and (2.6b) are temperature dependent, a temperature calibration of the PPE detector is necessary here. All the thermal parameters can be calculated as a function of the sample temperature, provided the temperature dependence of the pyroelectric detector parameters are known.

2.2.2 Calibration of the set up

In order to determine $e_s(T)$ and $\alpha_s(T)$ from the PPE amplitude and phase we need to know the temperature dependence of f_c, e_d and the factor $\frac{P(T)}{\rho_d(T)c_{pd}(T)}$ after considering the backing medium as thermally thick in the present experiments.

2.2.2(a) Frequency dependence of PPE signal

Fig. 2.2 shows the room temperature PPE signal amplitude versus frequency obtained using the pyroelectric transducer itself as the sample. Each point in the graph is an average of four measurements. Error bars are indicated and the maximum error in each measurement is less than 1%. The sample is considered to be thermally thin within the scanned frequency range such that $exp\left(\pm(1+j)\left(\sqrt{\pi f}/\alpha_s\right)L_s\right)\approx 1$. The backing material used is copper and the equivalent resistance and capacitance of the detection electronics are 100 MΩ and 800 pF respectively. Moreover, since the transducer is in air, $b_{sg} >> 1$.

So, application of these two conditions in Eq. (2.3) and (2.4) reduces the equation to a more simplified form.

If we define

$$F_1(f)=\left[e^{\sqrt{f/f_{cd}}}\left(b_{bd}+1\right)+e^{-\sqrt{f/f_{cd}}}\left(b_{bd}-1\right)\right]cos\sqrt{\frac{f}{f_{cd}}} \qquad (2.8a)$$

$$F_2(f)=\left[e^{\sqrt{f/f_{cd}}}\left(b_{bd}+1\right)-e^{-\sqrt{f/f_{cd}}}\left(b_{bd}-1\right)\right]sin\sqrt{\frac{f}{f_{cd}}} \qquad (2.8b)$$

and $$F_3=\frac{APRI_0\eta_s}{2\rho_d c_d L_s} \qquad (2.8c)$$

Equation (2.3) gets simplified to

$$V(f) = \frac{F_3}{\left[1 + \left(f/f_{ce}\right)^2\right]^{1/2}} \left(\frac{(F_1(f) - 2b_{bd})^2 + (F_2(f))^2}{F_1(f)^2 + F_2(f)^2} \right) \qquad (2.9a)$$

$$\phi(f) = \tan^{-1}\left(\frac{F_2(f)}{F_1(f) - 2b_{bd}}\right) - \tan^{-1}\left(\frac{F_2(f)}{F_1(f)}\right) - \tan^{-1}\left(\frac{f}{f_{ce}}\right) \qquad (2.9b)$$

In a frequency region, where $f >> f_{cd}$, pyroelectric detector is thermally thick and $f >> f_{ce}$, so that the approximation $exp\left(-\sqrt{f/f_{cd}}\right) \sim 0$ and $\left[1 + \left(f/f_{ce}\right)^2\right]^{1/2} \sim f/f_{ce}$ can be made.

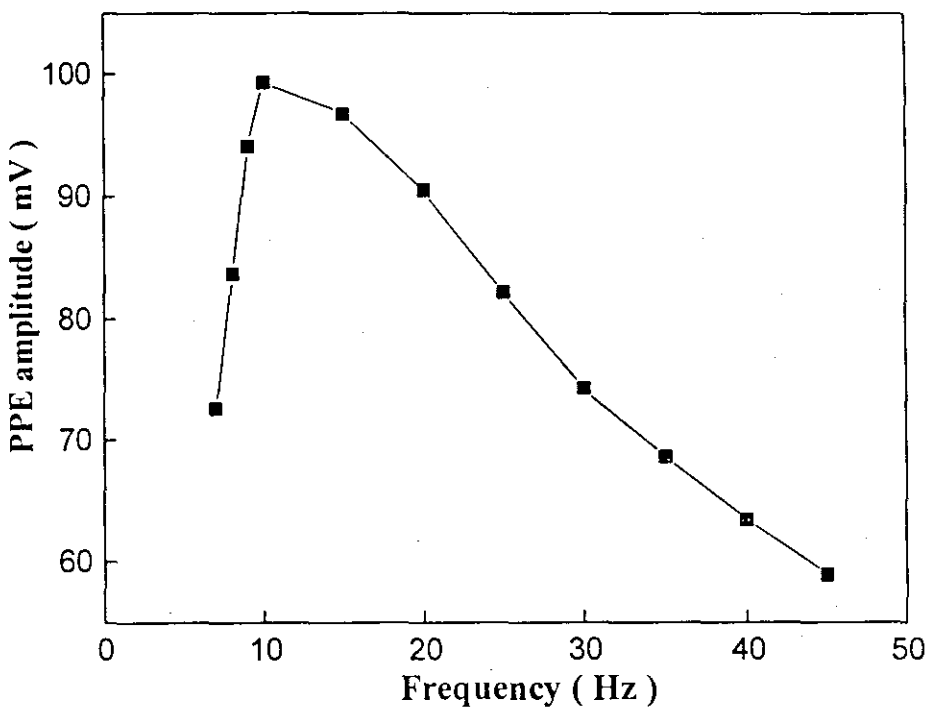

Fig. 2.2(a): Variation of PPE amplitude with frequency of PVDF film

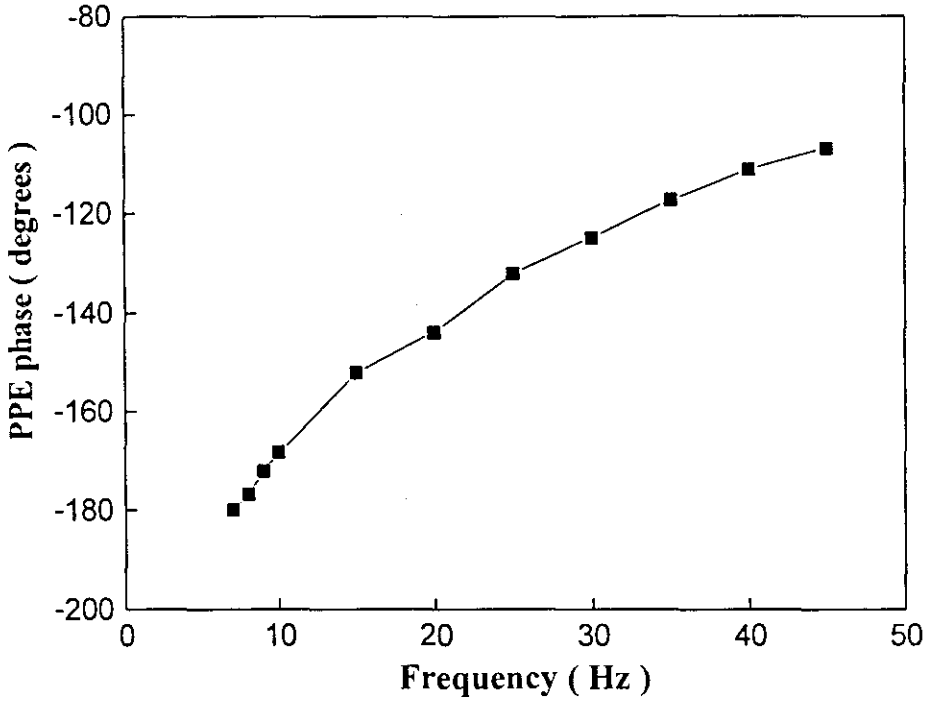

Fig. 2.2(b): Variation of PPE phase with frequency of PVDF film

So substituting these in Eq. (2.9a) we get

$$V(f) \sim F_3\left(f_{ce}/f\right) \tag{2.10}$$

The data in Fig. (2.2) shows frequency dependence according to Eq. (2.10) for frequencies greater than 20 Hz, because we are using a 28 μm PVDF film in our measurements.

On the other hand, if $f << f_{ce}$ and $f << f_{cd}$ (thermally thin pyroelectric), it can be assumed that $exp\left(\pm\sqrt{f/f_{cd}}\right) \approx 1 \pm \sqrt{\frac{f}{f_{cd}}}$. Bearing in mind that when $f << f_{ce}$, b_{bd} >> 1 comes to play as in the case of copper as the backing medium and from Eq. (2.9a), the PPE signal amplitude becomes

$$V(f) \approx \frac{F_3}{b_{bd}} \sqrt{f/f_{cd}} \qquad (2.11)$$

So a slope of 0.5 is clearly evident in Fig. (2.2) for frequencies smaller than 20 Hz.

These two observations confirm the validity of the theory developed from the simple equivalent representation of the pyroelectric detector and the detection electronics and suggest that f_{cd} and f_{ce} should be in the frequency range between 10 Hz and 20 Hz to make the sample and pyroelectric to be thermally thick. Also, since f^{-1} dependence for PPE amplitude for f > 20 Hz, indicates that b_{bd} remains essentially constant over the temperatures of interest, so that we can assume the room temperature value of b_{bd} to be valid throughout the entire temperature range.

Similar frequency scans using a β-PVDF pyroelectric transducer in contact with an optically opaque and thermally thin sample (very thin metal electrode) using air as the backing medium ($b_{bd} \sim 0$), have been reported by Coufal *et al.* [14]. They observed nearly constant PPE signal amplitude in the frequency region where $f << f_{cd}$ and $f << f_{ce}$. But for $b_{bd} \sim 0$, substitution in Eq. (2.9a) gives

$$V(f) = \frac{F_3}{\sqrt{1 + \left(f/f_{ce}\right)^2}} \qquad (2.12a)$$

and $$\phi(f) = -tan^{-1}\left(f/f_{ce}\right) \qquad (2.12b)$$

which is the frequency response of a low pass filter with f_{ce} as the cut off frequency. From Eq. (2.12a), it follows that the PPE signal amplitude remains constant even in the region where the transducer is thermally thin. This means that even if the thermal diffusion length in the pyroelectric is greater than the thickness of the pyroelectric, there is very little heat exchange with the backing medium.

2.2 2(b) Temperature calibration

The temperature dependence of the factor $\frac{P(T)}{\rho_d(T)c_{pd}(T)}$ appearing in Eq. (2.5a) can be isolated by considering the case of a thermally thin PVDF film as the sample on a thermally thin detector, as considered above. The modulation frequency in this calibration is limited to less than 20 Hz to ensure that both the PVDF film as well as the detector is thermally thin. Since we are considering a thermally thin sample, the effect of the thermally thick backing with the condition $b_{bd} > 1$ must be incorporated in to Eq. (2.4). Then the general expression for the PPE amplitude (Eq. 2.4); Then

$$V(f) = \left(\frac{APRI_o\eta_s}{2\rho_d c_{pd} L_d}\right)\left(\frac{f_c}{f}\right)\left[1 - \frac{4b_{bd}}{|S_1(f)|}\right] \tag{2.13a}$$

with $$|S_1(f)| = exp\left(\sqrt{f/f_{cd}}\right) b_{bd}\, cos\left(\sqrt{f/f_{cd}}\right) \tag{2.13b}$$

It is clear from this expression that the parameter b_{bd} is a decisive one in the calibration of the detector.

Fig. (2.3) shows the temperature variation of PPE amplitude and phase in the temperature range −173 ^{0}C to 65 ^{0}C. As seen from Fig. (2.3), the phase of the pyroelectric detector remains essentially constant with temperature in the temperature range of interest, so that the temperature dependence of f_c can be neglected.

Since the equivalent resistance of the detector has a constant value at room temperature, the temperature dependence of the amplitude of the PPE signal is assumed to be entirely due to the factor $\frac{P(T)}{\rho_d(T)c_{pd}(T)}$

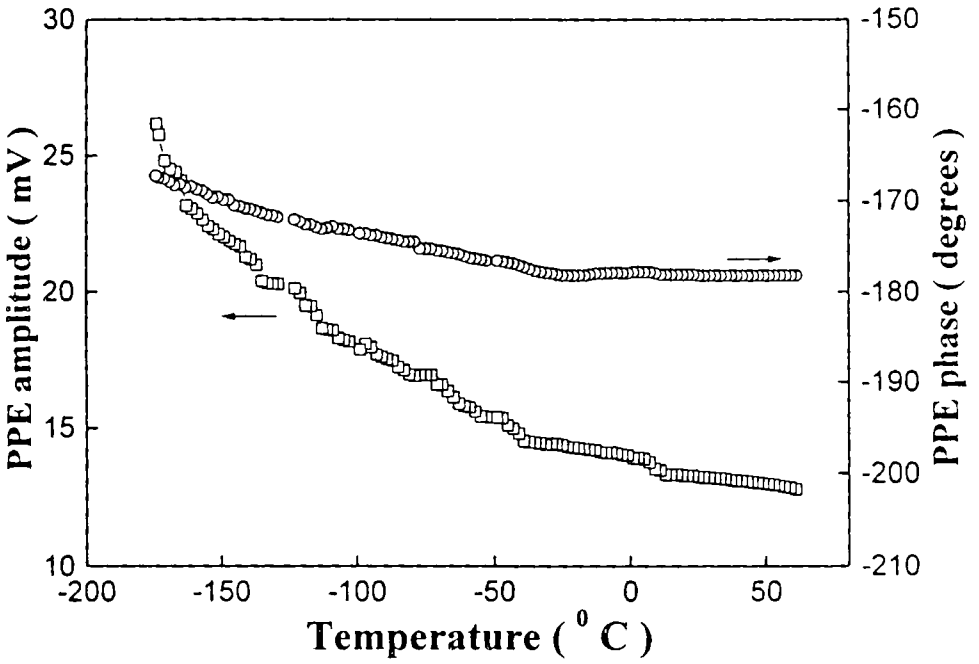

Fig. 2.3: Temperature dependence of PPE amplitude and phase of a PVDF film

On normalizing the amplitude with respect to the room temperature value where all the detector parameters are known, we get

$$\left(\frac{P(T)}{\rho_d(T)c_{pd}(T)}\right) = \left|\frac{V(T)}{V(T_0)}\right|\left(\frac{P(T_0)}{\rho_d(T_0)c_{pd}(T_0)}\right), \qquad (2.14)$$

where T_0 is the room temperature. The variation of $\frac{P(T)}{\rho_d(T)c_{pd}(T)}$ in the temperature range of interest is shown in Fig. (2.4).

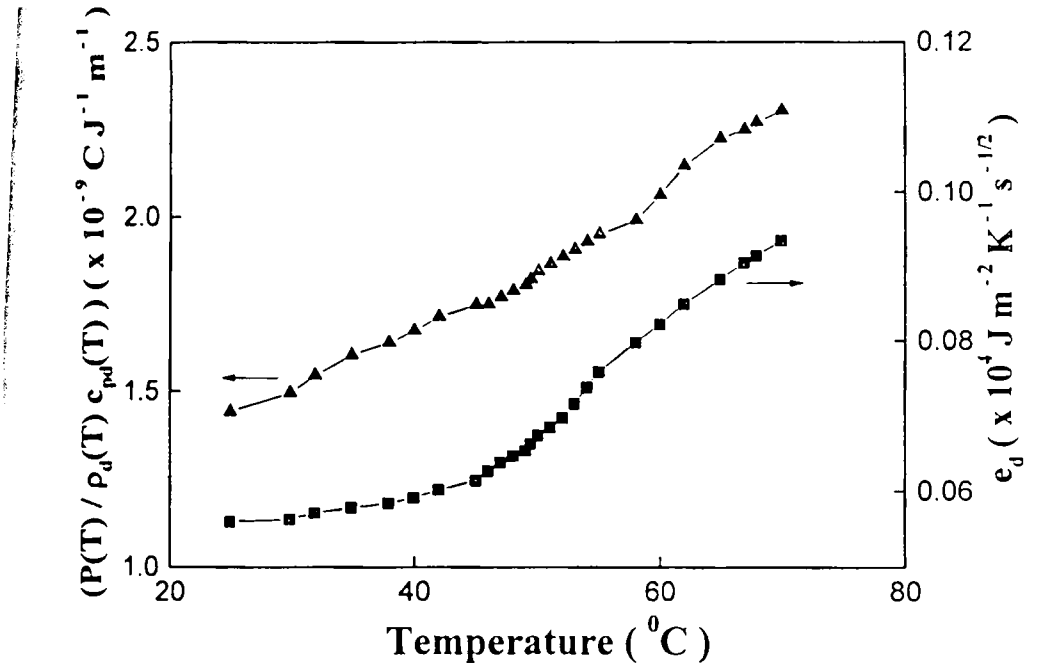

Fig. 2.4: Temperature variation of $\frac{P(T)}{\rho_d(T)c_{pd}(T)}$ and $e_d(T)$ of a PVDF film

In order to determine the temperature dependence of e_d, the thermal effusivity of the pyroelectric detector, we consider a thermally thin sample ($\mu_s > L_s$) whose thermal parameters are known at all temperatures of interest and satisfying the condition $exp\left[\pm\left(f/f_{cs}\right)\right] \approx 1 \pm \sqrt{f/f_{cs}}$. As a thermally thin sample, we have used a brass disc of thickness 0.6 mm and the frequency of measurement is kept at a value less than 20 Hz. At this frequency the pyroelectric detector is also thermally thin so that $exp\left[\pm\left(f/f_{cd}\right)\right] \approx 1 \pm \sqrt{f/f_{cd}}$. The variation of the thermal effusivity of PVDF detector with temperature is found out by considering Eq. (2.3) and applying the above condition with $b_{bd} > 1$ so that the expression for PPE amplitude becomes

$$V(T) = \left(\frac{APRI_0\eta_s}{2\rho_d c_{pd} L_d}\right)\left(\frac{f_c}{f}\right)\left[1 - \frac{4b_{bd}}{|S_1(f)|}\right]\frac{1}{\sqrt{2A(T)^2 + 2A(T) + 1}} \qquad (2.15a)$$

with $$A(T) = \rho_s(T)c_{ps}(T)L_s\frac{\sqrt{\pi f}}{e_d(T)} \qquad (2.15b)$$

From this expression the variation of thermal effusivity of PVDF detector with temperature throughout the temperature range of interest has been calculated. This is also plotted in Fig 2.4. It is seen that the value of e_d is in good agreement with the value already reported in literature [15], proving that the assumptions made are correct.

2.3 PPE spectrometer

In this subsection, the experimental set up for the photopyroelectric technique is described. The application of this technique for the determination of thermal diffusivity (α), thermal effusivity (e), thermal conductivity (K) and heat capacity (c_p) are outlined in detail.

A basic PPE spectrometer consists of a radiation source of sufficient intensity, a light intensity modulator, PPE cell in which the sample is placed with the PPE detector and a signal-processing unit. The basic instrumentation has been modified by different workers depending on their application areas. Details of various models in a PPE spectrometer, including those of our set up are outlined below.

2.3.1 Radiation source

The important parameters for the selection of the light source are the available power per usable bandwidth, the wavelength range, tunability and the ease of

intensity modulation. Both coherent and incoherent sources are widely used. Arc lamps and lasers are the popular types of light sources currently used in PPE experiments. Continuous tunability from infrared to ultraviolet can be provided by suitable lamp-monochromator combination. High-pressure Xe arc lamps, high-pressure Hg lamps, tungsten lamps etc. are the commonly used incandescent sources. The relatively low bandwidth-throughput product is the major drawback of these sources. Since the strength of the PPE signal is found to be proportional to the intensity of radiation, optical sources should have high spectral radiance. The high peak power available from pulsed lasers is especially attractive for measuring very weak absorption, but the limited tunability is the main drawback of laser sources in PPE experiments.

In our experiments we have used a 120 mW He-Cd laser of wavelength λ = 442 nm, as the optical heating source.

2.3.2 Modulation

For the generation of PPE signal, modulation of the incident light beam is essential. Either amplitude or frequency of the incident beam can be modulated. Amplitude modulation is the most commonly used one because it can be accomplished by relatively inexpensive mechanical chopping methods. The depth of modulation using a mechanical chopper is nearly 100 %. As we know, the major disadvantage of PPE spectroscopy is its susceptibility to synchronous acoustic noise [16]. So care should be taken to minimize the vibration noise, which may interfere with the PPE signal and can't be filtered away even by lock-in detection. So isolation of the mechanical chopping system form the optical table that supports the rest of the instrumentation needs to be done.

We have used a mechanical chopper (Model No. SR 540) for the intensity modulation of the laser beam, in our experiments. The experiments have been set up on a vibration free table to reduce noise pick up.

2.3.3 The PPE cell

A photopyroelectric cell which can be used over a wide range of temperatures has been designed and fabricated with which measurements can be made from 90 K to 350 K. The sample geometry is schematically shown in Fig. (2.5). The sample compartment is made of copper rod in the form of a cold finger, one end of which is in contact with liquid nitrogen chamber and to the other end a heater is wound. The sample cell is having a copper base, which forms the backing for the PPE detector. The sample cell is sealed against vacuum outside 'O' rings made of indium (for low temperature measurements) or silicone rubber (for high temperature and room temperature measurements). A cross-section of the sample chamber is shown in Fig. (2.6). The whole arrangement is kept in a metallic outer chamber of inner diameter 25cm and wall thickness 5mm, as in Fig. (2.7). The sample chamber is connected to the outer chamber by means of a thread, provided at one end of the cold finger. The sample temperature is detected with a platinum resistance sensor placed close to the sample inside the chamber.

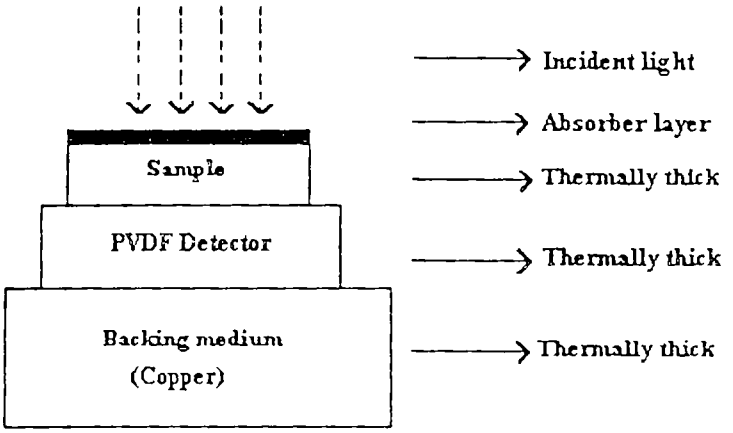

Fig. 2.5: Sample geometry of the PPE set up

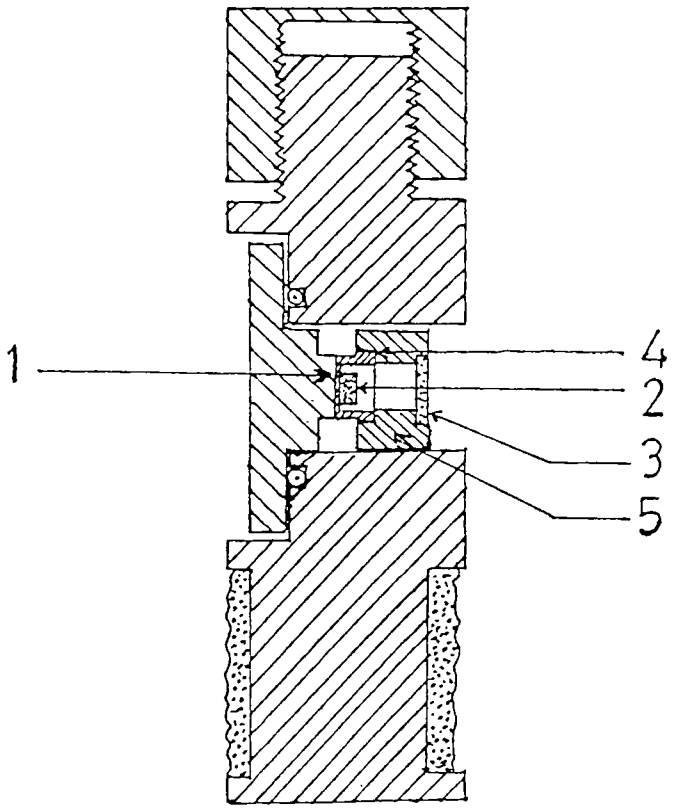

Fig. 2.6: Cross-sectional view of the PPE sample holder

1. PVDF detector 2. Sample 3. Glass window 4. Copper ring 5. Teflon outer cover

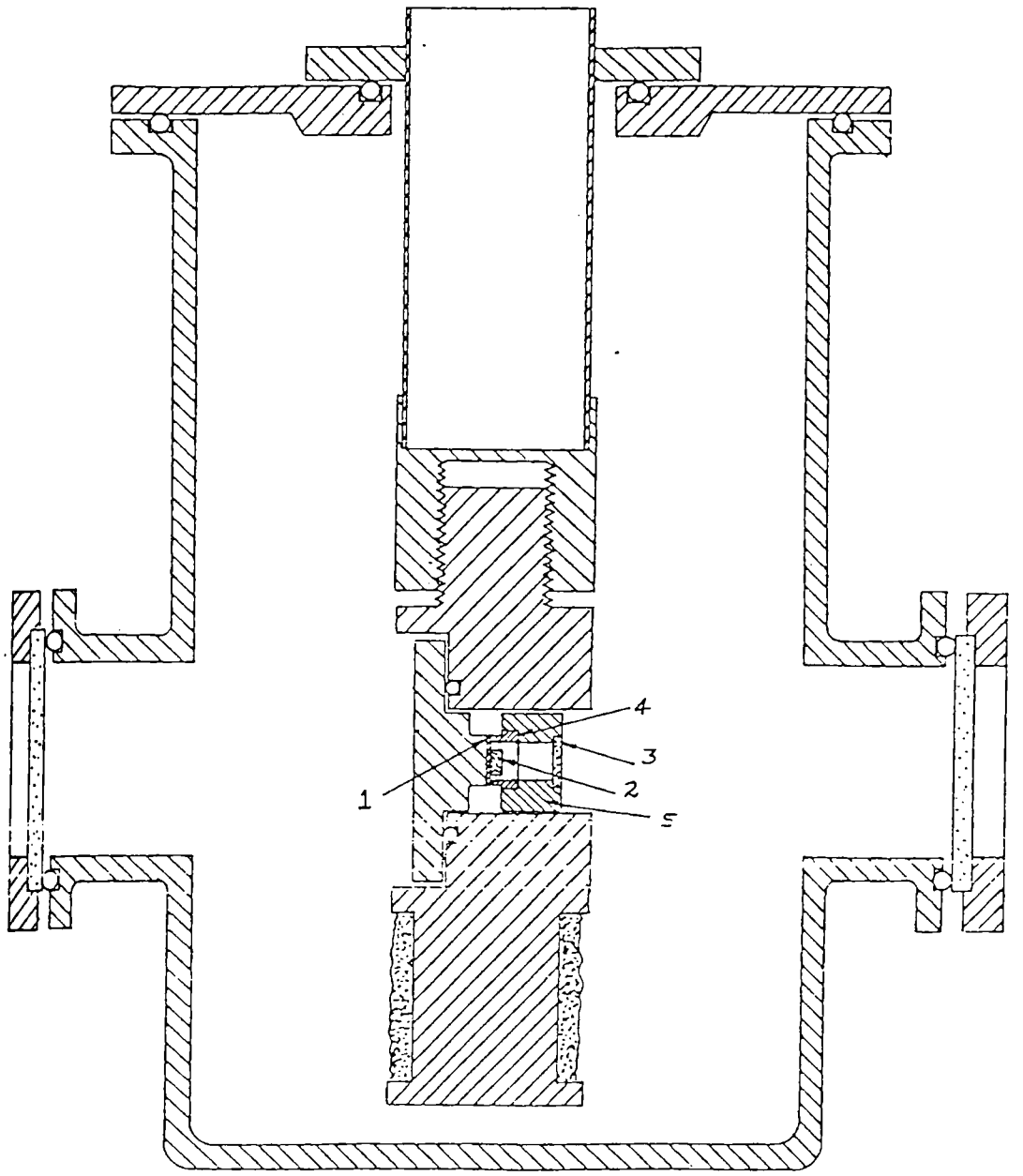

Fig. 2.7 Schematic diagram of the PPE cell

1. PVDF detector 2. Sample 3. Glass window 4. Copper ring 5. Teflon outer cover

2.3.4 PPE detector

The heart of the PPE spectrometer is the PPE detector using which the temperature variations arising in the sample due to optical irradiation (and absorption) can be detected with high accuracy. The necessary condition, for the choice of transducers to detect the thermal waves generated in the sample, is that it should be a pyroelectric material. Pyroelectricity is essentially the manifestation of spontaneous polarization dependence on temperature in certain non-centrosymmetric anisotropic solids. If there is a small change of temperature, the pyroelectric material becomes electrically polarized and a voltage arises between certain directions in the material. On placing a sample on the top of the pyroelectric (PE) film, the average temperature change in the film is approximately equal to the temperature changes at the interface between the sample and the sensor. It is then evident that the time response of the sensor is related to the time of the heat diffusion across the sample and in addition, the time required to reach thermal equilibrium within the PE film after thermal deexcitation. So one can obtain short time resolution by decreasing the thicknesses of the sample and the PE film [17]; so the type of PE measurements that one wants to perform determine the thickness of the pyroelectric detector. Polyvinylidene difluoride (PVDF), Lithium tantalate ($LiTaO_3$) are the most commonly used detectors. If short time responses are not needed, a thicker PE sensor can be used in order to have stronger signals as well as better signal-noise ratio.

A 28 μm thick PVDF film with pyroelectric coefficient $P = 0.25 \times 10^{-8}$ V/cm-K at room temperature has been used as the pyroelectric detector in our

measurements. The room temperature values of pyroelectric detector resistance and capacitance are 50 GΩ and 750 pF respectively [15].

2.3.5 Signal detection

The generated PE signal can be monitored directly with the appropriate electronic circuitry. In practical detection electronics the observed signal is, however, affected by the impedance of the sensor and electronics. In order to maximize the signal to noise ratio, the signal from the detector should be processed by an amplifier tuned to the chopping frequency. Generally, a phase sensitive lock-in detection is used for this purpose. Also by lock-in detection, the amplitude and phase of the PE signal can be measured and by using a dual phase lock-in amplifier, the measurements can be more easily when both amplitude and phase vary simultaneously.

We have used a dual phase lock-in amplifier (Stanford Researh Systems, Model SR 830) in our measurements.

2.4. Experimental details

A photopyroelectric set up of the type shown in Fig.2. 8 has been used in the present work. The sample is attached to the pyroelectric detector by means of a thermally thin layer of a heat sink compound whose contribution to the signal is negligible. The pyroelectric detector attached to the sample is placed on a thermally thick backing medium (copper) which satisfies the boundary condition $b_{bd} > 1$. The frequency of modulation of the light beam is kept above 30 Hz to ensure that the PVDF film, the sample and the backing medium are all thermally thick during measurements. The signal output is measured with a lock-in amplifier having 10MΩ input resistance and 50pF input capacitance. Since the backing material is copper

instead of air or vacuum, the equivalent resistance and capacitance may be as high as 100 MΩ and 800 pF respectively. So the equivalent resistance is reduced to 10 MΩ by using an additional parallel resistance to shift the value of f_c to the required range as per the assumptions made in the theory.

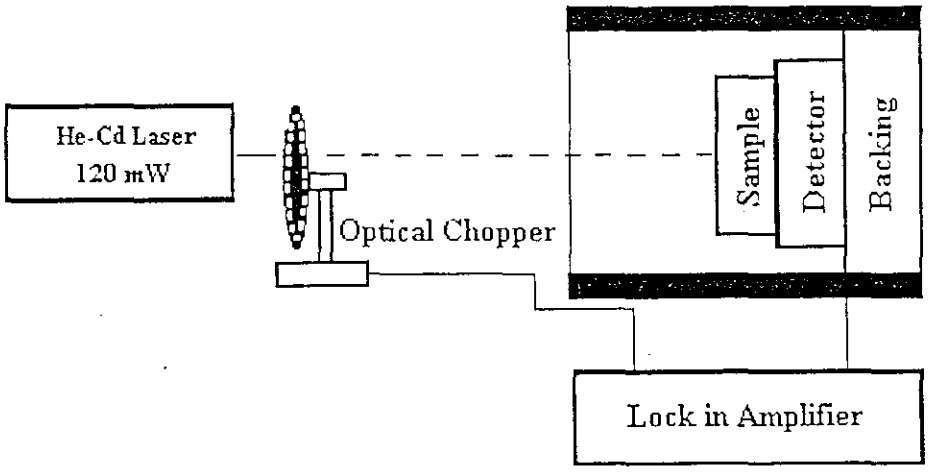

Fig. 2.8: Block diagram of the photopyroelectric set up

The sample-detector-backing assembly has been enclosed in a chamber whose temperature can be varied and controlled as desired. Measurements as a function of temperature have been made at a heating rate of approximately 0.5 K/min. and data collected in every 2 K interval normally and at closer intervals near the transition point. The temperature is measured with a platinum sensor placed close to the sample inside the chamber. The PPE amplitude and phase obtained at different modulation frequencies are measured with the lock-in amplifier.

2.5. Calibration of the cell

In order to determine whether the method gives accurate results, we carried out a series of measurements on selected samples whose thermal parameters are already known. The thermal conductivities and heat capacities of a number of such samples have been determined. The results are shown in Table 2.1. Averages of four amplitude and / or phase measurements have been used to calculate the parameters quoted in the table. The values of α_s, K_s and c_{ps} at room temperature obtained simultaneously by employing the present technique agree very well with the ones already reported in the literature [18, 19], establishing the reliability and accuracy of the technique. Taking into account various uncertainties in the measurements, the overall uncertainties in the values of α_s, K_s and c_{ps} are estimate to be ± 1%.

We have also measured the thermal diffusivity, thermal conductivity and heat capacity of a copper sample at temperatures between 160 K and 330 K. The results are shown in Fig. 2.10 and 2.11. The thermal thicknesses have been ensued by plotting PPE amplitude and phase (Fig. 2.9(a) and 2.9(b)) at various temperatures. The values of heat capacity and thermal conductivity agree very well with the values reported in literature [19].

Our main interest has been the measurement of changes in thermal conductivity and heat capacity across solid-state phase transitions. We give results of our measurements on Triglycine Sulfate (TGS), a ferroelectric crystal that undergoes a para-ferroelectric phase transition at 49.4 °C.

Sample	Sample thickness (mm)	Frequency used (Hz)	Thermal diffusivity α_s (x 10^{-4} m^2s^{-1})		Thermal conductivity K_s (x 10^2 $Wm^{-1}K^{-1}$)		Heat capacity c_{ps} (x 10^3 $Jkg^{-1}K^{-1}$)	
			Present measurement	Value reported in literature	Present measurement	Value reported in literature	Present measurement	Value reported in literature
Copper	1.2	40	**1.121 ±0.002**	1.12	**3.83 ±0.02**	4.01	**0.39 ±0.01**	0.385
Aluminium	1.0	45	**1.012± 0.002**	1.00	**1.99 ±0.02**	2.01	**0.92 ±0.01**	0.897
Silicon wafer	0.9	40	**0.918 ±0.002**	0.92	**1.45 ±0.02**	1.48	**0.70 ±0.01**	0.705
Brass	0.6	65	**0.348 ±0.002**	0.350	**0.993 ±0.02**	1.20	**0.37 ±0.01**	0.37
Nylon	0.3	45	**(1.263±0.02) x 10^{-3}**	1.28 x 10^{-3}	**(2.4±0.15) x 10^{-3}**	2.5 x 10^{-3}	**1.71 ±0.01**	1.70

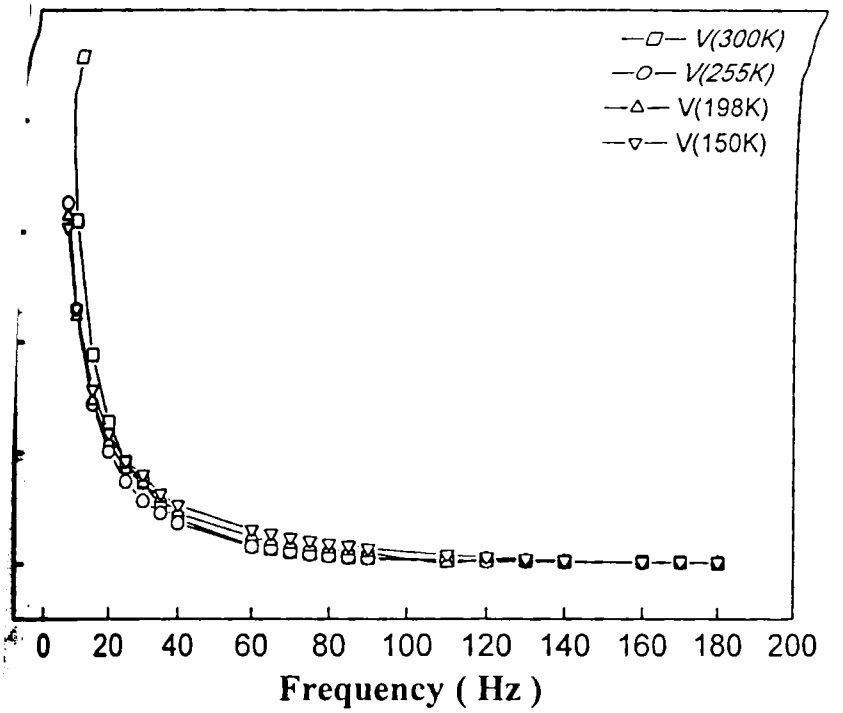

2.9(a): Variation of PPE amplitude with frequency of a Cu sample

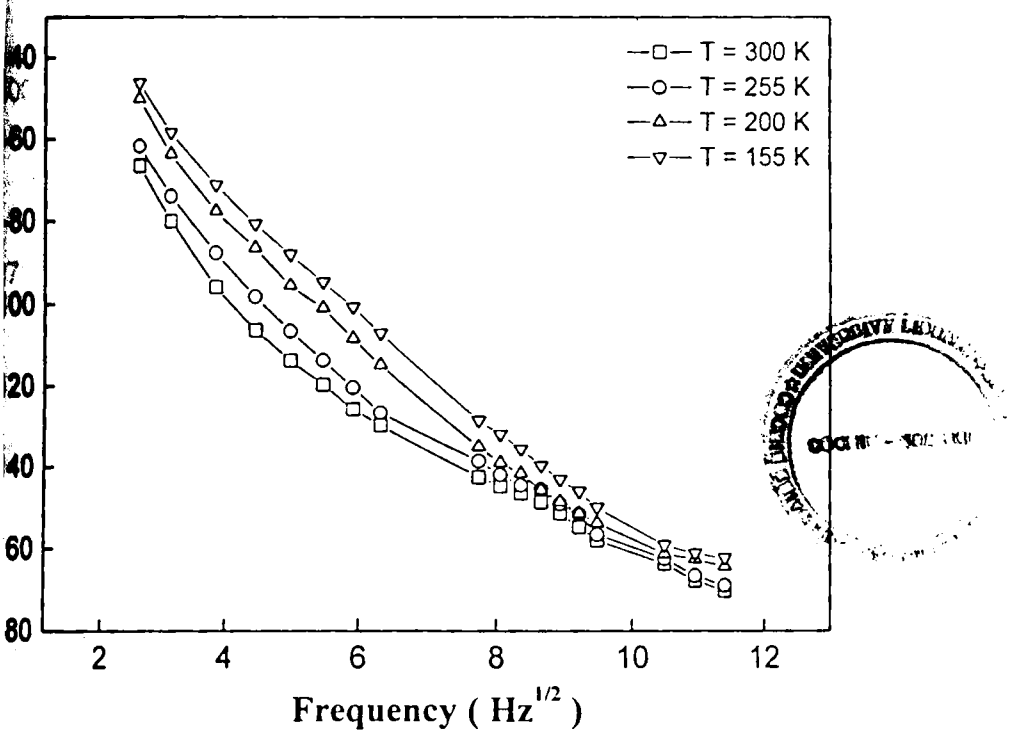

2.9(b): Variation of PPE amplitude with frequency of a Cu sample

G18516

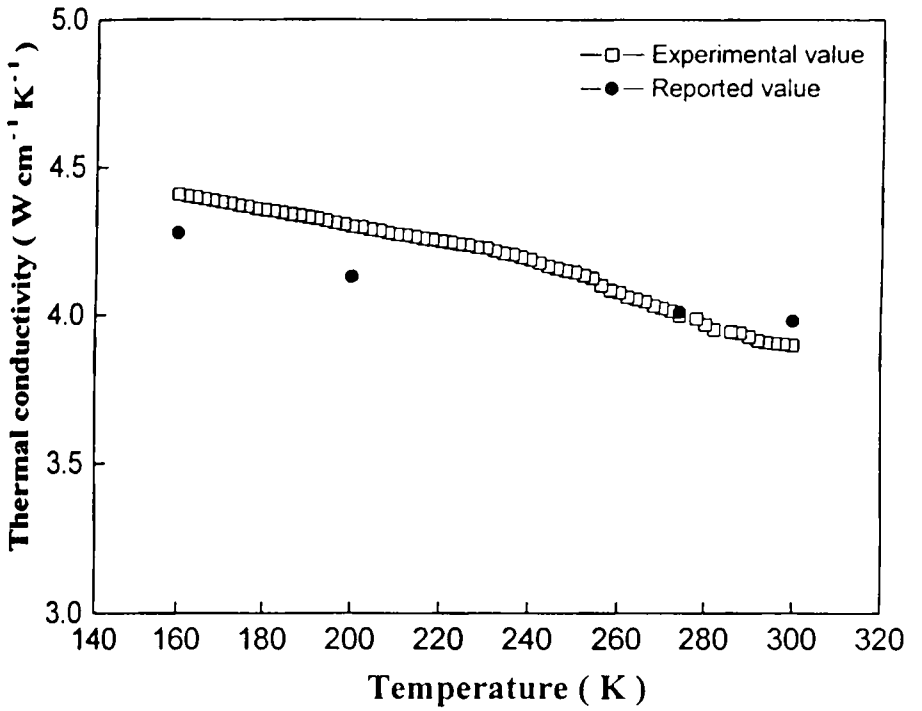

Fig. 2.10: Thermal conductivity of a Cu sample measured between 160 K and 300 K

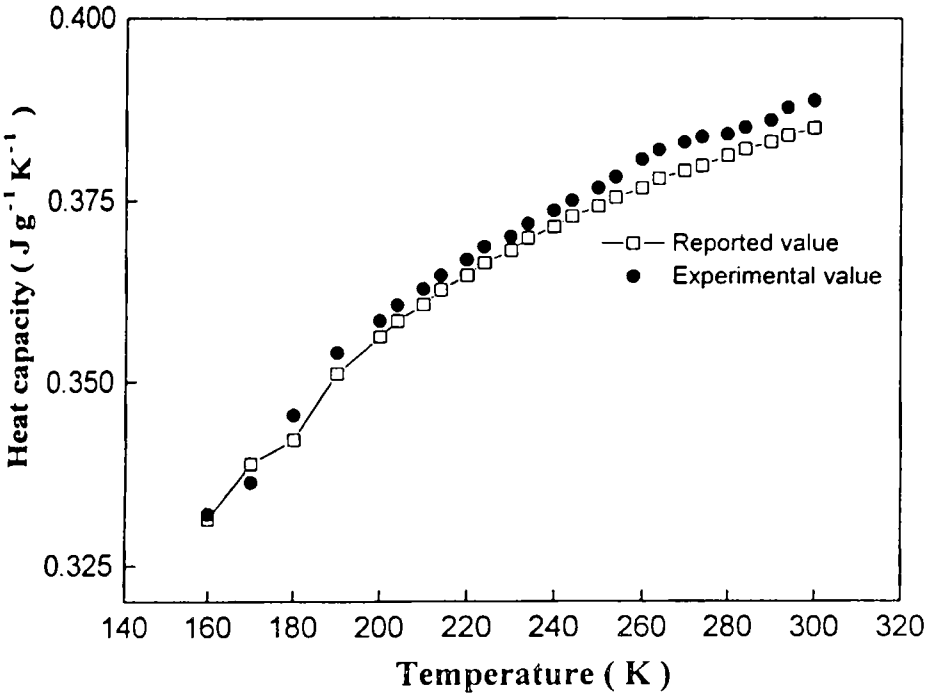

Fig. 2.11: Heat capacity of a Cu sample measured between 160 K and 300 K

2.6 Results on TGS

2.6.1 Properties of TGS

Triglycine sulfate (TGS) is a very well known ferroelectric crystal that is very interesting from fundamental physics as well as technological points of view. The ferroelectric behaviour at room temperature in single crystals of TGS and isomorphous TGSe (Triglycine Selenate) has been discovered by Mathias *et al.* way back in 1956 [20]. TGS $[(NH_2CH_2COOH)_3H_2SO_4]$ is a uniaxial ferroelectric crystal with Curie temperature about 322.6 K. The crystal is monoclinic both above and below the transition temperature [21, 22]. The transition is second order order-disorder type one. Below T_c the space group of the crystal is $P2_1$ and above T_c it changes to $P2_1/m$ that is centrosymmetric and is piezoelectric. In the ferroelecric phase, the spontaneous polarization is directed along the Y axis. TGS is used as a model system for the study of second order phase transitions through the critical region. The technological importance of TGS is primarily due to its pyroelectric properties. It is a widely used material in pyroelectric devices such as IR imaging sensors.

A great deal of work has already been done on the physical properties of TGS. The piezoelectric, electrostrictive and low frequency elastic properties of TGS have been thoroughly investigated by Ikeda *et al.* [23]. The static ferroelectric properties near the phase transition temperature have been studied in detail by several workers [24, 25]. Detailed theoretical studies on the acoustic as well as specific heat data have been carried out by several workers in the transition region

with a goal of verifying experimentally the logarithmic corrections in certain critical quantities as predicted by theory [26, 27].

TGS possesses very attractive pyroelectric properties and has the basic pyroelectric figure of merit $P/K \approx 1.1 \times 10^{-5}$ C m^{-2} K^{-1} where P is the pyroelectric coefficient and K is the dielectric constant of the crystal. A drawback of TGS crystal is its spontaneous polarization. A suggestion to get over this problem has been to dope TGS with foreign ions. Several dielectric and related studies have been done on TGS crystals doped with various dopants to understand the effect of doping on the properties of this material [28-33].

We have carried out phototopyroelectric measurements of the thermal parameters of TGS along the three principal crystallographic directions. The anisotropy obtained in thermal conductivity of triglycine sulfate indicate the potential of this technique to study the thermal parameters during phase transitions.

2.6.2 Sample preparation

Single crystals of triglycine sulfate for the present studies have been grown by the slow evaporation of the aqueous solutions at constant temperature of about 39 ^{0}C. All the crystals have been grown in the ferroelectric phase. TGS crystals are grown by the chemical reaction

$3NH_3CH_2COOH + H_2SO_4 \rightarrow (NH_3CH_2COOH)_3\ H_2SO_4$

The crystal morphology of TGS is given in Fig.2.12. The lattice parameters of TGS are a = 9.15 Å, b = 12.69 Å, c = 5.73 Å and β = 105.40. The faces are identified from crystal morphology [21] by measuring the interfacial angles using a contact goniometer.

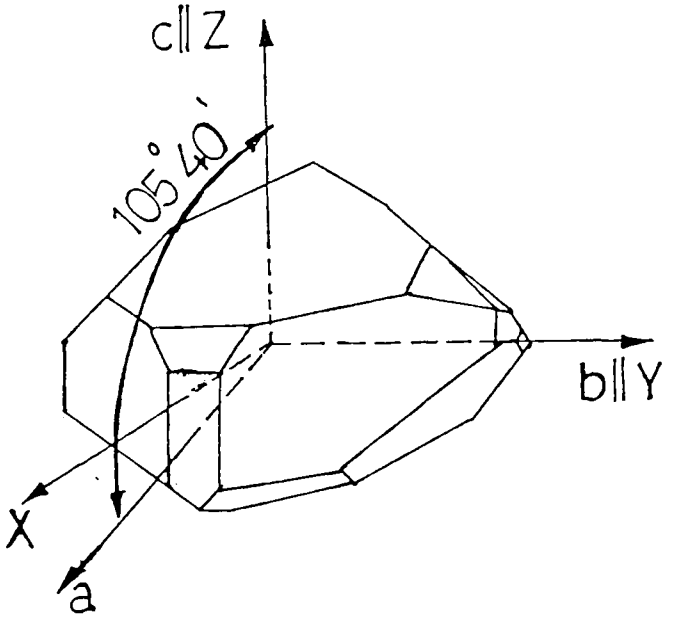

Fig. 2.12: Morphology of a TGS single crystal

The so obtained crystal has been cut and polished and platelets of the crystal of thickness 0.3 mm have been cut with faces normal to the *a*, *b*, and *c* axes so that the direction of propagation of thermal waves is along one of the axes. A very thin layer of carbon black from a benzene flame has been carefully coated onto the illuminated surface of the sample to enhance its optical absorption. Measurements as outlined already have been carried out as a function of temperature from room temperature (26^0C) to 55^0C.

2.6.3 Results and Discussion

The sample's thermal thickness has been verified by plotting the PPE amplitude and phase against frequency, at a number of temperatures between room temperature and 55^0C. The results for the *a*-, *b*- and *c*-axis are plotted in figures 2.13 - 2.15.

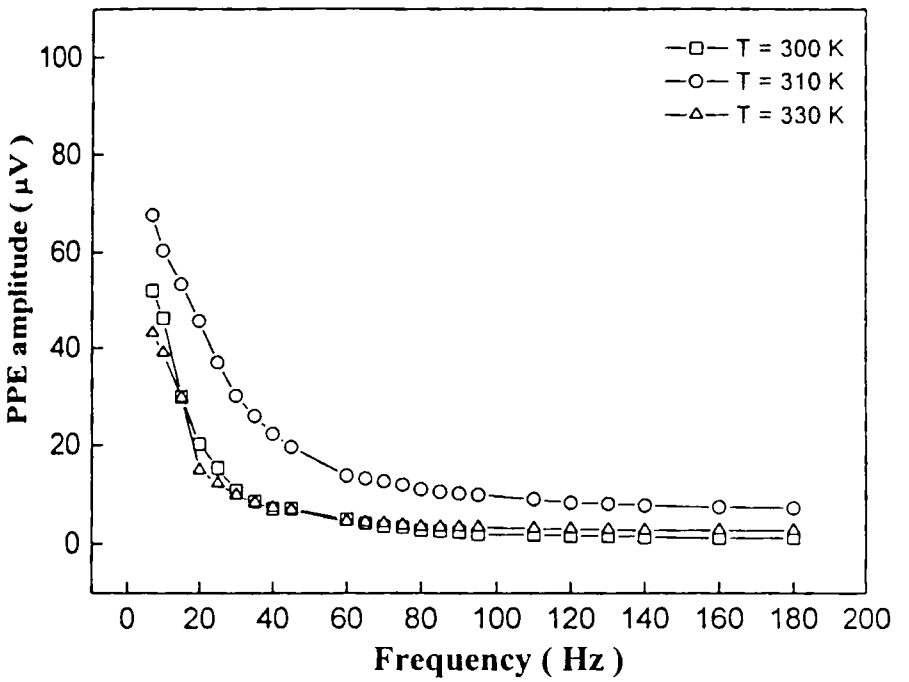

Fig. 2.13(a): Variation of PPE amplitude with frequency of TGS crystal along *a*-axis

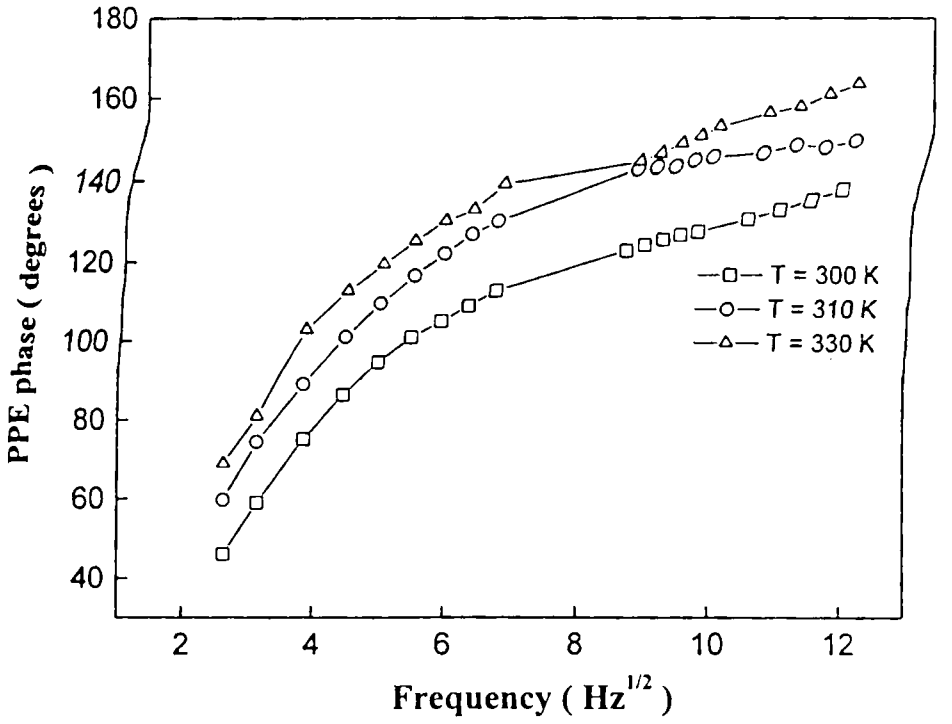

Fig. 2.13(b): Variation of PPE phase with frequency of TGS crystal along *a*-axis

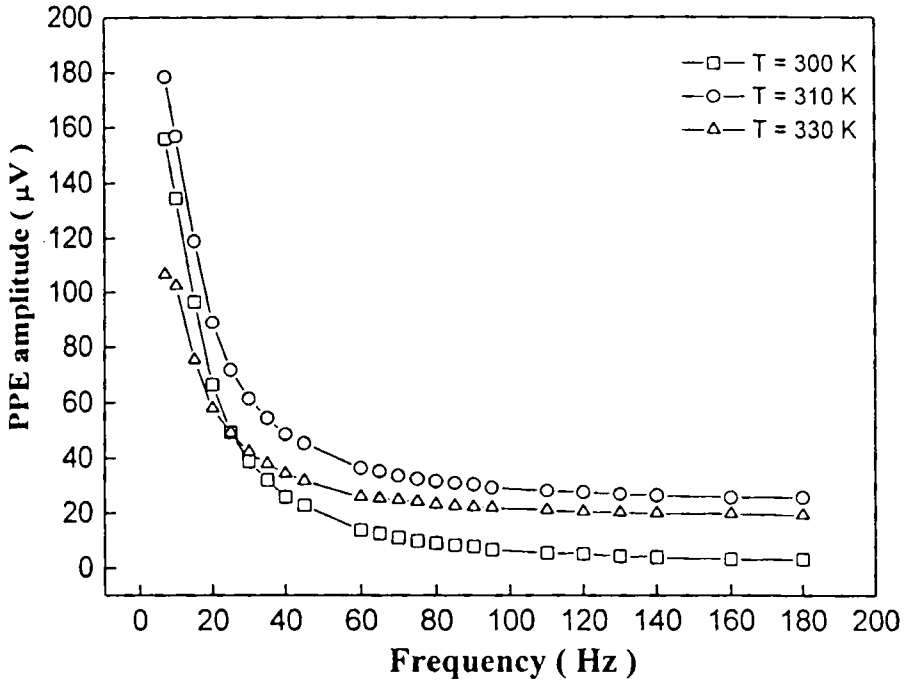

Fig. 2.14(a): Variation of PPE amplitude with frequency of TGS crystal along *b*-axis

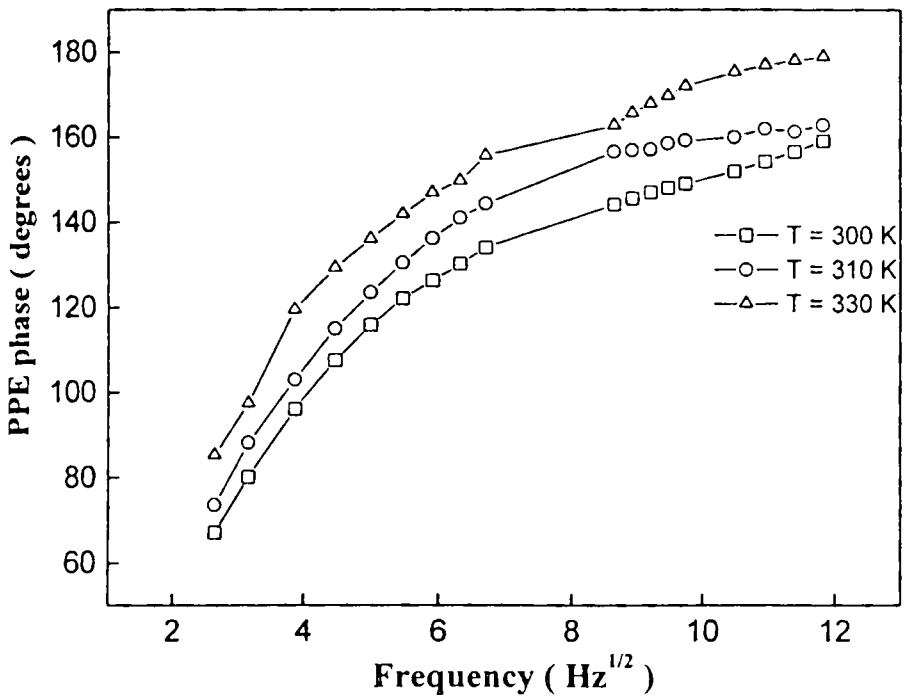

Fig. 2.14(b): Variation of PPE phase with frequency of TGS crystal along *b*-axis

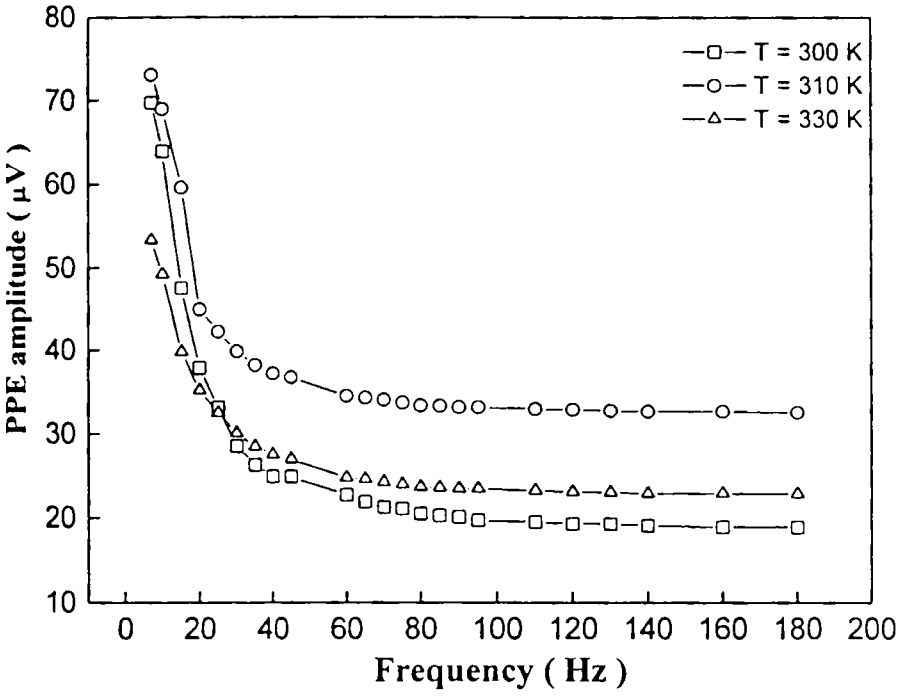

Fig. 2.15(a): Variation of PPE amplitude with frequency of TGS crystal along *c*-axis

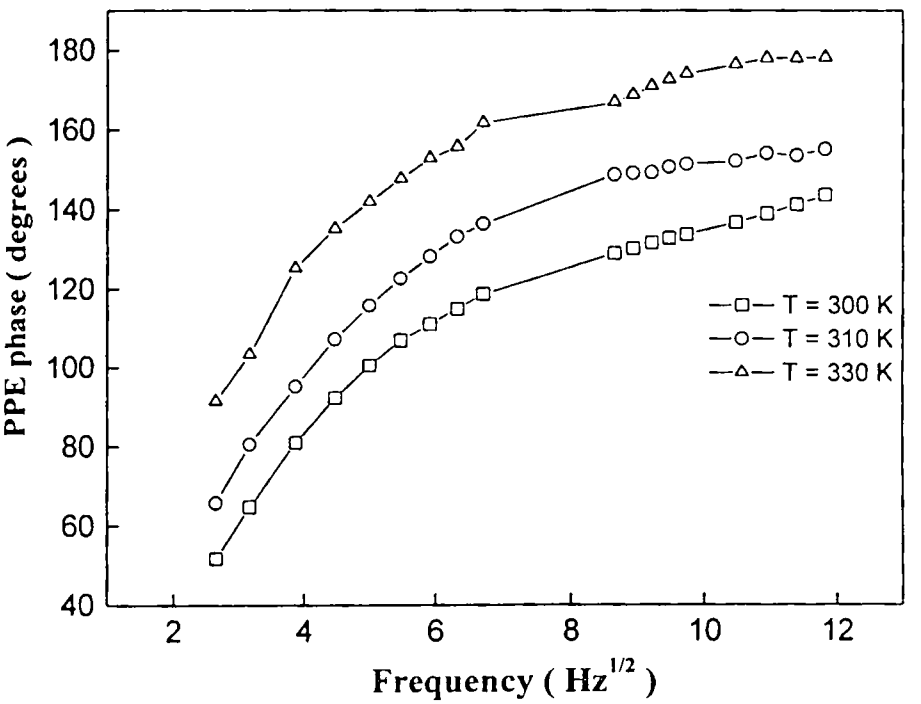

Fig. 2.15(b): Variation of PPE phase with frequency of TGS crystal along *c*-axis

The f^{-1} dependence of the PPE amplitude has been obtained at a number of temperatures, including two above the phase transition point.

The variations of PPE amplitude and phase as functions of temperature have been measured keeping the chopping frequency fixed at 40 Hz. The results along the *b*-axis are given in 2.16(a) and 2.16(b). From these the thermal diffusivity (α_s) and effusivity (e_s) along the *b*-axis at TGS have been determined as functions of temperature. These are shown in Fig. 2.17. The temperature variation of K_s along the *b*-axis and c_{ps} determined as already described are shown in Fig. 2.18. The heat capacity results presented in Fig. 2.18 agree very well (in absolute numbers) with those already reported in literature [34]. Since data on the variation of thermal conductivity across the phase transition point in TGS could not be found in literature, a direct comparison could not be made. It may be noted that the thermal conductivity along the *b*-axis takes a minimum value at the transition point.

The variations of PPE amplitude and phase along the *a*- and *c*- axis are given in Fig. 2.19(a), 2.19(b), 2.20(a) and 2.20(b) respectively. Measurements of the thermal diffusivity, thermal effusivity, thermal conductivity and specific heat along the *a* and *c* axes across the phase transition temperature are plotted in Fig. 2.21 - 2.24. It is seen that the maximum anomaly during the phase transition is along the *b*-direction. It is the direction of spontaneous polarization and is in agreement with thermal diffusivity measurements along different axes [29] reported earlier [35].

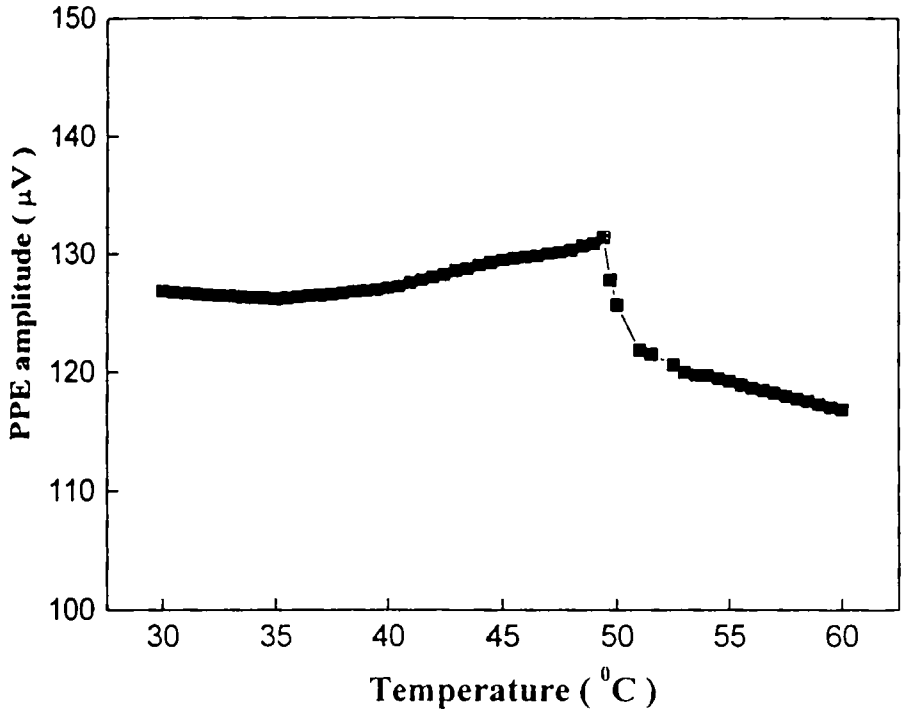

Fig. 2.16(a): Variation of PPE amplitude with temperature along the *b*-axis

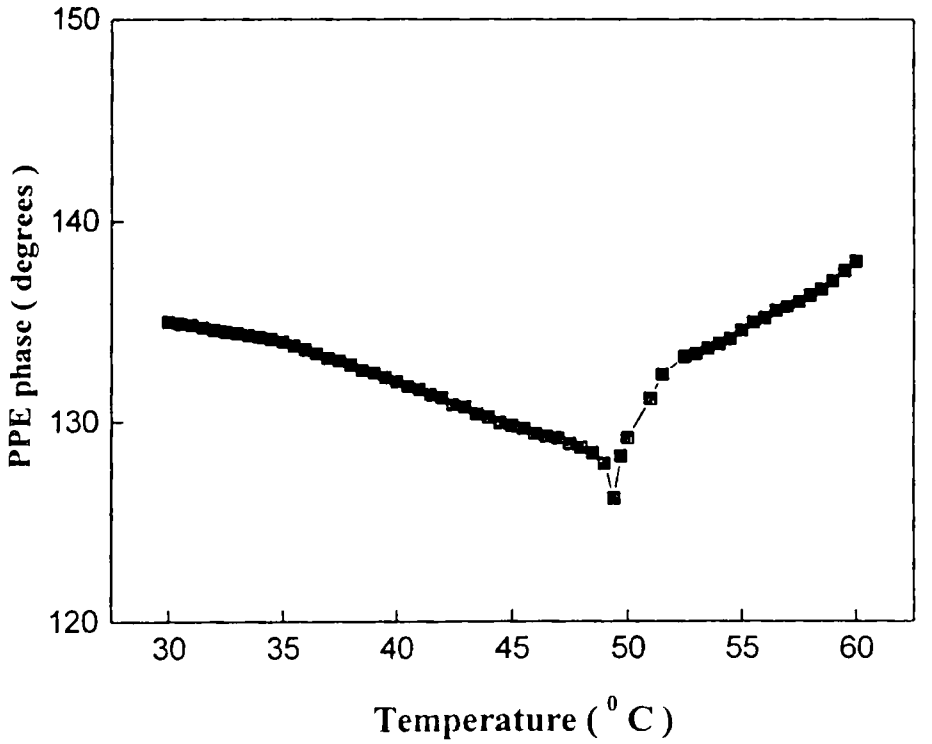

Fig. 2.16(b): Variation of PPE amplitude with temperature along the *b*-axis

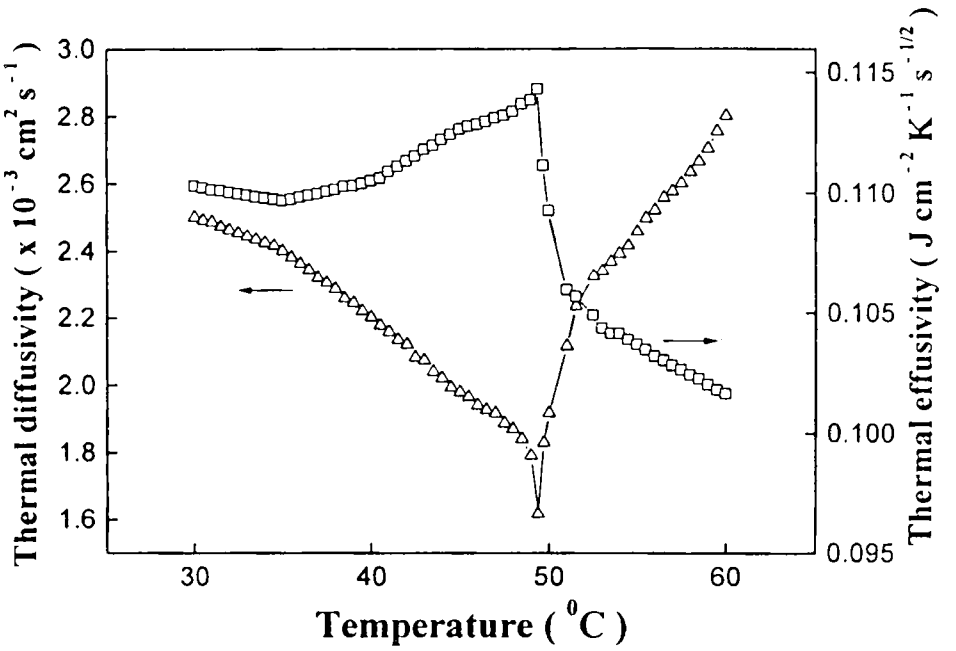

Fig. 2.17: Variation of thermal diffusivity and thermal effusivity with temperature along the *b*-axis

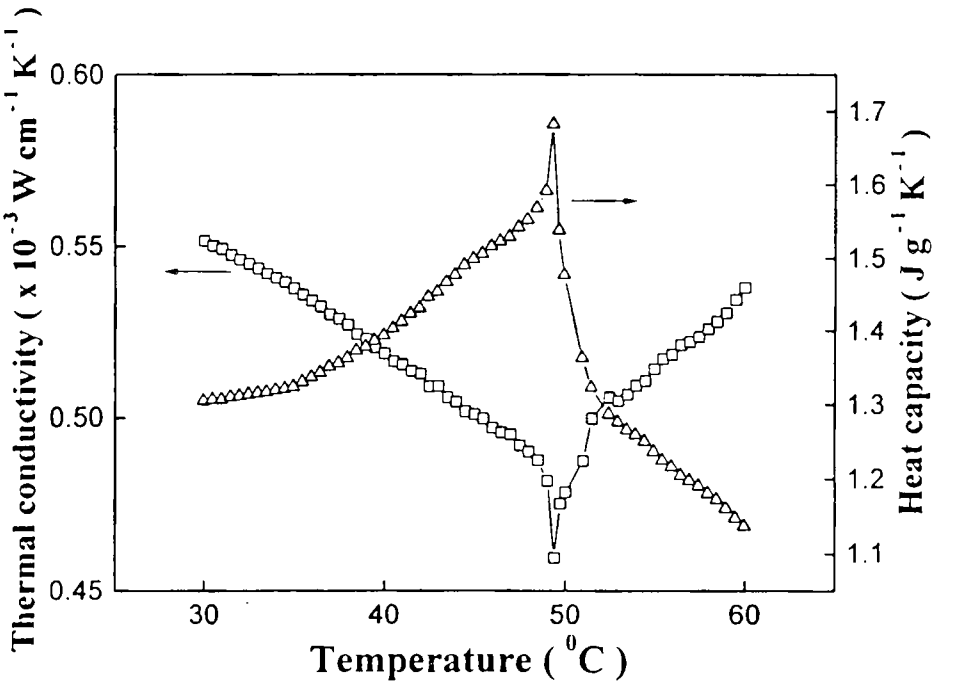

Fig. 2.18: Variation of thermal conductivity and heat capacity with temperature along the *b*-axis

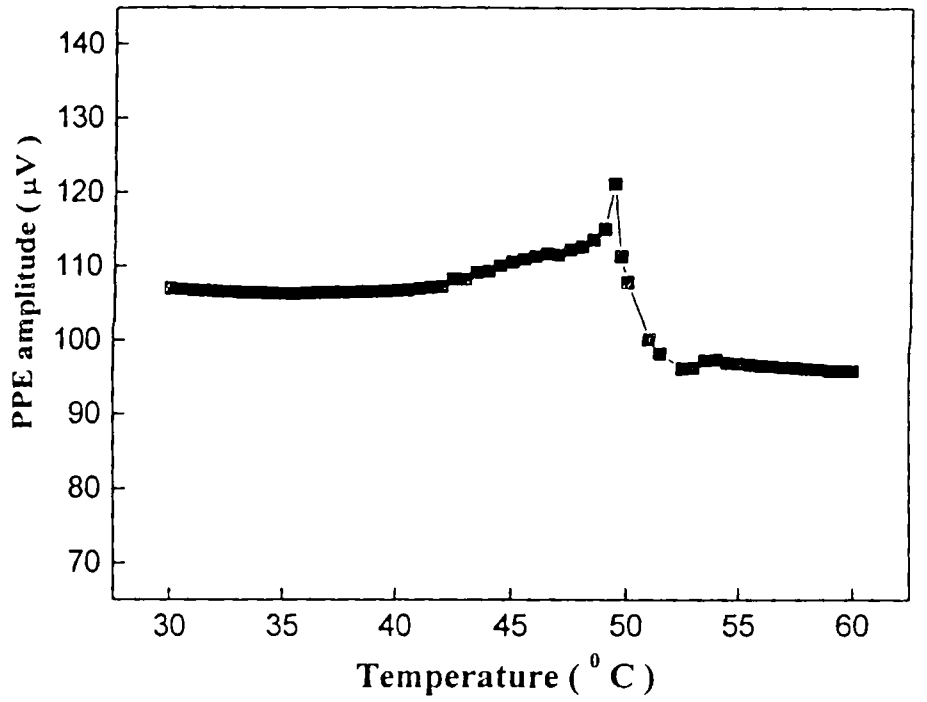

Fig. 2.19(a): Variation of PPE amplitude with temperature along the *a*-axis

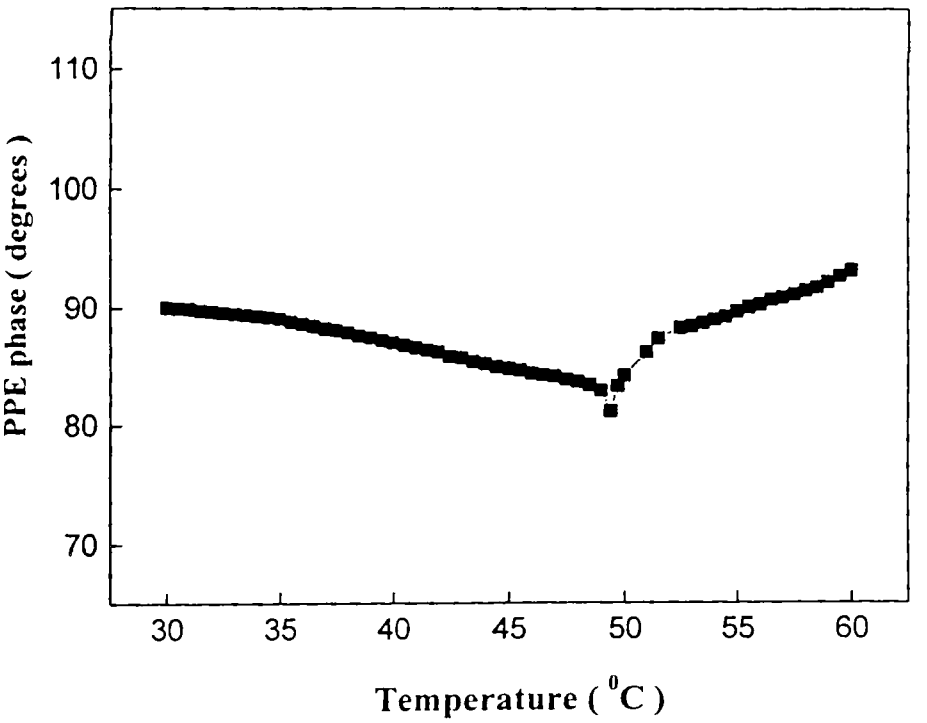

Fig. 2.19(b): Variation of PPE phase with temperature along the *a*-axis

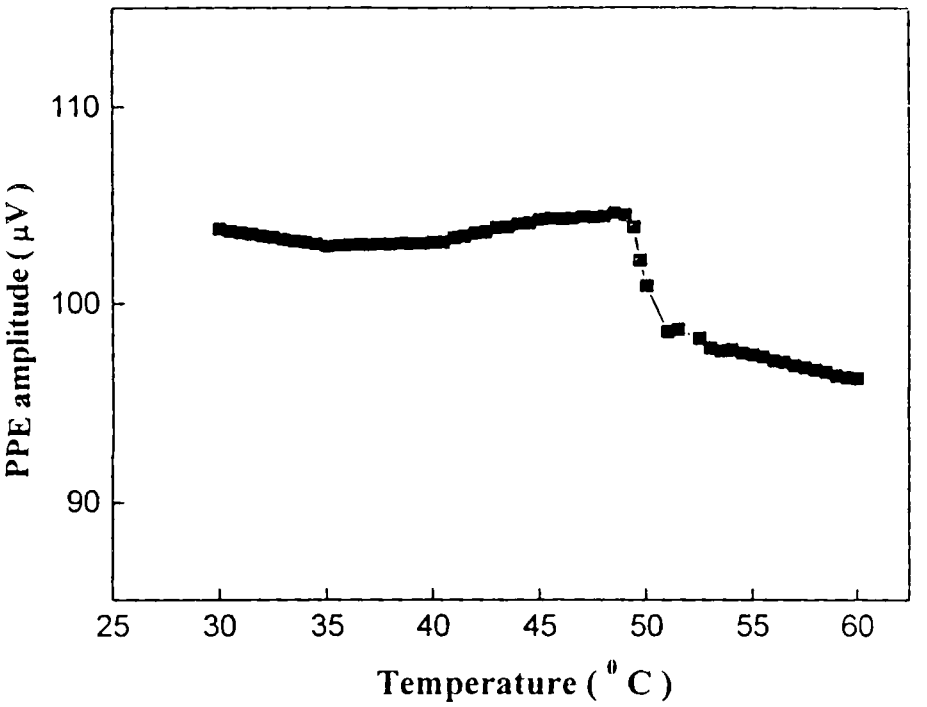

Fig. 2.20(a): Variation of PPE amplitude with temperature along the *c*-axis

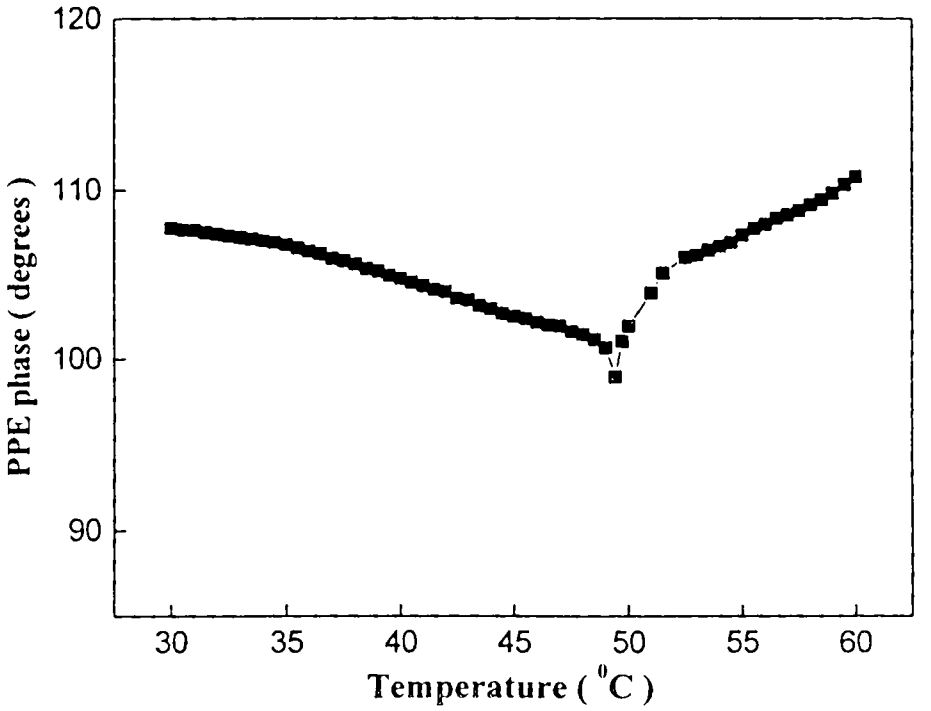

Fig. 2.20(b): Variation of PPE phase with temperature along the *c*-axis

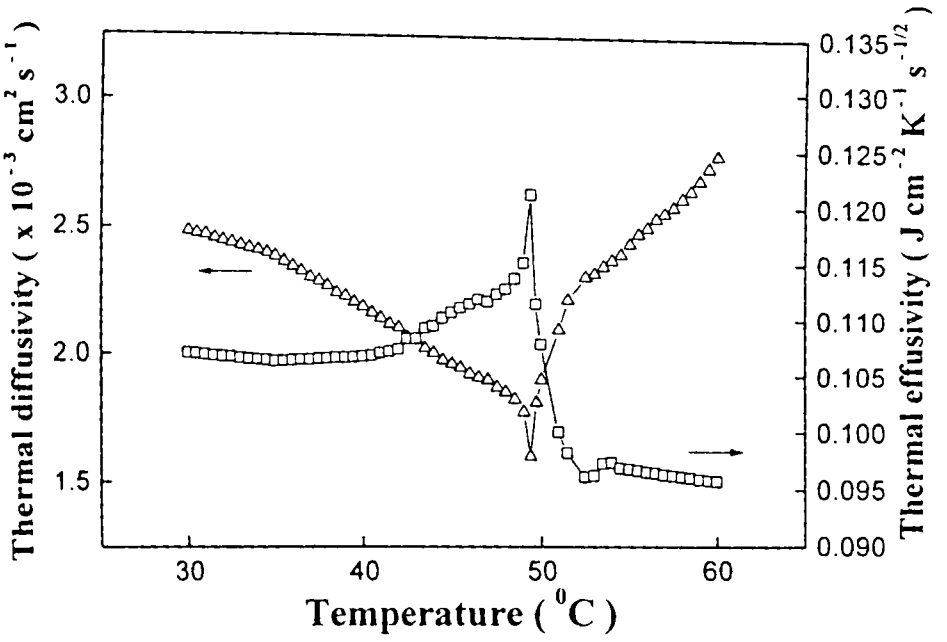

Fig. 2.21: Variation of thermal diffusivity and thermal effusivity with temperature along the *a*-axis

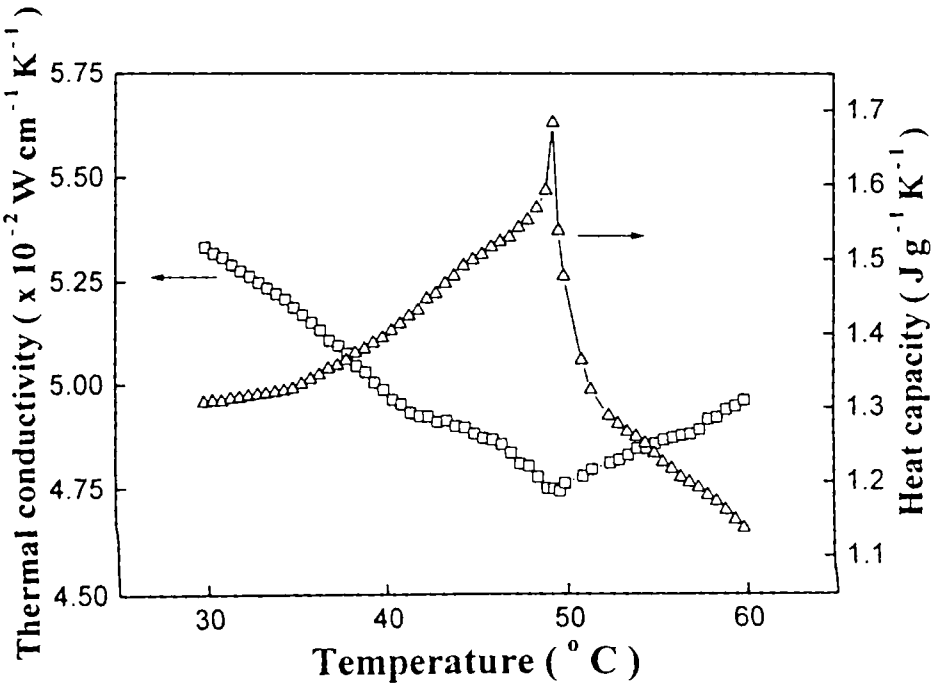

Fig. 2.22: Variation of thermal conductivity and heat capacity with temperature along the *a*-axis

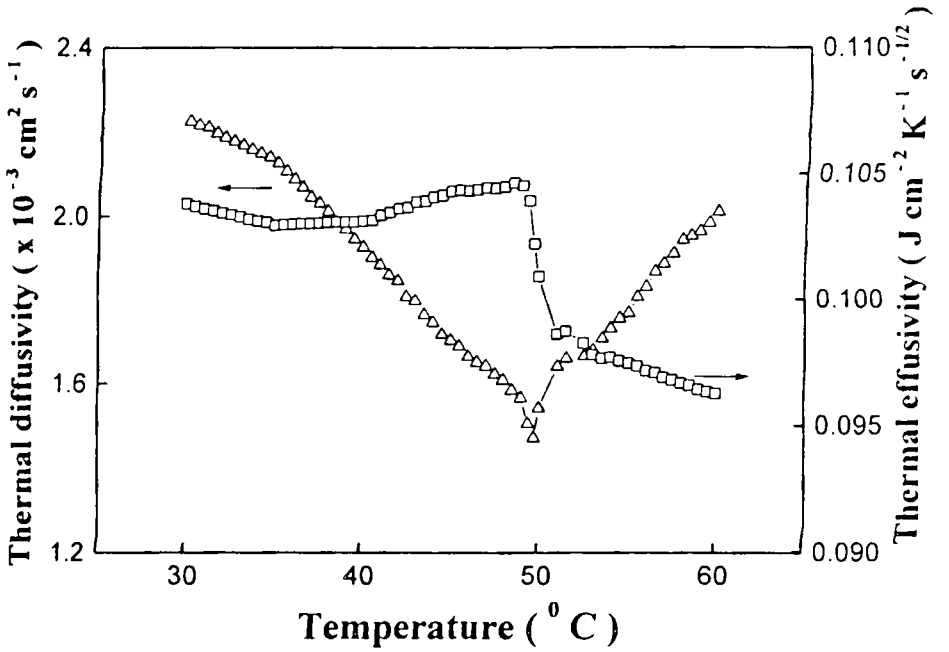

Fig. 2.23: Variation of thermal diffusivity and thermal effusivity with temperature along the *c*-axis

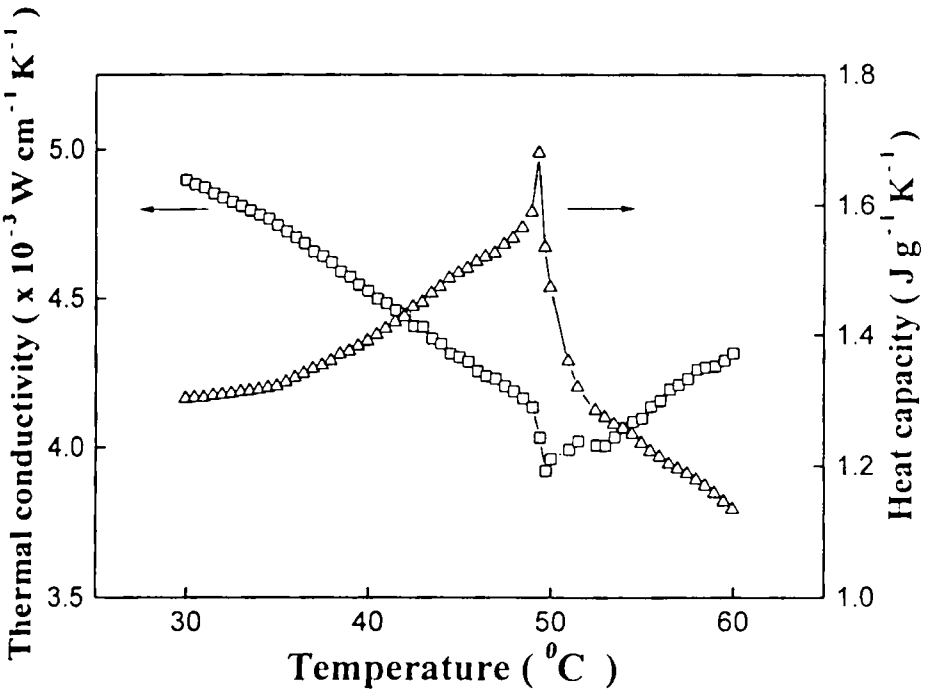

Fig. 2.24: Variation of thermal conductivity and heat capacity with temperature along the *c*-axis

2.7 Conclusions

Our results indicate that the PPE technique presented in this work is a powerful method for simultaneously measuring the thermal conductivity and heat capacity of a solid as functions of temperature. The technique is capable of making thermal conductivity measurements around critical points accurately, where conventional heat conduction methods face practical limitations. The technique can be used to investigate anisotropy in thermal conductivity of crystalline media. The improved sample boundary conditions assumed in this work allow one to make the measurements at all temperatures, the only limitation being the sensitivity to temperature and possible physical damage suffered by the detector at elevated temperatures.

1. J. H. Horrocks and E. Mclaughlin, Proc. R. Soc. A 273 (1963) 253.

2. Y. Tada, M. Harada, M. Tanigaki and W. Eguchi, Rev. Sci. Instrum. **48** (1978) 1305.

3. T. Akahane, M. Kondoh, K. Hashimoto and M. Nagakawa, Jpn. J. Appl. Phys. **26** (1987) 1000.

4. G. B. Kasting, C. W. Garland and K. J. Lushington, J. Physique **41** (1980) 879.

5. T. Thoen, H. Marynissen and W. Van Dael, Phys. Rev. A **26** (1982) 2886.

6. U. Zammit, M. Marinelli, R. Pizzoferrato, F. Scudieri and S. Martellucci, J. Phys. E **21** (1988) 935.

7. J. Extebarria, J. Fernandez, M. A. Arriandaga and M. J. Tello, J. Phys. C **18** (1985) L13.

8. U. Zammit, M. Marinelli, R. Pizzoferrato, F. Scudieri, S. Martellucci, Liquid Crystal **4** (1989) 619.

9. U. Zammit, M. Marinelli, R. Pizzoferrato, F. Scudieri and S. Martellucci, Phys. Rev. A **41** (1990) 1153.

10. A. Mandelis, F. Care, K. K. Chan and L. C. M. Miranda, Appl. Phys. A **38** (1985) 117.

11. P. K. John, L. C. M. Miranda and A. C. Rastogi, Phys. Rev. B **34** (1986) 4342.

12. M. Marinelli, F. Murtas, M. G. Mecozzi, U. Zammit, R. Pizzoferrato, F. Scudieri, S. Martellucci and M. Marinelli, Appl. Phys. A **51** (1990) 387.

13. A. Mandelis and M. M. Zver, J. Appl. Phys. **57** (1985) 4421.

4. H. J. Coufal, R. K. Grygier, D. E. Horne, J. E. Fromm, J. Vac. Sci. Technol. A **5** (1987) 2875.

5. *Kynar*^{TM} *Piezo Technical Manual* (Pennwatt Corp., 1983) p17.

6. A. Roscencwaig, *Photoacoustics and Photoacoustic Spectroscopy, Chemical Analysis*, Vol. 57 (Wiley-Interscience, New York, 1980).

17. H. Coufal, R. Grygier, D. Horne and J. Fromm, J. Vac. Sci. Technol. A **4** (1986) 2988.

18. Y. S. Touloukian, R. W. Powell, C. Y. Ho and M. C. Nicolasu, *Thermal diffusivity* (New York: Plenum 1973).

19. *CRC Handbook of chemistry and physics*, 75th ed. (Boca Raton Fl: CRC Press, 1995).

20. B. T. Mathias, C. E. Miller and J. P. Remeika, Phys. Rev. **104** (1954) 646.

21. E. A. Wood and A. N. Holden, Acta. Cryst. **10** (1975) 145.

22. S. Hoshino, Y. Okaya and R. Pepinsky, Phys. Rev. **115** (1959) 323.

23. T. Ikeda, Y. Tanaka and H. Toyoda, Jpn. J. Appl. Phys **1** (1962) 13.

24. J. A. Gonzalo, Phys. Rev. B **1** (1970) 3125.

25. K. Deguchi and E. Nakamura, Phys. Rev. B **5** (1972) 1072.

26. B. A. Strukov, K. A. Minaeva, N. M. Shirina, V. I. Telesheviskii and S. K. Khanna, Izv. Akad. Nauk. SSSR, Ser. Fiz **39** (1975) 180.

27. B. A. Strukov, Ferroelectrics **12** (1976) 97.

28. C. S. Fang, Yao Xi, A. S. Bhalla and L. E. Cross, Ferroelectrics **51** (1983) 9.

29. A. S. Bhalla, C. S. Fang, L. E. Cross and Yao Xi, Ferroelectrics **54** (1984) 151.

30. M. A. Gaffar, A. Abu Ei-Fadl and S. A. Mansour, Ind. J. Phys. **62A** (1988) 479.

31. M. A. Gaffar and A. Abu El-Fadl, Ind. J. Pure and Appl. Phys. **26** (1988) 28.

32. M. A. Gaffar, A. Abu El-Fadl and A. A. Mansour, J. Phys. D: Appl. Phys. **22** (1989) 327.

33. R. Sreekumar and J. Philip, Ferroelectrics **160** (1994) 23.

34. B. A. Strukov, Soviet Phys. - Solid State **6** (1965) 2278.

35. M. A. Gaffar, M. M. Mebed and A. Abu-El-Fadl, Phys. Stat. Solidi (a) **104** (1987) 879.

CHAPTER 3

Thermal properties of Glycine phosphite single crystals

3.1 Introduction

The α-aminoacid glycine forms addition compounds with several inorganic materials, especially inorganic acids. Some of them exhibit ferroelectric / ferroelastic phase transitions with interesting dielectric and elastic properties. The familiar ferroelectrics in this category include triglycine sulphate (TGS), triglycine selenate (TGSe), triglycine fluroberyllate (TGFBe) etc. [1]. A few betaine compounds have also been investigated for their ferroelectric, antiferroelectric and ferroelastic properties. The most well studied in this class is betaine phosphite $[(CH_3)_3NCH_2COOH_3PO_3]$ which exhibits atleast two phase transitions at 355K and 216K, with the lower temperature leading to a ferroelectric phase [2]. Glycine phosphite $[NH_3CH_2COOH_3PO_3]$, abbreviated as GPI, is a recently developed ferroelectric crystal in this category, which has been explored for its ferroelectric phase transitions [3].

Glycine phosphite is a representative hydrogen bonded ferroelectric crystal of phosphorous acid with an aminoacid, similar to betaine phosphite. Both these crystals are characterized by a typical layered structure [3, 4]. These crystals belong to the monoclinic system with similar space groups $P2_1/a$ and $P2_1/c$ for GPI and BPI respectively. The main structural difference between GPI and BPI lies in that the phosphite chains are oriented parallel and perpendicular to the b-axis in BPI and GPI

respectively. The GPI crystal has unit cell dimensions a = 9.792 Å, b = 8.487 Å, c = 7.411 Å and β = 100.43° and has four molecules per unit cell [3]. Spontaneous polarization of GPI appears along the b-axis.

The main structural feature of this crystal is that its atomic arrangement has a typical layer organization. Planes built by the phosphoric entities alternate with planes containing the organic group. These two layers develop parallel to the bc-planes and are separated by a distance of $a/2$. Inside the phosphoric layers, the $H(HPO_3)^-$ groups form an infinite chain along the crystallographic c-axis to which the amino acids are attracted by strong hydrogen bonds. The projection of the crystal structure, as viewed along the b-axis is given in Fig. 3.1. The phosphite anions are mutually linked by two kinds of strong double well potential hydrogen bonds (of lengths 0.2482nm and 0.2518nm) with equally populated wells at room temperature. The phosphite layers as interconnected by glycine ions forming three hydrogen bonds (of lengths 0.2861nm, 0.2875nm and 0.2899nm) to the phosphite oxygens via - NH_3 group from one side and single bond (of length 0.2598nm) via acidic oxygen from the opposite side.

Dielectric measurements performed on GPI crystal along the b-axis (polar axis for the monoclinic crystal) reveal a large anomaly in dielectric constant (ε) at 224.7 K, giving a clear indication of the transition temperature [5, 6]. The maximum value of spontaneous polarization P_s along its polar axis is about 5×10^{-23} Cm $^{-2}$, which is considerably smaller in comparison to other crystals of the family as BPI [2]. The b-axis of GPI is perpendicular to infinite chains of hydrogen bonded phosphite anions, similar to that observed in KDP family crystals [7]. Hence, the ordering of hydrogen bonds along the c-axis results in the appearance of

spontaneous polarization along the *b*-direction. Also any change in the phosphite layers which can appear as a result of proton ordering in the hydrogen bond, will influence the glycine orientation.

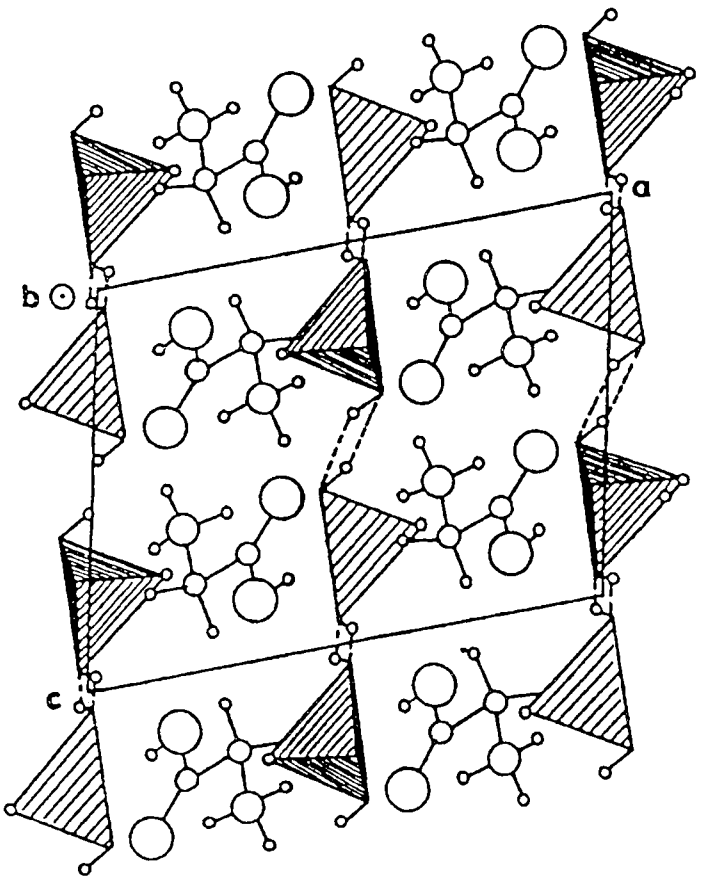

Fig. 3.1: Projection of crystal structure of GPI when viewed along the *b*-axis (Circles, in decreasing order of size represent N, O, C and H atoms respectively

The activation energy for GPI crystal is estimated to be ΔE = 17 kJ/ mol which is more than three times higher than other ferroelectric crystals in which the mechanism of paraelectric-ferroelectric phase transition is connected only with the ordering of protons in the strong hydrogen bonds. This suggests that the dynamics of the organic sub lattice (glycinium cations) of GPI could play a vital role in the long range ordering of the crystal. With the slowing of the glycine NH_3^+ group rotations,

the ordering of these protons takes place as seen in EPR measurements [8], as a result of which the GPI crystal undergoes a phase transition at 224 K. Several macroscopic and microscopic properties of GPI have been investigated by researchers to elucidate the mechanism underlying the phase transition [6, 8, 9-12]. However, investigations on the thermal properties of this crystal have not been reported.

In this chapter, we give a systematic study of the variations in thermal parameters- thermal diffusivity (α) thermal effusivity (e), thermal conductivity (K) and heat capacity (c_p) - of GPI single crystal along the three principal directions, when the crystal undergoes the para-ferroelectric phase transition, employing an improved photopyroelectric (PPE) technique [13]. Details of the experimental results obtained and discussion of the results are outline in the following sections.

3.2 Sample preparation

Single crystals of glycine phosphite are grown by the slow cooling of an equimolar solution of glycine [NH_2CH_2COOH] (AR grade) and orthophosphorous acid [H_3PO_3] solution (Aldrich). Prior to growth, GPI was re-crystallized for nearly 4-5 hours to yield purified materials. Slow cooling from a temperature of about 35°C to 29°C at a rate of 0.02°C / hour is achieved with a programmable temperature controller having a cooling rate of 0.01°C / hour. Crystals as large as 50 x 35 x 30 mm^3 have been grown by this method. Transparent good quality crystals so obtained are used in the present investigations.

The crystallographic directions of the crystal are identified by X-ray diffraction technique (XRD). The complete morphology of GPI crystal has been

generated using XRSHAPE software after measuring the interfacial angles using a contact goniometer and is given in Fig. 3.2. The crystallographic *b* and *c* axes are selected as the crystal physical *Y* and *Z*-axes respectively but the crystal physical *X*-axis lies in the (010) plane making an angle 10.43° to the crystallographic *a*-axis (β = 100.43°). The coordinate system chosen for measurement is not orthogonal, such that the (100) plane is normal to the crystallographic *a*-axis.

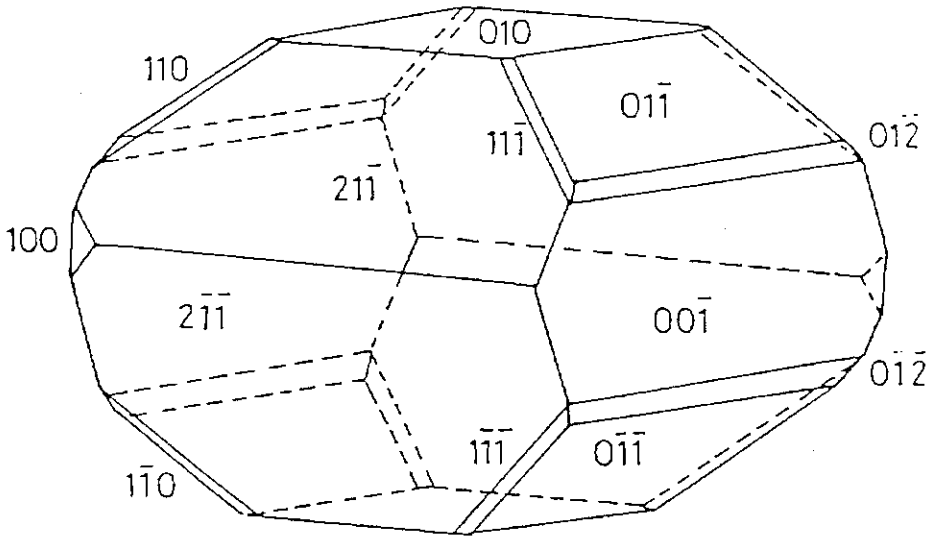

Fig. 3.2: Complete morphology of Glycine phosphite (GPI) single crystal

The oriented crystals are cut with a slow speed diamond wheel saw such that they have faces perpendicular to the [100], [010] and [001] directions or the crystallographic *a*-, *b*- and *c*- axes respectively. The samples are carefully polished, initially with water and finally with alumina powder, to get good surface finish. The samples prepared for the photopyroelectric measurements have a thickness of ≈ 0.3mm. The density of the sample is measured to be 1.722 gcm^{-3}. A very thin layer of carbon black from a benzene flame has been carefully coated on to the illuminated surface of each sample to enhance its optical absorption.

3.3 Experimental details

An improved photopyroelectric technique has been used to determine the thermal parameters of GPI single crystal. In this measurement, a thermally thick pyroelectric detector film is attached to one side of the sample, which is also thermally thick and the combination is mounted on a thermally thick backing medium. The other side of the sample is illuminated by an intensity-modulated beam of light, which gives rise to periodic temperature variations by optical absorption. The thermal waves so generated propagate through the sample and are detected by the pyroelectric detector.

A 120mW He-Cd laser of wavelength λ = 442nm (KIMMON), intensity modulated by a mechanical chopper has been used as the optical heating source. Polyvinylidene difluoride (PVDF) film of thickness 28μm, both sides coated with Ni-Cr film, with pyroelectric coefficient $P = 0.25 \times 10^{-8}$ $Vcm^{-1}K^{-1}$ is used as the pyroelectric detector. The detector is supported on a thermally thick backing medium, made of copper. The sample-detector-backing assembly has been enclosed in a chamber whose temperature can be varied and controlled as desired. The signal output is measured using a lock-in amplifier (SR 830). The frequency of modulation of the light is kept above 30Hz to ensure that the detector, the sample and the backing medium are thermally thick during the measurements. The thermal thickness of the GPI sample in this experiment has been verified by plotting the PPE amplitude and phase with frequency at different temperatures between room temperature and 180 K, along three principal directions are given in figures 3.3(a), 3.3(b), 3.4(a), 3.4(b), 3.5(a) and 3.5(b) respectively.

Measurements have been carried out illuminating the three cut sample faces so that the propagation of the thermal wave is along one of the symmetry axes. Measurement of the PPE signal phase and amplitude enable one to determine the thermal diffusivity (defined as $\alpha = K / \rho c_p$, ρ being the density) and effusivity (defined as $e = (K\rho c_p)^{1/2}$) respectively [13]. From the measured values of α and e, K and c_p of the sample are determined. A careful calibration of the experimental set up and procedure has been done prior to carry out the measurements, as described in detail in Chapter 2 of this thesis. The measurements as a function of temperature have been made at a heating rate of approximately 0.5 Kmin $^{-1}$ and data collected in every 1K interval normally and at closer intervals near the transition point. The temperature is measured with a platinum sensor placed close to the sample inside the chamber.

3.4 Results and discussion

Figures 3.6(a), 3.6(b), 3.7(a), 3.7(b), 3.8(a) and 3.8(b) show the variation of PPE amplitude and phase of GPI single crystal along the *a*-, *b*- and *c*- axes of the crystal. It is seen that, in all the three directions, PPE amplitude and phase reflect the para-ferroelectric phase transition at 224 K.

Figures 3.9, 3.10 and 3.11 show the variation of thermal diffusivity and thermal effusivity with temperature along the *a*-, *b*- and *c*- axes of GPI single crystal.

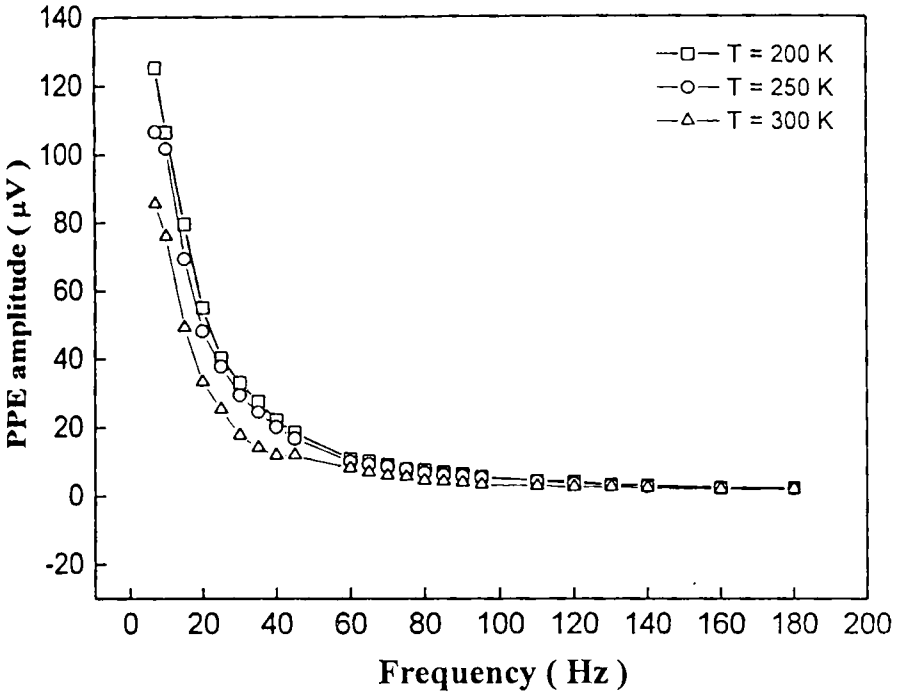

Fig. 3.3(a): Variation of PPE amplitude with frequency of GPI crystal along the *a*-axis

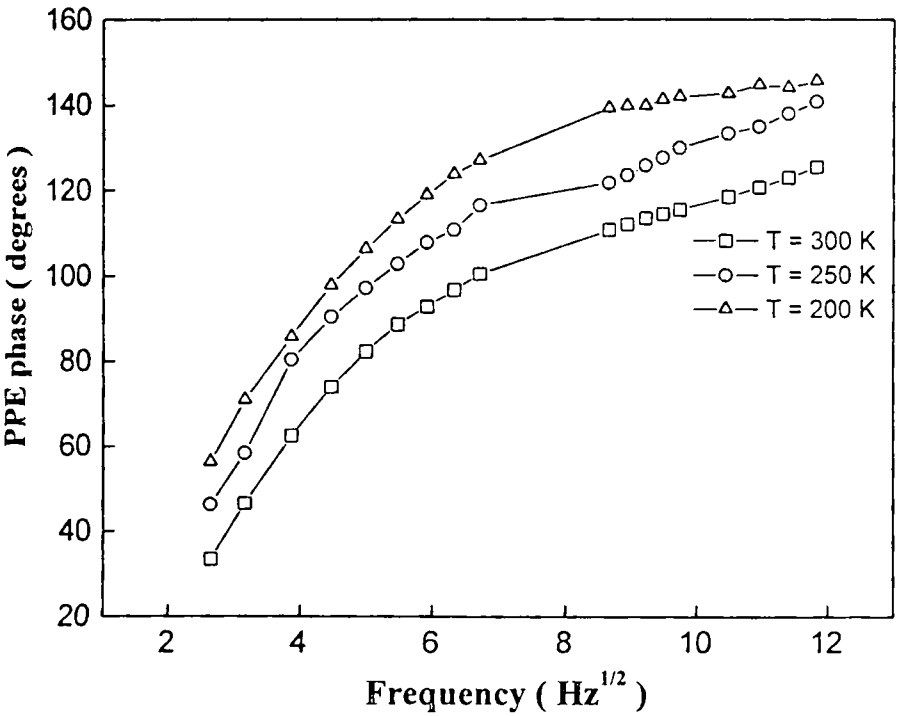

Fig. 3.3(b): Variation of PPE phase with frequency of GPI crystal along the *a*-axis

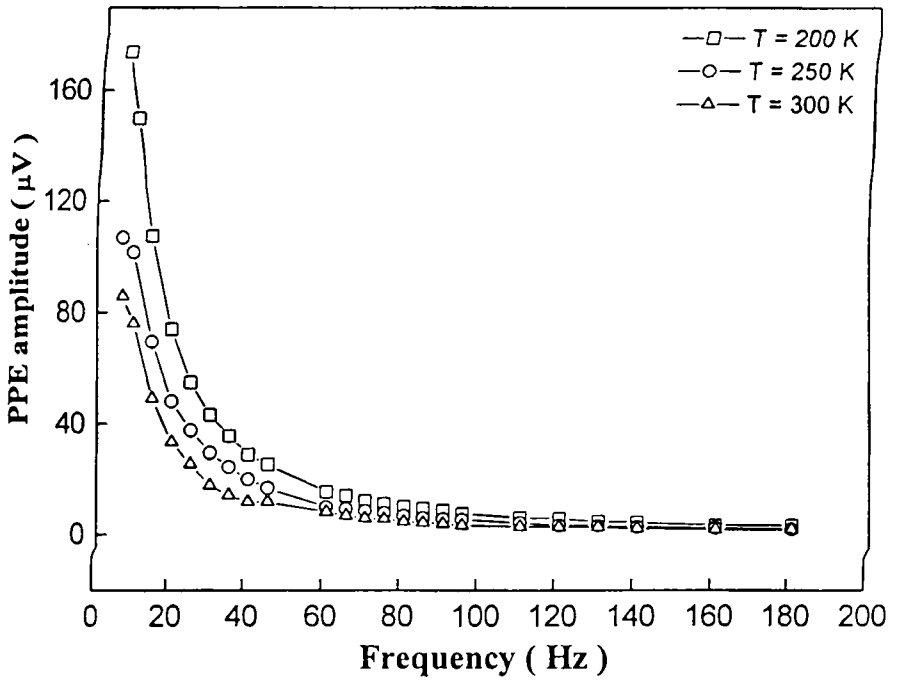

Fig. 3.4(a): Variation of PPE amplitude with frequency of GPI crystal along the *b*-axis

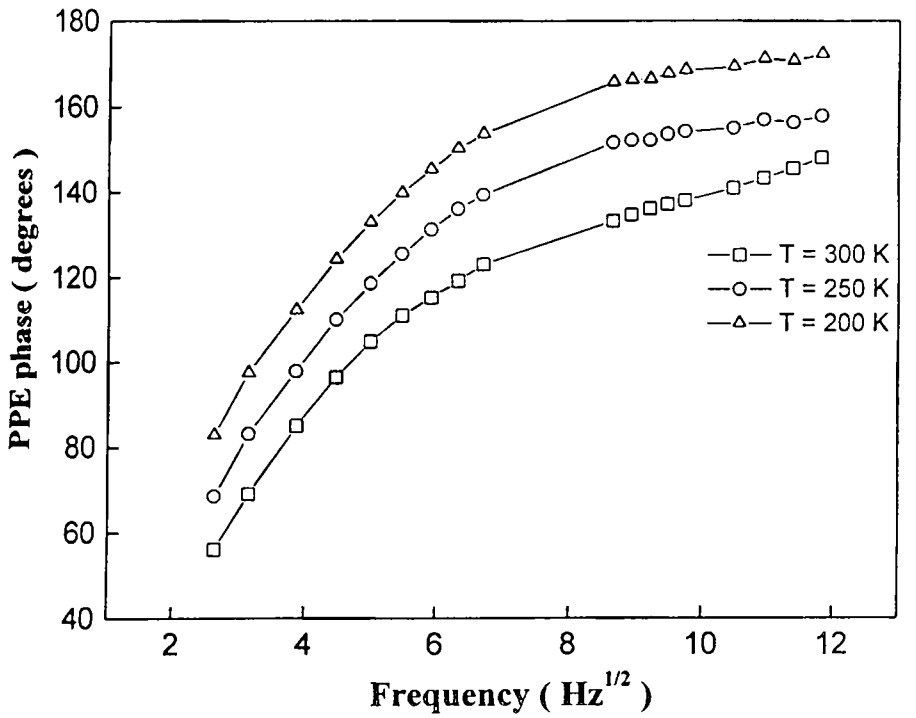

Fig. 3.4(b): Variation of PPE phase with frequency of GPI crystal along the *b*-axis

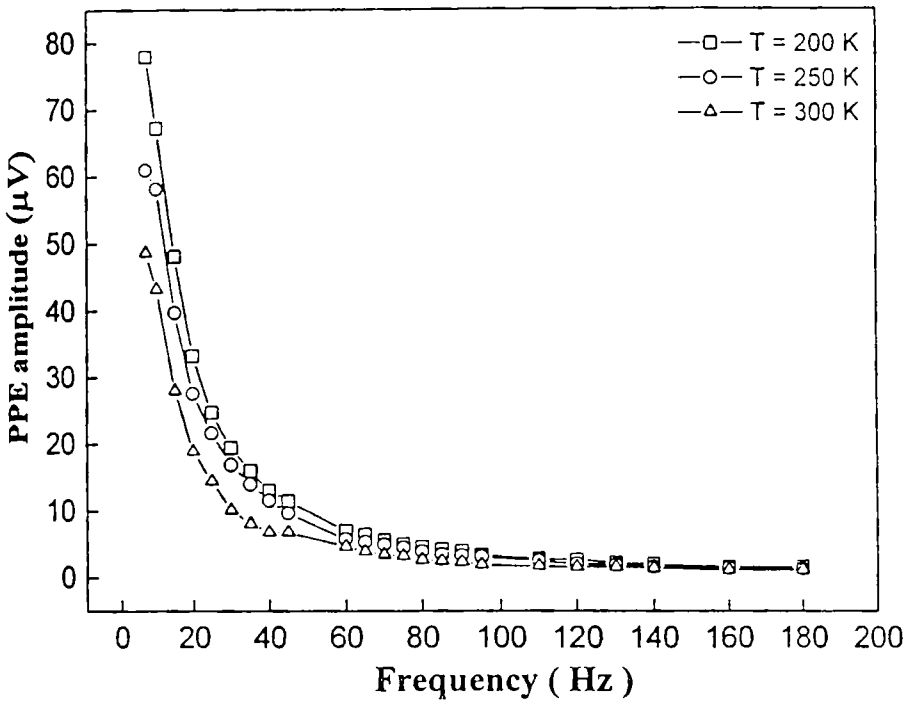

Fig. 3.5(a): Variation of PPE amplitude with frequency of GPI crystal along the *c*-axis

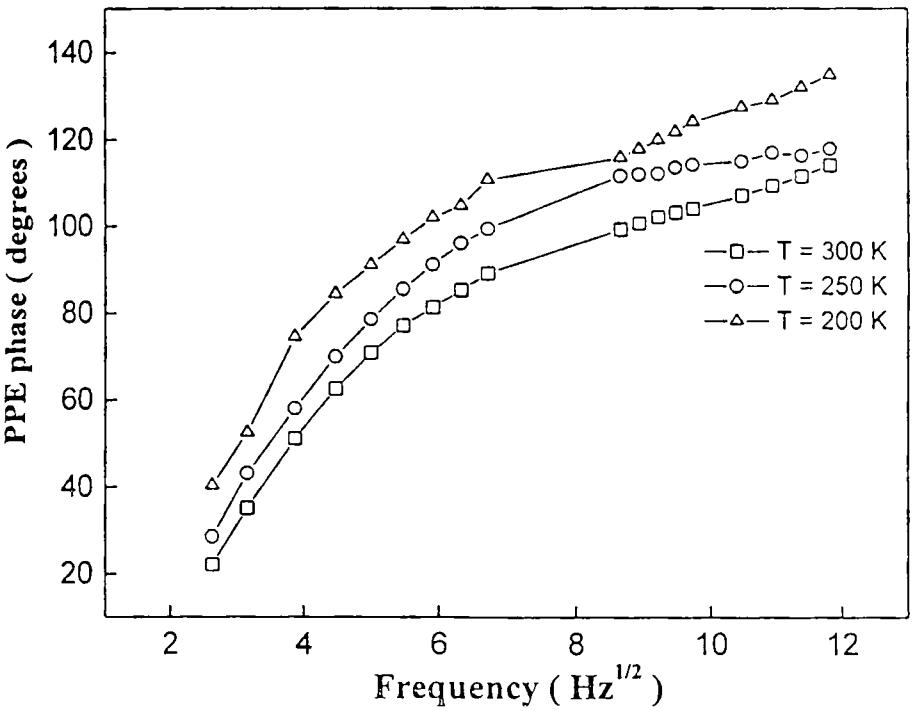

Fig. 3.5(b): Variation of PPE phase with frequency of GPI crystal along the *c*-axis

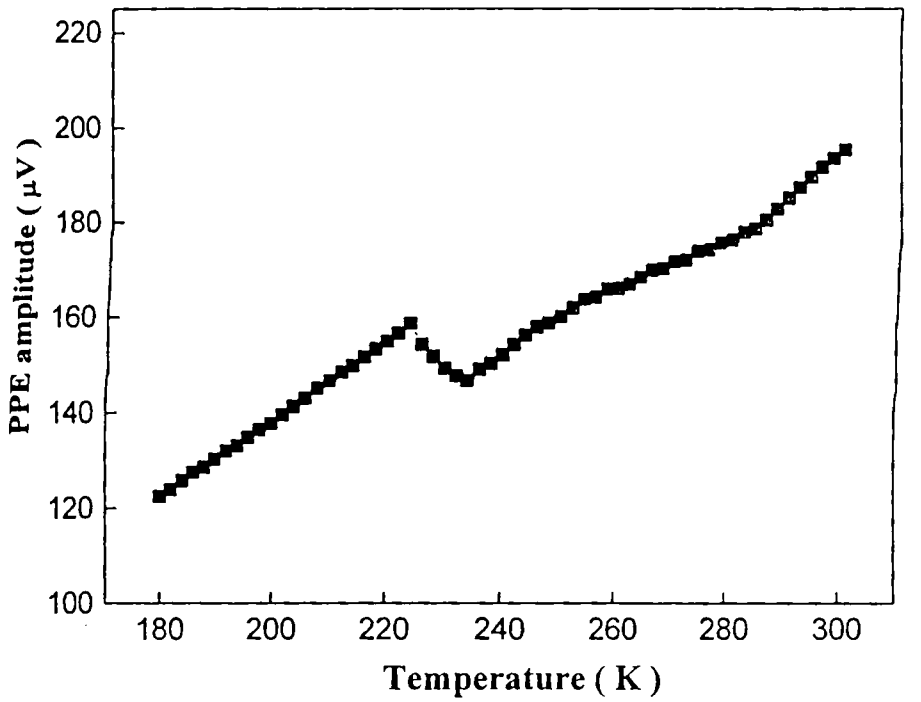

Fig. 3.6(a): Temperature variation of PPE amplitude of GPI crystal along the *a*-axis

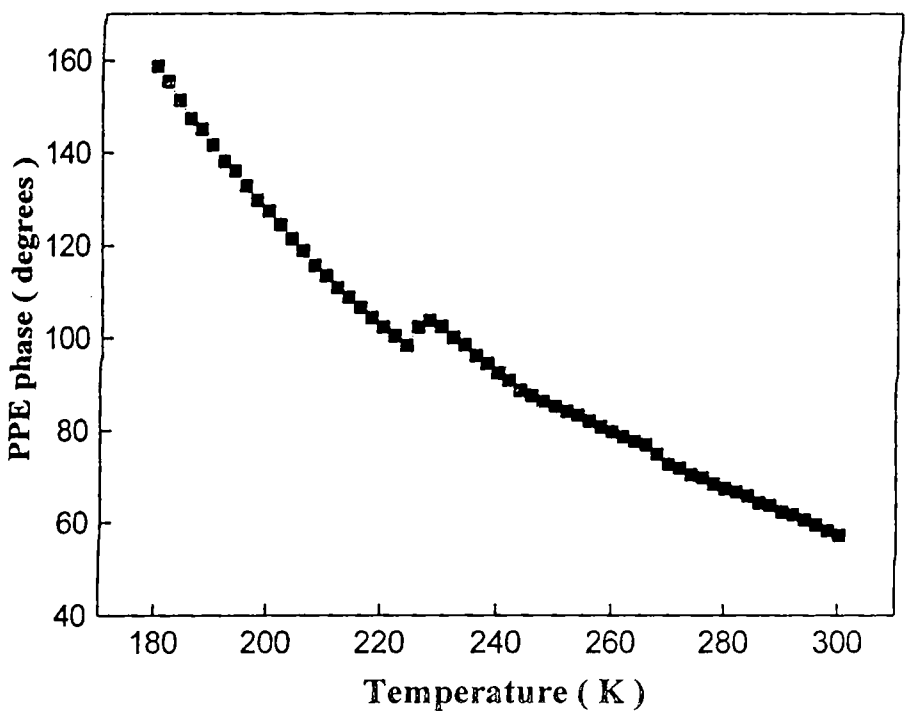

Fig. 3.6(b): Temperature variation of PPE phase of GPI crystal along the *a*-axis

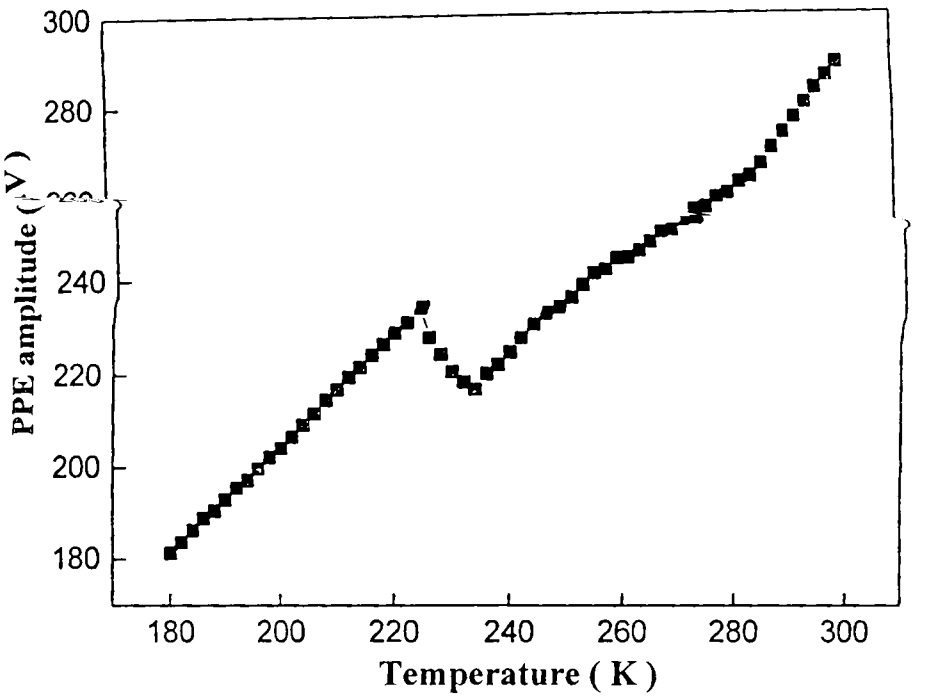

Fig. 3.7(a): Temperature variation of PPE amplitude of GPI crystal along the *b*-axis

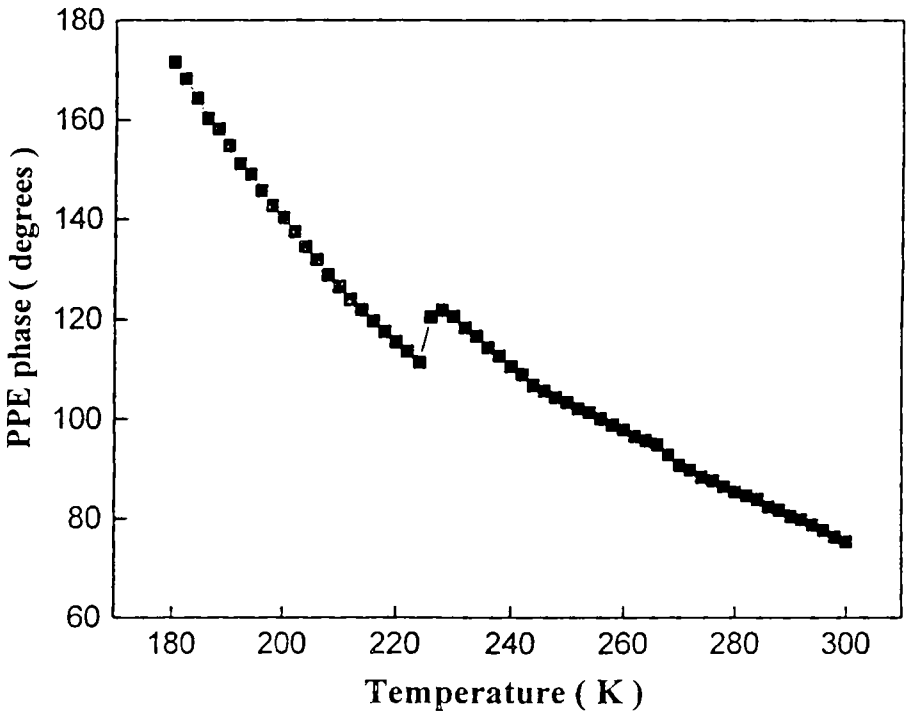

Fig. 3.7(b): Temperature variation of PPE phase of GPI crystal along the *b*-axis

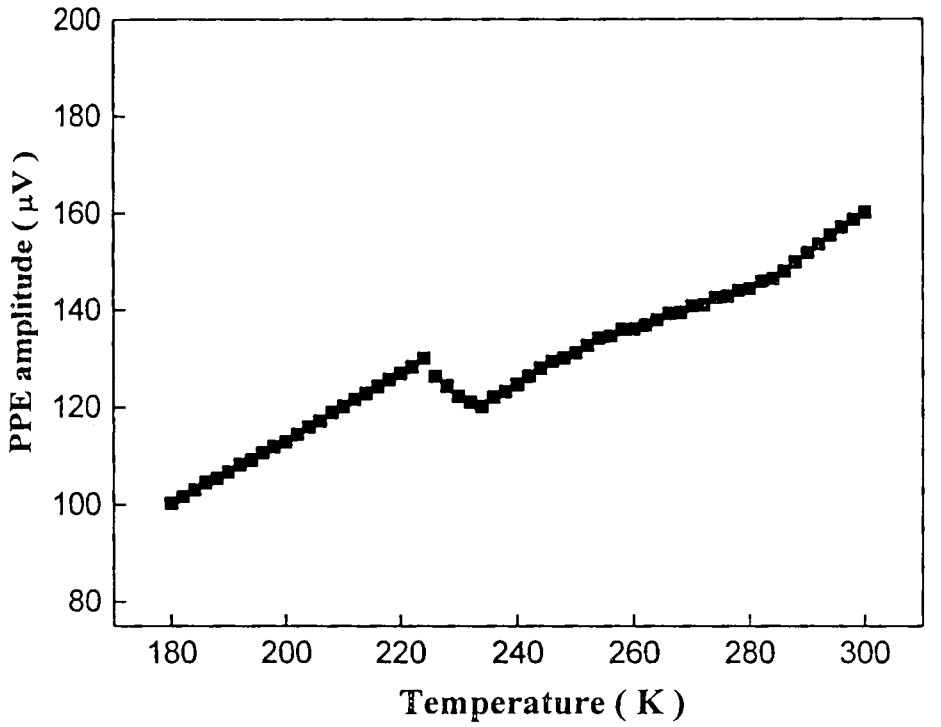

Fig. 3.8(a): Temperature variation of PPE amplitude of GPI crystal along the *c*-axis

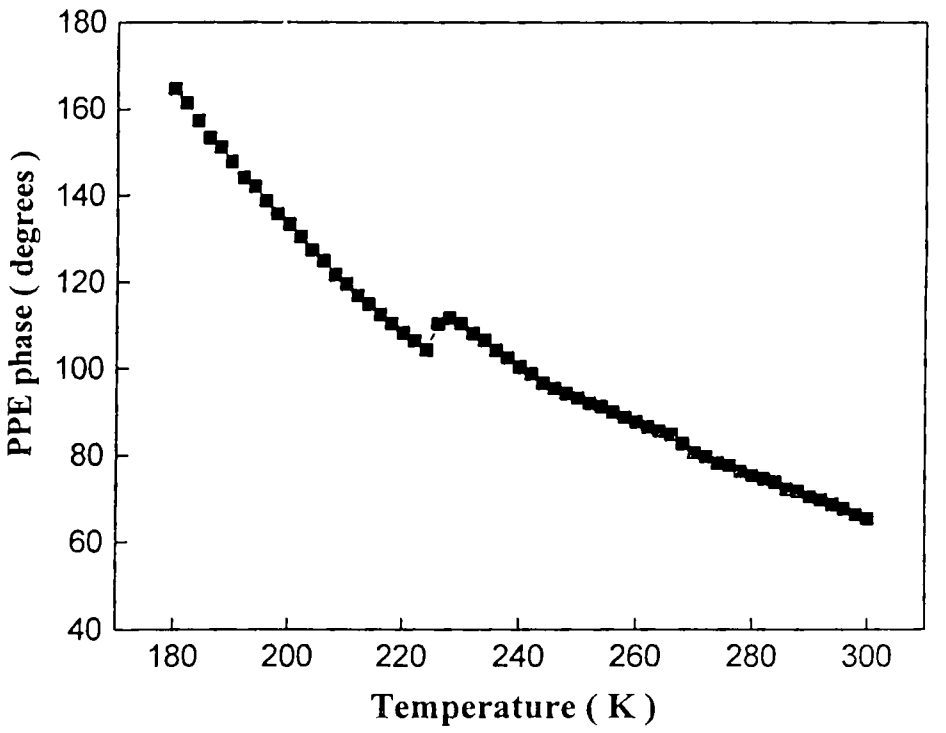

Fig. 3.8(b): Temperature variation of PPE phase of GPI crystal along the *c*-axis

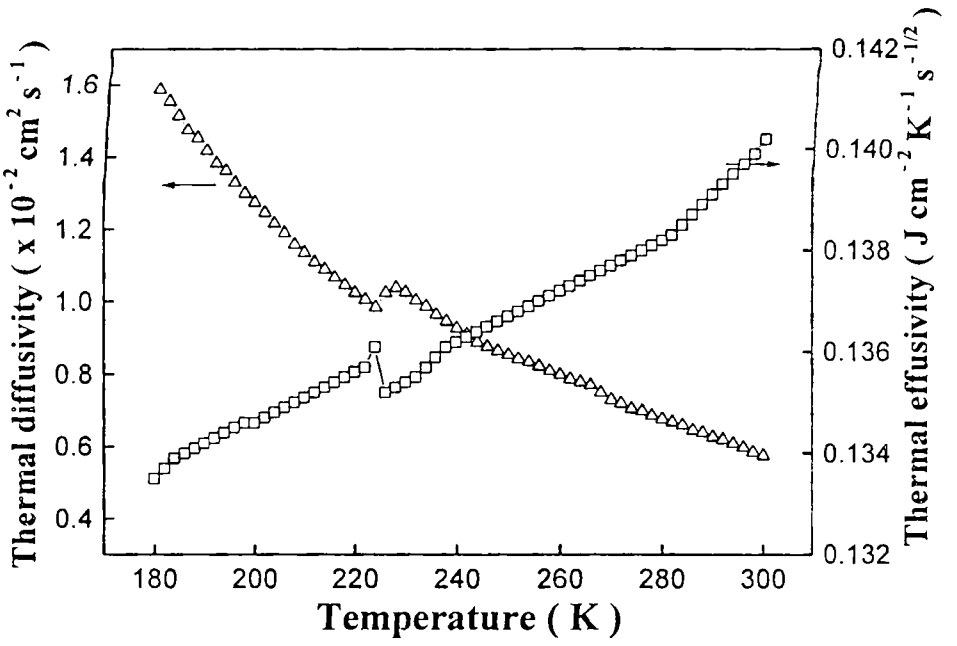

Fig. 3.9: Variation of thermal diffusivity and thermal effusivity with temperature of GPI crystal along the *a*-axis

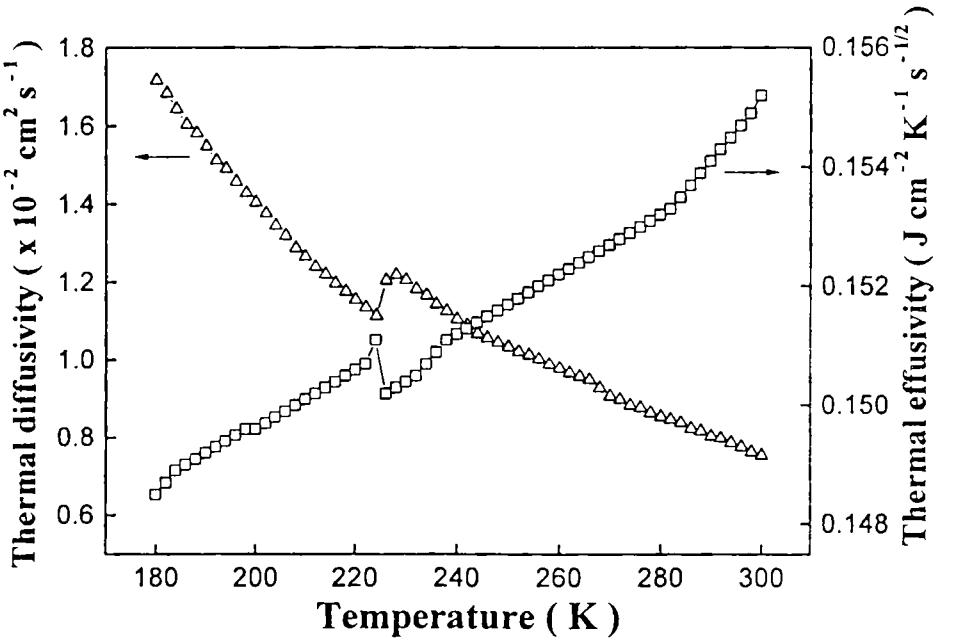

Fig. 3.10: Variation of thermal diffusivity and thermal effusivity with temperature of GPI crystal along the *b*-axis

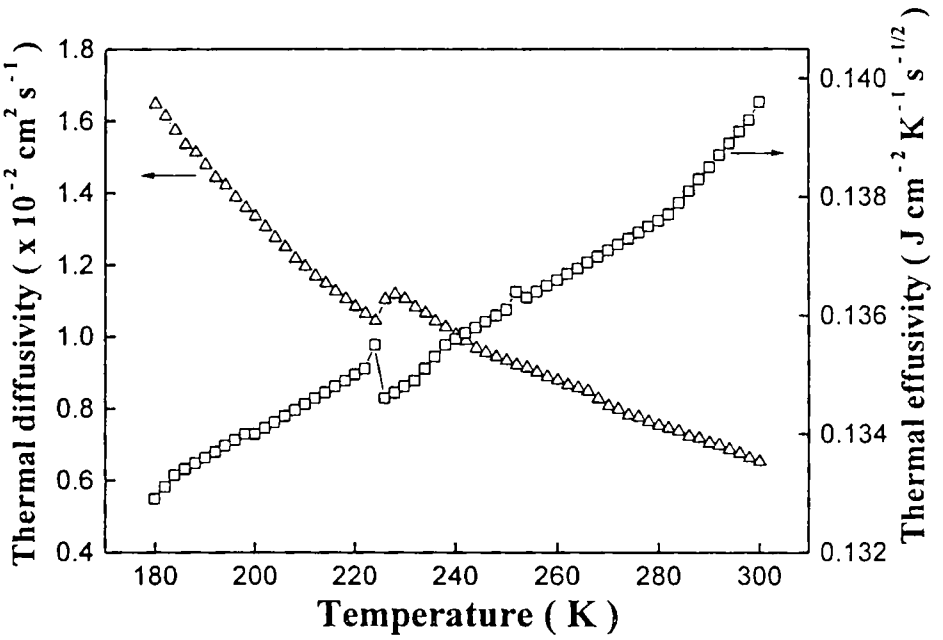

Fig. 3.11: Variation of thermal diffusivity and thermal effusivity with temperature of GPI crystal along the *c*-axis

As seen in figures, the thermal diffusivity follows the same pattern as PPE phase and decreases up to the point of para-ferroelectric phase transition at T = 224K, in agreement with the already reported value of transition temperature. At the transition temperature, there is a peak and there after thermal diffusivity steadily decreases with temperature. The thermal effusivity exhibits an opposite behaviour. It increases with temperature up to the transition point. At the transition temperature, there is a minimum in the thermal effusivity value but thereafter it increases steadily with temperature. Taking into account, the various limitations of the measurements, the overall uncertainties in the values of α and e are estimated to be ± 1%.

Figure 3.12 shows the variation of heat capacity of GPI single crystal as a function of temperature. The phase transition in GPI is reflected clearly in the

temperature variation of heat capacity as a clear anomaly at the transition point. These heat capacity results agree with the DSC measurements reported earlier [6]. As we can see, there is no direction dependence for heat capacity.

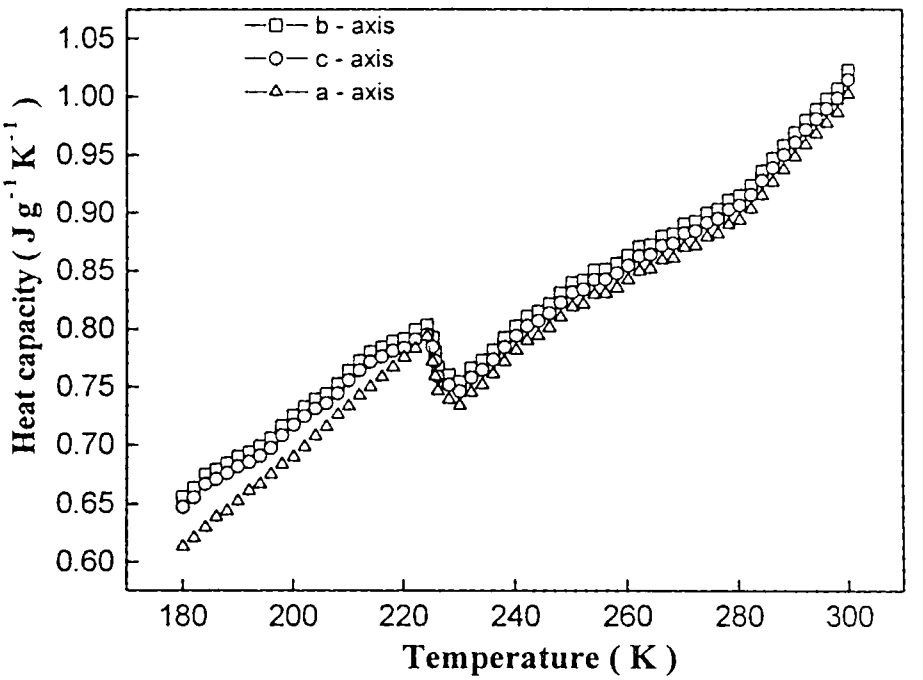

Fig. 3.12: Variation of heat capacity with temperature of GPI single crystal

Figure 3.13 shows the temperature variation of thermal conductivity along the three symmetry axes (*a*, *b* and *c*) of GPI. Thermal conductivity exhibits significant anisotropy as is evident from Fig. 3.13. A study of anisotropy in thermal conductivity enables one to draw important conclusions regarding intermolecular forces in the crystal. With such an intention, we have plotted the thermal conductivity ellipsoids for the *b*-*c*, *a*-*c* and *a*-*b* planes.

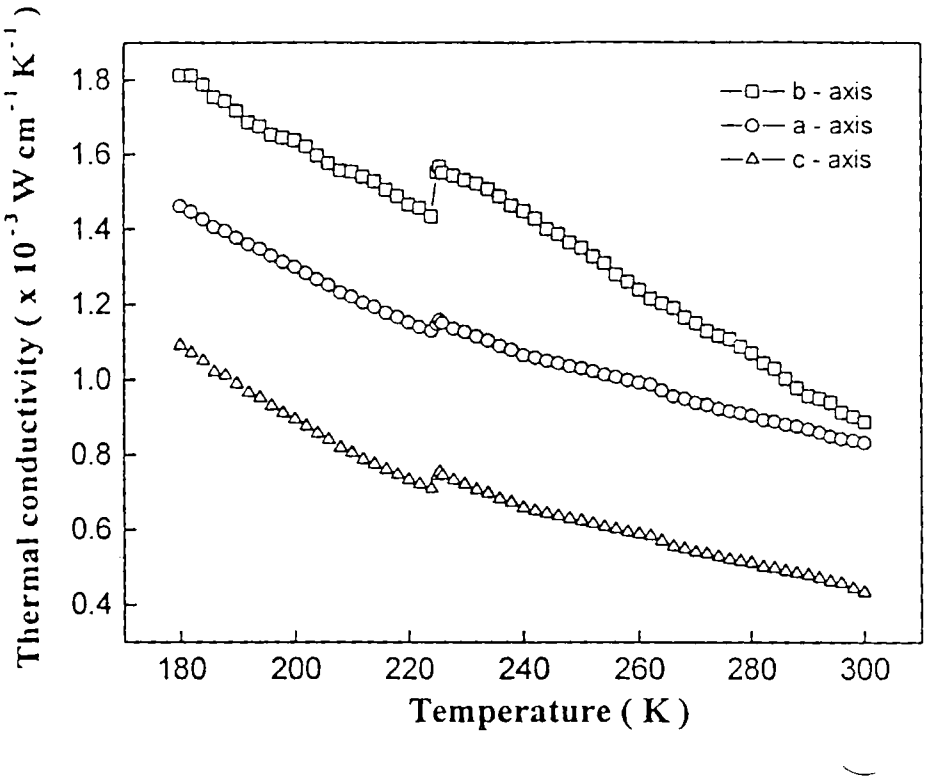

Fig. 3.13: Variation of thermal conductivity with temperature of GPI single crystal

The characteristic representation of quadric for thermal conductivity is given by [14]

$$K_{ij}\,\tilde{n}_i\,\tilde{n}_j = 1 \qquad (3.1)$$

where K_{ij} are the thermal conductivity tensor and $\tilde{n}$ are the direction cosines.

When we refer to the principal axes, we have

$$K_1 n_1^2 + K_2 n_2^2 + K_3 n_3^2 \;=\; 1 \qquad (3.2)$$

K_1, K_2 and K_3 are always positive and hence this represents the thermal conductivity ellipsoid.

Figures 3.14(a), 3.14(b) and 3.14(c) represent the projection of the thermal conductivity quadric lying in the *b-c*, *a-c* and *a-b* planes, when viewed along the *a-*, *b-* and *c* axes of the crystal respectively.

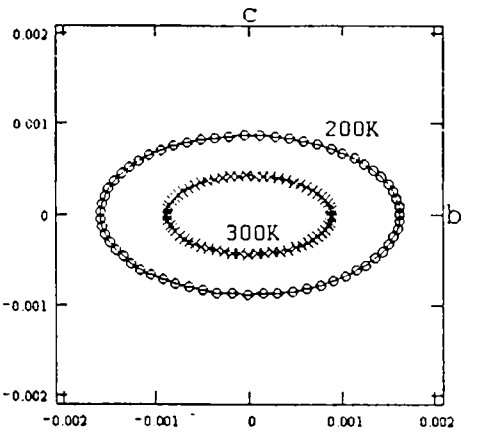

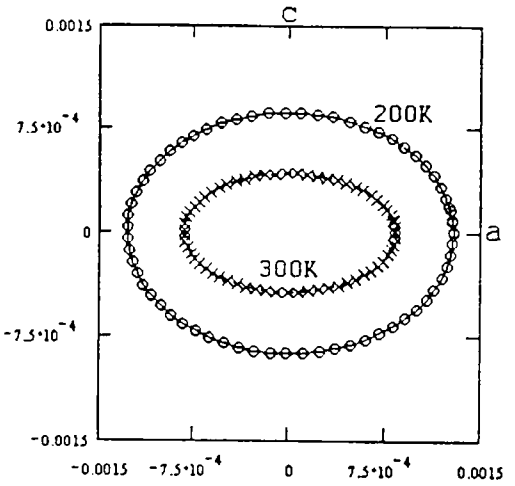

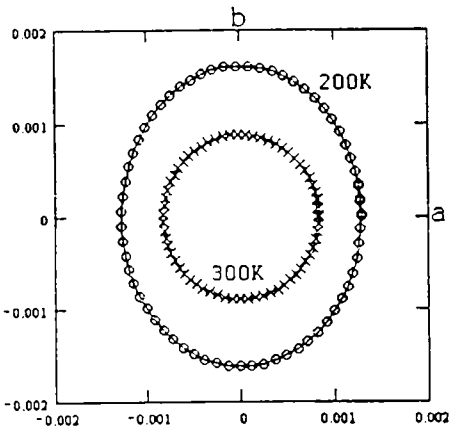

Fig. 3.14: Projection of the thermal conductivity quadric lying in the *b*-*c*, *a*-*c* and *a*-*b* planes when viewed along the *a*-, *b*- and *c*- axis of the crystal respectively

The thermal conductivity ellipsoid is a prolate one, both above and below the para-ferroelectric phase transition temperature for the *b-c* and *a-c* planes, where as for the *a-b* plane, it is similar to a spheroid, inferring that the values of *a*- and *b*-axes thermal conductivities have close values, as expected, whereas the *c*-axis thermal conductivity is much smaller.

The difference between *b* and *c* axes thermal conductivities can be attributed to the orientation dependence of the intermolecular forces in the crystal. It is seen that the maximum thermal conduction occurs in the direction of predominant covalent bonding, which is along the *b*-axis, where as minimum thermal conduction occurs in a direction perpendicular to the chains of glycine molecules connected by hydrogen bonding. The nature of the temperature dependence is similar for all the three directions.

Anisotropy in thermal conduction can be explained as follows. In the structure of GPI, planes containing infinite chains of phosphite $H(HPO_3)_n^{n-}$ anions alternate with those built by the organic cations. These two types of layers are parallel to the crystallographic *b-c* plane, i.e. they are arranged alternatively in the *a*-direction. This layer arrangement corresponds to the direction of weak coupling in the crystal. Within the phosphite layers, $H(HPO_3)^-$ groups are mutually linked by hydrogen bonds forming infinite chains extending along the crystallographic *c*-axis. The inter-molecular and intra-molecular interactions, which are also hydrogen bonded, are stronger along the *b*-axis. Correspondingly, thermal conductivity is high in this direction. So, the orientation dependence of the strength of the hydrogen bonds in the system may be responsible for the observed anisotropy in thermal conductivity.

A recent report [15] on the thermal expansion coefficient α of GPI in the para electric phase shows a relatively large thermal expansion coefficient along the *c*-axis, corresponding to the weak hydrogen bonded direction, while the strong intermolecular forces along the *b*-direction supports its low value in this direction. This is good agreement with the ultrasonic investigation of elastic constants of GPI crystal, reporting similar anisotropy in elastic properties with the stiffness constant C_{22} (corresponding to b-axis) being high, while C_{11} and C_{33} are low, in accordance with the bonding scheme in the crystal lattice [12].

We can thus conclude by saying that the results on the temperature variation of thermal properties of GPI are in tune with other measurements [6,12] confirming the occurrence of an order-disorder type para-ferroelectric phase transition at 224K in GPI crystals.

3.5 Conclusions

The four thermal parameters of glycine phosphite single crystals have been evaluated by photopyroelectric measurements. Correlation between crystal structure of GPI explains the high values of elastic constant along crystallographic *b* direction and smaller values along the *a* and *c* axes. The variation of these thermal parmeters across the phase transition temperature reveals an order-disorder type paraelectric to ferroelectric phase transition at 224 K.

References

1. M. E. Lines and A. M. Glass, *Principles and Application of Ferroelectric and Related Materials* (Clarendon Press, Oxford, 1977).
2. J. A. Albers and A. Klopperpieper, H. J. Rother and S. Haussuhl, Ferroelectrics **81** (1988) 27.
3. M. T. Averbuch-Pouchot, Acta-Cryst.C **49** (1993) 815.
4. W. Schildkamp and J. Spiker, Z. kristallogr **168** (1984) 159.
5. S. Dacko, Z. Czapla, J. Baran and M. Drodz, Phys. Lett. A **223** (1996) 217.
6. J. Baran, G. Bator, R. Jakubar and M. Sledz, J. Phys: Condens. Matt. **8**, (1998) 10647.
7. G. E. Bacon and R. S. Pease, Proc. R. Soc. Lond. A **230** (1955) 359.
8. P. Morawski and A. Pawlowski, Phys. Stat. Solidi B **210** (1998) R5.
9. R. Tchuvinsky, R. Cach, Z. Czapla and S. Dacko, Phys. Stat. Solidi A **165** (1998) 309.
10. J. Tritt-Goc, N. Pislewski, L. Szczepanska, R. Goc, Solid State Commun. **108** (1998) 189.
11. P. Morawski, M. Gramza, J. Goslar, W. Hilezer, L. Sczepanska, S. H. Hoffmann, Ferroelectr. Lett. Sect. **23** (1998) 121.
12. A. Deepthy, H. L. Bhat, A. V. Alex and J. Philip, Phys. Rev. B **62** (2000) 8752.
13. C. Preethy Menon and J. Philip, Meas. Sci. and Technol. **11** (2000) 1744.
14. J. F. Nye, *Physical Properties of crystals* (Clarendon, Oxford, 1957).
15. B. Andriyevsky, Z. Czapla, M. Romanyuk and O. Myshchyshyn, Phys. Stat. Solidi A **177** (2000) 575.

16. J. Furtak, Z. Czapla, A. V. Kityk, Z. Naturforsch A: Phys. Sci. **52** (1997) 778.

CHAPTER 4

Thermal properties of Thiourea studied using photopyroelectric technique

4.1 Introduction

Structural phase transitions through incommensurate (INC) phase regions have been of great interest to condensed matter physicists. The ferroelectric crystals, which are known to exhibit incommensurate phase transitions, include ammonium fluroberrylate [1], potassium selenate [2], sodium nitrite [3], thiourea [4] etc. Thiourea, with the chemical formula $SC(NH_2)_2$ undergoes successive phase transitions at 169 K (T_1), 176 K (T_2), 180 K (T_3) and 202 K (T_4). Among the five phases (called I, II, III, IV and V) in the order of increasing temperature, two of them (I and III) are ferroelectric and a superlattice structure appears in the II, III and IV phases [5]. A good picture of the successive phase transitions in thiourea can be obtained from Table 4.1 as well as in Fig. (4.1). The crystal structure in the room temperature phase V above T_4 is orthorhombic and belongs to the space group $D_{2h}^{16} - Pbnm$ with four molecules per unit cell (Z = 4). The phase I below T_1 is a ferroelectric phase having spontaneous polarization along the b- axis, whose crystal structure is also orthorhombic and belongs to the space group $C_{2v}^{2} - Pb2_1m$ with four molecules per unit cell (Z = 4).

Table 4.1: Successive phases in $SC(NH_2)_2$

Transition temperature		T_1 169	T_2 176	T_3 180	T_4 202 (K)
Phase	*I*	*II*	*III*	*IV*	V
Space group	*Ferroelectric* $P_s//b$ C_{2v}^2-$Pb2_1m$ Commensurate		*Ferroelectric* $P_s//b$ Incommensurate		D_{2h}^{16}-Pbnm
Lattice constants	*a* *b* *c*		*a* *b* ~10*c* ⟷ ~8*c*		*a* = 5.52Å *b* = 7.66 Å *c* = 8.54 Å

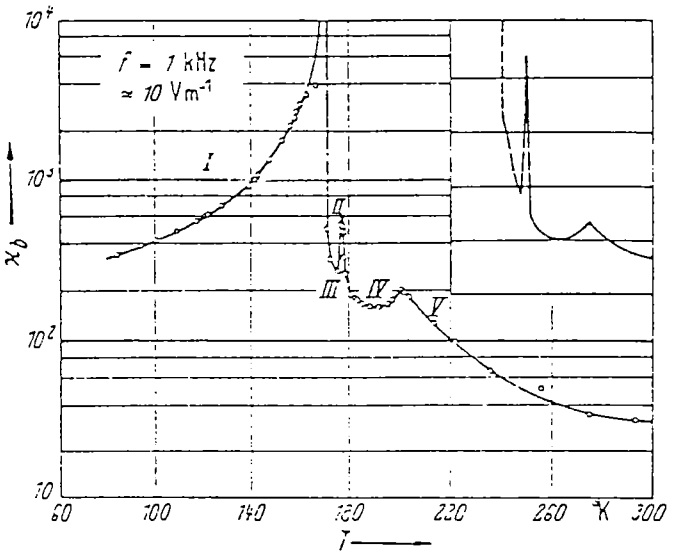

Fig. 4.1: Susceptibility vs temperature measured by means of a capacitance bridge for phases I to V of thiourea single crystal

In the three intermediate phases II, III and IV between T_1 and T_4, Shiozaki [6] observed the X-ray reflection and concluded that the crystal has an incommensurate structure. According to his analysis, just above T_4 the crystal has the superstructure with the period along the *c*-axis about eight times as large as that of phase IV. The period of the super structure increases as temperature decreases. So in the vicinity of T_1, the period is about ten times as large and at T_1, the crystal transforms to the ferroelectric phase I, where the period of the unit cell of the prototype is restored.

In the phase III region between T_2 and T_3, the crystal also shows weak ferroelectricity, but this weak ferroelectricity has been disregarded in most of the earlier works [7-10], and the phases II, III and IV are treated as if they were a single incommensurate phase. Thus the successive phase transitions of $SC(NH_2)_2$ can be regarded as a normal example of incommensurate successive phase transition sequence, that is to say, a transition from a prototype to an incommensurate phase and then a second transition from the incommensurate phase to the final commensurate phase.

A schematic projection of the (001) plane of the paraelectric phase V is shown in Fig. 4.2. The molecules are designated by solid lines that lie above than those designated by thin lines by *c*/2 [11]. In the *b*-direction, there are alternating sheets consisting of similar polar molecules having opposite '*average orientations*' as shown in Fig. 4.2 for the disordered phase (V) where the two systems correspond to each other by a symmetry element (*n*) which disappears in the low temperature phase (I). Consequently, the modulated phases can be regarded as two interacting sub lattices with proper polarization wave.

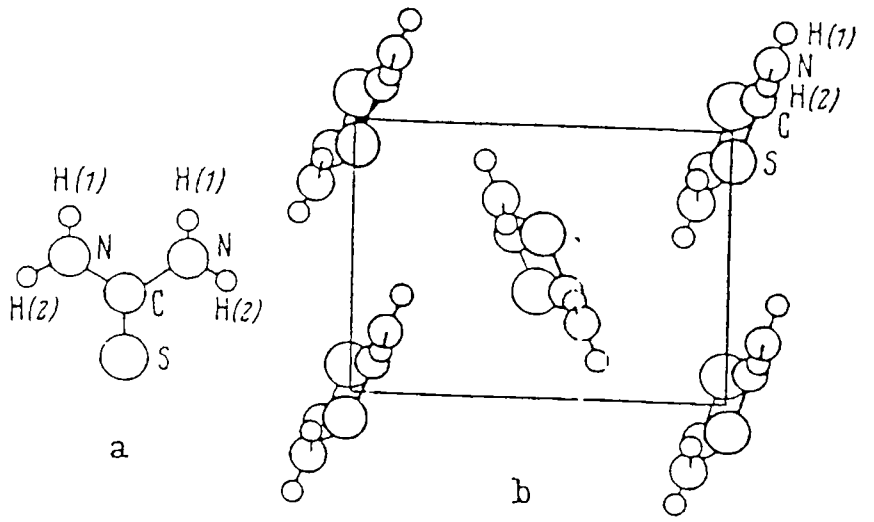

Fig. 4.2: Projection of the (001) plane of the paraelectric phase (V)

As for the transition mechanism of $SC(NH_2)_2$, Mc Kenzie [9, 10] reported his results of neutron diffraction studies. He found no low-lying and temperature sensitive phonon branch, and suggested that the mechanism was not of any displacive type. On the contray, Delehaigue *et al.* [12] Chapelle and Benoit [13] carried out the Raman scattering measurements of $SC(NH_2)_2$ and observed a soft mode whose frequency decreases as the transition temperature T_4 is approached from below, and concluded that the transition mechanism must be of some displacive type. Several questions remain unanswered regarding successive phase transitions exhibited by thiourea.

In order to throw more light on the discrepancies in the results already reported on thiourea and to understand the nature of anomaly in thermal parameters, we have measured thermal diffusivity (α), thermal effusivity (e), thermal conductivity (K) and heat capacity (c_p), during an incommensurate-commensurate

phase transition. We have employed the photopyroelectric technique to measure the above thermal parameters. Experimental details of the method are already given in Chapter 2 of this thesis. Measurements have been done along the three principal directions of thiourea and thermal anisotropy observed is discussed in detail. To the best of our knowledge, this is the first report of the measurement of thermal transport during incommensurate phase transitions in crystals.

Details of the sample preparation, measurement technique, results obtained and discussion of the results are given in the following sections.

4.2 Sample preparation

Single crystals of thiourea are grown by the slow evaporation method from methyl alcoholic solution at room temperature. Reagents used are equimolar solutions of thiourea [NH_2 CS NH_2] (AR grade) and methanol [CH_3 OH] (AR grade). Good quality crystals of sizes $\approx$ 30 x 25 x 25 cm^3 have been grown over a period of 3 weeks. Crystals obtained are colourless and transparent. The crystal axes are determined by measuring interfacial angles using a contact goniometer. The morphology of the thiourea single crystal has been generated and is shown in Fig. 4.3.

The so obtained crystals are cut with a slow speed diamond wheel saw such that they have faces perpendicular to the [100], [010] and [001] directions or the crystallographic *a*-, *b*- and *c*- axes respectively. The samples are carefully polished, initially with water and finally with alumina powder to get good surface finish. The samples prepared for the photopyroelectric measurements have a thickness of ~ 0.3 mm. The density of the sample is measured to be 1.406 g cm^{-3}. A very thin layer of

carbon black from a benzene flame has been carefully coated onto the illuminating surface of each sample to enhance its optical absorption.

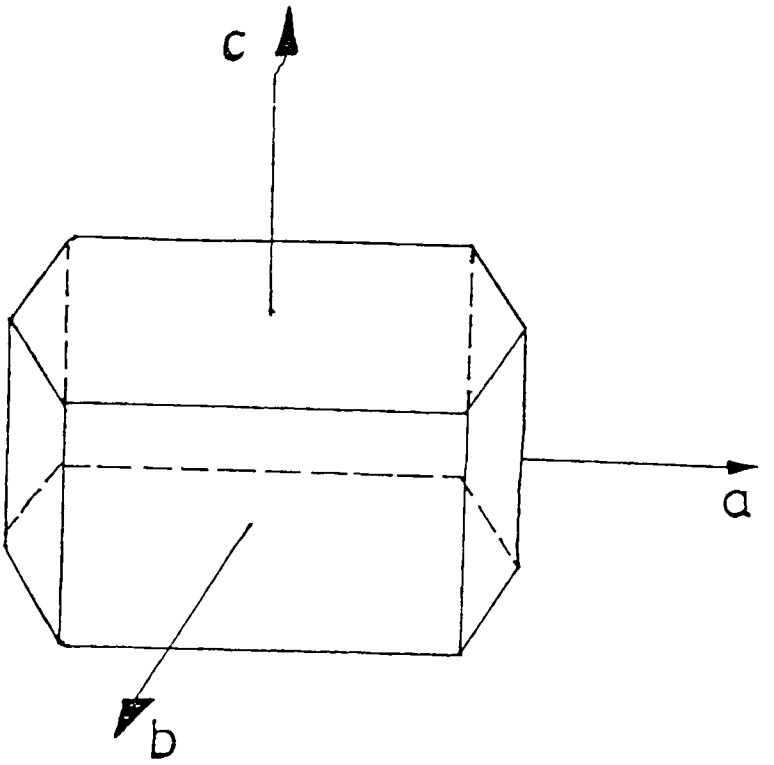

Fig. 4.3: Crystal morphology of single crystal of thiourea grown in the laboratory

4.3 Experimental details

An improved photopyroelectric technique (described in detail in Chapter 2) has been used to determine the thermal parameters of single crystals of thiourea. The necessary criterion that needs to be satisfied for such a measurement is that, the sample, the pyroelectric detector and the backing should be thermally thick during measurements. The sample is illuminated by an intensity-modulated beam of light, which gives rise to periodic temperature variations by optical absorption. The

thermal waves so generated propagate through the sample and are detected by the pyroelectric detector.

A He-Cd laser of (wavelength λ = 442nm (KIMMON)) of output power 120 mW has been used as the optical heating source. Light from the laser is intensity-modulated using a mechanical chopper (SR 540). A polyvinylidene difluoride (PVDF) film of thickness 28μm is used as the pyroelectric detector. The sample is attached to the pyroelectric detector by means of a thermally thin layer of a compound whose contribution to the signal is negligible. The signal output is measured using a lock-in amplifier (SR 830). The frequency of modulation of the light is kept above 30Hz to ensure that the detector, the sample and the backing medium are thermally thick during measurements. The thermal thickness of the thiourea samples in these experiments has been verified by plotting the PPE amplitude and phase with frequency at different temperatures between room temperature and 180 K. The variations along three principal directions are given in figures 4.4(a), 4.4(b), 4.5(a), 4.5(b), 4.6(a) and 4.6(b) respectively.

Measurements have been carried out illuminating the three cut sample faces so that the propagation of the thermal wave is along one of the symmetry axes. Measurement of the PPE signal phase and amplitude enable one to determine the thermal diffusivity (α) and thermal effusivity (e) [13]. From the measured values of α and e, thermal conductivity (K) and heat capacity (c_p) of the sample are determined using the relations

$$K_s(T) = e_s(T)\sqrt{\alpha_s(T)} \tag{4.1}$$

$$c_{ps}(T) = \frac{e_s(T)}{\rho_s(T)\sqrt{\alpha_s(T)}} \tag{4.2}$$

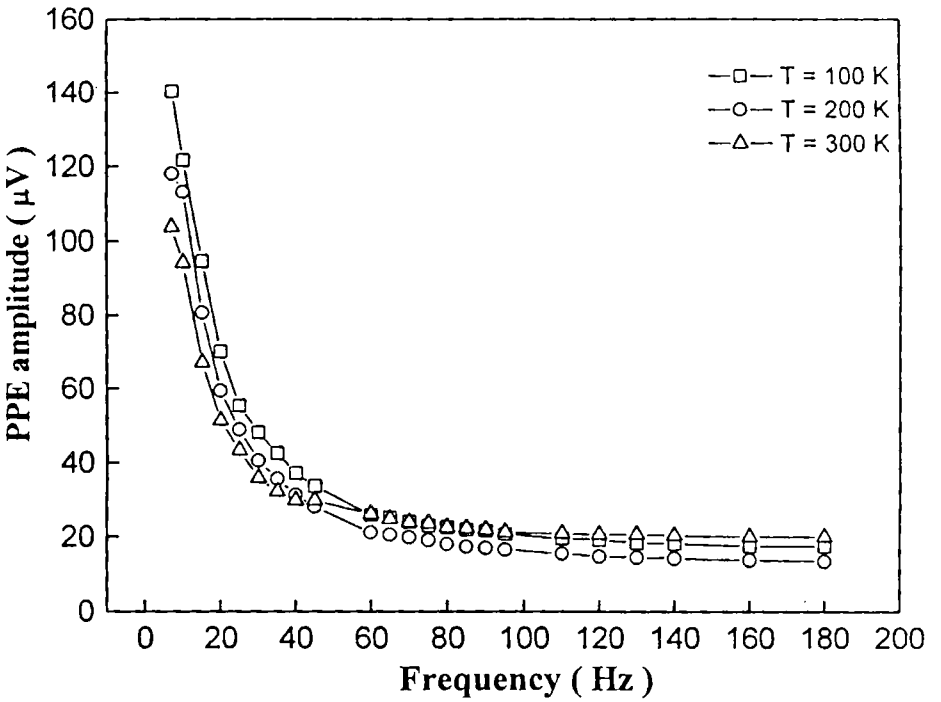

Fig. 4.4(a): Variation of PPE amplitude with frequency of thiourea along *a*-axis

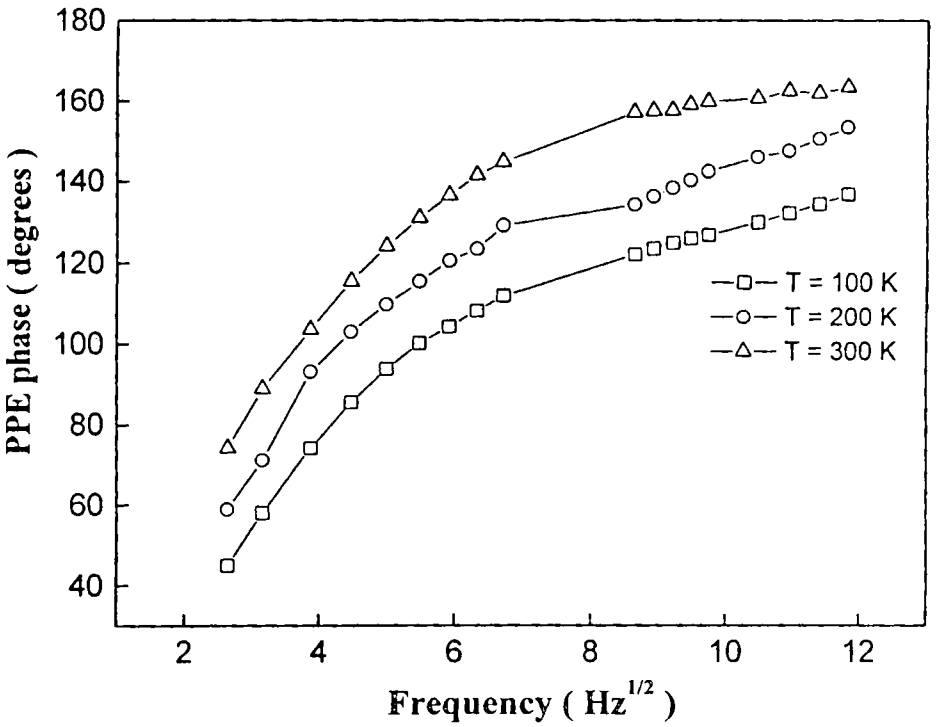

Fig. 4.4(b): Variation of PPE phase with frequency of thiourea along *a*-axis

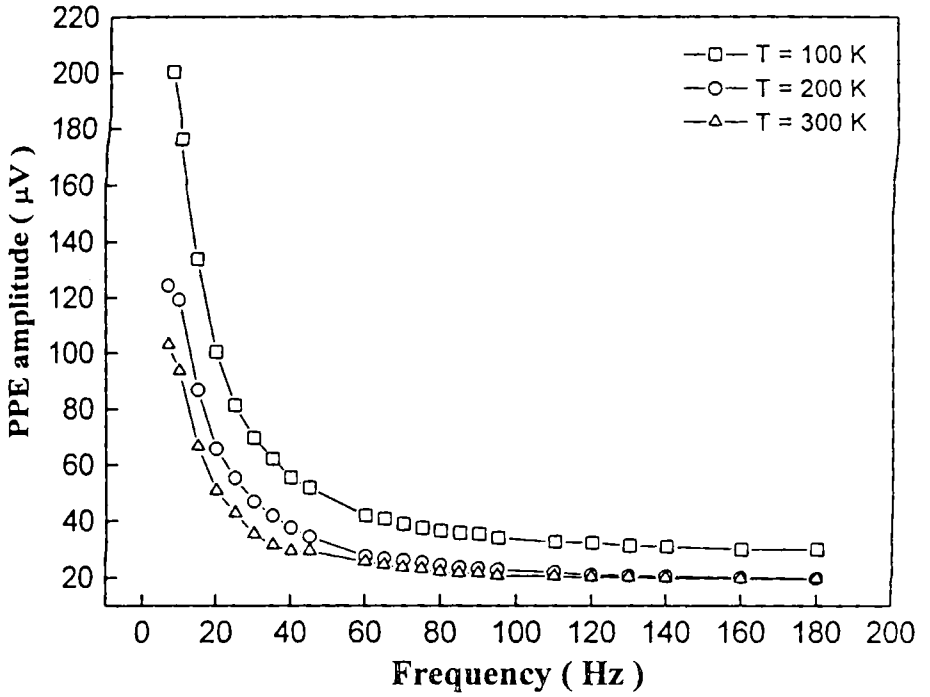

Fig. 4.5(a): Variation of PPE amplitude with frequency of thiourea along *b*-axis

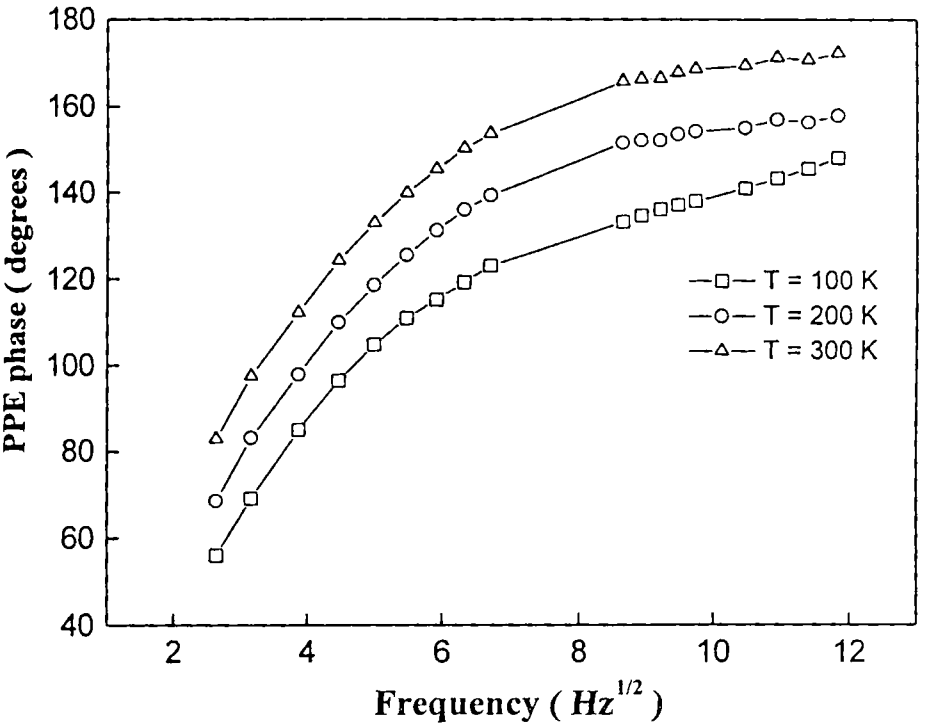

Fig. 4.5(b): Variation of PPE phase with frequency of thiourea along *b*-axis

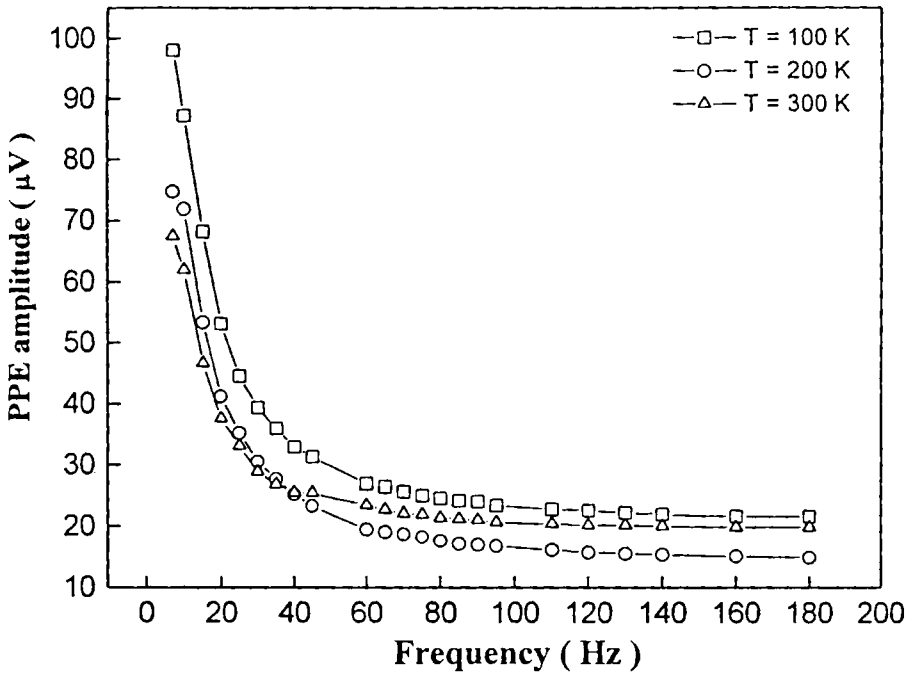

Fig. 4.6(a): Variation of PPE amplitude with frequency of thiourea along *c*-axis

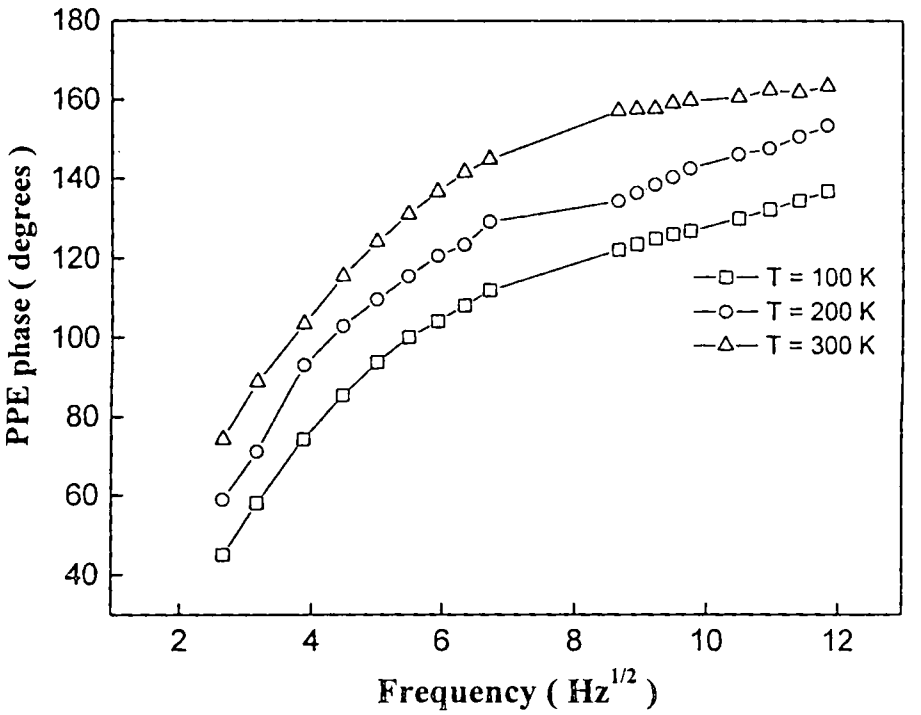

Fig. 4.6(b): Variation of PPE phase with frequency of thiourea along *c*-axis

The measurements as a function of temperature have been made at a heating rate of approximately 0.5 Kmin $^{-1}$ and data collected in every 1K interval normally and at closer intervals near the transition point. The temperature is measured with a platinum sensor placed close to the sample inside the chamber. Calibration of the experimental set up has been done prior to carry out the measurements, as described in detail in Chapter 2 of this thesis.

4.4 Results and discussion

Figures 4.7(a), 4.7(b), 4.8(a), 4.8(b), 4. 9(a) and 4.9(b) exhibit the variations of PPE amplitude and phase along the three principal directions of thiourea single crystal. It is seen that both amplitude and phase clearly reflect the three successive phase transitions in thiourea. The maximum anomaly is at T_1 = 169 K, the temperature corresponding to which transition to an incommensurate phase takes place, for all the three principal directions. The maximum variation is seen along the *b*-direction, the direction in which the crystal possesses spontaneous polarization.

Fig. 4.10, 4.11 and 4.12 show the variation of thermal diffusivity and thermal effusivity with temperature along the *a*-, *b*- and *c*- axis of thiourea single crystal. As seen in the figures, thermal diffusivity shows a decrease with temperature, with distinct minima at the three phase transition points at T_1 = 169 K, T_3 = 176 K and T_4 = 202 K, in agreement with the already reported values of transition temperatures. Thermal effusivity exhibits an opposite behaviour. It increases with temperature with sharp peaks occurring at the transition temperatures. Taking into account the various limitations of the measurements, the overall uncertainties in the value of α and *e* are estimated to be ±1%.

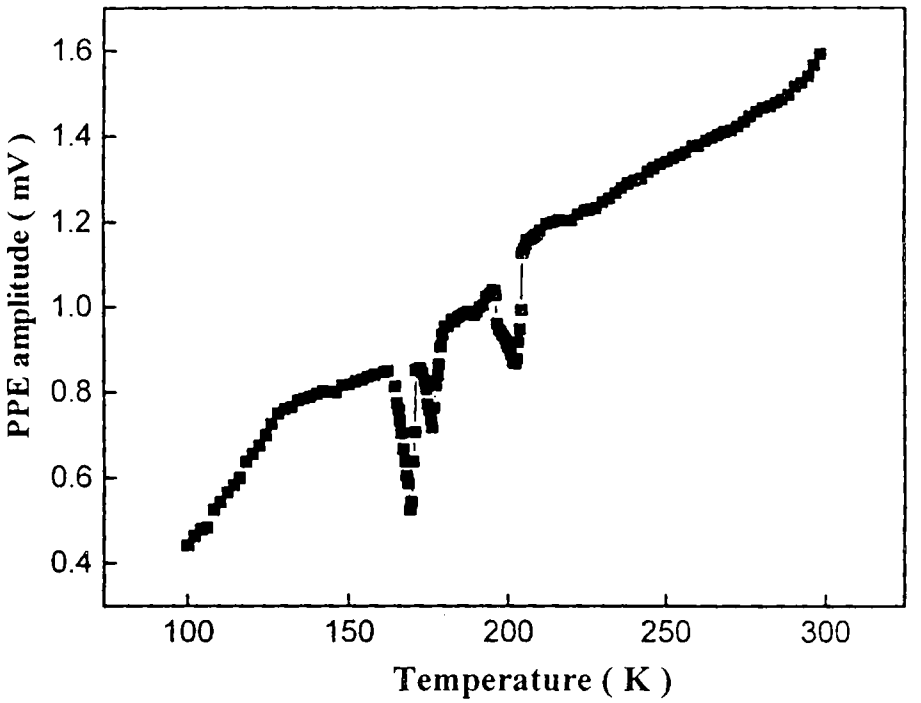

Fig. 4.7(a): Variation of PPE amplitude with temperature along the *a*-axis of thiourea

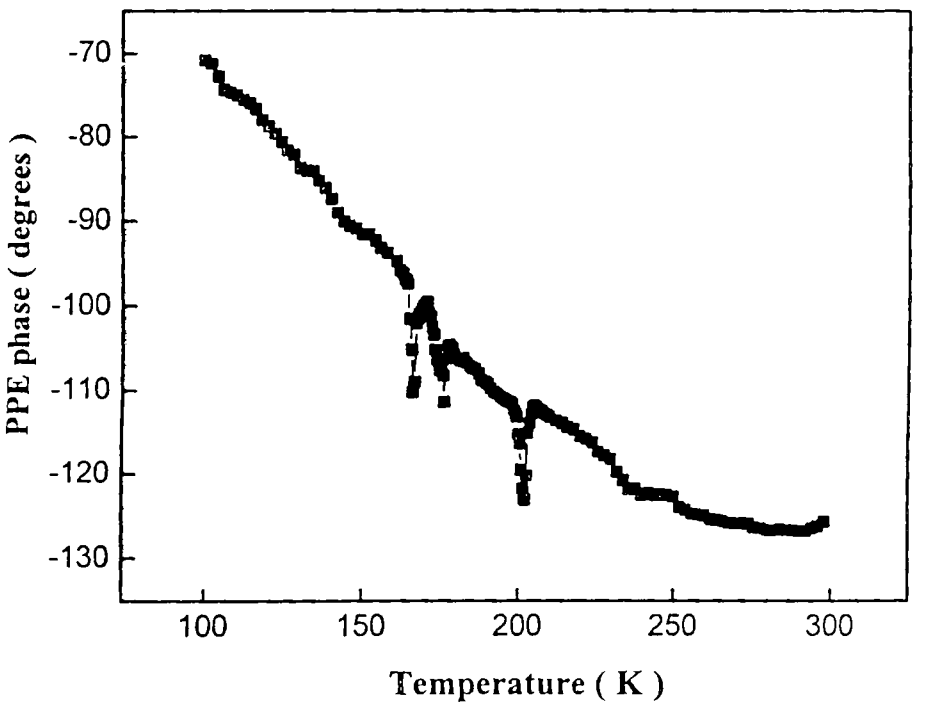

Fig. 4.7(b): Variation of PPE phase with temperature along the *a*-axis of thiourea

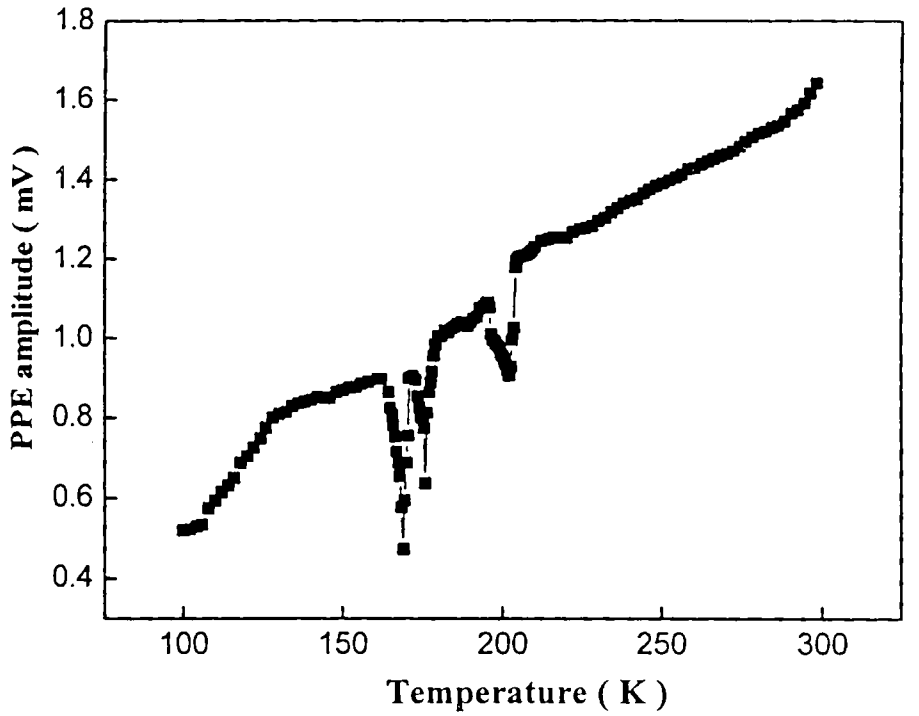

Fig. 4.8(a): Variation of PPE amplitude with temperature along the *b*-axis of thiourea

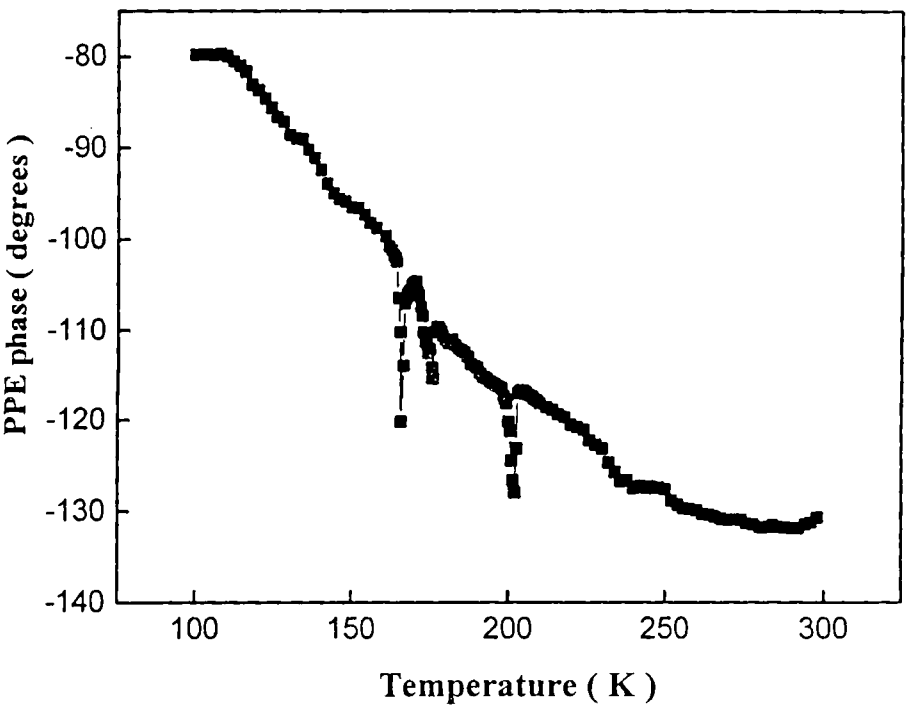

Fig. 4.8(b): Variation of PPE phase with temperature along the *b*-axis of thiourea

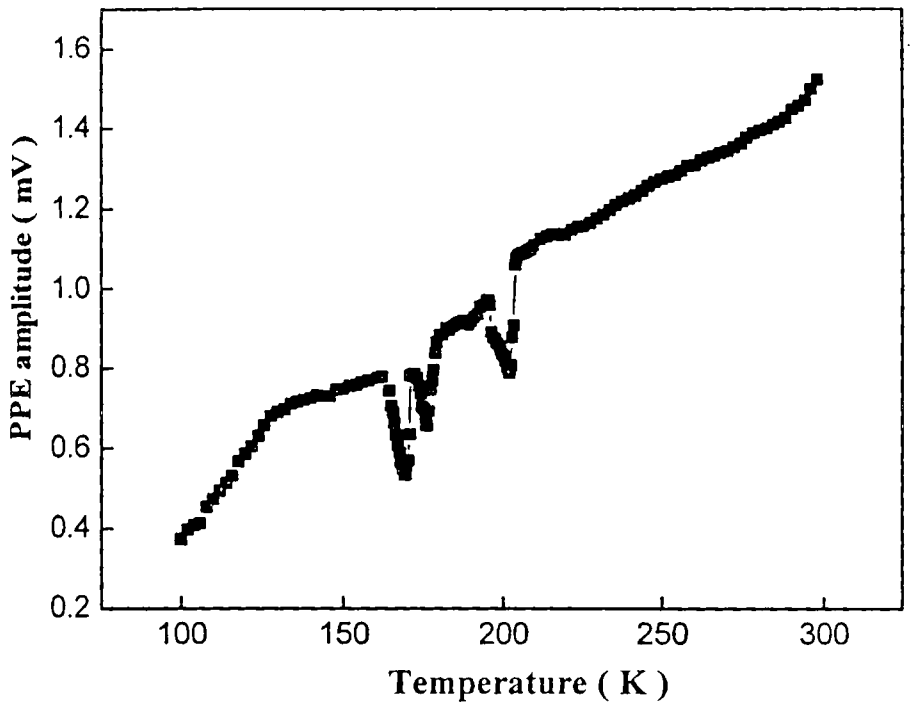

Fig. 4.9(a): Variation of PPE amplitude with temperature along the *c*-axis of thiourea

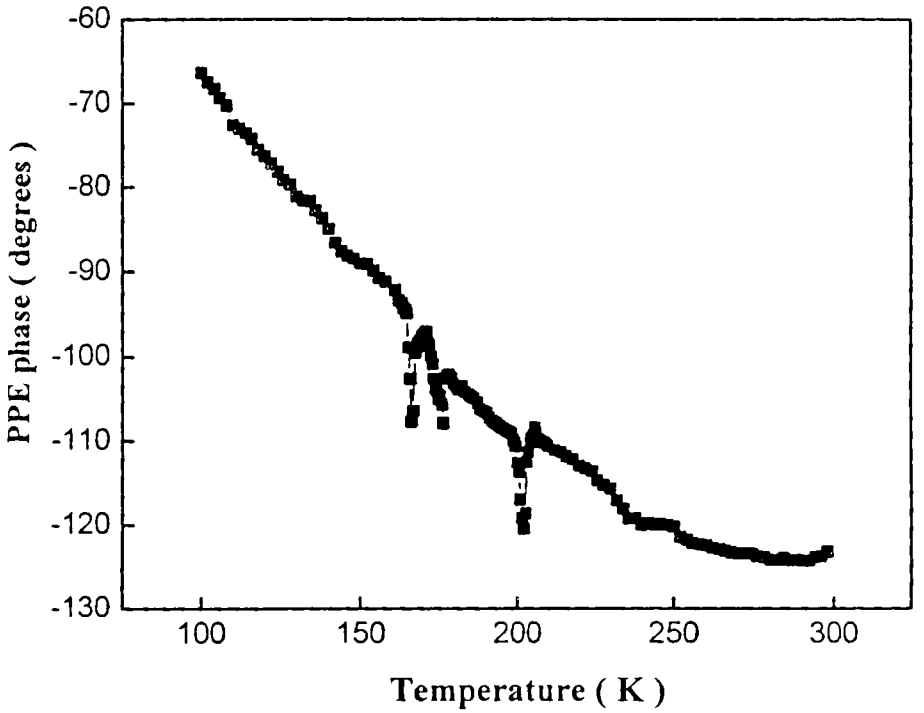

Fig. 4.9(b): Variation of PPE phase with temperature along the *c*-axis of thiourea

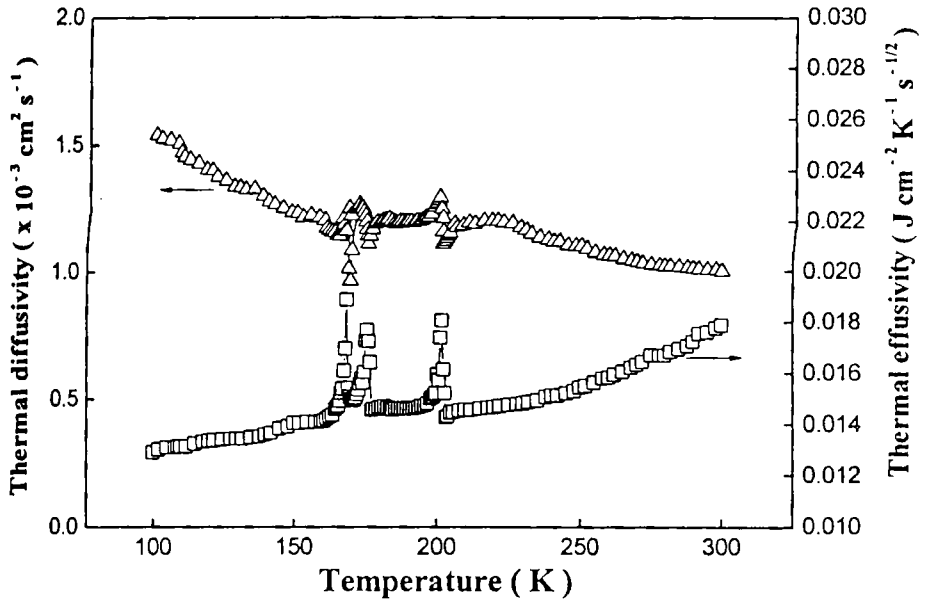

Fig. 4.10: Temperature variation of thermal diffusivity and thermal effusivity along *a*-axis of thiourea single crystal

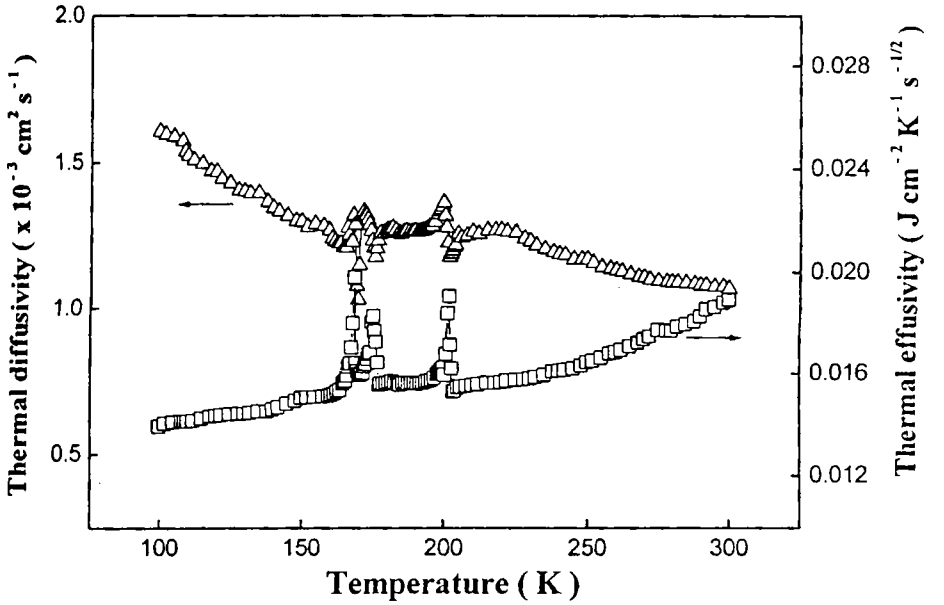

Fig. 4.11: Temperature variation of thermal diffusivity and thermal effusivity along *b*-axis of thiourea single crystal

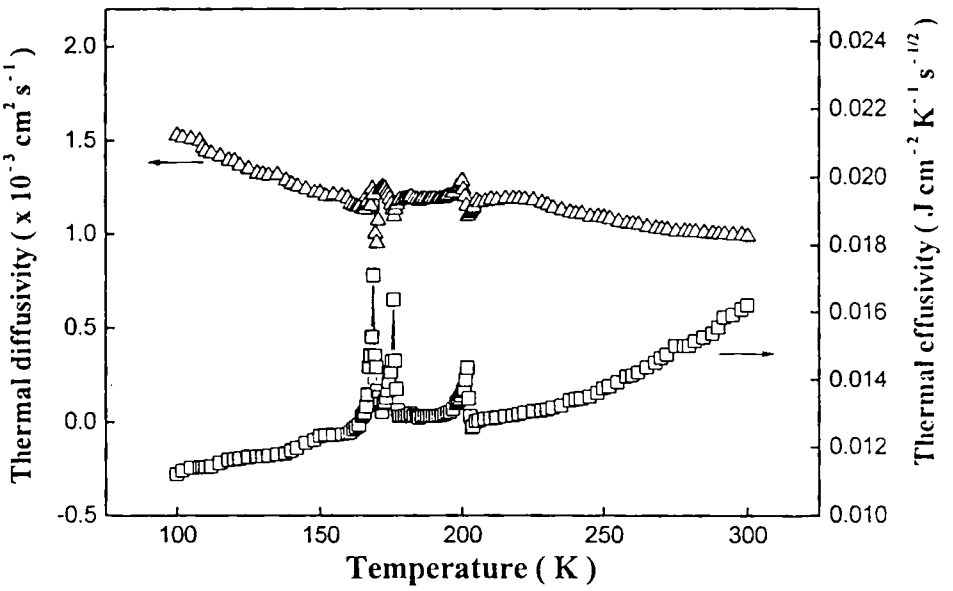

Fig. 4.12: Variation of thermal diffusivity and thermal effusivity along c-axis of thiourea single crystal

Fig. 4.13 shows the variation of heat capacity of thiourea with temperature. As seen in figure, the three transitions get clearly reflected in the temperature variation of heat capacity as clear anomalies at the transition points. These heat capacity results (in absolute numbers) agree with the result reported by earlier workers [14]. As we can see, there is no direction dependence for heat capacity.

Fig. 4.14 shows the temperature variation of thermal conductivity along the three symmetry axes (*a*, *b* and *c*) of thiourea. The thermal conductivity exhibits significant anisotropy as is evident from Fig. 4.14. The three transitions get reflected in the thermal conductivity variations. The maximum anomaly is seen along the *b*-axis. A study of anisotropy in thermal conductivity enables one to draw important conclusions regarding the nature of phase transitions and the phenomena associated with it.

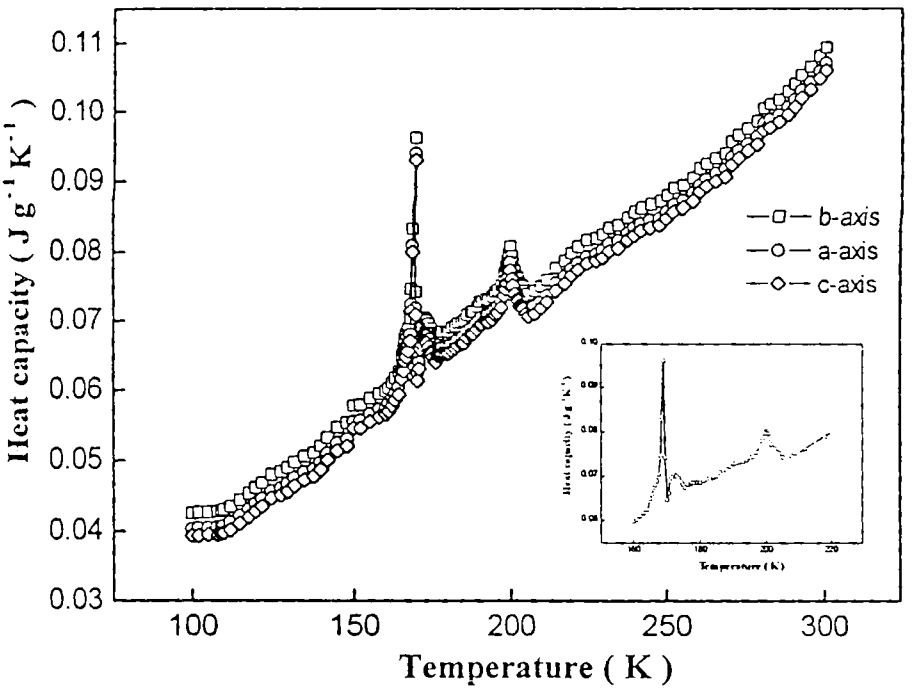

Fig. 4. 13: Temperature variation of heat capacity along the three principal directions of thiourea single crystal

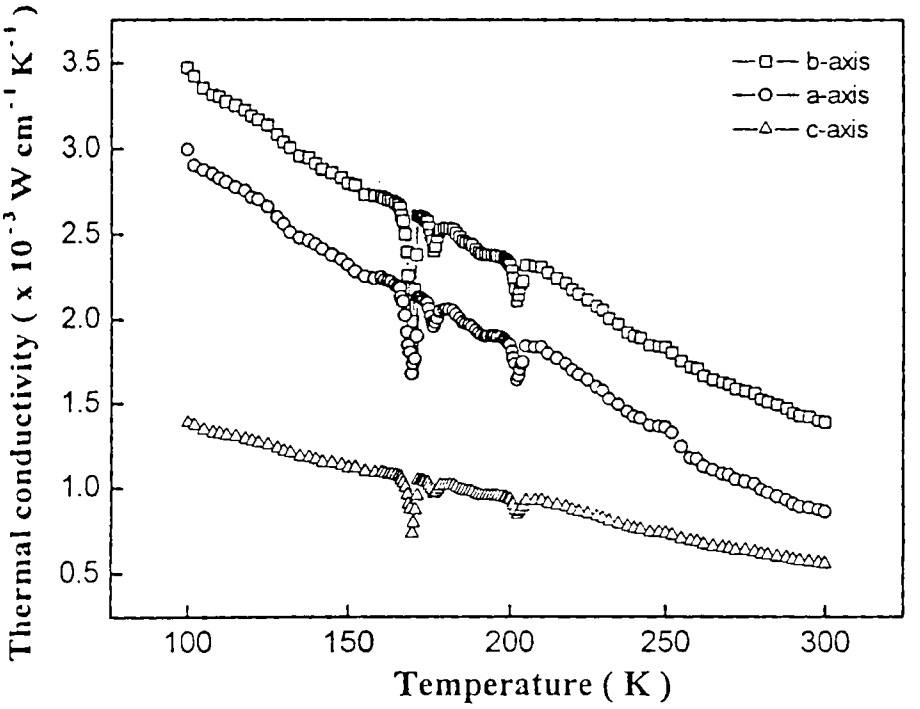

Fig. 4.14: temperature variation of thermal conductivity along three principal directions of thiourea single crystal

With such an intension, we have plotted the thermal conductivity ellipsoids for the *b-c*, *a-c* and *a-b* planes. As described in detail, in Chapter 3, the characteristic representation of quadric for thermal conductivity is given by [16]

$$K_{ij}\,\tilde{n}_i\,\tilde{n}_j = 1 \qquad (4.3)$$

where K_{ij} are the thermal conductivity tensor and $\tilde{n}$ are the direction cosines.

When we refer to the principal axes, we have

$$K_1 n_1^2 + K_2 n_2^2 + K_3 n_3^2 \;=\; 1 \qquad (4.4)$$

K_1, K_2 and K_3 are always positive and hence this represents the thermal conductivity ellipsoid.

Fig. 4.15(a), 4.15(b) and 4.15(c) show the projection of the thermal conductivity quadric lying in the *a-b*, *a-c* and *b-c* planes when viewed along the *c*-, *b*- and *a*- axis of the crystal respectively. The thermal conductivity ellipsoid is a prolate one both above and below the incommensurate-commensurate phase transition temperature for the *a-c* and *b-c* planes, whereas for the *a-b* plane it is closer to a spheroid indicating that the values of *a*- and *b*- axis thermal conductivities have closer values as expected, whereas the *c*-axis thermal conductivity is much smaller.

The difference between *b*- and *c*- axes thermal conductivities can be attributed to the orientation dependence of phonon modes present in the crystal. The maximum thermal conduction occurs in the direction of predominant covalent bonding, which is along the *b*-axis. The nature of the temperature dependence is similar for all the three directions.

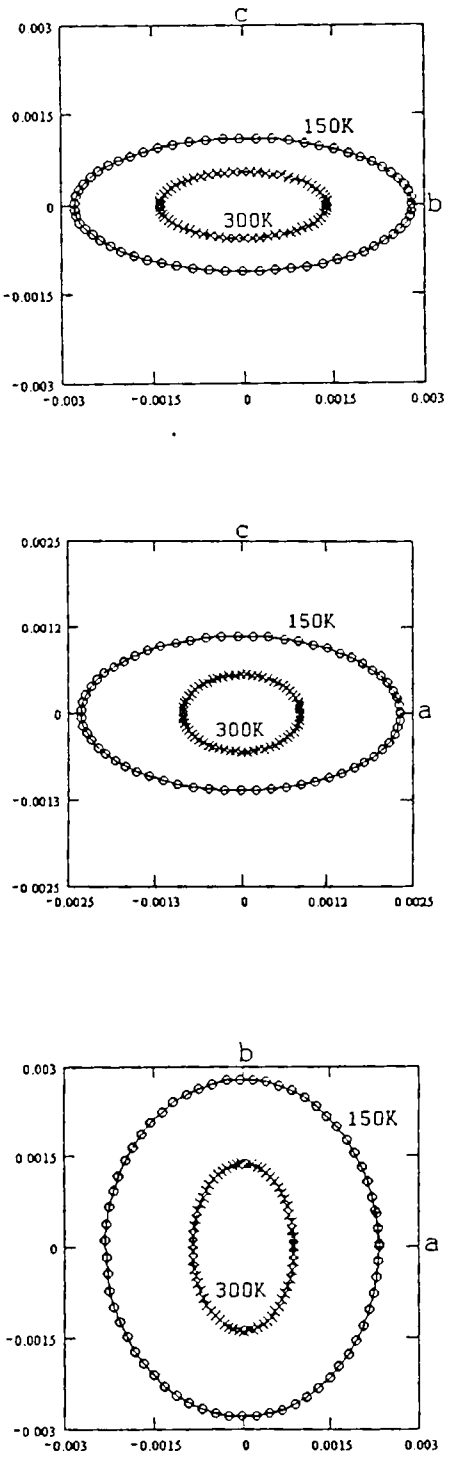

Fig. 4.15: Projection of the thermal conductivity quadric lying in the *b*-*c*, *a*-*c* and *a*-*b* planes when viewed along the *a*-, *b*- and *c*- axis of the crystal respectively

4.5 Conclusions

Thermal conductivity anisotropy of single crystals of thiourea has been investigated employing photopyroelectric technique. It is seen that the three successive phase transitions at T_1 = 169 K, T_2 = 176 K and T_4 = 202 K get reflected clearly in the thermal parameters as distinct anomalies. Maximum variation in thermal properties is along the *b*-axis, the direction of spontaneous polarization. The anisotropy in thermal conductivity can be attributed to the orientation dependence of phonon modes present in the crystal.

References

1. M. Iizumi and K. geis, Solid State Commun. **22** (1977) 37.
2. M. Iizumi, J. D. Axe, G. Shirane and K. Shimaoka, Phys. Rev. B **15** (1977) 4392.
3. Y. Yamada, I. Shibuya and S. Hoshino, J. Phys. Soc. Jpn. **18** (1963) 1594.
4. G. J. Goldsmith and J. G. White, J. Chem. Phys. **31** (1959) 1175.
5. M. M. Elcombe and J. C. Tayler, Acta. Cryst. A **24** (1968) 410.
6. Y. Shiozaki, Ferroelectrics **2** (1971) 245.
7. M. Wada, A. Sawada, Y. Ishibashi and Y. Takagi, J. Phys. Soc. Jpn **45** (1978) 1905.
8. A. H. Moudden, F. Denoyer, J. P. Benoit and W. Fitzgerald, Solid State Commun. **28** (1978) 575.
9. D.R. Mc Kenzie, J. Phys. C: Solid State Phys. **8** (1975) 2003.
10. D.R. Mc Kenzie, J. Phys. C: Solid State Phys. **8** (1975) 1619.
11. B. K. Vanishetein and V. F. Dvoryankin, Soviet Phys. **6** (1962) 742.
12. A.Delahaigue, B. Khelifa and P. Jouve, Phys. Stat. Solidi (b) **72** (1975) 585.
13. J. P. Chapelle and J. P. Benoit, J. Phys. C: Solid State Phys. **10** (1977) 145.
14. C. Preethy Menon and J. Philip, Meas. Sci Technol. **11** (2000) 1744.
15. *Landolt – Bornstein New Series*, Vol 3, edited by K. H. Hellwege and A. M. Hellwege (Springer-Verlag, New York, 1969) 477.
16. J. F. Nye, *Physical properties of crystals* (Clarendon, Oxford, 1957).

CHAPTER 5

Thermal properties of LCMO system exhibiting M-I transition

5.1 Introduction

The mixed valence perovskite manganese oxides $R_{1-x}A_xMnO_3$ (where A = La, Nd, Pr and A = Ca, Sr, Ba or Pb) have been the materials of intense experimental and theoretical studies over the past few years [1, 2]. The materials show colossal magnetoresistance (CMR) in samples with $0.2 < x < 0.5$. In such a doping region, the resistivity exhibits a peak at a temperature $T = T_p$, the metal-insulator transition temperature. The system is metallic with $\frac{d\rho}{dT} > 0$ below T_p and insulating $\frac{d\rho}{dT} < 0$ above T_p. Under an external magnetic field B, ρ is strongly suppressed and the peak position T_p shifts to a higher temperature. Thus, a huge magnetoresistance may be produced around T_p to give rise to the CMR phenomenon. It is widely believed that the CMR behaviour in these mixed valence oxides is closely related to their magnetic properties. This is supported by the fact that T_p is very close to the Curie temperature T_c, the transition temperatures from the ferromagnetic to the paramagnetic phase.

Despite intensive investigations on the CMR phenomenon, a number of questions still remain unanswered about the nature of the metal-insulator (M-I) transition. The manganese oxides are usually modeled by the double exchange

Hamiltonian [3-5] which describes the exchange of electrons between neighbouring Mn^{3+} and Mn^{4+} ions with strong on-site Hund's coupling. As pointed out by Mills *et al.* [6, 7], however the double exchange model alone doesn't explain the sharp change in the resistivity near T_c and associated CMR phenomenon. Based on the strong electron-phonon coupling in these materials, Mills *et al.* [6, 7] proposed that the M-I transition involves a cross over from a high-T polaron dominated magnetically disordered regime to a low-T metallic magnetically ordered regime. On the other hand, some authors have argued the possible importance of the quantum localization effects caused persumably by the strong magnetic disorder fluctuations in the system around and above the magnetic transition. They proposed that the M-I transition in CMR materials is the Anderson localization transition - a quantum phase transition [8-11] driven by magnetic disorder. So it will be interesting to examine the consequences of the Anderson localization theory against experimental results obtained on these types of samples.

In this chapter, we give the photopyroelectric measurements of thermal parameters, namely thermal diffusivity (α), thermal effusivity (e), thermal conductivity (K) and heat capacity (c_p) of $La_{0.7}Ca_{0.3}MnO_3$.and $La_{0.8}Ca_{0.2}MnO_3$ samples and analyze the results to compare with the scaling behaviour expected from an Anderson localization transition. Details of sample preparation, experimental details, results obtained and a discussion of the results are outlined in the following sections.

5.2 Sample preparation

$La_{0.7}ca_{0.3}MnO_3$ and $La_{0.8}Ca_{0.2}MnO_3$ samples were made from the stoichiometric mixtures of La_2O_3, $CaCO_3$ and $MnCO_3$ by the ceramic method [12, 13]. The mixture was initially heated at 950°C for decarbonation and then at 1000°C in air for 72 hours with six intermediate grindings. The resulting powder was pressed into pellets and sintered in air at 1000°C for 24 hours. The so prepared samples have been cut and polished to the required thickness. The thickness of the samples for the present measurements is about 0.5mm.

5.3 Experimental details

The thermal parameters, thermal diffusivity (α), thermal effusivity (e), thermal conductivity (K) and heat capacity (c_p) of $La_{0.7}Ca_{0.3}MnO_3$ and $La_{0.8}Ca_{0.2}Mno_3$ are determined employing an improved photopyroelectric technique, described in detail in Chapter 2. In this measurement, a thermally thick pyroelectric detector is attached to one side of the sample, which is also thermally thick and the combination is mounted on a thermally thick backing medium. Intensity modulated light from a 120mW He-Cd laser (KIMMON) of wavelength λ = 442 nm has been used as the optical heating source. Polyvinylidene difluoride (PVDF) film of thickness 28 μm, both sides coated with Ni-Cr film is used as the pyroelectric detector. The thermal waves so generated propagate through the sample and are detected by the pyroelectric detector. The pyroelectric detector is supported on a copper backing which is thermally thick. The sample-detector-backing assembly combination has been enclosed in a chamber whose temperature can be varied and controlled as desired. The signal output is measured using a lock in amplifier (SR 830). The

frequency of modulation of the light is kept above 30Hz to ensure that the detector, the sample and the backing medium are thermally thick during measurements. The thermal thickness of the two samples in this experiment has been verified by plotting the PPE amplitude and phase with frequency at different temperatures between room temperature and 180 K and are shown in figures 5.1(a), 5.2(b), 5.2(a) and 5.2(b).

Measurement of the PPE signal phase and amplitude enable one to determine the thermal diffusivity $\alpha = K/\rho c_p$, ρ being the density and effusivity $e = (K\rho c_p)^{1/2}$ respectively [14]. From the values of thermal diffusivity and effusivity, thermal conductivity and heat capacity are determined using the relations,

$$K_s(T) = e_s(T)\sqrt{\alpha_s(T)} \tag{5.1}$$

and

$$c_{ps}(T) = \frac{e_s(T)}{\rho_s(T)\sqrt{\alpha_s(T)}} \tag{5.2}$$

Densities of the samples are determined using Archimedes principle. A careful calibration of the experimental setup and procedure has been done prior to carry out the measurements, as described in detail in Chapter 2 of the thesis. The measurements as a function of temperature have been made at a heating rate of approximately 0.5 K/min and data is collected in every 1K interval normally and at closer intervals near the transition points. The temperature is measured using a platinum sensor placed close to the sample inside the chamber.

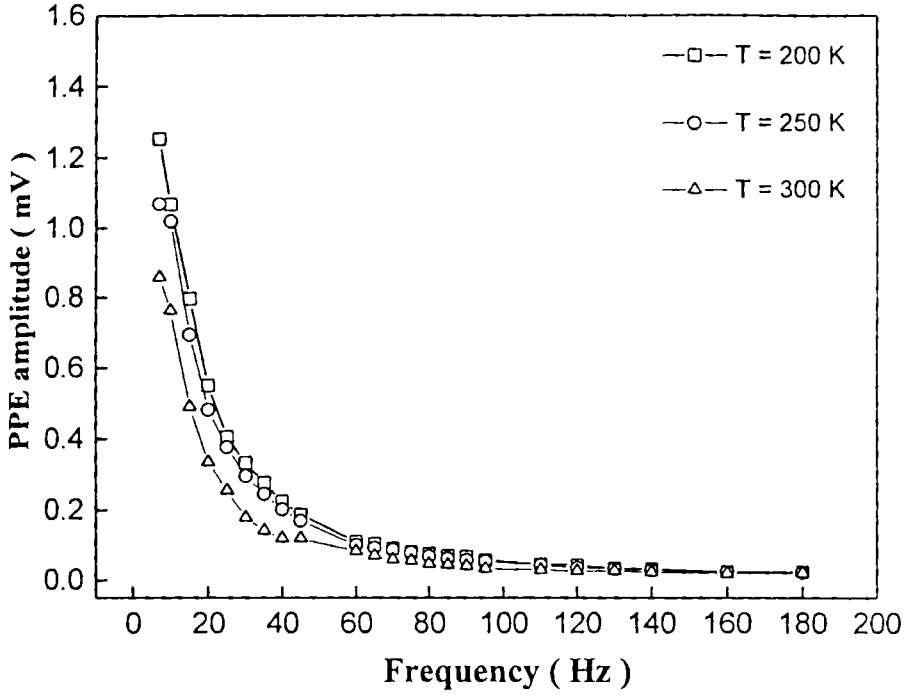

Fig. 5.1(a): Frequency dependence of PPE amplitude of $La_{0.7}Ca_{0.3}MnO_3$ sample at three different temperatures

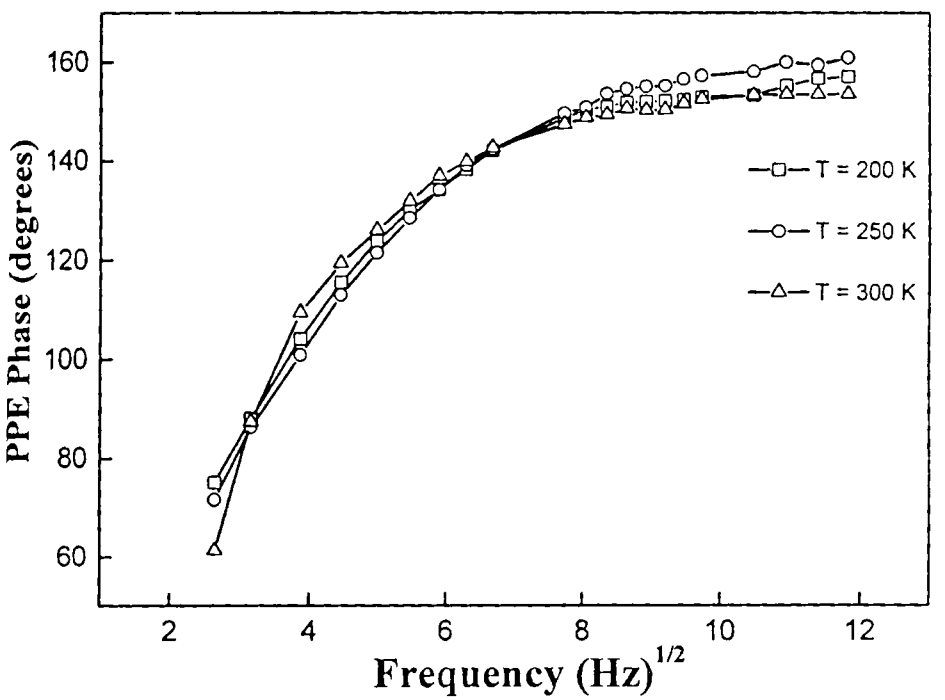

Fig. 5.1(b): Frequency dependence of PPE phase of $La_{0.7}Ca_{0.3}MnO_3$ sample at three different temperatures

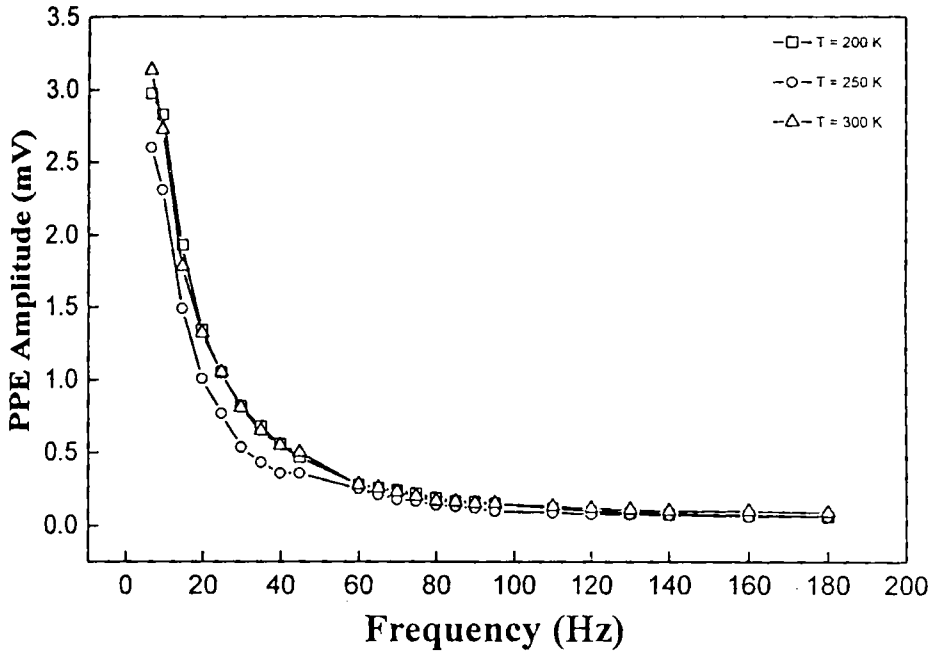

Fig. 5.2(a): Frequency dependence of PPE amplitude of $La_{0.8}Ca_{0.2}MnO_3$ sample at three different temperatures

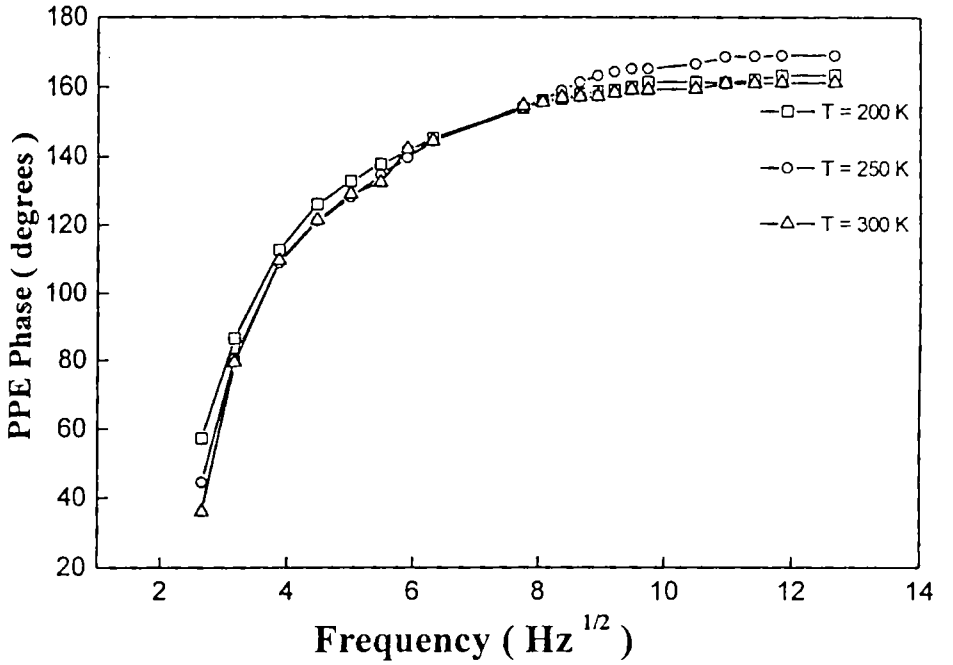

Fig. 5.2(b): Frequency dependence of PPE phase of $La_{0.8}Ca_{0.2}MnO_3$ sample at three different temperatures

5.4 Results

Figures 5.3(a) and 5.3(b) give the temperature variations of PPE amplitude and phase of the $La_{0.7}Ca_{0.3}MnO_3$ sample. The PPE amplitude decreases, reaches a minimum at T=238K, corresponding to the M-I transition temperature and then steadily increases with temperature. The PPE phase increases steadily and at the metal-insulator transition temperature, it exhibits a step-like behaviour and thereafter increases up to the room temperature. So both PPE amplitude and phase exhibit a clear anomaly at T = 238K, the M-I transition temperature.

Fig. 5.4 shows the variation of thermal diffusivity and thermal effusivity of $La_{0.7}Ca_{0.3}MnO_3$ as a function of temperature. Thermal diffusivity decreases with temperature, exhibits a step-like increase at the M-I transition temperature and thereafter decreases gradually. Thermal effusivity increases gradually up to the M-I transition temperature and then increases rapidly with temperature. At the transition point there is a step-like decrease and then it slowly increases with temperature. Fig. 5.5 shows the variation of thermal conductivity and heat capacity of $La_{0.7}Ca_{0.3}MnO_3$ with temperature. Thermal conductivity decreases with temperature and shows a minimum at T = 238K and thereafter increases steadily with temperature. The specific heat capacity variation with temperature is exactly the opposite, with a peak exhibited at the M-I transition temperature.

Fig. 5.6(a) and 5.6(b) show the variation of PPE amplitude and phase of $La_{0.8}Ca_{0.2}MnO_3$ sample. The PPE amplitude decreases, as in the previous sample, showing a minimum at T = 218K, which corresponds to its metal-insulator transition temperature and thereafter increases steadily. The PPE phase exhibits behaviour similar to $La_{0.7}Ca_{0.3}MnO_3$. Both PPE amplitude and phase variations with

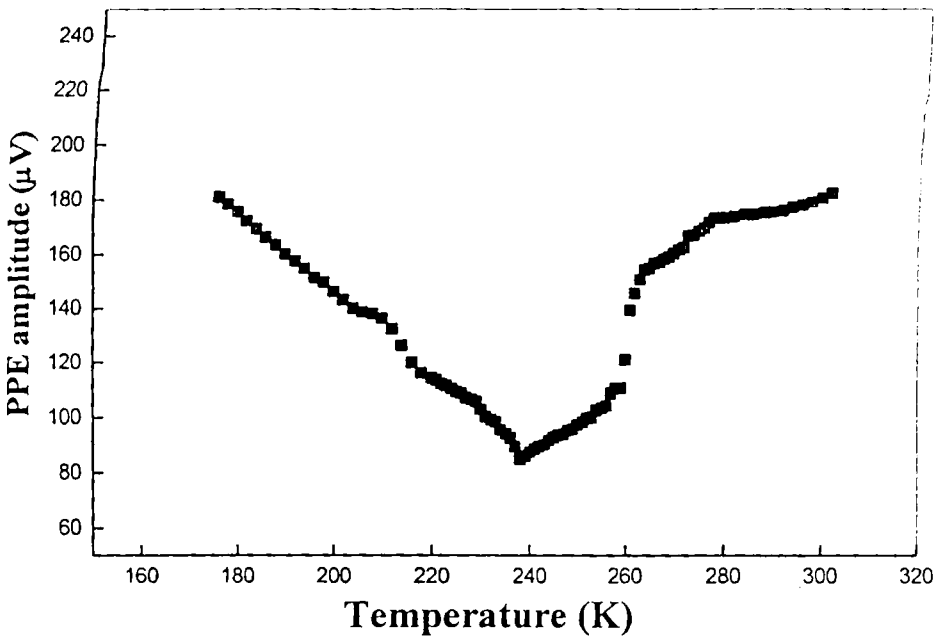

Fig. 5.3(a): Variation of PPE amplitude with temperature of $La_{0.7}Ca_{0.3}MnO_3$ sample

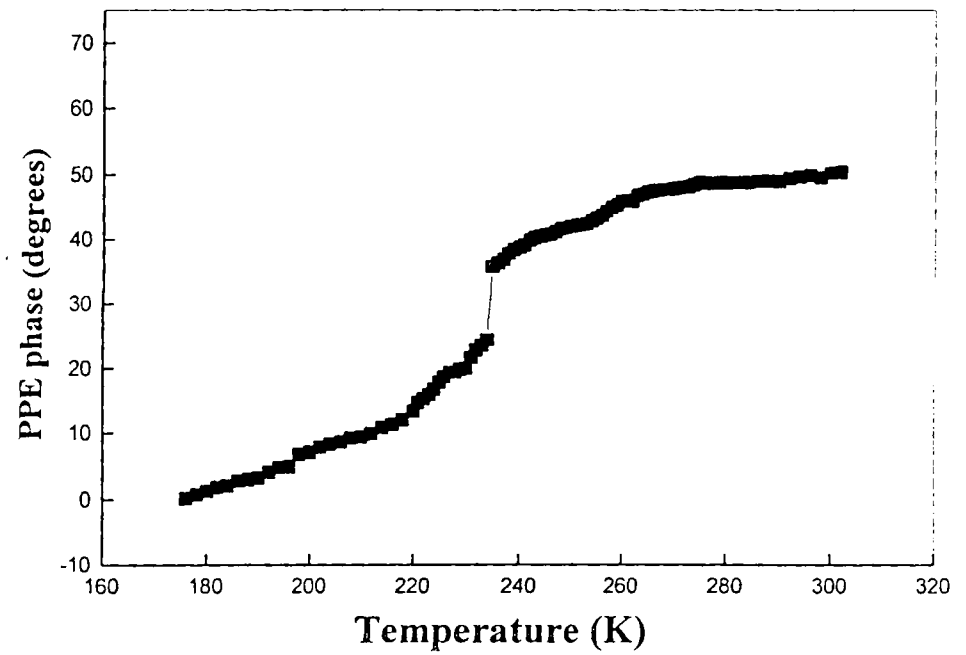

Fig. 5.3(b): Variation of PPE phase with temperature of $La_{0.7}Ca_{0.3}MnO_3$ sample

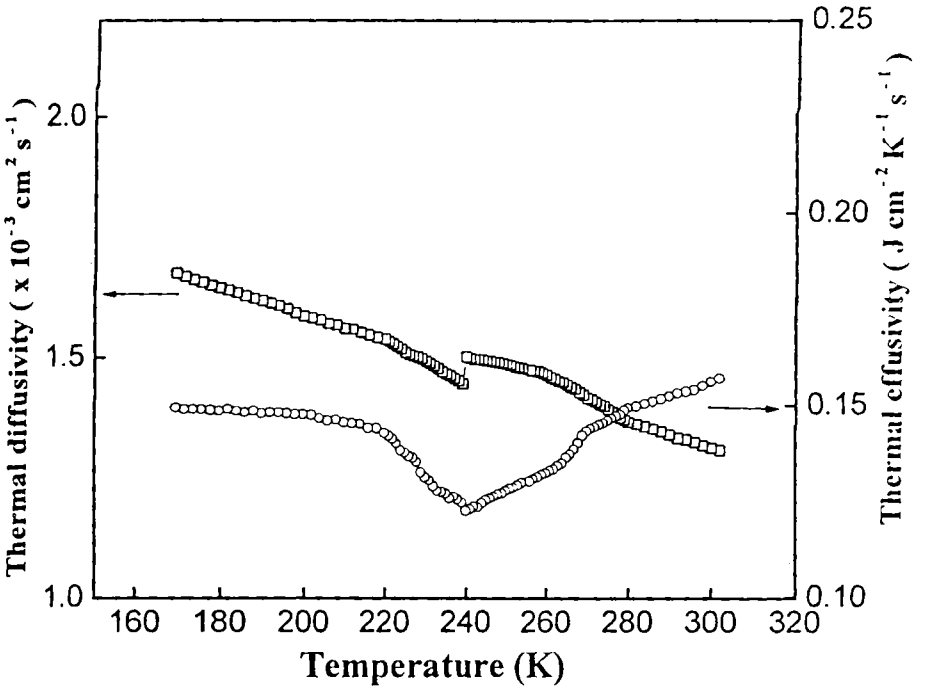

Fig. 5.4: Variation of thermal diffusivity and thermal effusivity with temperature of $La_{0.7}Ca_{0.3}MnO_3$ sample

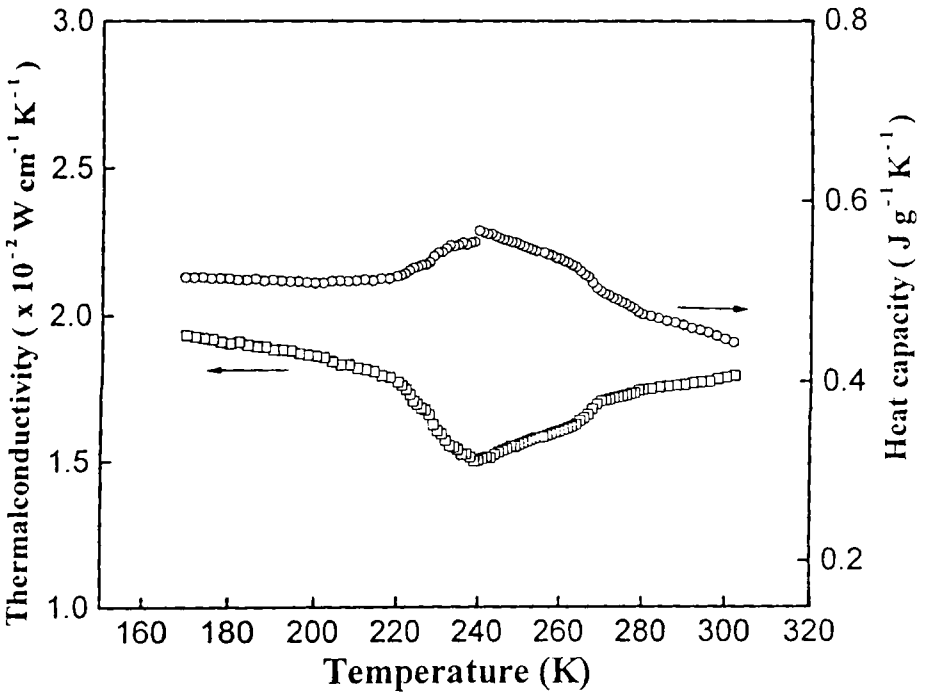

Fig. 5.5: Variation of thermal conductivity and heat capacity with temperature of $La_{0.7}Ca_{0.3}MnO_3$ sample

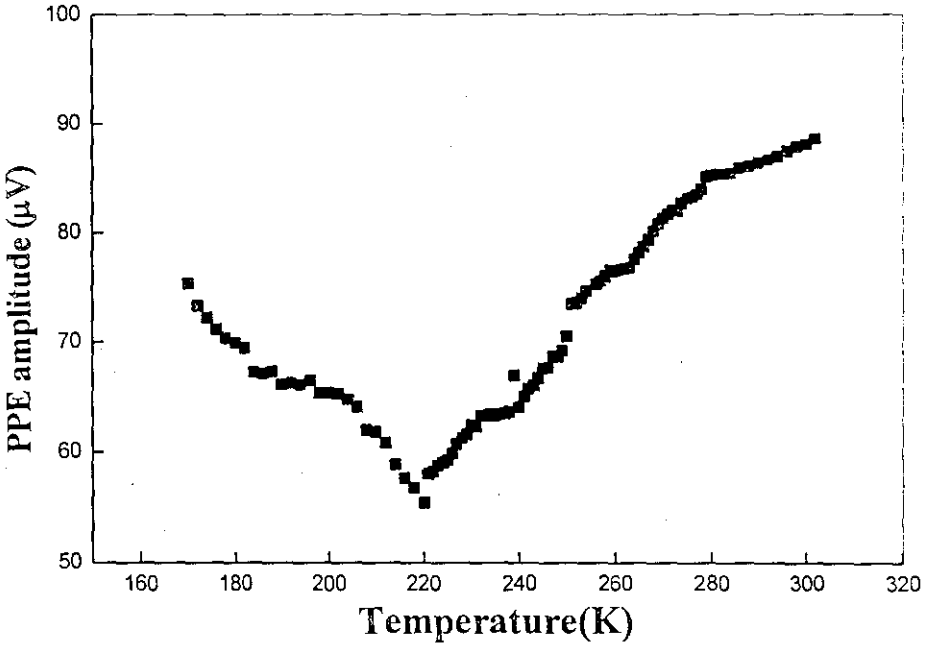

Fig. 5.6(a): Variation of PPE amplitude with temperature of $La_{0.8}Ca_{0.2}MnO_3$ sample

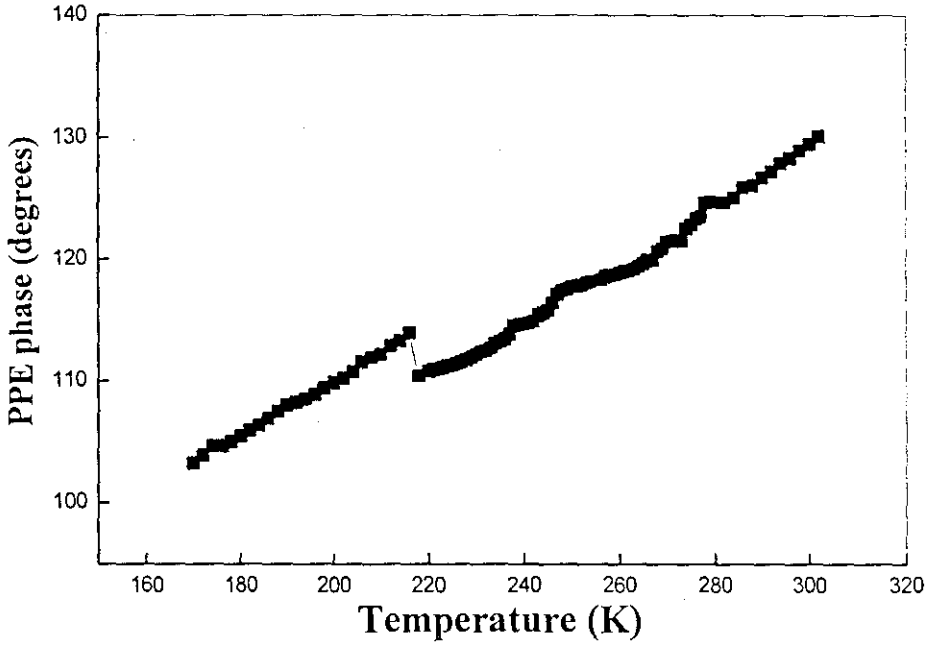

Fig. 5.6(b): Variation of PPE phase with temperature of $La_{0.8}Ca_{0.2}MnO_3$ sample

temperature give a clear evidence of M-I transition at T=218 K for $La_{0.8}Ca_{0.2}MnO_3$ sample.

Fig. 5.7 gives the variation of thermal diffusivity and thermal effusivity of $La_{0.8}Ca_{0.2}MnO_3$. Fig. 5.8 denote the variation of thermal conductivity and heat capacity. The behaviours of thermal parameters are similar to those of $La_{0.7}Ca_{0.3}MnO_3$ sample, with the M-I transition temperature being shifted to T = 218K for $La_{0.8}Ca_{0.2}MnO_3$ sample.

5.5 Discussion of results

The basis for the theoretical understanding of the Mn oxides usually is the notion of double exchange (DE) [3-5] that considers the exchange of electrons between neighbouring Mn^{3+} and Mn^{4+} sites with strong on-site Hund's coupling. Attempts based on mean-field treatments of a Kondo lattice model for DE [15] and a Hubbard-Kondo lattice model [16] have been suggested to account for the transport properties of the Mn oxides. However, sharp change in the conductivity near T_c and the CMR were not reproduced successfully in these works. Perturbative calculation carried out by authors of ref. [17] showed that double exchange (DE) alone could not explain the experimental data for Mn oxides and suggested that a strong Jahn-Teller distortion should be responsible for the thermal transport properties. But recently, contray to the above approaches, it was suggested that the localization in the DE model based upon non-perturbative treatments might be able to account for the novel properties of the Mn oxides.

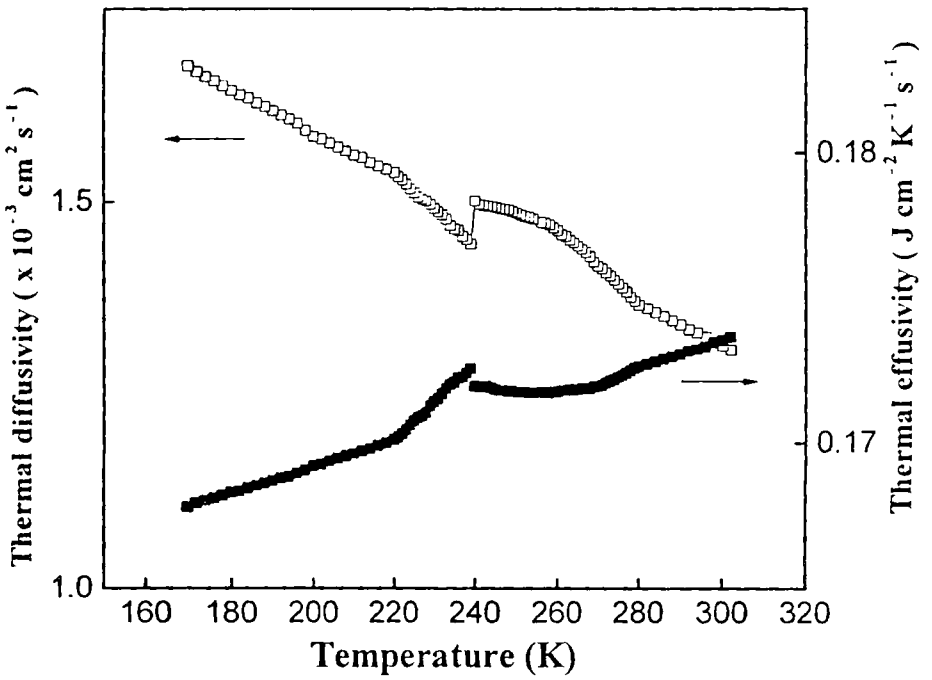

Fig. 5.7: Variation of thermal diffusivity and thermal effusivity with temperature of $La_{0.8}Ca_{0.2}MnO_3$ sample

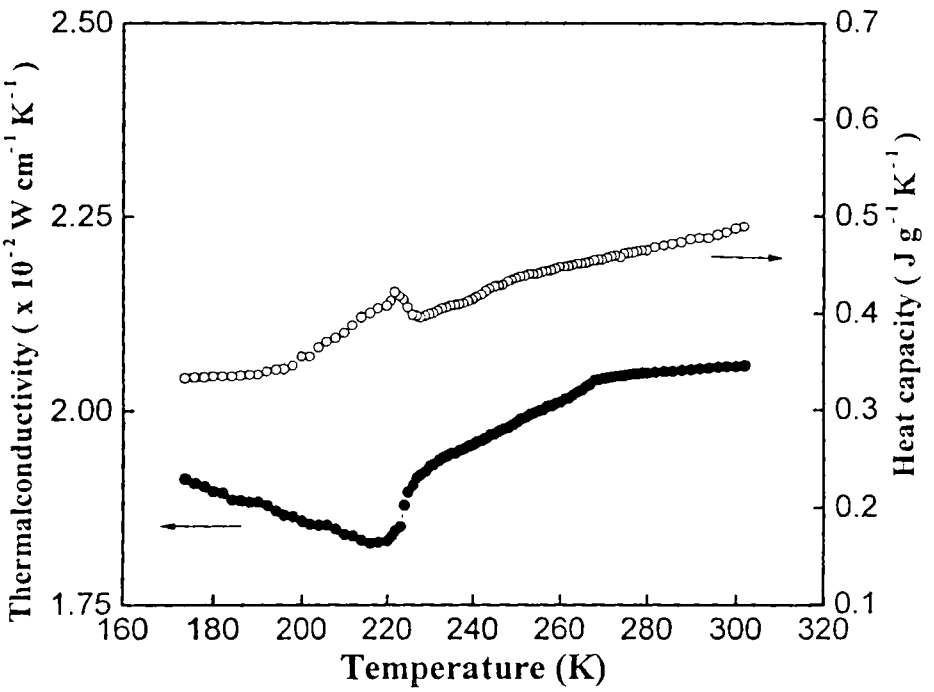

Fig. 5.8: Variation of thermal conductivity and heat capacity with temperature of $La_{0.8}Ca_{0.2}MnO_3$ sample

These mixed valence oxides can be considered as solid solutions between end members such as $LaMnO_3$ and $CaMnO_3$ with formal valence states $La^{3+}Mn^{3+}O_3^{2-}$ and $Ca^{2+}Mn^{4+}O_3^{2-}$ leading to mixed compounds such as $\left(La_{1-x}^{3+}Ca_x^{2+}\right)\left(Mn_{1-x}^{3+}Mn_x^{4+}\right)O_3$. The nominal electronic configurations of Mn^{3+} and Mn^{4+} are $3d^4$ and $3d^3$ respectively. For the Mn-oxides, metallic ferromagnetism occur in the composition range $0.2 < x < 0.5$, where it is associated with the simultaneous presence of Mn^{3+} and Mn^{4+} ions. Each Mn^{3+} ions has four $3d$ electrons, three in the t_{2g} state and the fourth in the e_g state. The Hund's rule coupling is very strong and so spins of all the d electrons on a given site must be parallel. Three t_{2g} electrons are localized on the Mn site and give rise to a local spin S of magnitude 3/2, while the e_g electron may hop into the vacant e_g states of surrounding Mn^{4+} ions. Due to the strong Hund's rule coupling, the hopping of an e_g electron between Mn^{3+} and Mn^{4+} sites are affected by the relative alignment of the local spins, being maximal when the localized spins are parallel and minimal when they are antiparallel.

It is widely accepted that there is a close correlation between the minimum in the conductivity and the ferromagnetic-paramagnetic transition. After analyzing the experimental data for these two samples [18] already reported, it is seen that both samples are associated with residual resistivity $\rho_0 = \rho\ (T = 0)$. A high residual electrical resistivity appears to be prerequisite to the occurrence of the sharp resistivity peak near T_c. Since ρ_0 in the ferromagnetic ground state arises from the nonmagnetic randomness rather than spin disorder, the results mentioned above suggest that nonmagnetic randomness play a significant role in determining the transport and magnetic properties of the Mn oxides. So we can hereby say that the

nonmagnetic randomness together with the spin disorder leads to an Anderson metal-*insulator transition* near T_c, from which the anomalous properties of transport magnetism of Mn oxides can be well understood.

Using the well established scaling theory [19], the electronic localization can be clearly understood by considering the diagonal disorder and off-diagonal disorder. The former is introduced to describe the nonmagnetic randomness and the latter comes from DE model. The off-diagonal disorder alone can only localize a small fraction of electron states close to the band edges but fails to cause the localization of the electron states at the Fermilevel for intermediate hole doping. So in the presence of a suitable strength of non magnetic disorder, the spin disorder frozen in at the FM-PM transition will cause the localization of electrons at the Fermi level and induce a M-I transition near T_c in the doping range $0.2 < x < 0.5$.

To make this point more clear, a theoretical approach has been introduced [10, 11]. With that, the Hamiltonian used to describe the Mn oxides is

$$H = -\sum_{ij} \tilde{t}_{ij} d_i^{+} d_j + \sum_j \varepsilon_i d_i^{+} d_j \qquad (7.1)$$

The first term is the Double exchange Hamiltonian of e_g electrons, with $\tilde{t}_{ij}$ being the effective integral between nearest neighbouring Mn sites. It was proposed recently that $\tilde{t}_{ij}$ has the form [9]

$$\tilde{t}_{ij} = t\left\{\cos\left(\theta_i/2\right)\cos\left(\theta_j/2\right) + \sin\left(\theta_i/2\right)\sin\left(\theta_j/2\right)\right\}\exp\left\{-i\left(\phi_i - \phi_j\right)\right\} \quad (7.2)$$

where t is the transfer integral in the absence of Hund's rule coupling and (θ_i, ϕ_i) are the polar angles characterizing the orientation of local spin S_i. The second term in Eq. (7.1) represents an effective onsite disorder Hamiltonian that includes all

possible diagonal disorder terms, such as the potential fluctuations due to the substitution of La^{3+} with Ca^{2+}. ε_i stands for random on-site energies distributed within the range $\left[-W/2, W/2\right]$

So for a given system, the disorder parameter W and the Fermienergy E_F are approximately unchanged, corresponding to a point in the phase diagram of Fig. 5.8.

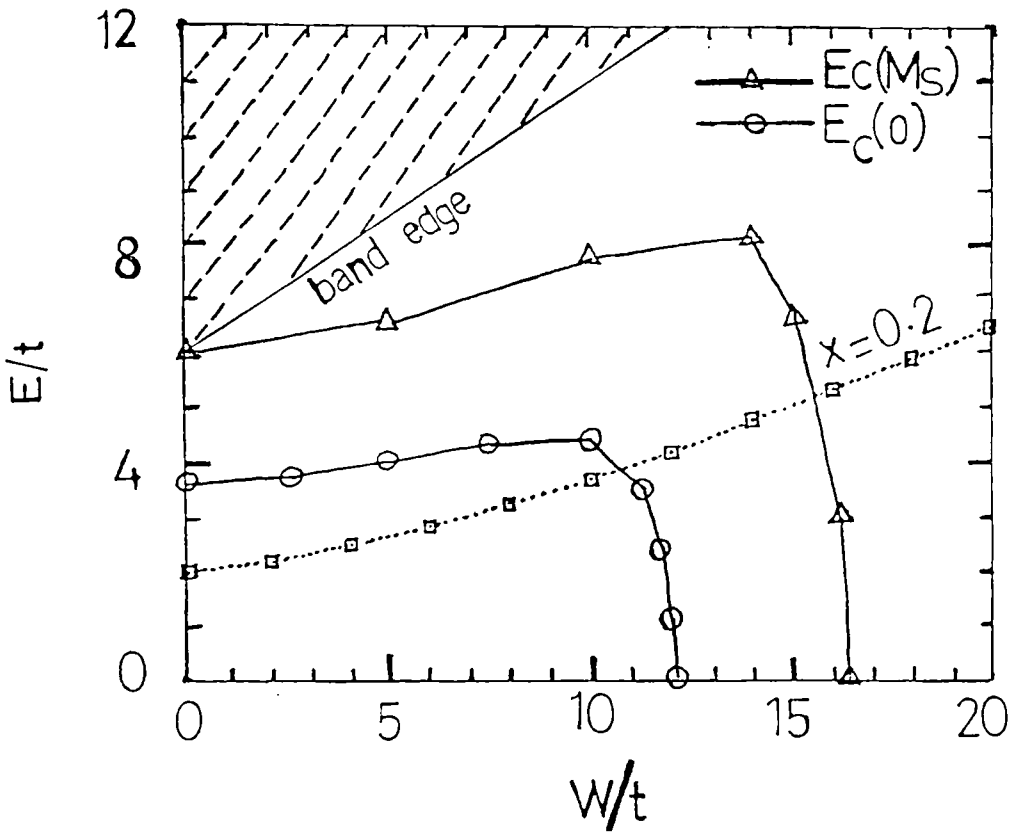

Fig. 5.8: Phase diagram for the La-Ca-Mn-O system

However, since the spin disorder is temperature dependent, the mobility edge varies with temperature. With the system changing from the FM ground state at T = 0 to the PM state at $T > T_c$ on warming, the mobility edge changes continuously from $E_c(M_s)$ to $E_c(0)$. $E_c(M_s)$ represents the mobility edge for the FM state in the

absence of off-diagonal disorder and $E_c(M = 0)$ for the PM state in the presence of the off-diagonal disorder. M_s represents the magnetization of completely aligned spins. The phase diagram is divided into three regions by the mobility edges $E_c(M_s)$ and $E_c(0)$. If (W, E_F) is in region I, the system always exhibits metallic behaviour in both the FM and PM states; while if it is in region III, the system exhibits insulator like behaviour. For (W, E_F) in region II, the system will undergo an Anderson M-I transition that is intimately related to the FM-PM phase transition. Such a transition is associated with a dip in the electrical conductivity and thermal conductivity. The same is observed in our case. So we can conclude by saying that the M-I transition in our samples are of the Anderson type, with T_p lying very close to the Curie temperature T_c, where the magnetization decreases sharply from $M = M_s$ to $M = 0$. In the range of $0.2 < x < 0.5$, relatively strong disorder $12t < W < 16.5t$ is necessary to make the M-I transition to occur [11].

The specific heat capacity versus temperature curves for these samples give the room temperature values for c_p in the range 98-108 $Jmol^{-1}$ K^{-1}. These values agree well with the previous high temperature specific heat measurements performed on this class of materials [12-14]. For these samples, we observe a clear anomaly in the specific heat versus temperature curves that marks the onset of long-range magnetic order. The temperature at which these peaks occur agree well with the critical temperature determined from other measurements.

5.6 Conclusions

Thermal properties of two samples belonging to the LCMO system have been studied in detail employing photopyroelectric technique. The samples selected for

investigations – $La_{0.7}Ca_{0.3}MnO_3$ and $La_{0.8}Ca_{0.2}MnO_3$ - are found to exhibit M-I transitions. The M-I transition in the samples gets reflected in thermal conductivity and specific heat capacity data. The observations are explained in terms of the existing models for these solids.

References

1. S. Jin *et al.*, Science **264** (1994) 413.
2. M. Imada *et al.*, Rev. Mod. Phys. **70** (1998) 1039.
3. C. Zener, Phys. Rev. **82** (1951) 403.
4. P. W. Anderson and H. Hasegawa. Phys. Rev. 100 (1955) 675.
5. P. G. deGennes, Phys. Rev. **118** (1960) 141
6. A. J. Mills *et al.*, Phys. Rev. Lett. **74** (1995) 5144.
7. A.J Mills ***et al.***, Phys.Rev.Lett 77 (1996) 175
8. C. M. Varma, Phys.Rev.B **54** (1996) 7328.
9. E. Muller-Hartmann and E. Daggoto, Phys. Rev. B 54 (1996) R6819.
10. L. Sheng *et al.*, Phys. Rev. Lett. **79** (1997) 1710.
11. L. Sheng *et al.*, Phys. Rev. B **56** (1997) R7053.
12. R. Mahendiran, S. K. Tiwari, A. K. Raychaudhuri, T. V. Ramakrishnan, R. Mahesh, N. Rangavittal and C. N. R. Rao, Phys. Rev. B **53** (1996) 3348.
13. P. S. Anilkumar, P. A. Joy and S. K. Date, J. Mater. Chem. **8** (1998) 1219.
14. C. Preethy Menon and J. Philip, Meas. Sci. Technol. **11** (2000) 1744.
15. N. Furukawa, J. Phys. Soc. Jpn. **63** (1994) 3214.
16. J. Inoue and S. Mackawa, Phys. Rev. Lett. **74** (1995) 3407.
17. A. J. Mills, P. B. Littlewood and B. I. Shariman, Phys. Rev. Lett. **74** (1995) 5144.
18. P. A. Joy, P. S. Anilkumar and S. K. Date, Mater. Res. Bull. **34** (1999) 2143.
19. A. Mackinnon and B. Kramer, Phys. Rev. Lett. **47** (1981) 1546; Z. Phys. B 53 (1983) 1.

CHAPTER 6

Photopyroelectric measurement of thermal properties of La-Pb-Mn-O system

6.1 Introduction

The colossal magnetoresistance (CMR) behaviour and other properties of some oxide materials have drawn extensive scientific and technological interest during the last decade. The well-known CMR materials are the mixed valence manganites with ABO_3 type perovskite structure. For example, $R_{1-x}A_xMnO_3$ (where R is the trivalent rare earth element like La, Pr etc. and A is the bivalent alkaline earth metal like Sr, Pb, Ca, Ba etc., belong to this group of samples [1, 2]. The parent compound, $LaMnO_3$, is a paramagnetic insulator (PMT) showing a phase transition to an antiferromagnetic (AFM) phase at about 140K. With the La site doping by the above-mentioned alkaline earth metal, the hole doped ($0.1 \leq x \leq 0.5$) oxide perovskites show the ferromagnetic metallic state below the Curie temperature, T_c. The transition temperature T_p, separating the insulating and metallic phase lies in the vicinity of Curie temperature T_c [1] around which resistivity decreases by several orders of magnitude under the application of magnetic field resulting in the CMR effect. However, in spite of enthusiastic efforts dedicated to this topic, detailed microscopic mechanism responsible for magnetic and transport properties of these

oxides is not yet well understood. Though several attempts have been made to explain the magnetic and other properties considering double exchange (DE) interaction [3] that renders Mn^{3+}-O^{2-}-Mn^{4+} bonds metallic, it has recently been emphasized that this DE mechanism alone cannot uniquely explain the available experiment data [4]. In many such samples, DE interaction between Mn^{3+} and Mn^{4+} gives rise to the simultaneous presence of ferromagnetism and metallic (FMM) behaviour. In addition to the DE, a strong electron-phonon interaction, giving rise to Jahn-Teller (JT) splitting of the outer *d* level plays an important role in the transport mechanism, especially at temperatures near and above T_p. One way to monitor the DE interaction is by the substitution of divalent ions at the R site, leading to the variation of the ratio $C = Mn^{4+} / Mn^{3+}$ which might lead to the lattice JT effect due to the change of La site ion size. Another way is by doping of transition metal ion at the Mn site, the center for the DE mechanism, which directly influences the DE interaction and hence the transport and magnetic properties.

Recently the La-Pb-Mn-O type system has been elaborately studied because of its high magnet ordering temperature (around room temperature). Like Mn, Chromium (Cr) also exists in two valence states, Cr^{2+} and Cr^{3+}. Since the electronic configurations of Cr^{3+} and Mn^{4+} are identical, there is a possibility of substitution of Mn by Cr. Recently Barnabe *et al.*, [5] have shown that among various doping elements, Cr was the most efficient one to induce metal insulator transition (MIT) in $La_{0.5}Ca_{0.5}Mn_{1-x}A_xO_3$. For the Cr doped system, the average A site cationic radius ($< r_A >$) is smaller than (~ 1.14 Å) that of the corresponding undoped system (~ 1.19 Å). It is well established that antiferromagnetic (AFM) ordering becomes

stronger as $< r_A >$ decreases, so that doping level at the B site (here Mn), depending on x, must be increased to counter balance the effect.

In this chapter we have studied the thermal properties, *viz*; thermal diffusivity (α), thermal effusivity (e), thermal conductivity (K) and heat capacity (c_p) of three samples, belonging to La-Pb-Mn-O system, employing the photopyroelectric technique. The samples selected for investigations are $La_{0.5}Pb_{0.5}MnO_3$, $La_{0.5}Pb_{0.5}Mn_{0.85}Cr_{0.15}O_3$ (to study the effect of the partial substitution of Mn by Cr on the transport properties of the La-Pb-Mn-O system) and $La_{0.7}Pb_{0.3}MnO_3$ + 2.5 wt. % Ag (to analyze the effect of Ag on the thermal conductivity of La-Pb-Mn-O system). The work done in this chapter is on sintered bulk samples. In the following sections, we describe in detail sample preparation, experimental details and discuss the results obtained.

6.2 Sample preparation

The samples for the present investigations have been prepared under almost identical thermodynamical conditions by solid-state reaction technique. To prepare $La_{0.5}Pb_{0.5}MnO_3$, high purity (each of purity 99.99%) La_2O_3, PbO and MnO_2 with appropriate stoichiometric proportions have been mixed and ground. The well-mixed oxides are then pre-heated around 250°C for 5 hours in air. The pre-heated samples have been re-ground and sintered at 900°C for 48 hours with intermediate grindings. Finally, the powdered samples have been pressed into pellets which are again annealed at 900°C for 24 hours and then slowly furnace cooled.

Bulk samples of $La_{0.5}Pb_{0.5}Mn_{0.85}Cr_{0.15}O_3$ are prepared by standard sold state reaction method with stoichiometric amount $La_2(CO_3)_3$, PbO, $Mn(C_2H_3O_2)$ and Cr_2O_3, each of purity 99.99% as the starting materials. The samples have been characterized by X-ray diffraction with CuK_α (λ = 1.541 Å) radiation.

The so prepared samples have been cut, polished and the samples for the photopyroelectric measurements are made to have a thickness of ≈ 0.5mm. An improved photopyroelectric has been used to determine the thermal parameters and the details of the experimental set up ad measurement procedure are given in Chapter 2 and subsequent chapters of this thesis.

6.3 Experimental details

A 120mW He-Cd laser of wavelength λ = 442nm has been used as the optical heating source and its intensity has been modulated using a mechanical chopper (Model SR540). A PVDF film of thickness 28μm, both sides coated with Ni-Cr, is used as the pyroelectric detector having a pyroelectric coefficient of $P = 0.25 \times 10^{-8}$ $Vcm^{-1}K^{-1}$. The signal output is measured using a lock-in amplifier (SR 830). The frequency of modulation of the light is kept above 30Hz to ensure that the detector, the sample and the backing medium are thermally thick during measurements. The thermal thickness of the three samples have been verified by plotting the PPE amplitude and phase with frequency at different temperatures between room temperature and 180K. These are given in figures 6.1(a), 6.1(b), 6.2(a), 6.2(b) 6.3(a) and 6.3(b) for the three samples.

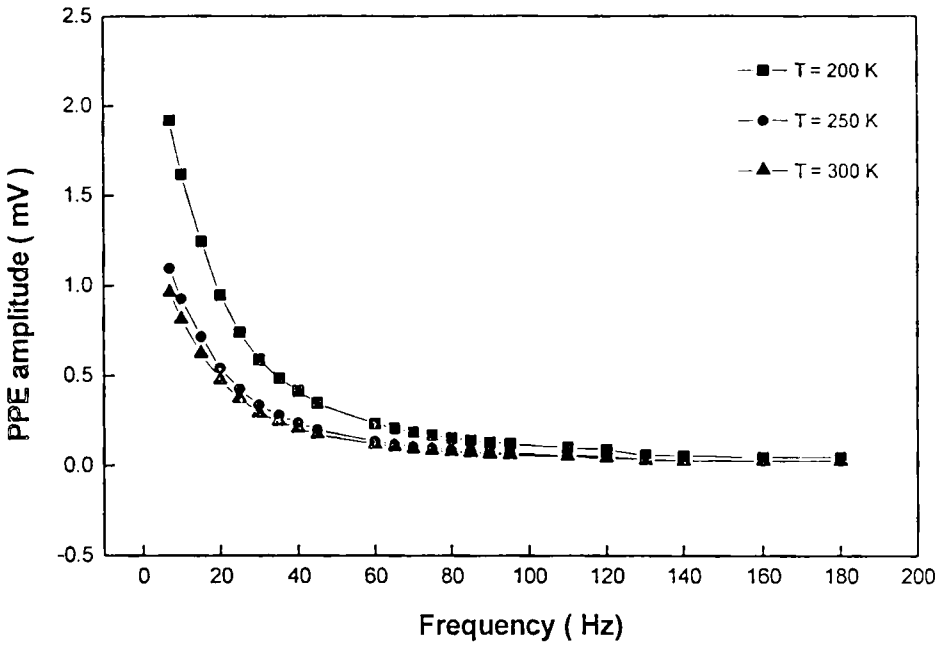

Fig. 6.1(a): Frequency dependence of PPE amplitude of $La_{0.5}Pb_{0.5}MnO_3$ at three temperatures

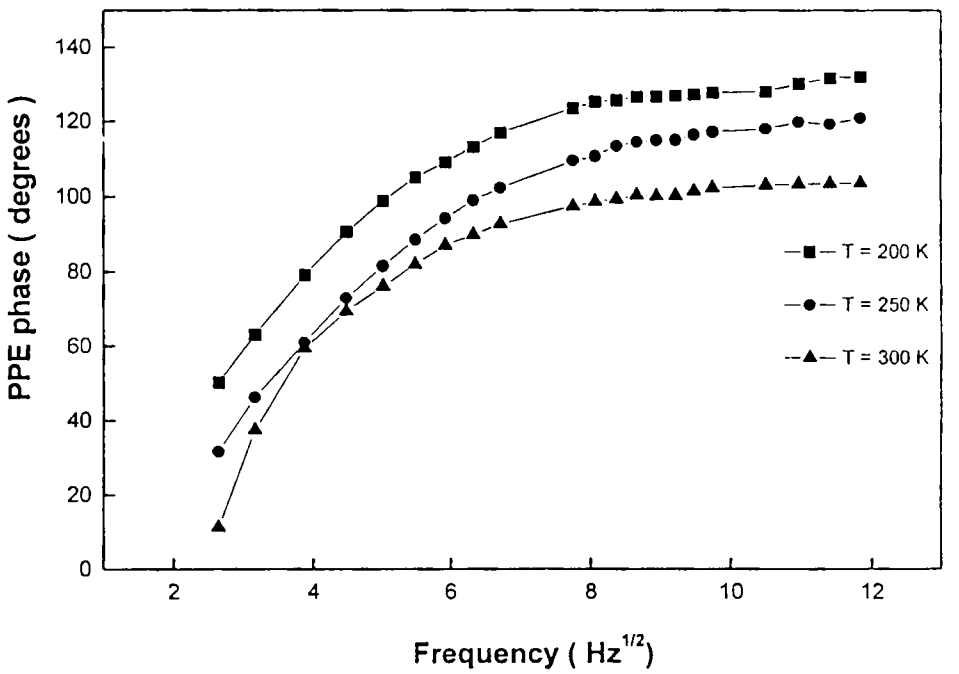

Fig. 6.1(b): Frequency dependence of PPE phase of $La_{0.5}Pb_{0.5}MnO_3$ at three temperatures

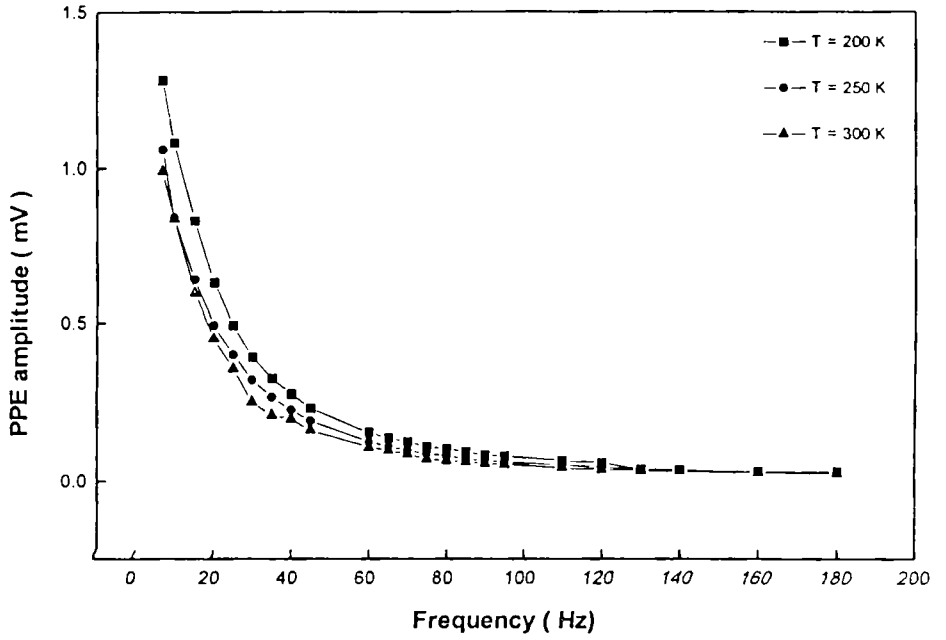

Fig. 6.2(a): Frequency dependence of *PPE amplitude of* $La_{0.5}Pb_{0.5}Mn_{0.85}Cr_{0.15}O_3$ at three temperatures

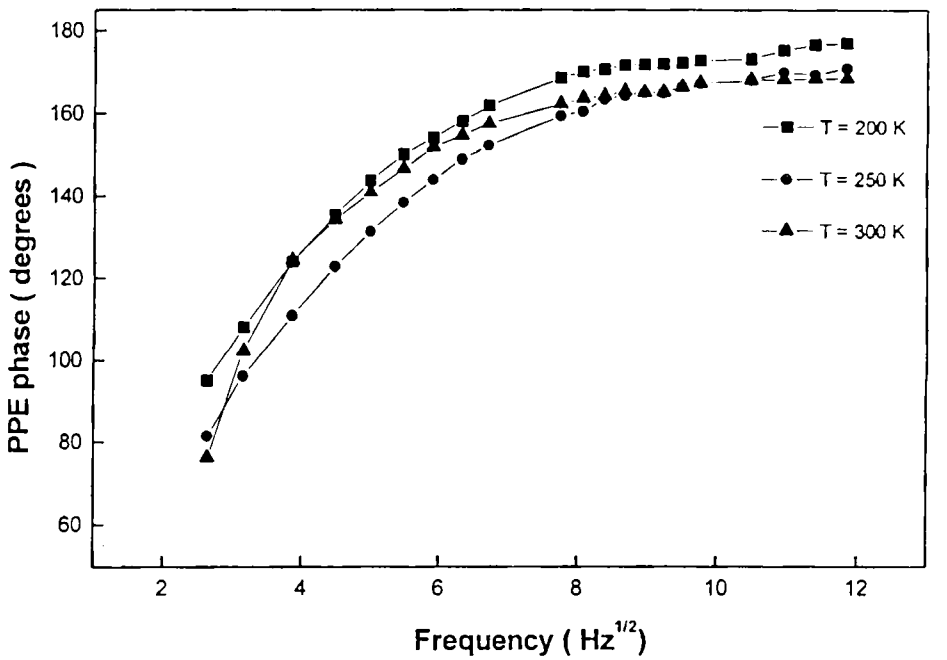

Fig. 6.2(b): Frequency dependence of PPE phase of $La_{0.5}Pb_{0.5}Mn_{0.85}Cr_{0.15}O_3$ at three temperatures

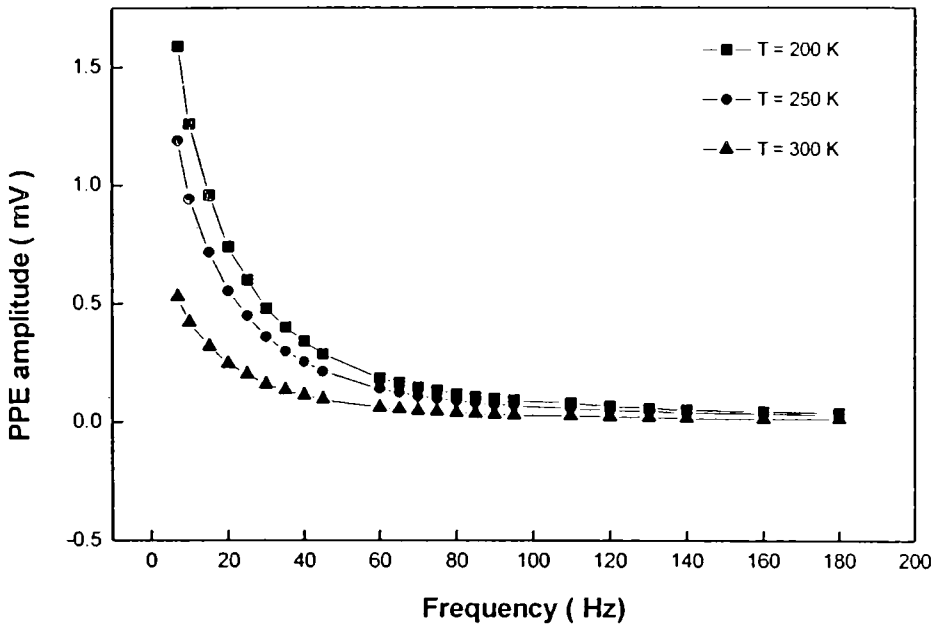

Fig. 6.3(a): Frequency dependence of PPE amplitude of $La_{0.7}Pb_{0.3}MnO_3$ + 2.5 wt. % Ag at three temperatures

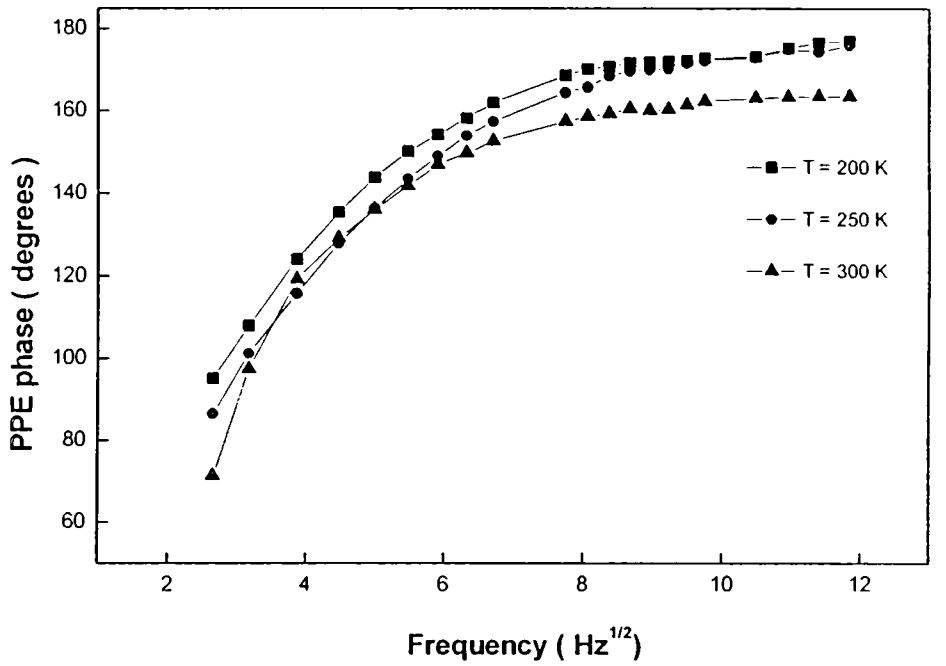

Fig. 6.3(b): Frequency dependence of PPE phase of $La_{0.7}Pb_{0.3}MnO_3$ + 2.5 wt. % Ag at three temperatures

Measurement of the PPE signal phase and amplitude enable one to determine thermal diffusivity, $\alpha = K/\rho c_p$, ρ being the density and effusivity $e = (K\rho c_p)^{1/2}$ respectively [16]. From the measured values of α and e, K and c_p of the samples are determined, once density ρ is known. Density of these samples is measured using Archimedes principle. The calibration of the experimental set up that has been done prior to carry out the measurements is described in detail in Chapter 2 of the thesis [7]. Measurements as a function of temperature have been made at a heating rate of approximately 0.5 K/min and data are collected in every 1K interval normally and at closer intervals near the M-I transition temperature. The temperature is measured with a platinum sensor placed close to the chamber.

6.4 Results

Figures 6.4(a) and 6.4(b) show the variation of PPE amplitude and phase with temperature of $La_{0.5}Pb_{0.5}MnO_3$ sample. The PPE amplitude decreases with temperature, reaches a minimum at $T \approx 276$K and then increases with temperature. The PPE phase decreases with temperatures normally and exhibits a step like behaviour at $T \approx 276$K, corresponding to the metal-insulator transition temperature. The M-I transition is clearly reflected in both PPE amplitude and phase variations with temperature. Fig. 6.5 gives the variation of thermal diffusivity (α) and thermal effusivity (e) of $La_{0.5}Pb_{0.5}MnO_3$ sample with temperature. Since thermal diffusivity is dependent only on PPE phase, the variation of thermal diffusivity has almost a constant value up to the transition and thereafter steadily decreases up to room temperature. Fig. 6.6 exhibits the variation of thermal conductivity and heat capacity with temperature.

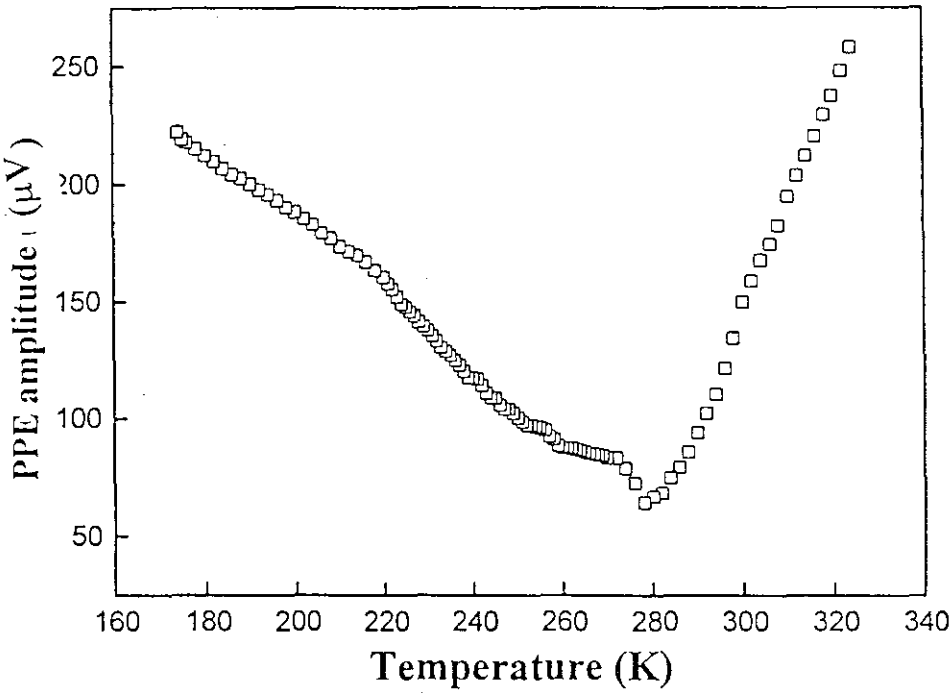

Fig. 6.4(a): Temperature dependence of PPE amplitude of $La_{0.5}Pb_{0.5}MnO_3$ sample

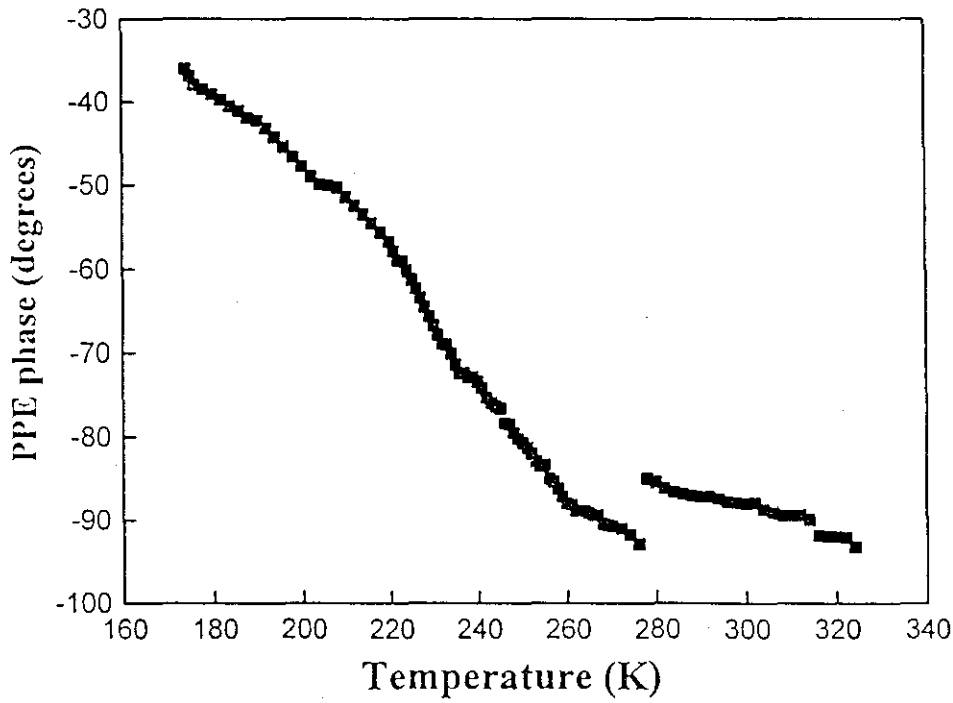

Fig. 6.4(b): Temperature dependence of PPE phase of $La_{0.5}Pb_{0.5}MnO_3$ sample

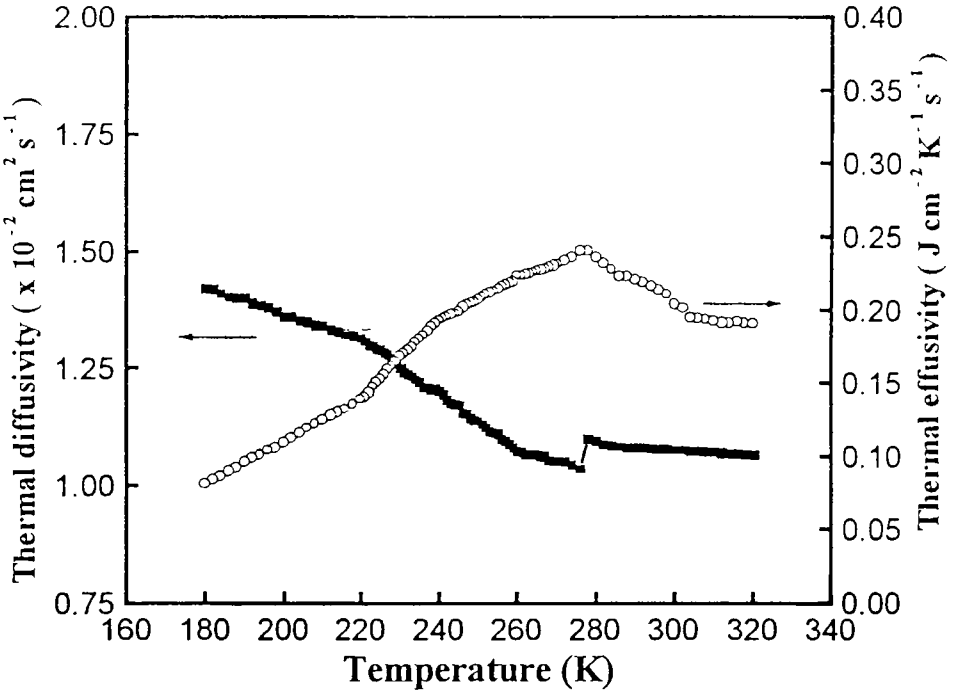

Fig. 6.5: Variation of thermal diffusivity and thermal effusivity of $La_{0.5}Pb_{0.5}MnO_3$ sample

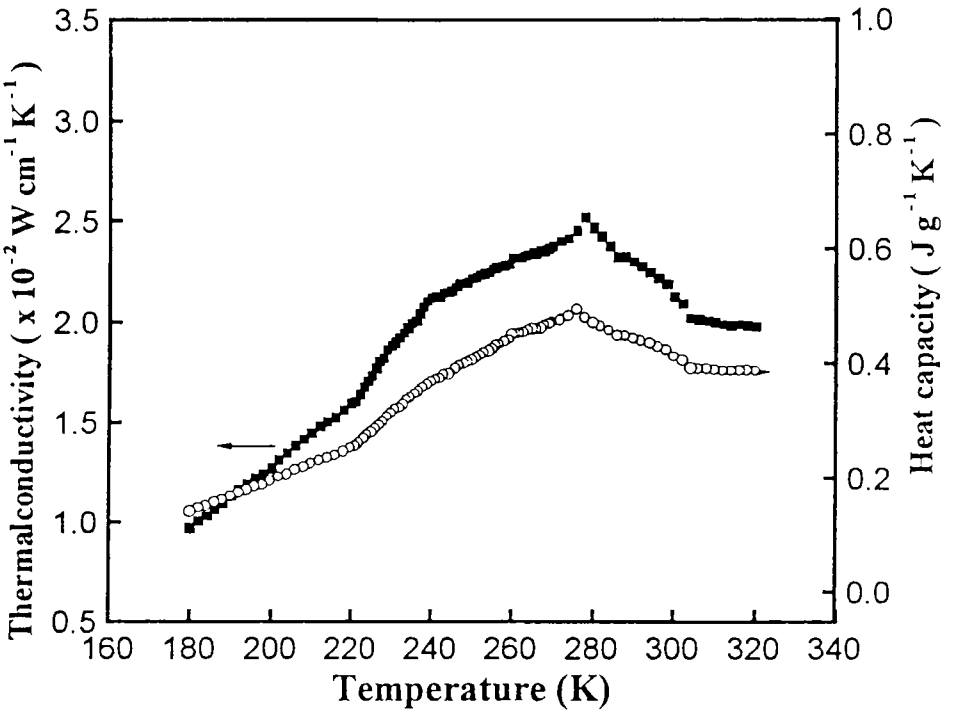

Fig. 6.6: Variation of thermal conductivity and heat capacity of $La_{0.5}Pb_{0.5}MnO_3$ sample

The behaviour of thermal conductivity and heat capacity are almost identical, exhibiting a peak at the transition temperature and thereafter decreases with temperature.

Figures 6.7(a) and 6.7(b) show the variations of PPE amplitude and phase with temperature of $La_{0.5}Pb_{0.5}Mn_{0.85}Cr_{0.15}O_3$. The variations of PPE amplitude and phase are similar to the former case, showing a clear anomaly at T=256K, the metal-insulator transition temperature. Fig. 6.8 denotes the variation of thermal diffusivity (α) and effusivity (e) of $La_{0.5}Pb_{0.5}Mn_{0.85}Cr_{0.15}O_3$ sample. It is seen that the M-I transition temperatures has been shifted to lower temperatures due to Cr doping. Fig. 6.9 shows the variation of thermal conductivity and heat capacity with temperature. The behaviours of K and c_p follow the same variation as in the former case, with the transition temperature shifting to a lower value.

Now in order to analyze the effect of Ag doping on the thermal conductivity of La-Pb-Mn-O system, we have studied the thermal parameters of $La_{0.7}Pb_{0.3}MnO_3$ + 2.5 wt. % Ag. Figures 6.10(a) and 6.10(b) show the variations of PPE amplitude and phase with temperature. There is a clear anomaly at the M-I transition temperature, T=262K, in this case. Fig. 6.11 shows the variation of thermal diffusivity (α) and thermal effusivity (e) of the $La_{0.7}Pb_{0.3}MnO_3$ + 2.5 wt % Ag. The variation is similar to the former two cases. Fig. 6.12 depicts the variation of thermal conductivity and heat capacity of this sample with temperature.

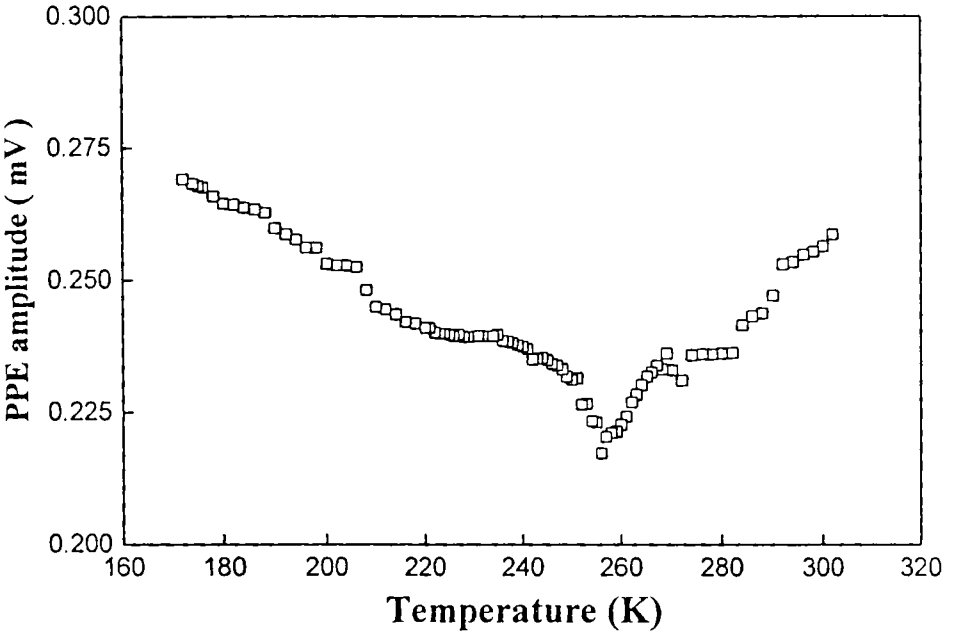

Fig. 6.7(a): Temperature variation of PPE amplitude of $La_{0.5}Pb_{0.5}Mn_{0.85}Co_{0.15}O_3$ sample

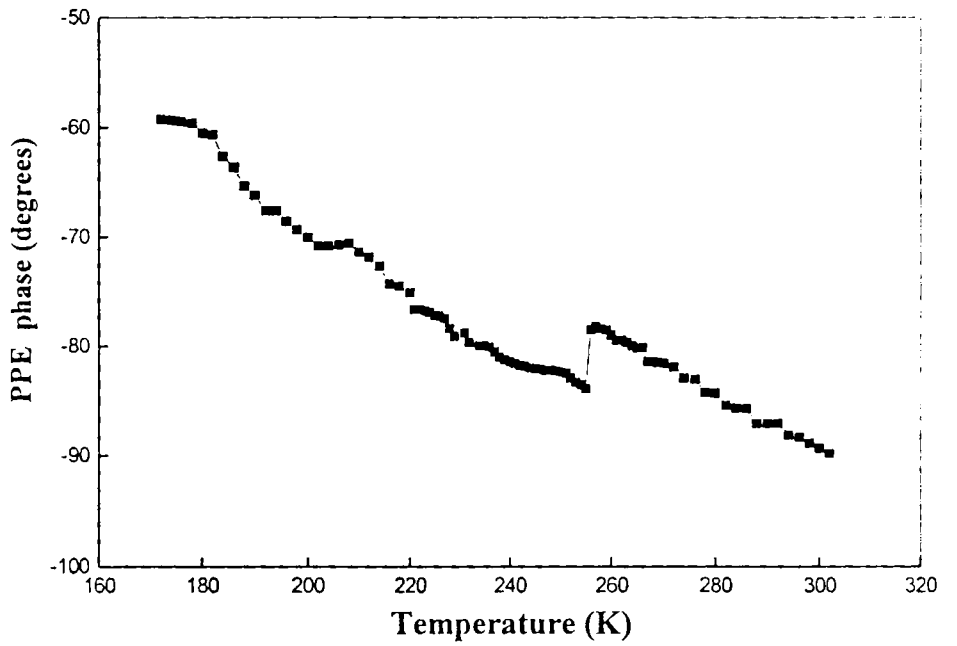

Fig. 6.7(b): Temperature variation of PPE phase of $La_{0.5}Pb_{0.5}Mn_{0.85}Co_{0.15}O_3$ sample

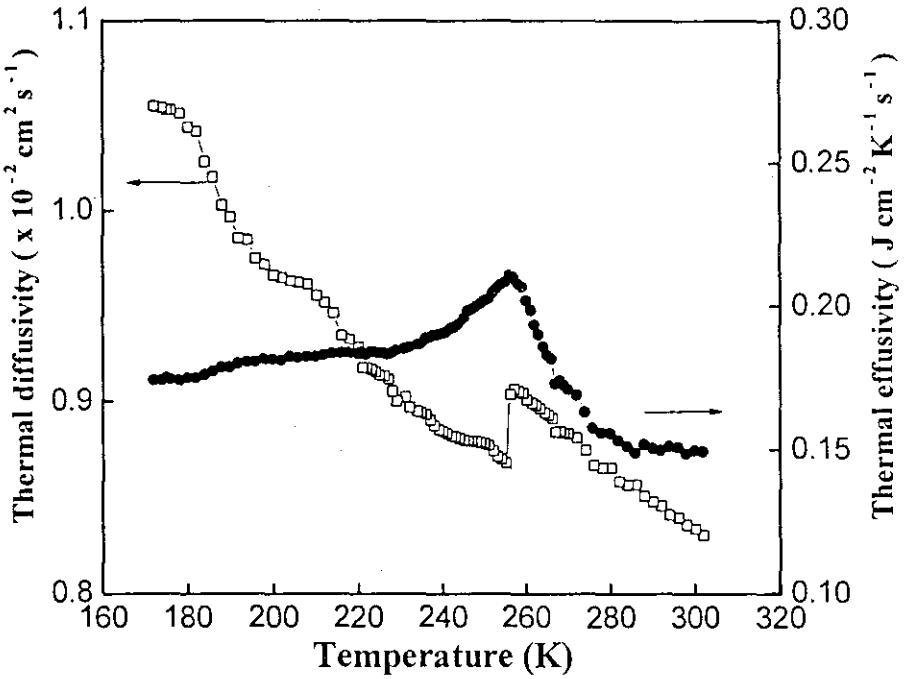

Fig. 6.8: Temperature variation of thermal diffusivity and thermal effusivity of $La_{0.5}Pb_{0.5}Mn_{0.85}Co_{0.15}O_3$ sample

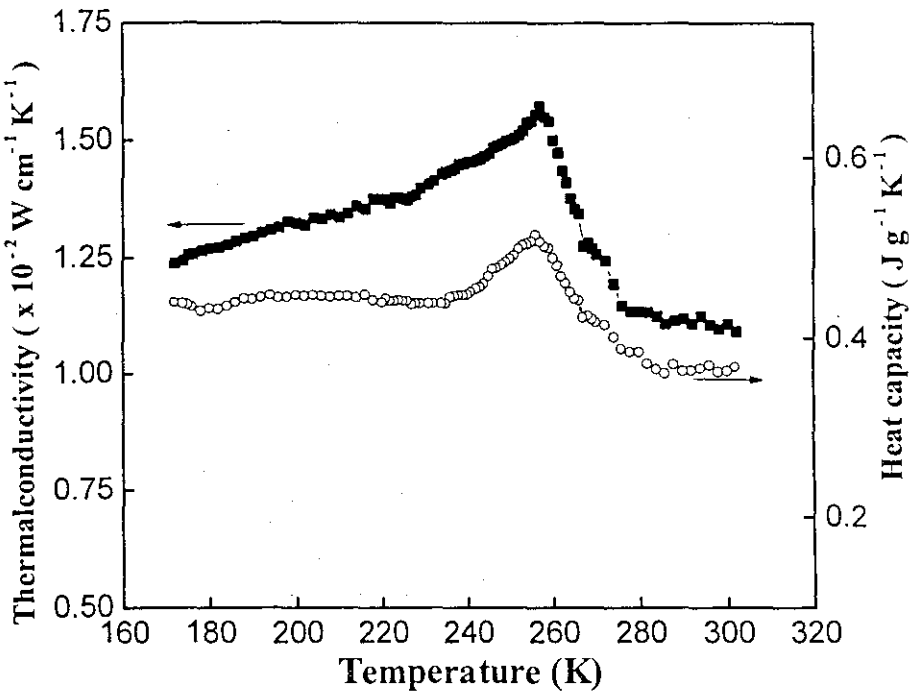

Fig. 6.8: Temperature variation of thermal diffusivity and thermal effusivity of $La_{0.5}Pb_{0.5}Mn_{0.85}Co_{0.15}O_3$ sample

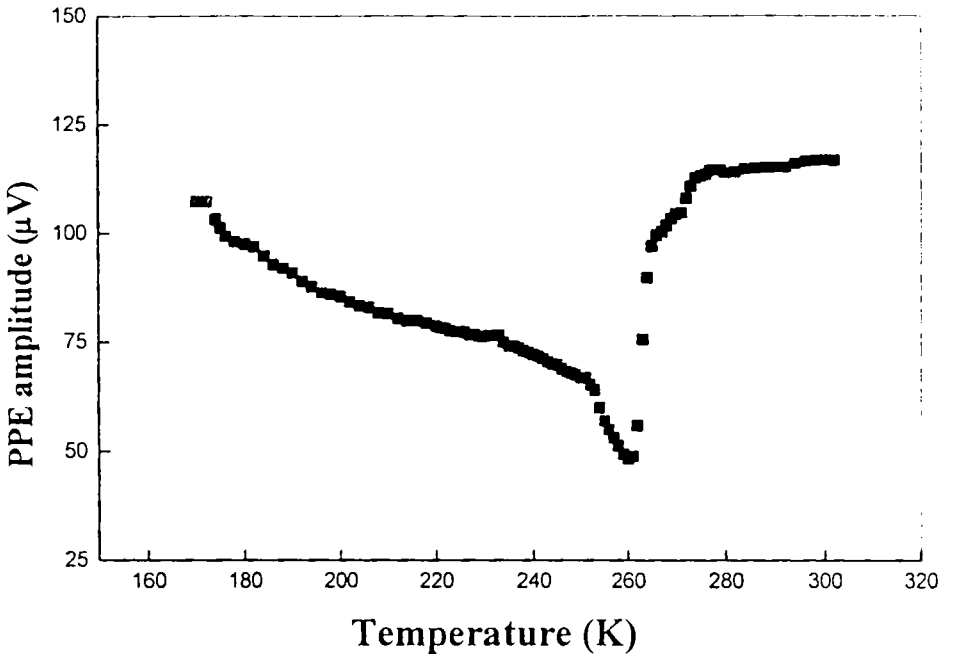

Fig. 6.10(a): Temperature variation of PPE amplitude of $La_{0.7}Pb_{0.3}MnO_3$ + 2.5 wt. % Ag

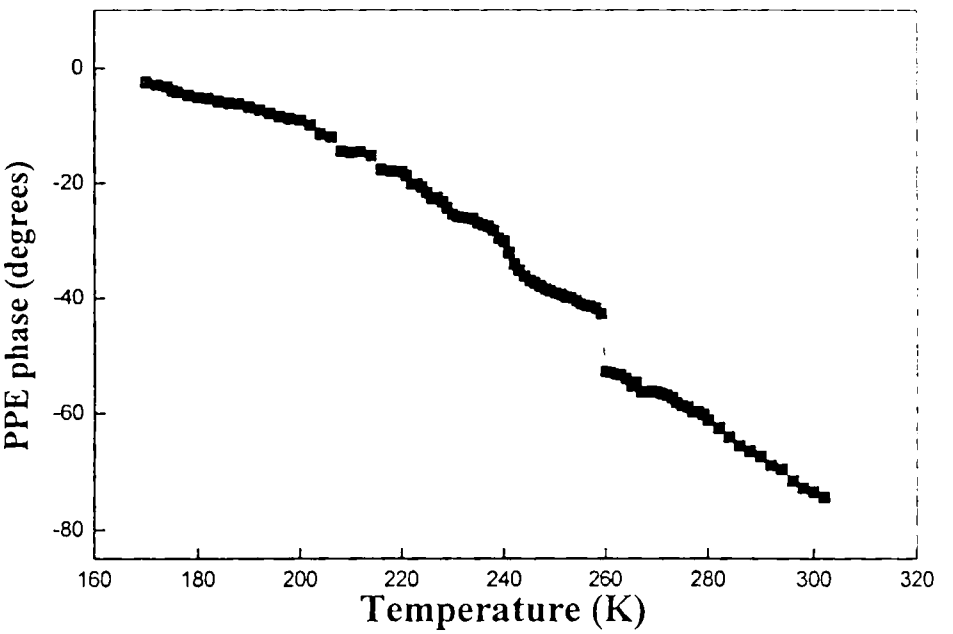

Fig. 6.10(b): Temperature variation of PPE phase of $La_{0.7}Pb_{0.3}MnO_3$ + 2.5 wt. % Ag

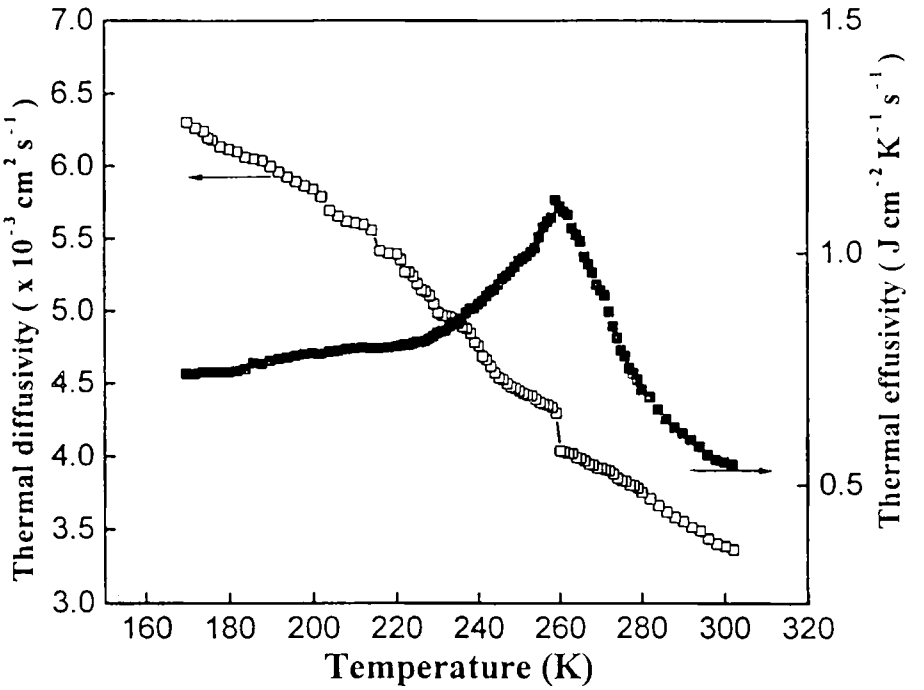

Fig. 6.11: Temperature variation of thermal diffusivity and thermal effusivity of $La_{0.7}Pb_{0.3}MnO_3$ + 2.5 wt. % Ag

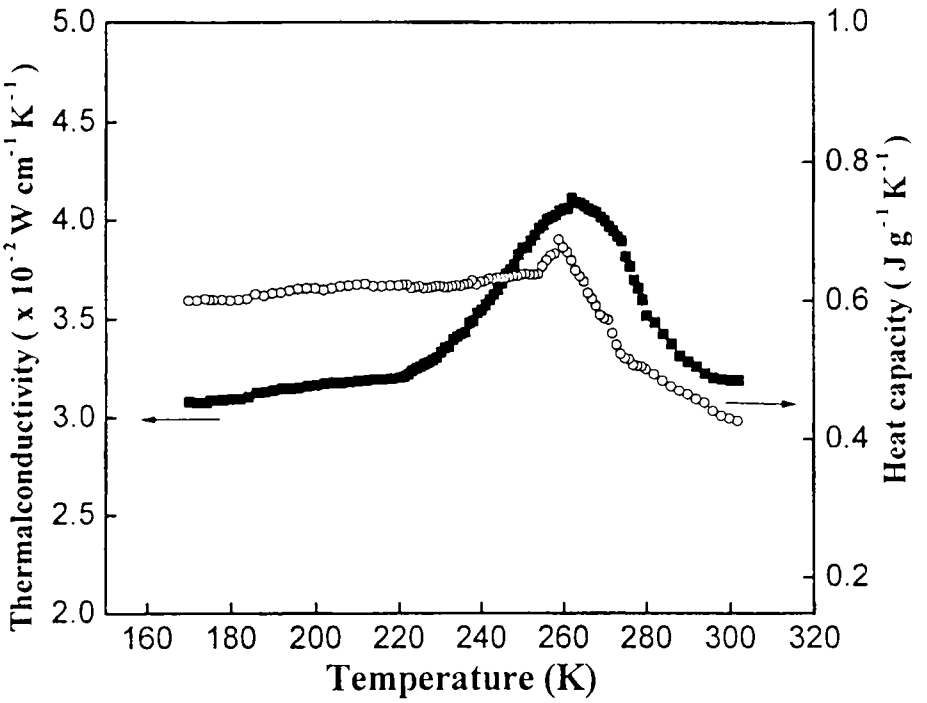

Fig. 6.12: Temperature variation of thermal conductivity and heat capacity of $La_{0.7}Pb_{0.3}MnO_3$ + 2.5 wt. % Ag

6.5 Discussion of the results

The observed peaks in thermal conductivities of three samples are explained as follows. The parent compound $LaMnO_3$ is an antiferromagnetic insulator where Mn ions are in the Mn^{3+} state. However, when doped with divalent ions (here Pb), contains both Mn^{3+} and Mn^{4+} ions. These ionic states fluctuate due to electron transfer between them. As a result of this electron transfer, antiferromagnetically ordered spin cants and both magnetization and conductivity appears simultaneously. Since the magnetic susceptibility of the sample arises mostly due to the presence of Mn^{4+} ions, from the nature of the susceptibility data one can have an idea about the number of Mn^{4+} ions. Mc. Gurie *et al.* [8] have shown that high ρ (resistivity) value is an evidence of weak double exchange because of low Mn^{4+} concentration. This has been verified in ref. [9], where the susceptibility value of La-Pb-Mn-O system is lower for sample showing high resistivity with relatively low Mn^{4+} concentration.

For the Mn oxides, metallic ferromagnetism occurs in the composition range $0.2 < x < 0.5$, where it is associated with the simultaneous presence of Mn^{3+} and Mn^{4+} ions. Each Mn^{3+} ion has four $3d$ electrons, three in the t_{2g} state, and fourth in the e_g state. The Hund's rule coupling is very strong so that spins of all the d electrons on a given site must be parallel. Three t_{2g} electrons are localized on the Mn site and give rise to a local spin S of magnitude 3/2, while the e_g electron may hop into the vacant e_g states of corresponding Mn^{4+} ions. Owing to the strong Hund's rule coupling, the hoping of an e_g electron between Mn^{3+} and Mn^{4+} sites is affected by the relative alignment of local spins, being maximal when the localized spins are parallel and minimal when they are antiparallel. The sharp increase in conductivity near M-I transition can be attributed to the fact that an increase in the magnetization

M upon cooling should reduce spin disorder scattering and this increases the carrier conductivity, consequently increasing thermal conductivity.

As pointed out by Mills *et al.*, [10, 11] however the double exchange model alone can't explain the sharp increase in the conductivity near T_c and associated CMR phenomenon. Based on the strong electron-phonon coupling in these materials, Mills *et al.*, [10, 11] proposed that the M-I transition involves a cross over from a high-T polaron dominated magnetically disordered regime to a low-T metallic magnetically ordered regime. On the other hand, some have argued the possible importance of the quantum localization effect caused presumably by the strong magnetic disorder fluctuations in the system around and above the magnetic transition and proposed that the M-I transition in the CMR materials is the Anderson localization transition – a quantum phase transition driven by magnetic disorder [12-15].

To make the discussion more concrete, let us consider a model discussed in Ref. 14 and 15 to describe the possible Anderson transition in Mn oxides.

$$H_{eff} = -\sum_{ij} \tilde{t}_{ij} d_i^+ d_j + \sum_j \varepsilon_i d_i^+ d_j + c.c \qquad (6.1)$$

Here, the first term is the double exchange Hamiltonian in which $\tilde{t}_{ij} = t\left\{cos\left(\theta_i/2\right)cos\left(\theta_j/2\right) + sin\left(\theta_i/2\right)sin\left(\theta_j/2\right)\right\}exp\left\{-i\left(\phi_i - \phi_j\right)\right\}$, with t the hopping integral in the absence of the Hund's coupling and the polar angles (θ_i, ϕ_i) characterizing the orientation of local spin $\vec{S}_i$. The second term in Eq. (6.1) represents an effective onsite disorder Hamiltonian (which should lead to the M-I Anderson transition in the model), such as the local potential fluctuations due to the substitution of R^{3+} and A^{2+}. Here ε_i stand for random on-site energies distributed

within the range $\left[-W/2, W/2\right]$. For a given composition, the diagonal disorder, namely, $\{\varepsilon_i\}$ or W, is fixed, but the bandwidth is controlled by the double exchange hopping integral. Therefore the effective strength of the disorder is determined by t'. Experimentally the disorder strength may be tuned by introducing an external magnetic field B and / or by changing the temperature T. As magnetic field B increases, the magnetic ions tend to align along the same direction so that the magnitude of t' and hence the bandwidth, increases. As T is lowered below T_c, there is spontaneous polarization that can also increase the bandwidth to reduce the disorder strength, causing an increase of thermal conductivity around the M-I transition temperature.

To analyze the effect of Cr doping, we have studied the variations of thermal parameters of $La_{0.5}Pb_{0.5}Mn_{0.85}Cr_{0.15}O_3$ sample. The present result in the Double Exchange (DE) framework suggests that Cr^{3+} must be partially ferromagnetically coupled to the Mn^{3+} and Mn^{4+} species. The doped Cr is a neighbour of Mn in the periodic table and it is generally believed that in the manganese oxides with perovskite structure, these elements exist in the form of Cr^{3+}, and Mn^{3+} and Mn^{4+} [16]. Their electronic configurations are Cr^3 : t_{2g}^3 (S = 3/2), Mn^{3+} : $t_{2g}^3 e_g^1$ (S = 2) and Mn^{4+}: t_{2g}^3 (S = 3/2), among which only the e_g^1 electron of Mn^{3+} is electronically active. The ionic radii of Cr^{3+}, Mn^{3+} and Mn^{4+} are 0.615, 0.645 and 0.531 Å respectively [17]. Due to the nearly same ionic radius, the doped Cr ions replace Mn^{3+} in the form Cr^{3+}. Cr^{3+} has the same electronic configuration (t_{2g}^3) as Mn^{4+} and hence there should be FM double exchange (FMDE) interaction between Mn^{3+} and Cr^{3+} just as that between Mn^{3+} and Mn^{4+}. It is evident that the presence of Cr^3 in the

Mn^{3+}- O^{2-}- Mn^{4+} network disturbs the lattice (increase of electron-phonon interaction) favouring the formation of polarons and hopping occurs between the different valence states of Mn in the insulating phase.

Several recent studies have suggested that the nature of the charge carriers responsible for transport in such systems above T_p is localized [10, 18-22]. The charge localization leads to a temperature dependence of thermal conductivity which can be described by two different aspects *viz.* charge localization due to lattice distortion (small polaron formation) and variable range hopping via coulomb gap. On the other hand, in low temperature phase, where the ordering of the carriers, takes place in the Mn network, favouring electron hopping from Mn^{3+} to Mn^{4+} sites leading to the FMM state due to double exchange. Hence with Cr doping in the La-Pb-Mn-O system, Mn^{3+} / Mn^{4+} ratio decreases (as Cr^{3+} acts as Mn^{4+}). But, since the Cr^{3+}- Mn^{3+} FMDE interaction is smaller than that of Mn^{3+}- Mn^{4+} [23]. The effective FMDE interaction becomes weaker with Cr doping, resulting in a gradual decrease of T_p with increasing Cr concentration. This is verified with our measurements, with T_p shifting to 256K for this sample.

For the $La_{0.7}Pb_{0.3}MnO_3$ + 2.5 wt. % Ag, it is seen that the variation of thermal conductivity and heat capacity follow the same pattern as the former two cases except for the transition temperature value. But the value of the thermal conductivity is significantly higher than the other two systems, giving an evidence of the increase in carrier concentration to Ag doping.

The specific heat capacity versus temperature curves for these three samples give the room temperature values for c_p in the range 98-108 J mol^{-1} K^{-1}. These values agree well with the previous high temperature specific heat measurements

performed on this class of materials [24-26] and with Dulong and Petit's law for a system made up of molecules containing five atoms including three light oxygen atoms. [26]. For these samples, we observe a clear anomaly in the specific heat versus temperature curve that mark the onset of long-range magnetic order. The temperature at which these peaks occur agree well with the critical temperature determined from other measurements.

6.6 Conclusions

Thermal properties of La-Pb-Mn-O system have been studied employing photopyroelectric technique. Thermal parameters of samples, namely $La_{0.5}Pb_{0.5}MnO_3$, $La_{0.5}$ $Pb_{0.5}Mn_{0.85}Cr_{0.15}O_3$ and $La_{0.7}Pb_{0.3}MnO_3$ + 2.5 wt.%Ag, are found to reflect metal-insulator transitions at temperatures 276K, 256K and 262K respectively. The results obtained are explained in terms of various models.

References

1. R. Mahendiran, R. Mahesh, A. K. Raychaudhuri and C. N. R. Rao, J. Phys. D **28** (1995) 1743.
2. R. Mahendiran, R. Mahesh, A. K. Raychaudhuri and C. N. R. Rao, Solid State Commun. **99** (1996) 149.
3. C. Zener, Phys. Rev. **82** (1951) 403.
4. A. J. Millis, B. I. Shraiman and R. Mueller, Phys. Rev. Lett. **77** (1996) 175.
5. A. Barnabe, A. Maignan, M. Hervicu, F. Damay, C. Martin and B. Ravcau, Appl. Phys. Lett. **71** (1997) 3907.
6. M. Marinelli, F. Murtas, M. G. Mecozzi, U. Zammit, R. Pizzoferrato, F. Scudieri, R. Martellucci and M. Marinelli, Appl. Phys. A **51** (1990) 387.
7. C. Preethy Menon and J. Philip, Meas. Sci. Technol. **11** (2000) 1744.
8. R. McGurie, A. Gupta, P. R. Ducombe, M. Rupp, J. Z. Sun, R. B. Laibowitz, W. J. Gallagher and G. Xiao, J. Appl. Phys. **79** (1996) 4549.
9. Aritra Banerjee, S. K. Pal and B. K. Chaudhary, Phys. Rev. B (in press).
10. A. J. Mills *et al.*, Phys. Rev. Lett. **74** (1995) 5144.
11. A. J. Mills *et al.*, Phys. Rev. Lett. 77 (1996) 175.
12. C. M. Varma, Phys. Rev. B **54** (1996) 7328.
13. E. Muller Hartmann and E. Daggoto, Phys. Rev. B **54** (1996) R6819.
14. L. Sheng *et al.*, Phys. Rev. Lett. **79** (1997)1710.
15. L. Sheng *et al.*, Phys. Rev. B **56** (1997) R7053.
16. J. Zhang, Q. Yan, F. Wang, P. Yuan and P. Z. Hang, J. Phys. Condens. Matter **12** (2000) 1981.

17. P. V. Vanitha, R. S. Singh, S. Natarajan and C. N..R. Rao, J..Solid State Chem. **137** (1998) 365.

18. H. Y. Hwang, S. W. Cheong, P. G. Radaelli, M. Marezio and B. Barlogg Phys. Rev. Lett. **75** (1995) 914.

19. G. Jettrey Synder, R. Hiskes, S. Dicarolis, M. R. Beasley and T. H. Geballe, Phys. Rev. B **53** (1996) 14434.

20. A. H. Booth, F. Bridge, G. J. Synder and T. H. Geballe, Phy. Rev. B **54** (1996) R 15606.

21. A. Gupta *et al.*, Phys. Rev. B **4** (1996) R15629.

22. M. Jaime, M. B. Salamon, M. Rubentein, R. E. Treece, J. E. Horwitz and D. B. Chrisey, Phys. Rev. B **54** (1996) 11914.

23. Aritra Banerjee, S. K. Pal and B. K. Chaudhary, J. Chem. Phys. (in press).

24. J. Tanaka and T. Mitshashi, J. Phys. Soc. Jpn. **53** (1984) 24.

25. J. E. Gordon, R. A. Fisher, Y. X. Jia, N. E. Phillips, S. E. Reklis, D. A. Wright and A. Zettl. J. Magn. Mater **177-181** (1998) 856.

26. M. R. Lees, O. A. Petrenko, G. Balakrishnan and D. Mekpaul, Phys. Rev..B **59** (1999)1298.

CHAPTER 7

Thermal properties of $La_{0.5}Sr_{0.5}Co_{1-x}Ni_xO_3$ system using PPE technique

7.1 Introduction

$LaCoO_3$ and other rare-earth cobaltates are of interest because of the peculiar way their magnetic and transport properties change with temperature [1-6]. To explain this behaviour, early work on $LaCoO_3$ established the existence of a thermally induced spin transition from low-spin Co to mostly high spin Co^{3+} [1]. Since then, many investigations have been carried cut in order to elucidate how this spin transition takes place and the material evolves from a semiconducting to a metallic behaviour as the temperature increases [7-12]. Substitution of Sr^{2+} for La^{3+} in $LaCoO_3$ brings about remarkable changes in the system [13-16]. While the $LaCoO_3$ shows high resistivity and antiferromagnetic exchange interactions, the $La_{1-x}Sr_xMnO_{3-\delta}$ materials evolve towards a ferromagnetic intermediate spin state.

Spin glass (SG) states have been found in a wide variety of systems including magnetic insulators or amorphous alloys with certain characteristic features-frozen in magnetic moments below some freezing temperature T_f, lack of periodic long-range magnetic order and magnetic relaxation over macroscopic time scales below T_f where there are changes of magnetic field. A modified version of the SG system, termed "*cluster glass*" (CG) can be considered to be a set of clusters, formed by short range ordering at some temperatures near the Curie temperature T_c.

Below T_c, the cluster glass system is expected to show SG-like behaviour with increased spin density [17, 18].

According to the phase diagram suggested for $La_{1-x}Sr_xCoO_3$ on the basis of magnetization measurements, $La_{0.5}Sr_{0.5}CoO_3$ belongs to the cluster glass phase. In this system the double exchange interaction between trivalent and tetravalent cobalt spins and exchange interaction between high spin Co^{4+} and Co^{III} is considered to be ferromagnetic, whereas the super exchange interactions between high spins Co^{3+} - Co^{3+} and Co^{4+} - Co^{4+} are antiferromagnetic. Co^{III} and Co^{3+} differs in their spin configuration, Co^{III} is in the $t_{2g}^6 e_g^0$, $^1A_{1g}$ state and Co^{3+} in $t_{2g}^4 e_g^2$, $^5T_{2g}$ state. The competition between ferromagnetic and antiferromagnetic interactions along with the randomness lead to the SG states observed for $0 \leq x \leq 0.18$. When the ferromagnetic exchange interactions first overcome the antiferromagnetic one, the cluster glass phase appears with short range ferromagnetic ordering for $0.18 \leq x \leq 0.50$ [19]. Anilkumar *et al.* [20] have concluded that the cluster glass like magnetic properties of $La_{0.5}Sr_{0.5}MnO_3$ originate from its magneto crystalline anisotropy and the compound is a long-range ordered ferromagnet. Caeiuffo *et al.* [21] have very recently reported that long-range ferromagnetic order between cluster is realized even for Sr doping as low as $x \cong 0.10$ and the transition to a spin glass state is observed only for $x \leq 0.1$. They have observed identical T_c for all compositions in the range $0.1 \leq x \leq 0.30$, contray to the previous reports that T_c varies with x in $La_{1-x}Sr_xCoO_3$.

The spin transitions in cobalt pervoskites induced by temperature and the doping of charge carriers are rather unusual and are as controversial today as when they were proposed initially [13, 22]. The ground state electronic spin configuration

of Co in its parent compound $LaCoO_3$ is the low-spin (LS) ($t_{2g}^6 e_g^0$) state. A broad transition in the magnetic susceptibility observed at ~ 100 K [6, 10] corresponds to the thermal activation of an excited state which could be either a high spin (HS) ($t_{2g}^4 e_g^2$) or an intermediate spin (IS) ($t_{2g}^5 e_g^1$) configuration. Several studies have provided evidence to support one transition type over the other but the issue still remains unsolved [3, 6-10] with the majority of new results pointing towards the sequence of LS-IS-HS with increasing temperature.

With doping, one observes a similar evolution in the magnetic and transport properties of $La_{1-x}Sr_xCoO_3$ as in the manganites [23, 24]. The competing mechanisms for activation, driven thermally and / or doping, result in the establishment of ferromagnetic Co-Co coupling through the creation of either IS or HS states. The fact that the cobalt perovskites do not exhibit colossal magnetoresistance (CMR) in spite of their high metallic conductivity suggests that fundamental differences in the strength of the spin to change and lattice coupling between the two systems exist [25].

In this chapter, we present the results of our investigations on the thermal properties of $La_{0.5}Sr_{0.5}CoO_3$ system employing the photopyroelectric technique already described. We have also taken seven samples of $La_{0.5}Sr_{0.5}Co_{1-x}Ni_xO_3$ with x = 0.0,0.1,0.2,0.3,0.4,0.5,0.6, to investigate the variation of thermal properties of $La_{0.5}Sr_{0.5}CoO_3$ upon Ni doping. Even though $LaNiO_3$ and $LaNi_{1-x}Co_xO_3$ have been studied in detail by several earlier workers [26-28], the system $La_{0.5}Sr_{0.5}Co_{1-x}Ni_xO_3$ has been studied for the very first time. Attempts have been made to explain variation of thermal properties upon Ni doping on the basis of existing models.

In the following subsections, we give details of sample preparation, experimental technique used and results obtained. A detailed discussion of the results is given at the end of the chapter.

7.2 Sample preparation

The sample $La_{0.5}Sr_{0.5}CoO_3$ was prepared by the high temperature ceramic method as reported earlier [13, 29]. Appropriate molar ratios of La_2O_3, which has been preheated at 1000 ^{0}C, cobalt oxide Co_3O_4 and $SrCO_3$ are thoroughly mixed and ball mixed for 24 hours. The powder is dried and then calcined at 1000 ^{0}C for 4 hours. The calcined powder is ground well in an agate mortar. The fine powder so obtained is pressed into pellets of thickness 1 mm and 10 mm diameter under a pressure of about 150 MPa. The so obtained sample is cut, polished and the thickness is made to $\approx$ 0.5mm for the photopyroelectric measurements.

The samples of $La_{0.5}Sr_{0.5}Co_{1-x}Ni_xO_3$ have been prepared by taking appropriate molar ratios of NiO, along with earlier constituents. The samples have been prepared by the high temperature ceramic method as already described. The so prepared samples are made to a thickness of $\approx$ 0.5mm for photopyroelectric measurements.

7.3 Experimental details

The improved photopyroelectric technique has been used to determine the thermal parameters of the samples. The details of the experimental set up have already been described in Chapter 2 of this thesis. A 120 mW He-Cd laser of wavelength λ = 442nm has been used as the optical heating source and the intensity modulation is

done by a mechanical chopper (SR540). A PVDF film of thickness 28μm, with Ni-Cr coating on both sides, is used as the pyroelectirc detector, with a pyroelectirc coefficient $P = 0.25 \times 10^{-8}$ $Vcm^{-1}K^{-1}$. The output signal is measured using a lock-in amplifier (SR830). Modulation frequency is kept above 40Hz to ensure that the detector, the sample and the backing medium are thermally thick during measurements. The thermal thickness of $La_{0.5}Sr_{0.5}CoO_3$ and $La_{0.5}Sr_{0.5}Co_{0.6}Ni_{0.4}O_3$ samples has been verified by plotting the PPE amplitude and phase with frequency at different temperatures between room temperature and 180 K and are given in figures 7.1(a) - 7.2(b) respectively.

Measurement of the PPE signal phase and amplitude enable one to determine thermal diffusivity $\alpha = k/\rho c_p$, ρ being the density and effusivity $e = \sqrt{kc_p\rho}$ respectively [30]. From the measured values of α and e, K and c_p of the samples are determined, knowing density ρ. Density of the samples is measured using Archimedes principle. The calibration of the experimental set up has been done prior to carry out the measurements as described in detail in Chapter 2 of the thesis. Measurements as a function of temperature have been made at a heating rate of approximately 0.5K/min and data collected in every 1K interval normally and at closer intervals near the M-I transition temperature. The temperature is measured with a platinum sensor placed close to the sample inside the measurement chamber.

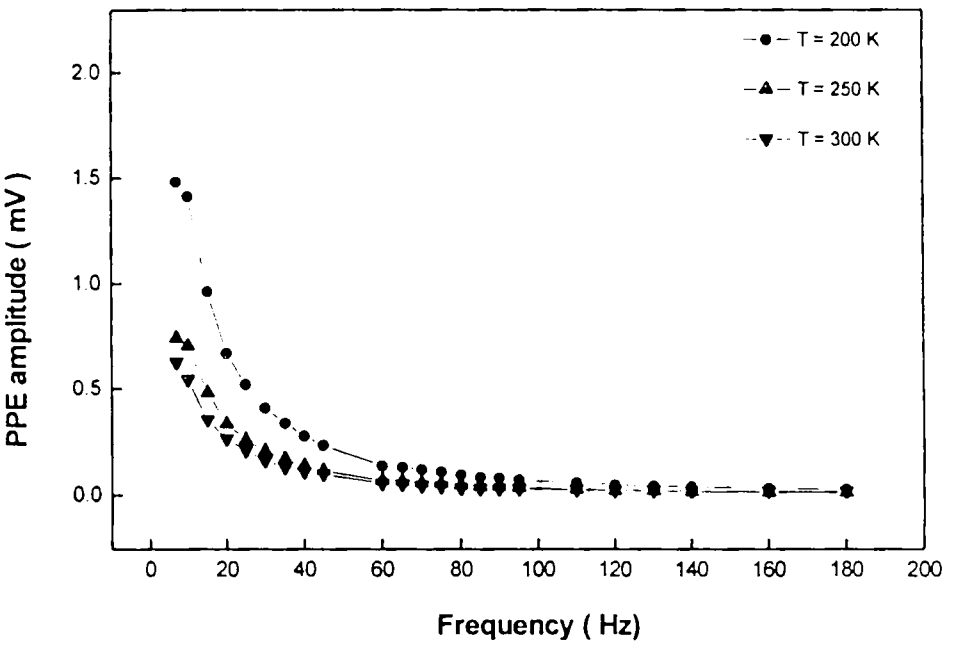

Fig. 7.1(a): Frequency dependence of PPE amplitude of $La_{0.5}Sr_{0.5}CoO_3$ sample at three temperatures

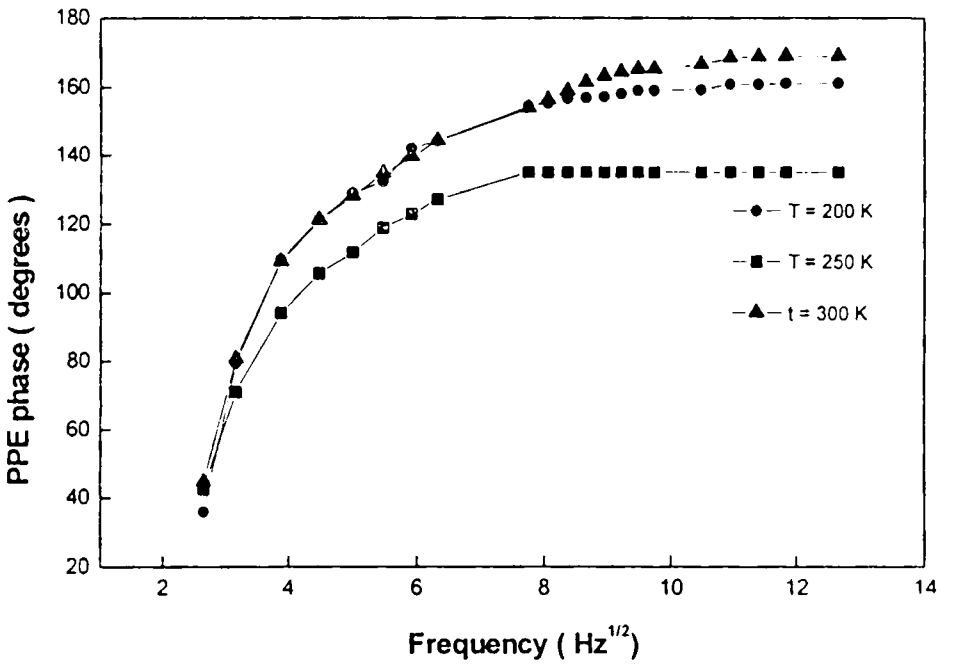

Fig. 7.1(b): Frequency dependence of PPE phase of $La_{0.5}Sr_{0.5}CoO_3$ sample at three temperatures

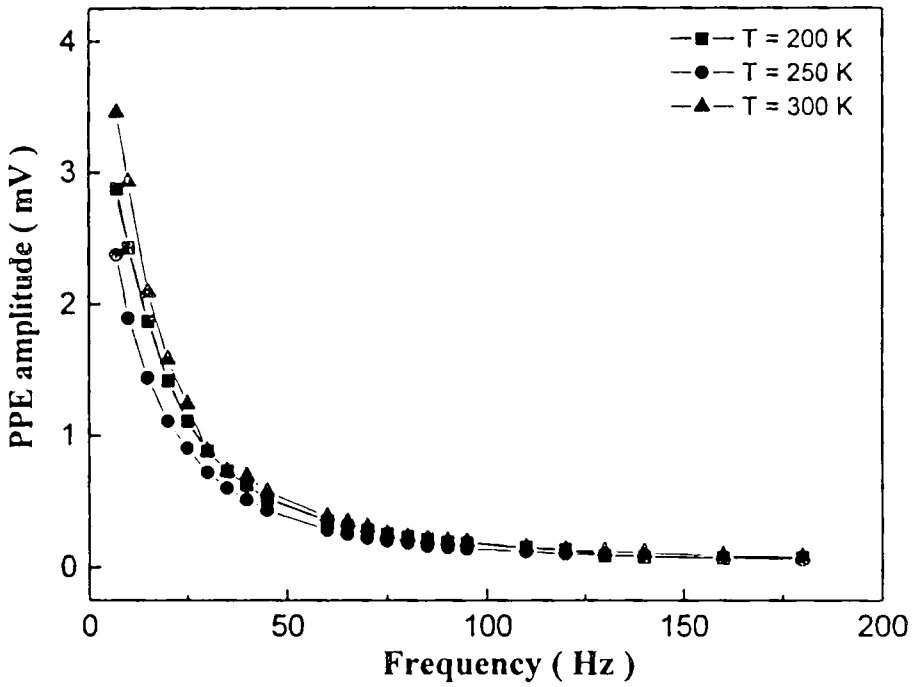

Fig. 7.2(a): Frequency dependence of PPE amplitude of $La_{0.5}Sr_{0.5}Co_{0.6}Ni_{0.4}O_3$sample at three temperatures

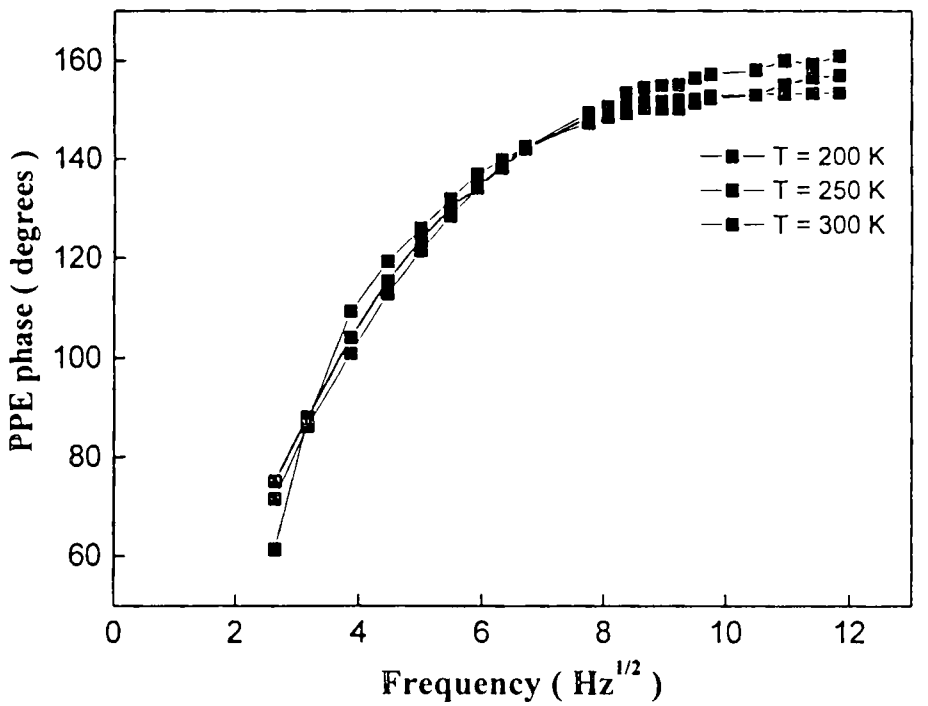

Fig. 7.2(b): Frequency dependence of PPE phase of $La_{0.5}Sr_{0.5}Co_{0.6}Ni_{0.4}O_3$sample at three temperatures

7.4 Results

Figures 7.3(a) and 7.3(b) show the variation of PPE amplitude and phase with temperature for the $La_{0.5}Sr_{0.5}CoO_3$ sample. It is seen that the PPE amplitude decreases monotonically with temperature, unlike the cases described in chapters 5 and 6. The PPE phase also behaves in a similar manner, with a gradual decrease in its value with temperature. No anomaly is observed in either the PPE amplitude or phase as the temperature is varied from room temperature to $\approx$ 150 K.

Fig. 7.4 shows the variation of thermal diffusivity and thermal effusivity of $La_{0.5}Sr_{0.5}CoO_3$ sample with temperature. It is seen that thermal diffusivity shows a gradual decrease, with no anomaly at any of the temperatures. Since the thermal diffusivity is directly proportional to PPE phase, behaviours of α vs T is almost identical to the variations in PPE phase. Thermal effusivity shows a gradual increase from 180 K upto room temperature. The behaviour of these two parameters is an indication that no M-I transition occurs for the $La_{0.5}Sr_{0.5}CoO_3$ sample, with the system showing pure metallic behaviour throughout the scanned temperature range.

Fig.7.5 shows the variation of thermal conductivity and heat capacity of $La_{0.5}Sr_{0.5}CoO_3$ sample with temperature. It is seen that thermal conductivity shows a pattern similar to thermal diffusivity variation, whereas heat capacity increases with temperature. Thermal conductivity variation with temperature highlights the metallic nature of $La_{0.5}Sr_{0.5}CoO_3$ sample with no M-I transition seen between 180 K and 300 K.

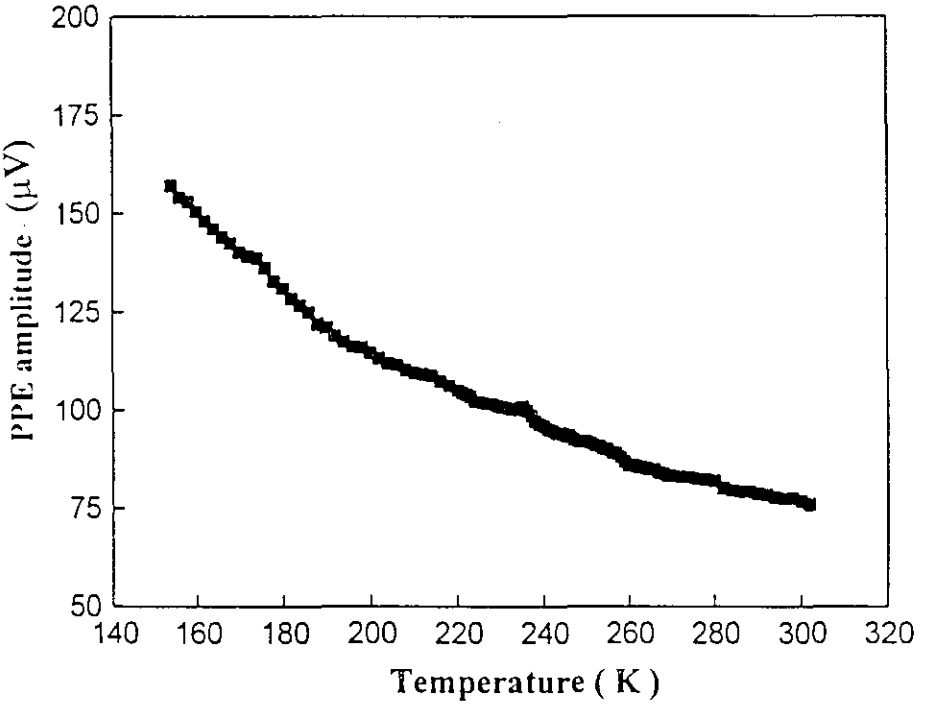

Fig. 7.3(a): Variation of PPE amplitude with temperature of $La_{0.5}Sr_{0.5}CoO_3$ sample

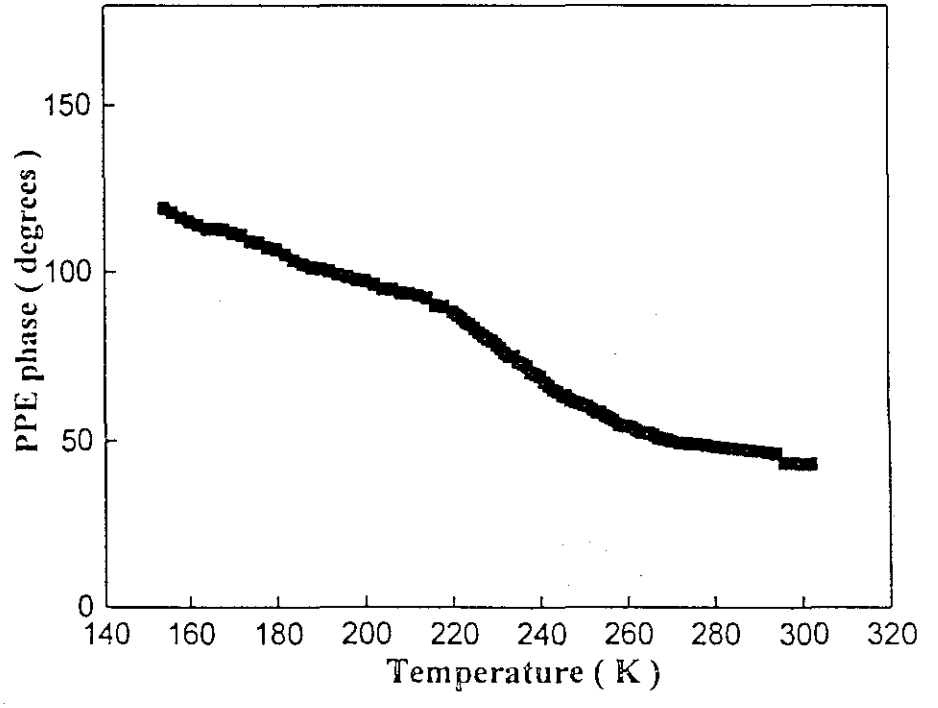

Fig. 7.3(b): Variation of PPE phase with temperature of $La_{0.5}Sr_{0.5}CoO_3$ sample

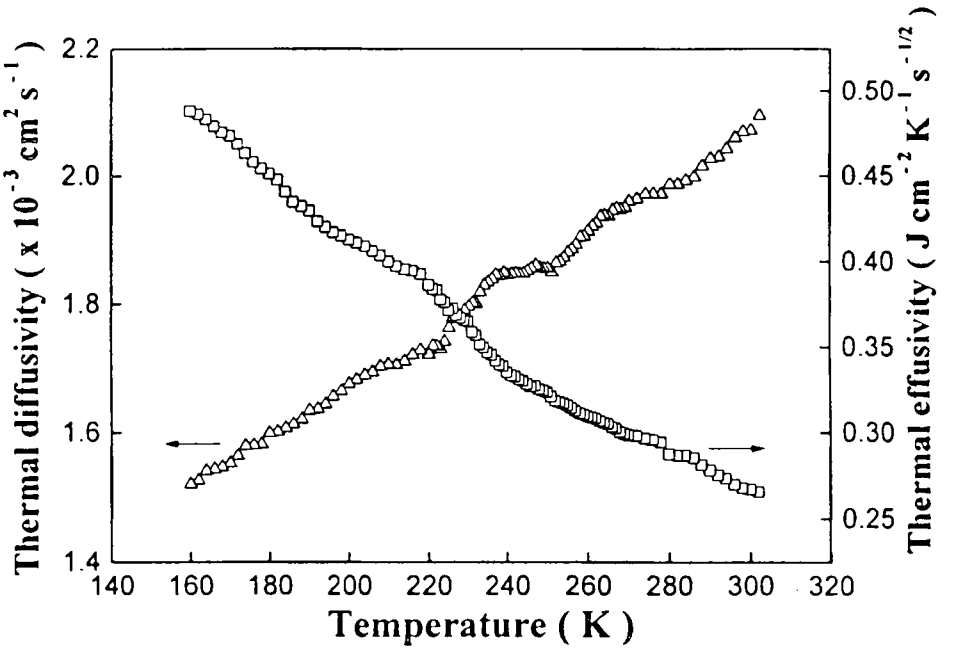

Fig. 7.4: Variation of thermal diffusivity and thermal effusivity with temperature of $La_{0.5}Sr_{0.5}CoO_3$ sample

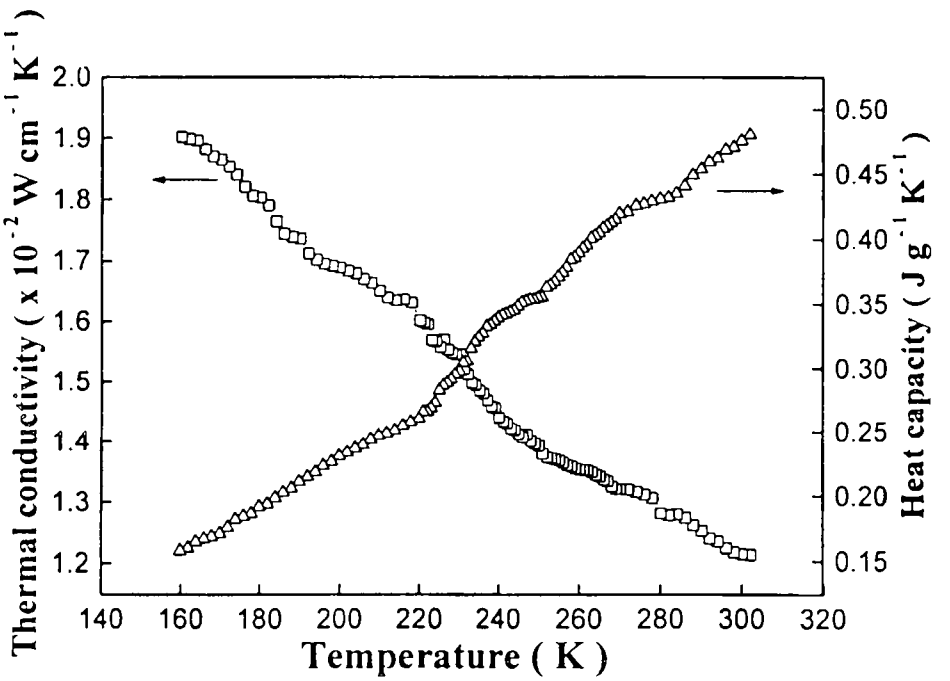

Fig. 7.4: Variation of thermal conductivity and heat capacity with temperature of $La_{0.5}Sr_{0.5}CoO_3$ sample

Now to highlight the effect of Ni doping on $La_{0.5}Sr_{0.5}CoO_3$ system we have measured the thermal parameters of Ni doped $La_{0.5}Sr_{0.5}Co_{1-x}Ni_xO_3$ system with x = 0.0, 0.1, 0.2, 0.4, 0.5, 0.6. Fig. 7.6 shows the variation of thermal diffusivity and thermal effusivity with Ni concentration. It is seen that up to 0.6 %, thermal diffusivity increases monotonically with Ni content, showing that Ni doped $La_{0.5}Sr_{0.5}CoO_3$ system shows a metallic nature up to 0.6 % of Ni. Thermal effusivity increases more rapidly up to 0.4 % and thereafter shows a slight decrease in its value.

Fig. 7.7 shows the variation of density with Ni concentration. It is seen that density shows almost a linear variation with Ni content. The maximum error expected in the value of density is ≈ 1%.

Fig. 7.8 shows the variation of thermal conductivity and heat capacity with Ni concentration. Unlike thermal diffusivity, which shows a gradual increase with composition, thermal conductivity shows a more rapid increase upto 0.4 % and thereafter the value is almost constant for the other two compositions. Heat capacity also behaves in a similar manner. These behaviours also suggest the metallic nature of Ni doped samples. So composition dependent M-I transition predicted for this system is not observed upto 0.6 at. % of Ni, which is in agreement wit earlier similar systems.

Now to analyze the temperature dependent behaviour of Ni doped $La_{0.5}Sr_{0.5}CoO_3$ system, we have done measurements from 180 K on 0.4 % Ni doped $La_{0.5}Sr_{0.5}CoO_3$ systems.

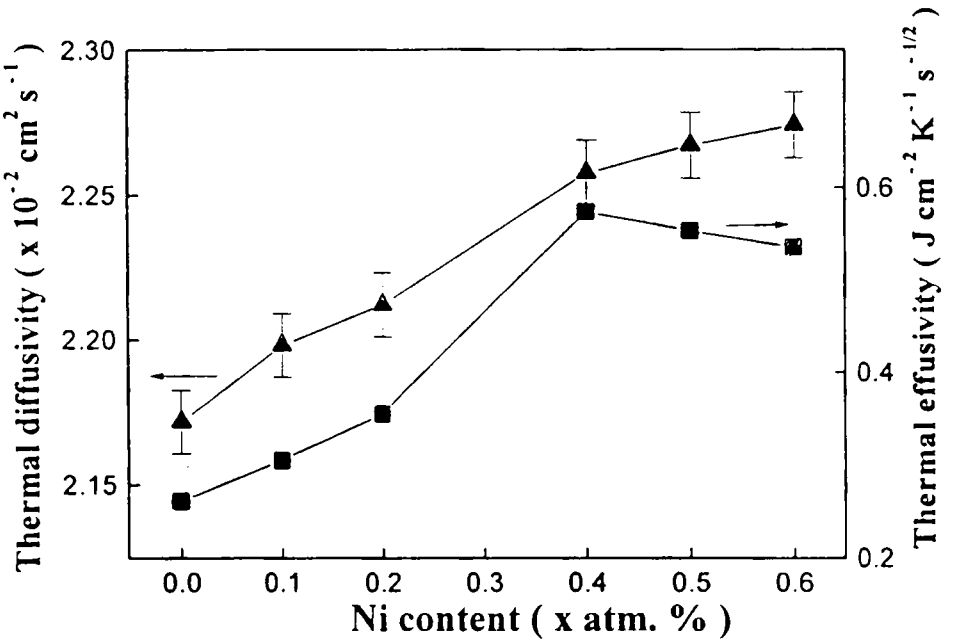

Fig. 7.6: Variation of thermal diffusivity and thermal effusivity with Ni content of $La_{0.5}Sr_{0.5}Co_{1-x}Ni_xO_3$ system

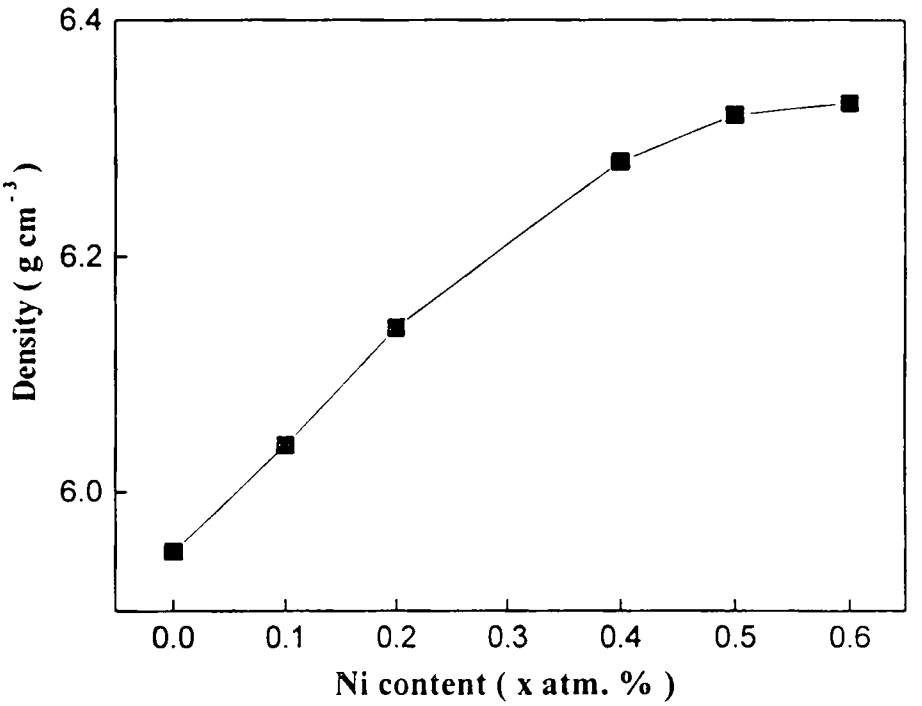

Fig. 7.7: Variation of density with Ni content of $La_{0.5}Sr_{0.5}Co_{1-x}Ni_xO_3$ system

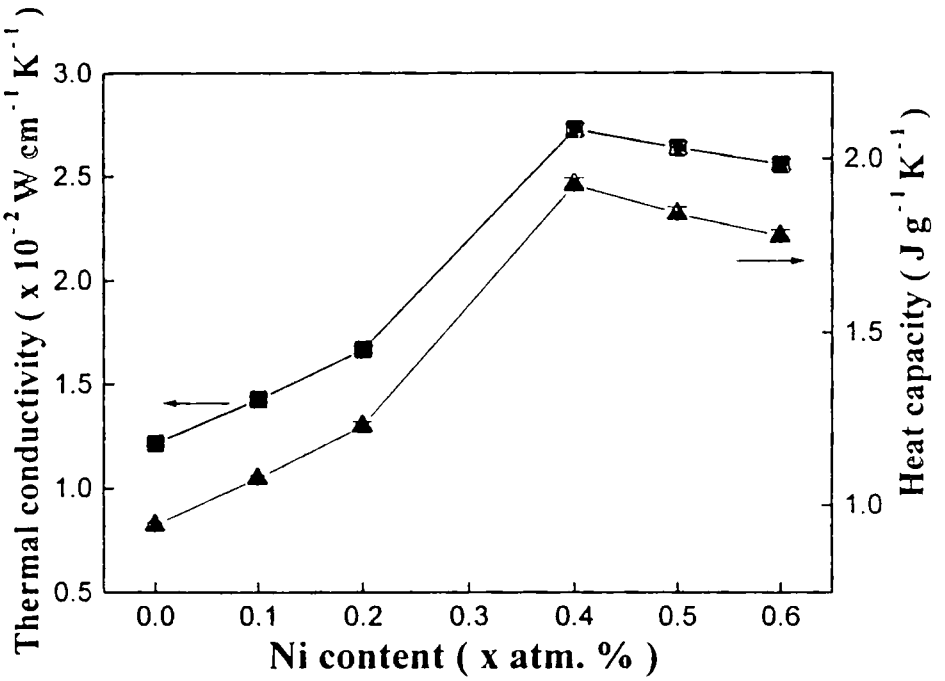

Fig. 7.8: Variation of thermal conductivity and heat capacity with Ni content of $La_{0.5}Sr_{0.5}Co_{1-x}Ni_xO_3$ system

Fig. 7.9(a) and 7.9(b) exhibit the variation of PPE amplitude and phase with temperature for $La_{0.5}Sr_{0.5}Co_{0.6}Ni_{0.4}O_3$ sample. As in the earlier case, both PPE amplitude and phase do not show any anomaly throughout the temperature range. The observed variation follow the pattern seen in $La_{0.5}Sr_{0.5}CoO_3$ sample.

Fig. 7.10 shows the variation of thermal diffusivity and thermal effusivity with temperature. Thermal diffusivity decreases with temperature, similar to the PPE phase variation and thermal effusivity increases with temperature. The values of α throughout the temperature range has been increased substantially upon Ni doping. Thermal effusivity shows an increasing behaviour with temperature.

Fig. 7.11 shows the variation of thermal conductivity and heat capacity of this sample. The variations of both K and c_p are identical to that of the parent sample $La_{0.5}Sr_{0.5}CoO_3$. As in the case of α, value of K increases substantially upon Ni doping.

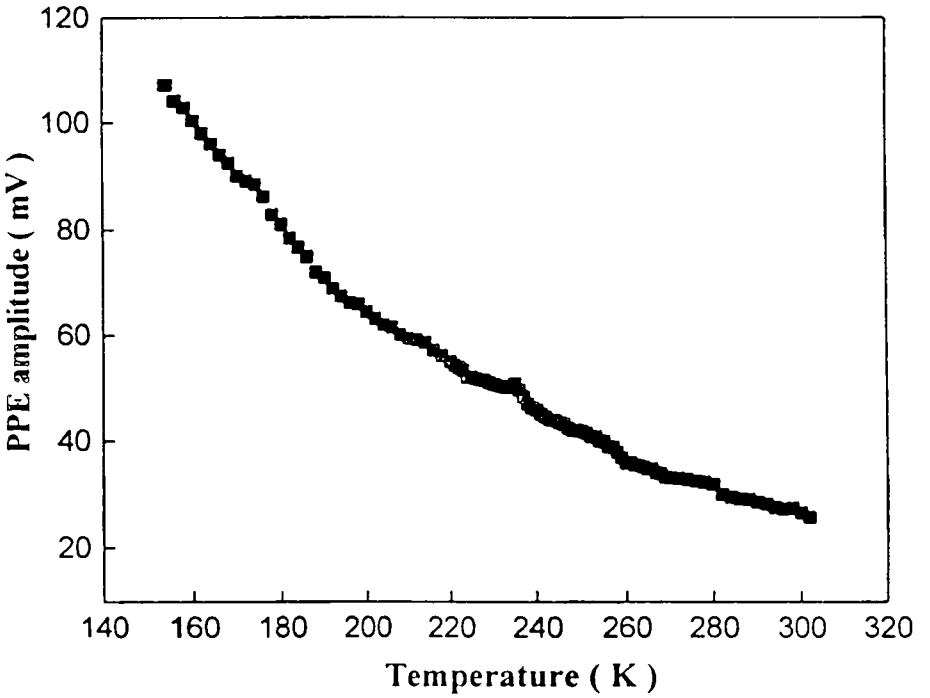

Fig. 7.9(a): Variation of PPE amplitude with temperature at $La_{0.5}Sr_{0.5}Co_{1-x}Ni_xO_3$ system

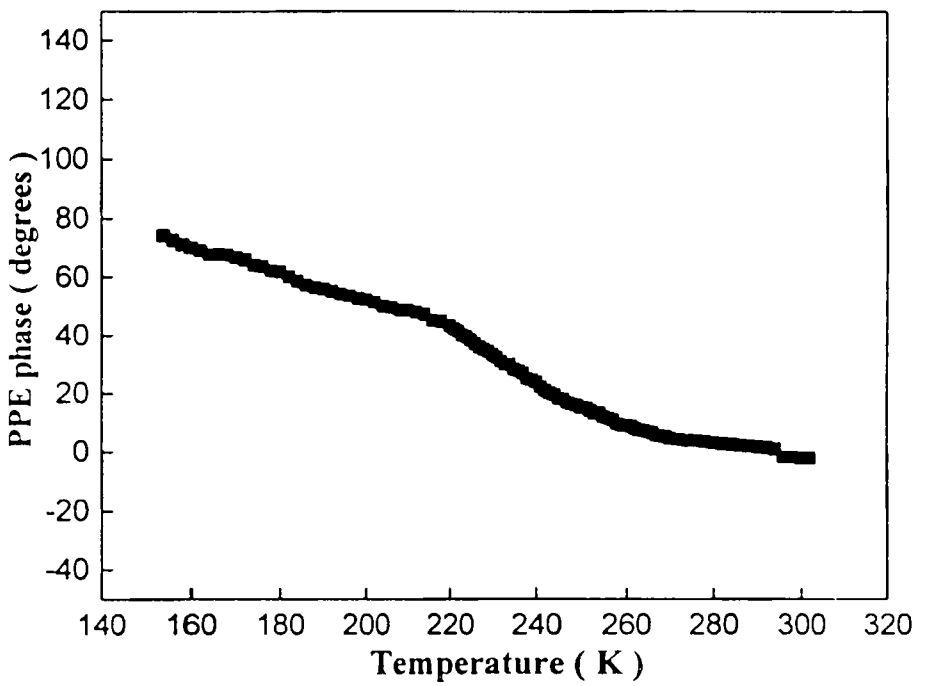

Fig. 7.9(b): Variation of PPE phase with temperature at $La_{0.5}Sr_{0.5}Co_{1-x}Ni_xO_3$ system

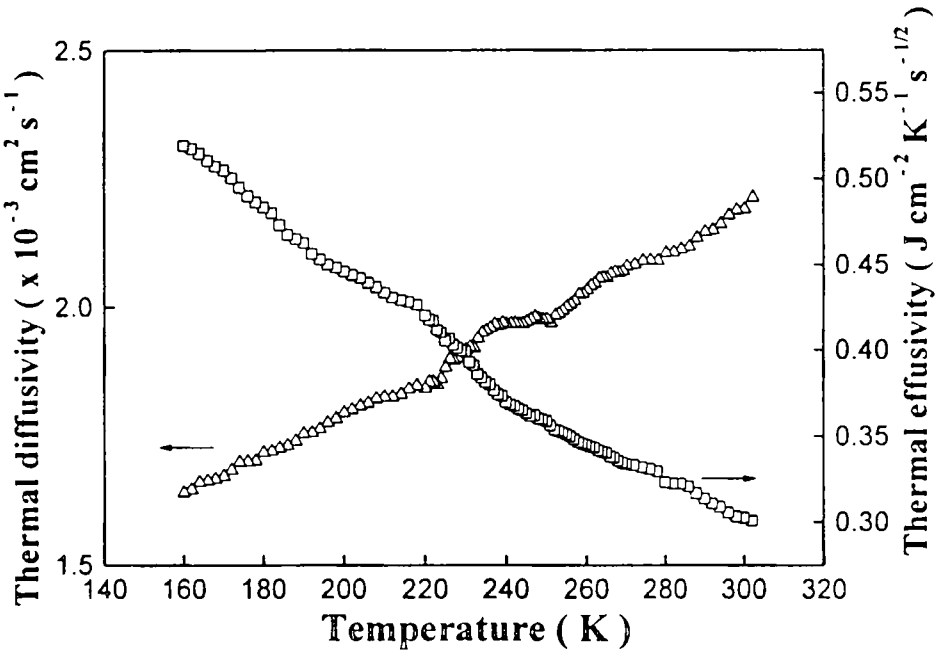

Fig. 7.10: Variation of thermal diffusivity and thermal effusivity with temperature of $La_{0.5}Sr_{0.5}Co_{1-x}Ni_xO_3$ system

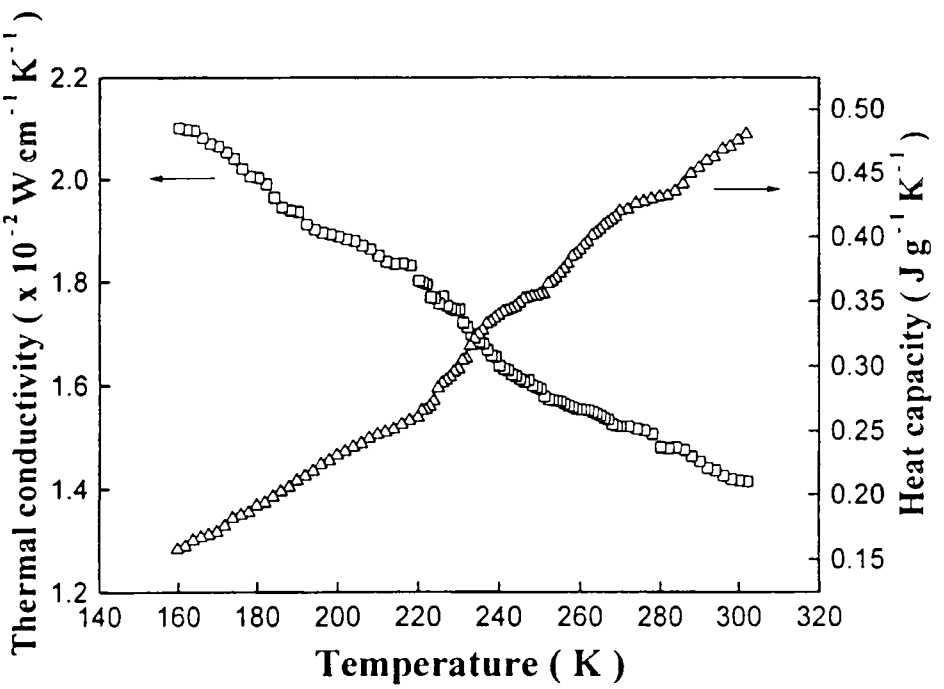

Fig. 7.11: Variation of thermal conductivity and heat capacity with temperature of $La_{0.5}Sr_{0.5}Co_{1-x}Ni_xO_3$ system

7.5 Discussion of the results

The observed variation of thermal parameters in $La_{0.5}Sr_{0.5}CoO_3$ can be explained as follows. In $LaCoO_3$, all the cobalt ions are in the diamagnetic low-spin configuration at very low temperatures. The low spin Co^{III} ($t_{2g}^6 e_g^0$, $^1A_{1g}$) is, however, more stable with respect to high spin Co^{3+} ($t_{2g}^4 e_g^2$, $^5T_{2g}$) by only about 0.05 eV. With increase of temperature, the Co^{III} ions transform to Co^{3+}. Raccah and Goodenough [14] identified a symmetry change from $R\bar{3}$ to $R\bar{3}$ after this ordering and also observed a transition due to de localization of the e_g electrons (localized at lower temperatures at high-spin Co^{3+} ions) to σ^*- band electrons at 1210 K. Beyond this e_g - σ^* transition, $LaCoO_3$ becomes metallic.

Substitution of Sr^{2+} for La^{3+} in $LaCoO_3$ leads to high resistivity and antiferromagnetic exchange interactions; the $La_{1-x}Sr_xCoO_3$ materials evolve towards a ferromagnetic intermediate spin state with σ^* electrons, as x increases [22]. Bahadur *et al.* [31] have reported Mössbauer data supporting the intermediate spin state for the ferromagnetic regions of their samples. According to early literature, the x = 0.5 composition is a good conductor ($\rho < 10^{-1}$ Ωcm) and has a metallic temperature coefficient. In addition, it is a ferromagnet. Early studies on $La_{1-x}Sr_xCoO_3$ led to the suggestion that in the doped samples, paramagnetic La^{3+} regions coexist with ferromagnetic Sr^{2+} rich clusters in the same crystallographic phase, the ferromagnetic component increasing with x.

The ferromagnetism observed in the system $La_{1-x}Sr_xCoO_3$ could be due to one of the following three mechanisms (1) ordering of high spin and low spin cations through ferromagnetic super exchange between them via the intervening

oxygen ion [22, 33] (2) Zener double exchange [33] (3) itinerant-electron ferromagnetism [14, 22]. The first mechanism, based on a localized electron model due to Anderson, was modified by Goodenough to account for the ferromagnetic interactions observed in the system. He showed that if octahedral site magnetic cations are located on opposite side of a common anion, they interact ferromagnetically if one cation has completely empty e_g orbitals and the other was half filled e_g orbitals. But, later this mechanism was abandoned in favour of the itinerant electron ferromagnetism

As per the phase diagram for $La_{1-x}Sr_xCoO_3$, shown in Fig. 7.14, suggested by Goodenough, $La_{0.5}Sr_{0.5}CoO_3$ belongs to the cluster glass phase. In this system, the double exchange between the trivalent and tetravalent cobalt spins and the exchange interaction between high spin Co^{4+} and low spin Co^{III} is considered to be ferromagnetic whereas the super exchange interactions between high spin (Co^{3+}-Co^{3+}, Co^{4+}-Co^{4+}) are antiferromagnetic. The competition between the ferromagnetic and antiferromagnetic interactions along with the randomness lead to SG states observed for $0 \leq x \leq 0.18$ – when the ferromagnetic exchange interactions just overcome the antiferromagnetic one, the cluster glass phase appears with short range ferromagnetic ordering ($0.18 \leq x \leq 0.5$) [22].

In addition to the difference between the field dependences of magnetoresistance, doped cobaltates and manganates have other important differences. One noteworthy difference is between their zero-field resistivities. In the manganate system $La_{1-x}A_xMnO_3$, the resistivity is activated in the paramagnetic state (i.e., for $T > T_c$, $d\rho/dT < 0$) and as T is decreases it shows a peak at $T \cong T_c$, and for $T < T_c$, ρ shows metallic behaviour (*i.e.*, $d\rho/dT > 0$). This peak in ρ is taken as a

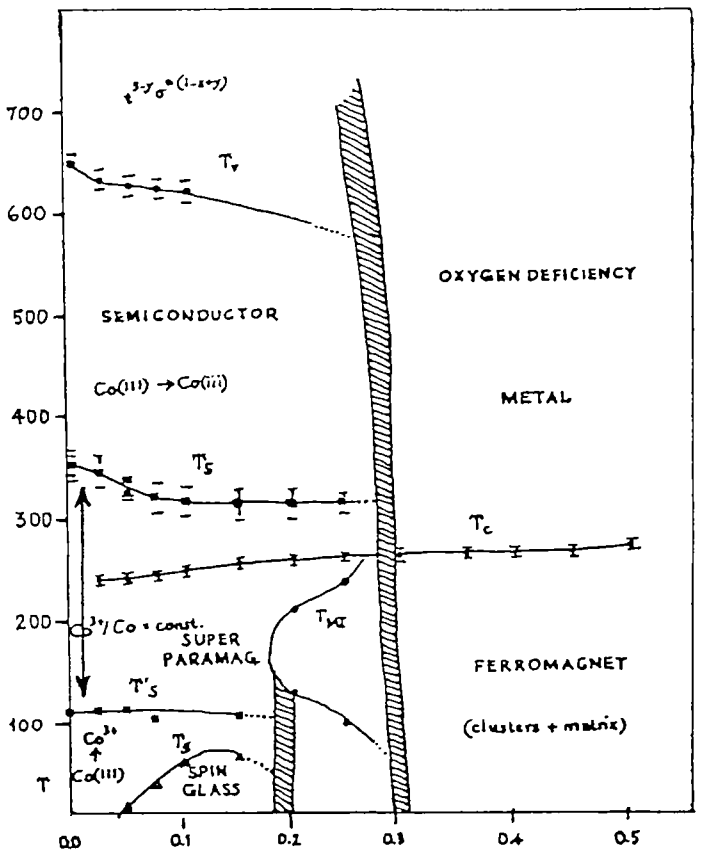

Fig. 7.14: Phase diagram of $La_{1-x}Sr_xCoO_3$ system

signature of an insulator-metal transition. In the cobaltate system, no such peak is seen in ρ as a function of T, implying that there is no temperature-driven insulator-metal transition in the system. In this system the insulator-to-metal transition is brought about by changing the composition and occurs when the system is already ferromagnetic as well as metallic due to the mixed valency of the transition properties. The main difference is likely to arise from the electronic / spin structure and the coupling of the lattice distortions to the spins. Mn^{4+} has a $t_{2g}^3 e_g^0$ configuration, while Co^{4+} in the high-spin state has a $t_{2g}^3 e_g^2$ configuration. The existence of empty e_g orbitals in Co^{4+} may be responsible for the qualitative difference in the electronic transport behaviour.

The effect of Co doping on the La-Ni-O system has been studied in detail by earlier workers. Thermal and electric properties of $LaNi_{1-x}Co_xO_3$ have been dealt with in detail in ref. [26]. It is seen that while $LaNiO_3$ is metallic, $LaCoO_3$ is an insulator. Co^{3+} is in the low-spin state (t_{2g}^6, e_g^0) at low enough temperature ($T <$ 200K), the conduction band σ^* band formed by the e_g state and oxygen p-orbitals is empty and the t_{2g} band is full. At higher temperatures, $T >$ 200 K, the Co ion undergoes a transition to a high-spin state $t_{2g}^4\ e_g^2$; which populates the σ^* band and the conductivity increases. [26]. The substitution of Co also introduces disorder because of the difference in the 3*d* levels [$E^{3d}(Co) - E^{3d}(Ni) \cong 1eV$]. Most probably, *the M-I transition in this material occurs in the* σ^* *band. Previous studies on* $LaNi_{1-x}Co_xO_3$ have shown that as x is increased, $d\sigma/dT$ (at room temperature) changes sign for x =0.4, which corresponds to $n \cong 10^{22}$ / cm^3. This electron concentration is estimated from the assumption that each Ni^{3+}contributes one electron to the conduction band.

The results we obtained on thermal conductivity also have similar pattern, with the thermal conductivity increasing up to x = 0.6 (corresponding to Co concentration of 0.4), suggesting that Ni doping introduces disorder in the system causing as increase in the thermal conductivity.

7.6 Conclusions

Thermal parameters viz., thermal conductivity, thermal diffusivity, thermal effusivity and heat capacity of $La_{0.5}Sr_{0.5}CoO_3$ have been measured between 180 K and 300 K. It is seen that the system is metallic throughout the temperature range and we can say that no temperature dependent M-I transition is observed. To analyze

the effect of Ni doping on of $La_{0.5}Sr_{0.5}CoO_3$, we have measured composition dependent variations of α, e, K and c_p. The thermal conductivity is found to increase with Ni content. We have also measured the temperature dependence of thermal conductivity and heat capacity on $La_{0.5}Sr_{0.5}Co_{0.6}Ni_{0.4}O_3$ sample. As in the former case, this system also does not exhibit any temperature dependent M-I transition.

References

1. W. C. Koehler and E. O. Wollan, J. Phys. Chem. Solids **2** (1957) 100.
2. R. R. Heikes, R. C. Muller and R. Mazelsky, Physica **30** (1964) 1600.
3. P. M. Raccah and J. B. Goodenough, Phys. Rev. **155** (1967) 932.
4. N. Menyuk, K. Dwight and P. M. Raccah, J. Phys. Chem. Solids **28** (1967) 549.
5. G. Thornton, B. C. Tofield and D. E. Williams, Solid State Commun. **44** (1982) 1213.
6. V. G. Bhide, D. S. Rajoria, G. R. Rao and C. N. R. Rao, Phys. Rev. B **6** (1972) 1021.
7. G. Thornton, F. C. Morrison, S. Parrington, B. C. Tofield and D. E. Williams, J. Phys. C: Solid State Phys. **21** (1988) 287.
8. K. Asai, P. Gehring, H. Chou and G. Shirane, Phys. Rev. B **43** (1989) 10982.
9. T. Arunakavalli, G. U. Kulkarni and C. N. R. Rao, J. Solid State Chem. **107** (1993) 299.
10. M. Abbate, J. C. Fuggle, A. Fcyimori, L. H. Tjeng, C. T. C. R. Potze, G. A. Sawatzky, H. Eisaki and S. Uchida, Phys. Rev. B **47** (1993) 16124.
11. S. R. Barman and D. D. Sharma, Phys. Rev. B **49** (1995) 13979.
12. M. A. Señaïs-Rodrïguez and J. B. Goodenough, J. Solid State Chem. **116** (1995) 224.
13. G. H. Jonker and J. H. vansanten, Physica **19** (1953) 120.
14. P. M. Raccah and J. B. Godenough, J. Appl. Phys. **39(2)** (1968) 13.
15. V. G. Bhide, D. S. Rajoria, C. N. R. Rao, G. Rama Rao and V. G. Jadhao, Phys. Rev. B **12** (1975)

16. C. N. R. Rao, O. M. Parkash, D. Bahadur, P. Ganguly and S. Nagabhushana, J. Solid State Chem. **22** (1977) 353.

17. *Spin glasses*, edited by K. H. Fischer and J. A. Hertz (Cambridge University Press, Cambridge, England, 1991).

18. J. A. Mydosh, *Spin glasses: An Experimental Introduction* (Taylor and Francis, London, 1993).

19. M. Itoh, I. Natori, S. Kubota and K. Motoya, J. Phys. Soc. Jpn. **63** (1994) 1486.

20. P. S. Anilkumar, P. A. Joy and S. K. Date, J. Phys: Condens. Matter **10** (1998) L487.

21. R. Caciuffo, D. Rinaldi, G. Barucca, J. Mira, J. Rivas, M. A. Senaris – Rodrigues, P. G. Radaelli, D. Fiorani and J. B. Goodenough, Phys. Rev. B **59** (1999) 3025.

22. J. B. Goodenough, J. Phys. Chem. Solids 6 (1958) 287; Mater. Res. Bull. **6** (1971) 967.

23. H. Yamaguchi, H. Taniguchi, H. Takagi, T. Arima and Y. Sakata, J. Phys. Soc. Jpn. **64** (1995) 1885.

24. A. R. Ibalta, R. Mahendiran, C. Marguina, B. Garcialanda, Phys. Rev. B **57** (1998) R3217.

25. Y. Yamaguchi, Y. Okimoto, H. Taniguchi and Y. Tokura, Phys. Rev. B **53** (1996) R2926.

26. K. Sreedhar, J. M. Honig, M. Darwin, M. Mc Elfresh, P. M. Shand, J. Xu, B. C. Crooker and J. Spalek, Phys. Rev. B **46** (1992) 6382.

27. K. P. Rajeev and A. K. Raychaudhuri, Phys. Rev. B **46** (1992) 1309.

28. K. P. Rajeev, G. V. Shivasankar and A. K. Raychudhuri, Solid State Commun. **79** (1991) 591.

29. P. Ganguli, P. S. Anilkumar, P. N. Santhosh and I. S. Mulla, J. Phys.: Condens. Matter. **6** (1994) 533.

30. C. Preethy Emnon and J. Philip, Meas. Sci and Technol **11** (2000) 1744.

31. D. Bahadur, S. Kollali, C. N. R. Rao, M. J. Patni and C. K. Srivastava, J. Phys. Chem. Solids **40** (1979) 981.

32. P. W. Anderson, Phys. Rev. **79** (1950) 350; **79** (1950) 705.

33. C. L. Zener, Phys. Rev. **82** (1951) 403.

CHAPTER 8

Summary and Conclusions

A complete characterization of thermal properties of a material requires the determination of thermal properties such as thermal diffusivity, thermal effusivity, thermal conductivity and heat capacity. Simultaneous determination of thermal conductivity and heat capacity, as a function of temperature would be highly informative since it would allow studies of critical behaviours of thermal parameters when the material undergoes a phase transition. The overall aim of the work presented in this thesis is to present the photopyroelectric spectroscopy as an ideal technique for the thermal characterization of samples near solid-state phase transitions.

The photopyroelectric (PPE) technique involves measurements of the temperature increase of a sample due to the absorption of radiation by placing a pyroelectric detector in thermal contact with the sample. The photopyroelectric effect has a number of advantages over other temperature detection techniques, such as its extreme simplicity, good sensitivity and non-destructive probing ability. PPE spectroscopy is less complex and less expensive than photoacoustic and photothermal deflection spectroscopies. In PPE measurements, the sample is heated by a modulated light beam on one side and a pyroelectric detector detects the temperature oscillations on the opposite side of the sample.

This thesis presents in detail, the theoretical developments and calculations which are used for the simultaneous determination of thermal parameters, namely

thermal diffusivity (α), thermal effusivity (e), thermal conductivity (K) and heat capacity (c_p) employing photopyroelectric technique. In our calculations, we have assumed that the pyroelectric detector is supported on a copper backing, so that there will be sufficient heat exchange between the heated pyroelectric detector and the backing so that the signal fluctuations are reduced to a minimum. Since the PPE signal depends on the properties of the detector that are also temperature dependent, a careful temperature calibration of the system need to be carried out. APPE cell has been fabricated for the measurements that can be used to measure the thermal properties of solid samples from $\approx$ 90 K to $\approx$ 350 K. The cell has been calibrated using standard samples and the accuracy of the technique is found to be of the order of $\pm$ 1%.

In this thesis, we have taken up work n photopyroelectric investigation of thermal parameters of ferroelectric crystals such as Glycine phosphite ($NH_3CH_2COOH_3PO_3$), Triglycine sulfate and Thiourea as well as mixed valence perovskites samples such as Lead doped Lanthanum Manganate ($La_{1-x}Pb_xMnO_3$) Calcium doped ($La_{1-x}Ca_xMnO_3$) and Nickel doped Lanthanum Stroncium Cobaltate ($La_{0.5}Sr_{0.5}Ni_xCo_{1-x}O_3$).The three ferroelectric crystals are prepared by the slow evaporation technique and the mixed valence perovskites by solid state reaction technique.

Mixed valence perovskites, with the general formula $R_{1-x}A_xMnO_3$ (R = La, Nd or Pr and A = Ba, Ca, Sr or Pb) have been materials of intense experimental and theoretical studies over the past few years. These materials show '*colossal magnetoresistance*' (CMR) in samples with $0.2 < x < 0.5$ in such a doping region, resistivity exhibits a peak at $T = T_p$, the metal – insulator transition temperature. The

system exhibits metallic characteristics with $^{d\rho}/_{dT} > 0$above T_p (whereρ is the resistivity) and insulating characteristics with $^{d\rho}/_{dT} < 0$ above T_p. Despite intensive investigations on the CMR phenomena and associated electrical properties, not much work has been done on the variation of thermal properties of these samples. We have been quite successful in finding out the nature of anomaly associated with thermal properties when the sample undergoes M-I transition.

The ferroelectric crystal showing para-ferroelectric phase transitions - Glycine phosphite, Thiourea and Triglycine sulfate – are studied in detail in order to see how well the PPE technique enables one to measure the thermal parameters during phase transitions. It is seen that the phase transition gets clearly reflected in the variation of thermal parameters. The anisotropy in thermal transport along different crystallographic directions are explained in terms of the elastic anisotropy and lattice contribution to the thermal conductivity. Interesting new results have been obtained on the above samples and are presented in three different chapters of the thesis.

In summary, we have carried investigations of the variations of the thermal parameters during phase transitions employing photopyroelectric technique. The results obtained on different systems are important not only in understanding the physics behind the transitions but also in establishing the potentiality of the PPE tool. The full potential of PPE technique for the investigation of optical and thermal properties of materials still remains to be taken advantage of by workers in this field. There is lot of scope for doing good work to get important results on the thermal properties of materials and to do instrumentation development work in the field.